CRANFIELD UNIVERSITY

WILLIAM SEAN JAMES

WIRE + ARC ADDITIVE MANUFACTURING FOR HIGH-SPEED FLIGHT

SCHOOL OF AEROSPACE, TRANSPORT AND MANUFACTURING
Welding and Additive Manufacturing Centre

PhD in Manufacturing

PhD
Academic Year: 2022 - 2023

Supervisor: Dr Supriyo Ganguly
Associate Supervisor: Dr Goncalo Rodrigues Pardal
January 2023

CRANFIELD UNIVERSITY

SCHOOL OF AEROSPACE, TRANSPORT AND MANFACTURING
Welding and Additive Manufacturing Centre

PhD in Manufacturing

PhD

Academic Year 2022 - 2023

WILLIAM SEAN JAMES

Wire + Arc Additive Manufacturing for High-speed Flight

Supervisor: Dr Supriyo Ganguly
Associate Supervisor: Dr Goncalo Rodrigues Pardal
January 2023

This thesis is submitted in partial fulfilment of the requirements for the degree of Doctor of Philosophy

ABSTRACT

The use of Wire + Arc Additive Manufacturing (WAAM) to manufacture high-speed projectiles, such as missiles, is currently an industry challenge due to the nature of high-speed flight and the extreme environment that components are exposed to. Alloys that are suitable for high-speed flight are creep resistant superalloys, this is due to the aggressive heating environment experienced by objects in high-speed flight, and the need for performance at extremely high temperatures. These materials are currently expensive and difficult to manufacture, which is less than ideal for non-recoverable systems such as airborne weapons. The development of missile systems requires flight tests to be affordable and operate in quick succession, to which rapid prototyping offers a significant advantage. The use of traditional manufacturing methods and supply-chain for this purpose are logistically challenging and expensive, mainly due to loss of material though machining. The use of WAAM in a rapid prototyping capability is the driver for this research. To be able to use the process to manufacture and prototype components for high-speed applications, would, if possible, be an excellent solution to reducing the amount of time and money that it currently costs to flight-test and develop these systems. WAAM could also be used for final design production.

The effect WAAM route has on the high temperature properties of superalloys is largely unknown. This research is therefore focused on the development of the WAAM process, and selection of alloys suitable for high-speed flight and for WAAM deposition. Four creep-resistant superalloys underwent deposition using a plasma WAAM process and the resulting material was characterised to understand how WAAM affects high temperature performance. The research also investigates post-deposition heat-treatment of these alloys and develops parameters for inter-pass machine hammer peening to improve material performance.

The findings from this project increases the understanding between the WAAM process and superalloy strengthening mechanisms and develops a method to increase the performance of additive manufactured material. The most appropriate alloys for both WAAM and the high-speed flight application were ranked and down selected based on their anticipated performance and weldability. The selected alloys then underwent extensive testing from room temperature to 1000 °C, to understand the performance of WAAM built structures at high temperature. The microstructure is examined throughout and found key differences between solid-solution strengthened and age hardened alloys which effects performance. Finally, in-process machine hammer peening was investigated for age hardened Rene 41 and found to greatly increase the performance to match that of the wrought material.

Keywords: Additive manufacturing, WAAM, Rene 41, Haynes 188, Inconel 718, Inconel 625, heat-treatment, mechanical properties, microstructure, fractography, machine hammer peening.

ACKNOWLEDGEMENTS

Firstly, I would like to acknowledge my sponsor the Defence Science and Technology Laboratory (DSTL) for funding my PhD project. Thank you also to my industrial supervisors for their guidance during the project, Mr Graham Simpson, Dr Matthew Lunt and Dr Sarah Baker.

I would like to wholeheartedly thank both my supervisors and good friends, Dr Supriyo Ganguly and Dr Goncalo Pardal. Supriyo, for providing me with the opportunity to work on this project, supporting me academically and also outside of academia, by going beyond the call of duty on several occasions during my 3.3 years at Cranfield. My thanks also go to my associate supervisor, Goncalo, for his expert guidance throughout the PhD and with whom there is always something interesting to discuss.

I would also like to thank all my WAMC friends and colleagues, particularly the support of the technical team, Mr Nisar Shah, Mr Flemming Nielsen, and Mr John Thrower, without whom the practical work would not have been possible. My appreciations also to Dr Yongle Sun for providing useful constructive feedback during my review sessions. Special mention also to the Cranfield metallography and materials characterisation department, Mr Steve Pope, Dr Tracey Roberts, Mr Kris Bramley and Dr Christine Kimpton for all their help.

Finally, to my family and friends, thank you for always being there for me, especially during the most difficult times for me, and when the future of my time at Cranfield looked uncertain. Lastly, to my girlfriend, Karolina, thanks for putting up with me!... but seriously your support and kindness has been invaluable, I love you.

I would like to dedicate this PhD thesis to my father Mr Anthony David James, without his passion for technology and his encouragement, I would not have gone to university nine years ago and I wouldn’t be where I am today. He is very much missed.

LIST OF PUBLICATIONS

Journals

W.S. James, S. Ganguly, G. Pardal, Selection and Performance of AM Superalloys for High-speed Flight Environments, International Journal of Advanced Manufacturing Technology. (2022)

W.S. James, S. Ganguly, G. Pardal, High Temperature Failure and Microstructural Investigation of Wire – Arc Additive Manufactured Rene 41, International Journal of Advanced Manufacturing Technology. (2023)

W.S. James, S. Ganguly, G. Pardal, A Performance Comparison of Additive Manufactured Creep-Resistant Superalloys, Science and Technology of Welding and Joining. (2023)

W.S. James, S. Ganguly, G. Pardal, High Temperature Performance of Wire-Arc Additive Manufactured Inconel 718, Scientific Reports. (2023)

Conferences

W.S. James, S. Ganguly, G. Pardal, Microstructure and Mechanical Properties of Inconel 718 and Inconel 625 Produced Through the Wire + Arc Additive Manufacturing Process, in: AVT-356 Physics of Failure for Military Platform Critical Subsystems, STO NATO, Nov. 2021. (Paper & Presentation)

W.S. James, Microstructure and Mechanical Properties of Inconel 718 and Inconel 625 Produced Through the Wire + Arc Additive Manufacturing Process. Defence and Security Doctoral Symposium, Cranfield, Nov. 2021. (Poster)

W.S. James, Selection and Performance of AM Superalloys for High-Speed Flight Environments. 1st International Conference on Advanced Manufacturing for Air, Space and Land Transportation, ESA & NASA, Mar. 2022. (Presentation)

W.S. James, S. Ganguly, G. Pardal, In-process Mechanical Working of Additive Manufactured Rene 41, in: International Additive Manufacturing Conference I-AM 2022, ASME, Oct. 2022. (Paper & Presentation)

TABLE OF CONTENTS

LIST OF FIGURES

LIST OF TABLES

LIST OF EQUATIONS

LIST OF ABBREVIATIONS

AD	As deposited
AM	Additive Manufacturing
ASM	American Society for Metals
ASTM	American Society for Testing and Materials
bct	Body-centred tetragonal
BD	Build direction
BSE	Back-scatted electron
CNC	Computer numerical control
DCR	Deep cold rolling
DED	Directed energy deposition
DR	Deep rolling
DSTL	Defence Science and Technology Laboratory (UK)
EBM	Electron beam melting
EBSD	Electron backscatter diffraction
EDS	Energy-dispersive spectrometry
fcc	Face-centred cubic
FIB	Focused ion beam
GMAW	Gas-metal arc welding
HAZ	Heat affected zone
hcp	Hexagonal close-packed
HIP	Hot isostatic pressing
HP	Hammer peening
HT	Heat-treated
H188	Haynes 188
H230	Haynes 230
H282	Haynes 282
ICP-OES	Inductively coupled plasma – optical emission spectroscopy
IN625	Inconel 625
IN718	Inconel 718
LCF	Low cycle fatigue
LMD	Laser melted deposition
LPBF	Laser powder-bed fusion

LSP	Laser shock peening
MHP	Machine hammer peening
MIG	Metal inert gas
MMPDS	Metallic Materials Properties Development and Standardisation
NASA	National Aeronautics and Space Administration (USA)
PAW	Plasma arc welding
PTA	Plasma-transferred arc
PWHT	Post-weld heat-treatment
RE41	Rene 41
RT	Room temperature
SE	Secondary electron
SEM	Scanning Electron Microscope
SLA	Stereolithography
SP	Shot peening
STG	Superalloys – a Technical Guide (Donachie)
tcp	Topologically close packed
TIG	Tungsten inert gas
TOFSIMS	Time-of-flight secondary ion mass spectrometry
TT	Through-thickness
UTS	Ultimate tensile strength
WA	Wall axis
WAAM	Wire + Arc Additive Manufacturing
Wro	Wrought
YS	Yield strength

1 INTRODUCTION

1.1 Research Background

Additive Manufacturing (AM) is a continually developing technology which is capable of significantly reducing material wastage through the production of near net-shape parts. Metal AM is a particularly evolving area, and most technologies are based on lasers and powders, the deposition rates however of these systems are often very low, making the production of metre-scale parts logistically challenging and time consuming. Cranfield University specialises in the development of Wire + Arc Additive Manufacturing (WAAM) which can achieve significantly higher deposition rates and is based on arc welding processes.

Many defence related applications require strength at high temperatures which necessitates the use of specialist alloys such as nickel-based and other superalloys. Production of these alloys using WAAM will create significant cost reductions and greatly reduced lead times over conventional manufacturing techniques, such as milling or turning of components from stock. In addition, it will greatly accelerate development of new designs because prototypes can be manufactured more quickly and more cost effectively. This project will explore what high temperature alloys can be deposited with the WAAM process as well as the consequent high temperature material properties. This will facilitate the production of a demonstrator component.

1.2 Research Gap

The gap in the research to be investigated in this project includes defining which high temperature alloys can be deposited using a plasma WAAM process and the effect the WAAM process has on the material properties of the high temperature alloys. Note that in most cases WAAM process variables have been based on previous studies The following gaps have been established:

1. Identification of high temperature alloys suitable for the high-speed flight application and which can be manufactured by WAAM process.
2. Understanding the effect WAAM has on the material properties of such alloys.

3. Development of a WAAM process with cold working to achieve the full material properties or better of the alloys.

1.3 Aims & Objectives

The overall aim is the development of wire-based deposition for materials used in high-speed flight environments experienced in defence applications, with a focus on high temperature material properties.

This will be achieved with the following objectives:

1. Evaluation of the weldability and high temperature material properties of a range of metals deposited with WAAM, which will enable the selection of a preferred alloy for further investigation.
2. Development of parameters and tool paths to create a range of wall widths and features contained within the DSTL application for the selected alloy.
3. Study of suitable cold working techniques which would preserve, or increase tensile performance.

1.4 Thesis Structure

This thesis is structured in ‘paper format’ as prescribed by Cranfield University (Guidance Document: Format options for PhD Thesis V1.3 Jan 2017). The thesis consists of nine chapters in total including seven technical chapters formatted as one literature review and six research papers. The literature review chapter includes a more general background on the project subject and each research paper has its own more focused literature review. A brief overview of the contents of each chapter follows.

Chapter 1 – Introduction, including research background, aims and objectives, and structure of the thesis.

Chapter 2 – General literature review to supplement following chapters.

Chapter 3 – Presents the process of selecting suitable alloys, initial room-temperature tensile testing and overall microstructure of WAAM material.

Chapter 4– Presents both mechanical data and microstructural findings from the pilot study conducted using Inconel 718 and 625.

Chapter 5 – Presents high temperature performance data and microstructural findings in WAAM manufactured Rene 41.

Chapter 6 – Presents high temperature performance data and microstructural findings in WAAM manufactured Haynes 188

Chapter 7– Compares and discusses the findings of high temperature testing in alloys: Inconel 718, Rene 41 and Haynes 188.

Chapter 8 – Present the performance results of combining WAAM with in-process mechanical working of Rene 41.

Chapter 9 – Summary, including overall discussion of research, contribution to knowledge, conclusions of the project and potential areas of future work.

2 LITERATURE REVIEW

2.1 Introduction

2.1.1 Additive Manufacturing

Additive Manufacturing (AM), specifically stereolithography (SLA) was first invented in 1986, as a means to provide rapid prototyping to the aerospace industry [1] and AM has since been undergoing rapid development, in many industries, in the decades following [2].

It can be argued, in fact, that AM is not an invention of man but has been in use for millennia by nature. The paper wasp, found in Japan, constructs its nest using a surprisingly similar AM process. The wasps deposit a fibrous material consisting of decayed wood and saliva, which is moulded and deposited in a layer-by-layer process to build a honeycomb structure to form their nests [3]. Rather than removing material to construct the nests the wasps have evolved to build using an additive process. AM, as in the man-made development, has been consistently evolving albeit on a much more rapid pace than occurs in nature.

AM has become more appealing to industries such as aerospace as the advantages of this relatively new manufacturing system becomes more widely understood. The term ‘AM’ covers many different types of systems and materials and is simply understood to be defined as “a process of joining materials to make objects from 3D model data, usually layer upon layer, as opposed to subtractive manufacturing methodologies.” [4]. AM has been widely covered in the media in recent times and is often referred to by the synonym ‘3D printing’. AM is defined in the ISO/ ASTM standard 52900 as “the general term for those technologies that successively join material to create physical objects as specified by 3D model data.” [5]

2.1.2 Wire + Arc Additive Manufacturing

Wire + Arc Additive Manufacturing (WAAM) has been undergoing development since the 1990’s. WAAM is “the combination of an electric arc as heat source and wire as feedstock”[6]. WAAM is not dissimilar to more traditional manual welding technologies such as TIG/MIG welding [7], with the exception that WAAM uses traditional arc welding technologies with wire feedstock and a motion control system, such as a robotic system or a retrofitted computer numerical control (CNC) system [6]. To build shapes and subsequent components, WAAM deposits the wire feedstock in a layer-by-layer manner [8]. Unlike other more well established AM methods, such as powder-bed AM, WAAM is often not used to manufacture a finished product, instead WAAM is used to deposit a near net-shape product [9], which can then be further processed, if required, to achieve a finished product.

As a method to rapid prototype metal structures WAAM is often advantageous over more traditional methods such as machining. As WAAM only deposits the near net-shape of the product, compared with machining, WAAM is capable of: reducing the waste material, hence also reducing the cost, and lead times. [9].

2.1.3 WAAM & Welding Processes

There are many different types of welding processes and not all are useful for WAAM. Fusion welding is the most appropriate category of welding for use in AM, and within fusion welding there are several types of process that have been tried and tested for use with WAAM. In general metal-inert gas (MIG) is considered the easiest process for WAAM [6]. MIG also known as gas-metal arc welding (GMAW) is a process that joins metal by “heating them with an arc established between a continuously fed filler wire” [7]. Another process that has previously been adapted for WAAM includes cold metal transfer (CMT) which is a brand name of the most commonly used process in industry; gas-tungsten arc welding (GTAW) or sometimes referred to as tungsten-inert gas welding (TIG). TIG uses an arc from an electrode made of tungsten, to heat the metal. A filler wire is then pushed into the weld pool to deposit material.

Plasma arc welding (PAW), which is similar in principle to TIG, is better suited to the WAAM process. PAW however shields and constricts the arc with plasma, which is fed into the nozzle alongside the electrode, a shielding gas is then also used to shield the plasma to further stabilise the arc. In PAW the filler metal wire is generally fed into the arc, as opposed to the weld pool as in TIG, [10] although both are possible in PAW due to the larger standoff. Use of PAW has several benefits over GTAW. The collimated arc used in PAW is less sensitive to arc length variations making it easier to operate than GTAW (which is highly beneficial for WAAM). The recessed electrode in PAW makes it impossible for the electrode tip to come into contact with the weld pool, reducing the risk of tungsten contamination [7].

2.1.4 Advantages of WAAM

Advantages of WAAM over other processes include:

- Deposition of a large range of alloys
- Low capital cost for system setups
- Low-cost raw materials
- Excellent structural integrity
- Scalability
- High build rates
- Non-frozen design method, i.e., designs can be adjusted per production, meaning each production run of a product can be individually customised if required.

  [11]

2.1.5 Disadvantages of WAAM

- Near-net-shape process
- Free-form micro-casting
- Restricted suppliers list (for commercial applications)

  [11]
- Irregular property generation through variable thermal cycles

2.2 High-speed Flight

2.2.1 Application

The application of the research conducted in this project is towards developing an AM process for a superalloy specifically for use as structural components in high-speed missiles with short flight times of < 1 hour. With a focus on very good short-term properties and a particular importance on high temperature performance of the alloy. In service temperatures could reach 1000 K (727 °C) for external structural components, or 1200 K (927 °C) for components in the propulsion flow path. These components will be highly stressed to minimise structural mass. The desired aim is to achieve properties similar to currently available wrought materials, such as Inconel 718 (standard) or Haynes 282 (best case), and ideally have a low thermal expansion.

2.2.2 Heating Environment

The heating environment that missiles experience is generally quite a large range of temperatures, from standard atmospheric temperatures to high temperatures experienced at high velocities, to sub-zero temperatures that may be experienced at high altitudes. Further to this, high-speed aircraft experience large thermal cycles as they move between different stages of flight and different zones of the aircraft will experience a different heating effect, as heat is generated by several different methods. For example, the nose is expected to experience the highest temperatures at high velocities, and will be heated primarily from pressure forces, whereas if there are any fins installed, heating will be primary from shear forces [12].

This varied heating effect on different areas of this missile may make more logical sense for different alloys to be used in the construction of different zones of the missile structure, as mentioned above Further investigation will need to be made on any possible financial savings on materials that can be made, in comparison with the added complexity of depositing several different alloys and the time affect this will have on the *rapid* prototyping capability.

2.2.3 Aerothermal Issues

As a result of flying at increasing speeds, aircraft are subject to increased heating, aerodynamic, and aeroacoustics loads. Aeroacoustics loads are experienced by aircraft subject to acoustic shocks, such as sonic booms. There is the potential for aircraft to suffer from acoustic fatigue damage, in areas subject to shocks or in areas of flow separation, due to suddenly increased strain rates. As acoustic damage and the impact of shock physics is somewhat more of a design related issue [13], it seems unlikely that this will be tested for in the course of this project. Fatigue damage is also unlikely to present an issue for the missile application, given the relatively short lifespan and its use ordinarily in single use missions.

2.2.4 Temperature Profile

The temperature profile across a high-speed aircraft varies quite significantly depending on which component and how fast the aircraft is traveling. From Figure 2-1 it can be seen that at a speed of Mach 5 for example there is a significant difference between the lower fuselage and wing, compared with the engine inlet, tail and flaps [13]. Of course, for the application of a missile there will be differences compared to the aircraft profile. However, it is reasonable to assume the temperature profile will vary in a somewhat similar way for a missile shaped system.

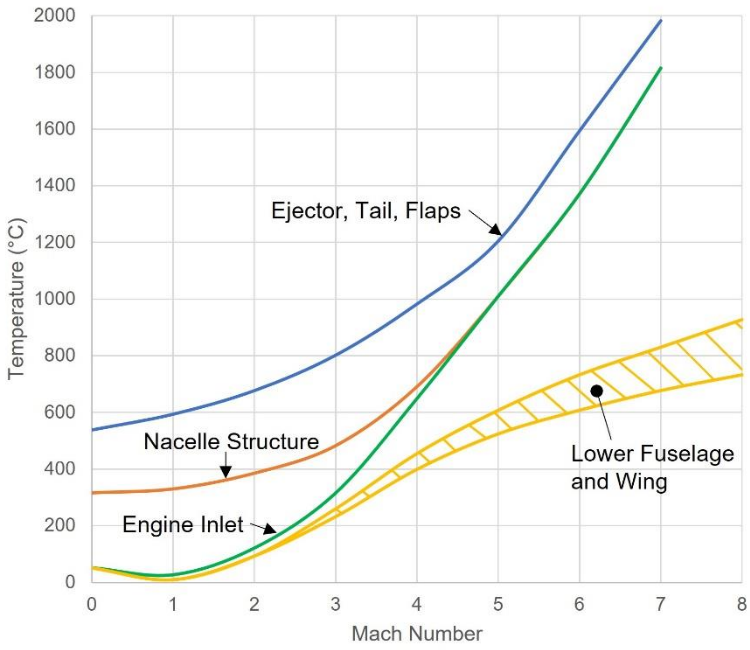

Figure 2-1 A typical temperature profile for a high-speed aircraft. Adapted from Gilman P.S. ‘Light High-Temperature Aluminium Alloys for Supersonic and Hypersonic Vehicles’. [13]

2.2.5 Stress Mechanism & Thermal Fatigue

High temperature testing of the thermal stress effect of superalloys in the past has focused largely on reusable applications, such as Concorde. Concorde which began development in the 1950s and entered service in 1976 as the first and to date only mainstream supersonic commercial airliner. The airliner had a cruising speed of Mach 2 and allowed for the use of an aluminium alloy, the thermal tests and stress mechanism may be of interest for this project. The overall thermal cycle of the aluminium alloy used in the skin of the airliner was subjected to temperatures of 100 °C at cruise, however this could then drop as low as -20 °C during deceleration and the decent phase of the flight, followed by a rise to ambient air temperature on landing [14]. Due to the likelihood of the thermal stresses to cause fatigue related issues testing was conducted. Thermal fatigue testing on Concorde used airflow to heat and cool the aircrafts surfaces, instead of radiant lamp heating that had been used previous to Concorde [14]. The missile for development in this project is expected to be a disposable item, however to a limited extent thermal fatigue may be a factor, depending on the cruising speed and altitude of the missile.

A more extreme thermal fatigue case would be that of the Space Shuttle. The Space Shuttle’s aluminium alloy frame was designed for temperatures of 180 °C, however the Thermal Protection System (silica tiles) of the shuttle provided protection from more extreme heating effects on re-entry [14]. As is well documented, without the protection of the silica tile system, the underlying aluminium frame and the whole vehicle was susceptible to the thermal stresses of high-speed flight.

2.3 Materials for High-speed Flight

2.3.1 Introduction

The material which will be most suitable for the application in this project will be largely dependent on the speed of the missile. Traditional aircraft materials become unsuitable at speeds above Mach 2. “Aluminium alloys can be used up to speeds of about Mach 2, but at Mach 3 and above more refractory metals such as stainless steel and titanium have to be used” [15].

High temperature alloys can be defined as materials that provide strength and remain stable at temperatures between 206 – 1200 °C. These alloys have been used in high temperature environments such as in combustion operations such as piston engines and power plants. Superalloys however are defined as “a group of nickel-, iron-nickel-, and cobalt-based materials that are used at temperatures of 540 °C and above” [16].

Superalloys were initially developed for use in superchargers in aircraft piston engines, however much of their later development was in components for gas-turbines. Nickel-based superalloys can be found in gas-turbines of a variety of applications from aerospace to power generation. It is not uncommon for nickel superalloys to experience operating temperatures of between 150 - 1500 °C [16].

The hottest part of a gas turbine engine is commonly known to be the combustion and turbine stages of the engine, as such alloys have had to be specifically designed for service at these temperatures, which can be in the range of 1400 - 1500 °C. Alloys for use at these temperatures have undergone continuous development; as the gas turbine has been made increasingly more efficient, the maximum temperature requirement has also increased. The development of nickel-based superalloys has seen nickel combined with numerous other elements in an effort to achieve the best high temperature material properties possible. Pollock describes that the outcome of this research has been a collection of complex alloys, each containing between 8-10 major alloying elements [17].

2.3.2 WAAM

The use of WAAM to manufacture high-speed projectiles, such as missiles, is currently an industry challenge due to the nature of high-speed flight, the environment that the missile would be exposed to, and the largely unknown effect the WAAM process has on the high temperature material properties of these alloys. Current alloys suitable for high-speed flight include nickel-based superalloys, due to the aggressive heating environment experience by objects in high-speed flight and the high temperature material properties of these alloys [18]. These materials are currently expensive and difficult to manufacture [19], which is less than ideal for non-recoverable systems such as missiles.

High temperature metals that have been deposited using WAAM in the past include Ti–6Al–4V [20]. Tungsten – WAAM is capable of depositing high purity tungsten and other refractory metals [21]. Deposited by WAAM at Cranfield University previous to this project include nickel alloys: 625, 718. Refractory metals: tungsten, molybdenum, tantalum. Titanium: grade 2, grade 5, grade 5 with O2 doping, grade 23, 5553, Timetal 407. As well as other alloys less suited to high temperature service [22].

WAAM also allows for the possibility of creating a new alloy. It is assumed that the alloy will be required to have excellent resistance to high temperature corrosion, due to the applications high in service temperatures. This immediately makes a nickel-based alloy a good option. Dependant on what elements the nickel is alloyed with will dictate its high temperature properties.

2.3.3 Nickel Alloys

Nickel alloys have historically been used for a variety of purposes. Nickel alloyed with copper, known as cupro-nickels, forms a series of useful alloys. At 30% Ni, the alloy that forms is very resistant to corrosive environments and have been used extensively in condenser tubes. At 40% Ni the alloy forms an electrical resistance that varies with temperature, which has led to its use in electrical resistors. Nickel silver, an alloy of 18% Ni, 18% Zn in Cu, forms a silver colour and good corrosion resistance and has been commonly used in tableware. [15]

Nickel superalloys originate from the creation of nickel-based chromium alloys for electrical heating elements, at the end of the 19th century [23]. The development of high-temperature, creep-resistant alloys began in the 1920s with the development of materials for the power industry and has steadily moved into the aerospace industry with the development of the alloys for gas turbines. With the development of nickel-based superalloys for gas turbines, Nimonic alloys were discovered. The nickel matrix has been found to be extraordinarily good at maintaining its strength at high temperatures and are capable of maintaining good strength at temperatures up to about 70 % of the melting temperature [15]. Nimonics can be strengthened by precipitation hardening, this can be through several different alloying elements that can provide a number of different advantages and detriments depending upon the chosen elements.

Nickel based superalloys with excellent high temperature properties are often precipitation hardened by the inclusion of alloying elements specifically put there for that purpose. The following list describes the effect different elements provide in nickel superalloys.

Nickel alloying elements:

Chromium (Cr) provides a nickel alloy with a chromium-oxide scale that will protect the underlying nickel from exposure to atmospheric air and hence provides corrosion resistance, much in the same way chromium provides the same scale in stainless-steels. Cr also has the effect of increasing the solid solution with Ni, however this property is better served by other alloying elements.

Aluminium (Al) will provide the alloy with a further protected scale if used in addition to chromium. Using aluminium will form a second scale on the outer surface over the chromium scale and has the effect of stabilising the chromium scale, allowing the alloy to be used at higher temperatures. Al can also be used to provide precipitation hardening, which increases the strength of the alloy but reduces the toughness.

Molybdenum (Mo) can provide Ni alloys with pitting resistance, however if also alloyed with Cr, Mo can cause embrittlement. Mo also provides resistance to oxidisation at high temperatures. Mo in Ni alloys forms Molybdenum-carbides at the Ni grain boundaries which increases the alloys resistance to creep.

Copper (Cu) forms 100% solid solution with Ni. Cu allows the alloy to resist oxidising and reducing environments, providing it with resistance to acids.

Cobalt (Co) provides the Ni alloy with strengthening, hardening, and sulphide resistance.

Titanium (Ti) provides precipitation hardening and is often used in combination with Al for the same effect. Ti along with Tantalum and Zirconium are carbide stabilisers.

Silicon (Si) can be used to increase high temperature corrosion resistance; however, this is often to restricted performance comparatively. Like Al, Si stabilises a Cr scale.

Niobium (Nb) increases solid solution and is a carbide stabiliser, Nb can also provide age hardening however this occurs over longer periods.

Iron (Fe) is a neutral alloying element and is a non-harmful replacement for Ni. Fe can be included in the alloy to reduce the cost. In Ni alloys with over 50% Fe, Fe can provide limited sulphide resistance.

Tungsten (W) increases solid solution significantly. [24]

2.3.4 Nickel alloy strengthening

Superalloy strength is primarily derived from their solid-solution hardeners and precipitated phases. The main strengthening phases precipitated in most Ni-based alloys are γ’ and γ’’. Carbides can also provide some limited strengthening through dispersion hardening, but mostly provide strength through their formation at grain boundaries which provides resistance against shearing. Phases that are useful in controlling wrought structures include δ and η, their contribution to strengthening depends on alloy composition and processing.

Other than elements that produce solid-solution hardening and those which promote carbide formation. Elements are added to the composition to improve mechanical and chemical properties, these include B, Zr, and Hf. Note that these elements are not generally added to Co-based alloys.

In addition to phases that are beneficial to performance, other phases can form which are detrimental to performance when found in significant amounts, these include topologically close-packed (tcp): σ, μ and Laves phase.

Ni-based superalloys tend to be strengthened through the precipitation of intermetallic compounds in an austenitic fcc matrix, although solid-solution strengthened Ni-based alloys do exist. For alloys containing Ti and Al, the strengthening phase is likely to be γ’. In alloys strengthened with Ni, γ’’ is likely to be the main strengthening phase, although these alloys are often found with Ti and Al in which case are jointly strengthened by both γ’ and γ’’.

Some Ni-based alloys are oxide-dispersion-strengthened, which include inert particles, such as yttria. [25]

2.4 Deposition of Creep Resistant Superalloys

2.4.1 High melting point

The seemingly obvious difference to the WAAM process with creep resistant alloys, would be the need for a higher temperature output from the welding equipment in order to melt the filament wire. However, Ti-6Al-4V is somewhat of a standard feedstock for WAAM [6] and has a melting temperature above 1600 °C [26], which is higher than most Ni-based superalloys, Inconel 718 for example has a melting range of 1260 – 1336 °C [27]. Although the heat required to melt superalloys at first appears problematic, Ti-6Al-4V as well as refractory metals have been deposited via WAAM in the past [28], which confirms this is not an issue.

2.4.2 Ductile-to-brittle transition temperature

The ductile-to-brittle transition temperature is the specific temperature at which the metal changes its fracture mechanism. For example, generally metals tend to become more brittle at a lower temperature and less brittle and more ductile at higher temperatures, causing the materials fracture method to change under the same loading conditions. The transition temperature is the temperature range at which the material’s toughness changes rapidly. The fracture type can also be changed at faster strain rates, for example a short but powerful shock to an otherwise ductile material can induce a brittle fracture [29]. Careful consideration needs to be given when welding as ductility is required for bonding, and a mismatch in ductility between two components can cause fractures to occur [30]. This point is important for consideration when depositing onto substates if using a different alloy.

2.4.3 Thermal stress applied to the deposit

Thermal stresses are applied to the material during deposition can lead to significant deformation which is dependent on how the heat from the welding process propagates across the work piece. This effect can be minimised if the temperature outside the weld area is carefully controlled, and the work piece is allowed to cool in a controlled manner. The heat applied to the metal nonetheless has the effect of applying a thermal stress to the work piece, which ideally should not be allowed to have an adverse effect on the desired material properties [7] and residual stresses.

The WAAM process subjects the material to repeated thermal cycles as part of the process of depositing multiple layers to build a structure. As such the material can be subjected to a partial aging effect. As WAAM structures are built from the bottom-up, the bottom layers are more susceptible to this partial aging effect as they experience the most thermal cycles during the deposition of sub-sequential layers. Due to the top layers experiencing fewer thermal cycles it is common to find less precipitates in the top layers, whereas they become more common in the older layers. Xu et al. describes that “the bottom part has larger, around twice, the amount of precipitates than the top part” [8]. This has the effect of making the bottom part of products made in WAAM harder than the top sections, which can make products less consistent. There exists the chance to make products more consistent in contents by aging the WAAM material after deposition. Xu et al found “After 3 hours of aging, the amount of precipitates near the top part increase significantly” [8], Ni_3Mo increased from 0.0974 % to 0.189 % and Ni_3Ti from 0.0656 % to 0.159 %. “The increase near the bottom is less significant” [8].

2.4.4 Cracking

There are various mechanisms for a crack to occur in a welded component.

Solidification / hot cracking, more common in cast metals, can occur as a result of fusion welding and again there are several methods by which a solidification crack can occur. Solidification cracking has been known to occur because of the following reasons: impurities in the weld metal, reactions during solidification, wide temperature range across the component, and irregularities in the grain structure. This is a limited list and cracking can occur for several different reasons and is different dependant on the properties of the alloy or metal being used [7]. Cracking of nickel based alloys should be limited in the issues it creates, due to the alloys high thermal conduction rate, however solidification cracking in the fusion zone is a well understood mechanism in nickel based alloys; the exact impact and characteristics of this cracking varies amongst particular alloys [31].

Cracking issues that are somewhat particular to precipitation strengthened nickel alloys include: fusion zone solidification cracking, heat-affected-zone (HAZ) liquation cracking, strain-age cracking, and ductility dip cracking. HAZ liquidation cracking occurs due to grain boundary segregation and constitutional liquation mechanisms and has been found to be more common with nickel alloyed with niobium. Strain-age cracking, which is a solid-state phenomenon, is most common to alloys strengthened through the precipitation of γ' phase titanium and aluminium, it has been suggested this is due to the high rate of aging in these alloys. There have only been limited reports of ductility dip cracking occurring and its cause is still somewhat un-investigated [31].

Cracking can also occur in Ni-base alloys due to exposure to oxygen that causes embrittlement at the grain boundary. For this reason any post-weld heat treatment that is applied to the work piece, it is often desirable for this to be completed in either a vacuum or an inert gas environment to control the exposure to oxygen [7].

2.4.5 Environmental

The effect the ambient environment has on the welding process could become an issue. For example, oxygen in the atmosphere can react with the weld pool, due to the high temperature. Oxygen reacting with a Ni-Cr alloy creates the Cr scale over the nickel which has the effect of protecting the Ni from corrosion, however too much oxygen can cause the Cr scale to become very thick which can be an issue dependant on application. Also, large amounts of oxygen reacting with the weld pool can result in the Cr scale becoming trapped in the weld pool, which can lead to inconsistences in the underling Ni, such as trapped oxides [32].

A solution to the Oxygen issue can be to use an enclosure. An enclosure seals the work piece and welding equipment inside a controlled area, and is often filled with an inert gas in order to carefully control the atmospheric gasses the weld pool is exposed to, enclosures used in the past have included argon filled tents [32]. Another solution to controlling oxidisation can include the use of a local shielding device, which is capable of providing a controlled oxygen environment in the area of deposition, the benefit of which would be to eliminate the set-up time of filling an enclosure with an inert gas and the added flexibility of using additional equipment that would otherwise not be practical to use inside an enclosure. [33]

Oxygen also affects the surface tension characteristics of the weld pool, which could have an impact on the consistency of WAAM deposition. Fluid flow within the weld pool in WAAM is mainly controlled by the Marangoni force [34]. While oxygen does have an effect on the surface tension characteristics of weld pools, the formation of oxides had little effect on surface tension [35].

Although oxides can be found to be entrapped in the weld pool; largely dependent of the flow characteristics in the weld pool, this can lead to oxides being found inside the structure. It is, however, more common for oxides to float to the surface of the weld pool, due to the lower density of the oxides over the liquid metal. This can also lead to the entrapment of oxides on successive passes and is more common where the deposition involves an increasing number of passes, as the scale thickness increases [32]. Larger amounts of oxides on the surface and a thicker scale can have adverse effects on the surface finish of the weld, as the oxides can destabilise the arc and weld pool, this again can be controlled through the use of an enclosure filled with an inert gas [32]. The concentration of oxygen can be closely monitored by using an oxygen analyser.

It should also be noted that oxygen can have positive effects, dependant on the desired material properties. For example, Abdulsalam found that oxygen included in the shielding gas had the positive effect of increasing the impact toughness of the weld metal, with the best results experienced at sub-zero temperatures and a oxygen content of 19.9 % (Ar + 25 % CO_2) [36], which could be relevant for the application of this project. Abdulsalam also found that larger amounts of oxygen dissolved into the weld metal had the effect of decreasing the tensile strength [36]. Xu et al. investigated the process factors affecting the mechanical properties of WAAM Inconel 718. They found that although Inconel 718 should be processed in an oxygen environment of less than 3 ppm to minimise oxide formation, this is not possible to achieve with WAAM, even with global shielding where oxygen content remains above a few hundred ppm. The oxidisation of WAAM material is therefore inevitable and the effect of this on the mechanical properties of WAAM Inconel 718 can be detrimental to performance [37]. This further demonstrates the need for a carefully controlled environment to achieve desired material properties.

2.4.6 Suitable WAAM methods

There are several different welding methods that are compatible with the WAAM process that would be suitable for the deposition of high melting point metals, these are as follows:

Tungsten Inert Gas (TIG) welding was used previously for the WAAM deposition of refractory metals [21]. This suggests TIG could also be a viable option for the deposition of the superalloys used in this project.

Plasma Arc Welding (PAW) presents another method that could be relevant for the deposition of the alloys in this project as it is similar to TIG.

PAW is more appropriate for use in this project due to the bigger stand-off between the work piece and torch allowing for greater flexibility with wire insertion, PAW is also less sensitive to arc length variations which makes it a good choice for WAAM deposition [7]. An enclosure will likely be necessary for the control of gasses that could react with the weld metal if this cannot be satisfactorily achieved by shielding gas.

2.5 Testing of Creep Resistant Superalloys

With aerodynamic heating of the structure thought to be the primary testing criteria for the missile application, it makes sense to explore some of the thermal structural testing methods that have traditionally been used in the past by aerospace engineers.

Aerodynamic heating becomes a significant factor at and above Mach 2.5. Flow is considered supersonic up to Mach 5 and over Mach 5 considered hypersonic. Hypersonic flow induces effects on materials that become more challenging to overcome than supersonic. Other than the increased heating effect, hypersonic flow can induce chemical reactions in alloys [14].

The following heating methods for the testing of aerodynamic heating have been developed over the last ~50 years:

Ovens, clam-shell furnaces used to test materials with testing machines applying mechanical loads. Typically, up to 425 °C or more with cooling equipment.

Heaters, electrical heaters such as cartridge, coil, strip, blanket heaters. Low level heating of structures can be achieved with etched heating elements on polymer strips bonded to a structure, similar to strain gages.

Radiant heat lamps, tungsten filaments enclosed in quartz glass tubes. Filaments can reach temperatures of 3000 °C. Heat lamps are not a good method to replicate aerodynamic heating as it is unable to replicate the convective heat transfer process. For this reason, the surface temperature of the test specimen must be closely measured, and the lamps adjust to ensure the heat output is correct for the test.

High intensity heating, supplementing radiant heat lamps with graphite heaters and arc lamps, capable of testing of 2200 °C. Arc lamps can be used to heat small areas effectively and are used to simulate hypersonic stagnation heating, shock-shock interactions, and localised heating within engines.

High temperature wind tunnels: developed by NASA in the 1960s for the testing of problems encountered by space vehicles on re-entry. Originally limited to Mach 3 flows, facilities have been developed for flows of up to Mach 7. These tunnels were used extensively for the testing of the space shuttle silica tile system, thermal protection systems, shock-shock interactions and hypersonic air-breathing propulsion systems [14].

2.5.1 Creep testing

Creep is the process by which metals deform plastically under steady loads over a long period of time. Creep has been proven to occur at all temperatures, however, in practice creep only becomes a significant factor at temperatures in excess of 50 % of the melting point [15]. Creep is defined well by Beddoes when he says “Creep refers to the accumulation of time dependent strain which becomes significant in structural alloys at temperatures greater than approximately half the absolute melting temperature of the alloy.” [38].

Creep testing involves the heating of a test piece under loading. The time and deformation of the test piece are recorded as variables. The temperature can be varied as a percentage of the metal’s melt temperature, in order to investigate the performance of the material [39]. Beddoes also says that the extrapolation of creep properties from temperature-stress results is inaccurate, and that regulatory agencies often require multiple stress tests under different conditions [38].

It is understood that since creep normally occurs over long periods, it should not be necessary for this project to investigate any alloy to its failure via creep. However, it is important to investigate the rate at which the material is susceptible to creep to ensure any alloy selected is in line with the specification. For example, if excessive deformation occurs in a short amount of time at a specific temperature, then the alloy would not be suitable as it would compromise the design aim.

2.6 Post-processing

Because WAAM is a near net-shape production process, manufactured products are likely to require some level of post-processing to achieve the final product.

It may be possible for post-processing to be used as a surface treatment technique to finally adjust the material properties for the design. The most common mechanical surface treatments according to Nagarajan include shot peening, laser shock peening, low plasticity burnishing and deep rolling [40].

Shot Peening (SP) and Laser Shock Peening (LSP) are techniques used to improve the fatigue life of the material, by introducing distributed dislocations near to the surface of the product. A disadvantage of SP is its effect on the surface finish of the product, often leading to further finishing where required. Like SP, LSP improves fatigue life of materials. However as described by Nagarajan "LSP typically produces stresses deeper into the material than shot peening with lesser cold work (5–7 %) and increased twinning" [40]. LSP introduces stresses that penetrate deeper into the material than SP, again LSP leaves the finished product with a poor surface finish [40].

Deep Rolling (DR) also known as Deep Cold Rolling (DCR), typically involves the use or rollers or balls on the material to induce surface and subsurface deformations. DCR creates deeper compressive stresses than can be achieved through SP, and DCR leaves a smooth surface finish. DCR is also a good preventive process for crack growth and nucleation. DCR of nickel-base alloys is not common practice [40], hence there may be some reservations on its use, as this is a relatively new area of study. Nagarajan investigated the effect DCR has on several nickel-base alloys and came to the following conclusions; the process resulted in an increase in surface hardening, and compressive stresses, the process did however vary considerably with each particular alloy being tested [40].

Hot isostatic pressing (HIP), has been used in the past with nickel-base superalloys as a method to eliminate casting defects among other defects as described by Xu “HIP also acts as the important post-process to heal the internal defects [32], such as voids, and internal microcracks.” [41]. It may be possible to use HIP to correct defects created as a result of the WAAM process, to ensure desired properties are maintained.

Hammer peening (HP) also known as Machine hammer peening (MHP), often uses a steel pin that is driven pneumatically, into the material being treated, at high frequencies. There are several different variations on HP which include ultrasonic, piezoelectric, electromagnetic, and as above pneumatic. HP has been used for some time in post-weld surface treatments. HP introduces deep plastic deformation, which can result in improvements in fatigue life by inhibiting fatigue crack propagation, material hardening, surface smoothening, and improvements to tribological properties. HP has also been used previously in AM applications [42].

As well as the above, heat-treating of superalloys is usually required to achieve the maximum performance. Age/ precipitation hardening treatments allow the alloys strengthening phases to precipitate.

2.7 Alloys of Interest

2.7.1 Inconel 718

2.7.1.1 Overview

Inconel 718 (IN718) is a nickel-based superalloy. Originally developed by Elseistein of the International Nickel Company, IN718 was first developed for use in is wrought condition [43]. Its uses have included several high temperature applications such as components for: gas turbines, turbo chargers, nuclear reactors, liquid fuelled rockets as well as a variety of other structural and corrosive applications. The Inconel alloys were developed in the 1940s by Wiggin Alloys based in Hereford, and one of its first notable uses was in the development of the Whittle engine [44][45]. The Inconel name is now a trade name of Special Metals Corporation [45]. IN718 in its current use was discovered as somewhat of a happy accident. “The alloy development effort that would lead to Inconel Alloy 718 was a search for a solid-solution-strengthened non-age-hardenable alloy” [46], it was metallurgists at General Electric-Evandale that first recognised the significance of the alloy for its high temperature material properties, when they discovered its resistance to strain-age cracking [46].

IN718 has been so successful in gas turbines that it makes up more than 30 % of the total weight of engines [47], and up to 55 - 70 % of the nickel based superalloys in modern jet engines [48]. The reason behind the alloys extensive use is its oxidation and corrosion resistance and its relatively good strength at elevated temperatures [43]. What makes IN718 a good choice for review in this project is its ability to maintain its strength at elevated temperatures; Inconel superalloys are capable of being used at temperatures in excess of 80 % of their incipient melting temperatures under load-bearing applications [49].

Dependent upon the type of heat-treatment IN718 receives, it is usually applied in one of two applications: high resistance to creep and stress rupture to about 700 °C or high strength at cryogenic temperatures. It also has good oxidation resistance up to about 980 °C [50].

Due to the high hardness of IN718 it is difficult to manufacture using common methods such as machining and can be expensive due to the excessive wear on tools and the limited material removal rate at room temperature which can increase the time required for machining [47]. This therefore makes IN718 a good candidate for a WAAM production.

2.7.1.2 Chemical composition

The chemical composition of IN718 is as shown in Table 2-1.

Table 2-1 Chemical composition of Inconel 718 (wt. %) [27].

Ni	Cr	Fe	Nb	Mo	Ti	Al	Co	Mn	Si	Cu	C	P	S	Bo
50-55	17-21	12.82-24.17	4.75-5.5	2.8-3.3	0.65-1.15	0.2-0.8	<1	<0.35	<0.35	<0.3	<0.08	<0.015	<0.015	<0.006

2.7.1.3 Mechanical properties

The mechanical properties of IN718 are shown in Table 2-2.

Table 2-2 Mechanical properties of IN718 [31].

Tensile		Elongation (%)	Hardness (R_c)	Rupture stress for 1000hr exposure (MPa)		
Strength (MPa)	0.2 % Yield Strength (MPa)			650°C	760°C	870°C
1035-1590	900-1240	14-30	30-40	580	195	-

2.7.1.4 Metallurgy

IN718 contains a complexed microstructure, it is formed of a face-centre-cubic (fcc) matrix of γ (A1) as well as a large amount of carbides strengthening the structure and intermetallic phases; which are described by Hosseini in their review of IN718's mechanical properties; "namely fcc γ′ $Ni_3(Al,Ti,Nb)$ (L12), ordered tetragonal γ″ Ni_3Nb (D022), and fcc MX (Nb,Ti)(C,N) (B1)". Undesirable microstructure elements could also include "topologically close-packed (TPC) phases, such as hexagonal Laves $(Ni,Fe,Cr)_2(Nb,Mo,Ti)$ (C14), orthorhombic δ $Ni_3(Nb,Ti)$ (D0a), and tetragonal σ CrFe (D8b) phases". [47]

Elements which give IN718 its inherent strength is the inclusion of “metastable γ″ and γ′ phases which are coherent with the γ fcc matrix.” [47]. Heat treatments are often employed to further strengthen the microstructure.

The sluggish ageing response which is widely regarded as to why IN718 has such good high temperature material properties, as Xu et al describes “The age hardening Nb-Al-Ti alloying system of IN718 has a very slow aging response as compared to the Al-Ti system.” This allows IN718 to undergo heating cycles with relatively small amounts of age hardening taking place, allowing the alloy to maintain its ductility and softness [51].

2.7.1.5 Welding

Although the alloy is regarded as being easily weldable it still suffers from issues such as micro-fissuring and solidification cracking, as mentioned previously. Welding of IN718 is possible with both similar and dissimilar metals with different levels of success. The majority of studies into the weldability of IN718 have concluded that to minimise the risk of micro-fissuring and solidification cracking, a reduced grain size had the desired effect [43].

2.7.1.6 Additive manufacturing

IN718 as a standard Ni-based superalloy has been used previously in numerous AM processes. Different AM process are characterised by both their feedstock, generally either a powder or wire and their power source such as laser or arc. IN718 has previously been deposited using both wire and powder bed processes, such as direct laser deposition (DLD), direct electron beam deposition (DEBD), selective laser melting (SLM), electron beam melting (EBM) [47], and of course WAAM [51].

2.7.2 Rene 41

2.7.2.1 Overview

Rene 41 (RE41) is an age hardening nickel-based superalloy developed for the aerospace industry as a high temperature and high strength alloy for use in gas turbines. RE41 is also among a limited number of Ni-Co-Fe alloys which can be used at high temperatures for prolonged periods. RE41 offers oxide resistance and mechanical strength in a wide range of temperatures [52]. RE41 was developed in the mid 1950’s by General Electric and was developed as a high temperature, high strength alloy for use in the stationary structural components in gas turbines. Such as the General Electric J79 aircraft engine [52].

2.7.2.2 Chemical composition

The chemical composition of RE41 is as shown in Table 2-3.

Table 2-3 Chemical composition of Rene 41 (wt. %) [53].

Ni	Cr	Fe	Mo	Ti	Al	Co	C	B
55.0	19.0	<0.3	10.0	3.1	1.5	11.0	0.09	0.01

2.7.2.3 Mechanical properties

The mechanical properties of RE41 are shown in Table 2-4.

Table 2-4 Mechanical properties of RE41 [31].

Tensile		Elongation (%)	Hardness (R_c)	Rupture stress for 1000hr exposure (MPa)		
Strength (MPa)	0.2 % Yield Strength (MPa)			650°C	760°C	870°C
1345	1070	15	33-40	580	235	60

2.7.2.4 Metallurgy

RE41 is a precipitation hardened nickel based superalloy [52]. The mechanical properties of RE41 vary with solution and aging treatment. “Higher solution temperatures result in better room temperature ductility and elevated temperature creep-rupture strength. Lower solution temperatures give higher tensile strengths.” [54].

“Many nickel-base superalloys consist of a solid solution strengthened austenitic face-centred-cubic gamma (γ) phase matrix, a major precipitate gamma prime (γ’) phase coherent with the matrix, and various types of carbides and other phases distributed throughout the matrix and along the grain boundaries. Carbides most commonly encountered in the nickel-base superalloys are MC, $M_{23}C_6$,and M_6C.” [52].

At temperatures between 815 - 980 °C M_6C forms with $M_{23}C_6$ in RE41 due to the higher Mo and W content. M_6C is more commercially valuable for controlling the grain sizes as a grain boundary precipitate than $M_{23}C_6$ as it is more stable at higher temperatures [53].

2.7.2.5 Welding

RE41 is known to be sensitive to strain age cracking during welding. GTAW joining requires cooling by backup bars or water-cooled fixtures [54]. Cracking in the HAZ and base metal of RE41 has been a known problem with welding and post weld heat-treatments. Cracks can range in size from micro-cracking to several millimetres. Kayacan explains “the summation of residual welding, aging contraction and thermal stresses result in cracking during exposure to a temperature range in which precipitation of the primary age-hardening constituent gamma prime (γ’) occurs”. Use of RE41 and other similar alloys in highly restrained components has generally been avoided [52].

2.7.2.6 Additive manufacturing

RE41 has previously been deposited using the following powder AM processes. Laser powder bed fusion (LPBF) as presented by Atabay et al. [55]. Laser melting deposition (LMD) in the work of Li and Wang [56]. Outside of this research project, RE41 is not believed to have been deposited using a wire-based AM process.

2.7.3 Haynes 230

2.7.3.1 Overview

Haynes 230 (H230) is a nickel-based superalloy which is a purely solid-solution and carbide-strengthened Ni-Cr-W alloy. H230 is known for its use in gas turbines as hot section components and in the nuclear and chemical industries. H230 is also used in solid-oxide fuel cells and in furnace technology [57][58]. H230's properties demonstrate reasonably good creep and weldability, which makes the alloy suitable for combustor applications [59]. H230 is manufactured by Haynes International Inc., one of the largest producer of high temperature alloys in the world and is one of the oldest having been formed in 1912 by Elwood Haynes; a teacher, inventor and businessman [60]. Haynes products mainly include the Hastelloy and the Haynes alloys which are nickel-based alloys [61]. Developed in the 1980s when alloy development was moving at a fast pace, H230 was introduced alongside Haynes's other nickel-based alloys and became a standard engineering material across several applications.

H230 "combines excellent high-temperature strength, outstanding resistance to oxidizing environments, great stability and resistance to grain coarsening with long-term thermal exposures, and a low thermal-expansion coefficient." [62]

H230 has good room temperature ductility which allows it to be worked on using common methods for nickel-cobalt based alloys. H230 and Haynes 188 have similar strain-hardening characteristics, however H230 has a slightly lower tensile strength than 188, this could be due to the cobalt-base of 188 which can lead to a higher strain-rate in comparison [63].

A weakness of H230 is grain boundary sliding in harsh environments and is the primary damage mechanism for the alloy in creep conditions. It has however been suggested by Yoon et al and Jiang et al [64][65], that the introduction of serrated grain boundaries in H230 and in similar superalloys can help to reinforce ground boundary weaknesses [57].

2.7.3.2 Chemical composition

The chemical composition of H230 is shown in Table 2-5.

Table 2-5 Chemical composition of Haynes 230 (wt. %) [66].

Ni	Cr	W	Mo	Fe	Co	Mn	Si	Nb	Al	Ti	C
57	22	14	2	<3	<5	0.5	0.4	<0.5	0.3	<0.1	0.1

La	Bo
0.02	<0.015

2.7.3.3 Metallurgy

The chemical composition of H230 is mainly a Ni-Cr-W alloy in solid solution [64]. The addition of Tungsten “reduces the stacking fault energy of nickel, which provides for restricted cross-slip of glide dislocations”. The addition of chromium, lanthanum, silicon, and manganese provide the alloy with its oxidation resistance [63].

H230 like IN718 contains a fcc microstructure in solid solution, with a lattice constant of 3.6 A (0.36 nm). The grain size averages ASTM No. 4 or finer [63], ASTM No. 4 is 89.8 μm average grain diameter [67]. Yoon et al. found that conventionally cast H230 had a grain size of 150 μm [64].

H230 is also a carbide strengthened alloy. Tawancy et al identified that the primary carbide in H230 is of the M_6C-type, which was identified by x-ray and electron diffraction and exposure to temperatures below approx. 1150°C results in precipitation of Cr-rich $M_{23}C_6$ carbides [63]. The carbide structure is characterised by Haack el al “it has been shown that chromium-rich $M_{23}C_6$-carbides of a planar morphology accompany GBS [grain boundary segregation] in slow-cooled conventionally processed H230” [57]. The only secondary carbide known to exist on samples exposed for 1000 hours at 650°- 980 °C is the $M_{23}C_6$ carbide. H230 has a resistance to the precipitation of these topologically close-packed phases, which would otherwise have an unfavourable effect on its mechanical properties. H230 does this by retaining high room-temperature tensile elongation following prolonged exposure to elevated temperatures [63].

H230 shows a greater resistance to oxidation compared with alloys: X, 617, 86, and 188. As all these alloys contain 22 wt.% Cr, the greater resistance of H230 to oxidation could be due to the effects of chromium, nickel, and the smaller amounts of lanthanum, silicon, and manganese; as described by Tawancy et al [63].

The creep performance of H230 is considered excellent [68]. “The high creep strength of alloy H230 is partially attributed to the precipitation of fine particles of $M_{23}C_6$ carbide on slip dislocations” [63]. H230 was creep tested by Lee et al against RE41 and Hastelloy X at temperatures ranging from 760 – 927 °C, under ASTM standard E647-99 with a 2min hold time. The creep-fatigue resistance of H230 was found to be second to that of R41 but better than the performance of Hastelloy X [69]. The creep resistance of H230 is primarily due to the tendency of fine precipitates to form along stacking faults and twin boundaries [70].

2.7.3.4 Welding

H230 has good weldability and as a solid solution strengthened alloy, performs better for weldability than its precipitation hardened alternatives. H230 is commonly welded using a variety of traditional welding methods, including: TIG, MIG, and electron beam welding. Traditional welding methods often lead to strains in the material which creates the tendency for heat-affected-zone (HAZ) related cracking. The resistance to HAZ cracking in H230 is similar to that of 188 alloy [63].

In their book ‘Welding Metallurgy and Weldability of Nickel-Base Alloys’ DuPont et al describes various issues associated with the welding of nickel based alloys [31]. Liquation cracking occurs in H230 along the grain boundaries in the partially melted zones, and has been known to occur when a grain boundary is formed by the liquidation of W_6C carbides. [71]. This phenomenon is described by Schneider et al “liquid film forms as a result of a eutectic reaction between a secondary phase and the matrix due to non-equilibrium heating resulting in constitutive liquation.” The subsequent tensile stresses cause a crack to propagate through a liquid film at the grain boundary due to the differences in the coefficient of thermal expansion [72].

Cracks can also occur along grain boundaries as the alloy solidifies after fusion welding. This is often due to quantities of $Cr_{23}C_6$ carbides, which were in solution under fusion welding temperatures, solidifying along the grain boundaries in excessive amounts as the alloy cools. The difference in the coefficient of thermal expansion in this case can cause cracking to appear along the grain boundaries at lower temperatures when the ductility of H230 is reduced [72].

2.7.3.5 Additive manufacturing

H230 has been deposited using powder-bed processes such as LPBF in the work of Yang et al. [73] and SLM in the work of Bauer et al. [74].

2.7.4 Haynes 188

2.7.4.1 Overview

Haynes 188 (H188), like the alloys of the previous sections, has excellent high temperature properties including: strength, ductility, and resistance to corrosion. H188 has seen application in several different components in gas turbines and has even seen use in the main engine of the space shuttles [75].

H188 is a Co-Ni-Cr-W alloy where Co is the principal element and is the only such alloy investigated in this project, alongside the nickel-based alternatives. Although H188 is known to be resistant to oxidisation, as a cobalt-based alloy, it is not as resistant as the nickel alternatives [76]. It is generally understood that H188 can be exposed for longer durations at temperatures below 1095 °C, and for temperatures in excess of 1095 °C for limited periods, after which a nickel-based alloy is better suited [77].

H188, developed by Haynes International; information on which can be found in the corresponding subsection for H230 (see section 2.7.3.1). H188 alloy which was developed by Haynes in the 1960s was one of the first alloys developed by the company after taking advantage of the then new technology Argon Oxygen Decarburization (AOD) and Electro Slag Re-melting (ESR), to enable the manufacture of low carbon alloys. H188 became widely used in the components of jet engine afterburners and its most notable use at the time was in the Pratt and Whitney F-100 engine. Sponaugle describes, “H188 allowed jet engine designers to increase the temperature in the engine by 300 °F [149 °C], resulting in substantially greater thrust and performance.”[60]. H188 is often used in combination with H230 in engine programs, with H230 considered to have improved properties over H188 [78].

H188 is commonly used in applications where low-cycle-fatigue (LCF) and creep resistance are important factors where the damage caused by the mechanisms are likely to limit component lifetimes [79].

2.7.4.2 Chemical composition

The chemical composition of H188 is shown in Table 2-6.

Table 2-6 Chemical composition of Haynes 188 (wt. %) [77].

Co	Ni	Cr	W	Fe	Mn	Si	C	La	B
39	22	22	14	<3	<1.25	0.35	0.1	0.03	<0.015

2.7.4.3 Mechanical properties

The mechanical properties of H188 are shown in Table 2-7.

Table 2-7 Mechanical properties of Haynes 188 [77].

Tensile		Elongation (%)	Hardness (R_c)	Rupture stress for 1000hr exposure (MPa)		
Strength (MPa)	0.2 % Yield Strength (MPa)			650°C	760°C	870°C
991	483	50.6	21.8	407	179	80

2.7.4.4 Metallurgy

H188 is a solid solution strengthened cobalt-based alloy which has a fcc matrix, a random distribution of M_6C carbides, and a lanthanum-rich phase that is associated with some of the M_6C carbides. When H188 is aged between 704 - 982 °C, $M_{23}C_6$ carbides are known to precipitate at the grain boundaries. With extended exposure time $M_{23}C_6$ carbides are also known to form at twin boundaries and Laves phase forms. The effect these have on the alloy is to increase the hardness and reduce the ductility. The ductility of the alloy can be restored by annealing further at 1178 °C; according to Kalluri et al [80].

Cobalt-based alloys are generally not as resistant to oxidisation as nickel-based alternatives. It is hypothesised that this is due to the formation of less chromium oxide (Cr_2O_3) scale and a tendency of the alloy to precipitate more cobalt-tungsten oxides ($CoWO_4$), which Levi et al surmises may have the effect of developing low melting point eutectics and accelerate the corrosion of the alloy. Levi et al does however say “the chromium in H188 does partially address the issue of Co–Cr–O forming less protective oxides at intermediate temperatures however at the lower temperature tested 1050 °C significant grain boundary attack was seen.” [76], this would suggest that at temperatures above what would be considered intermediate, requires further investigation to determine the exact cause of the alloy’s susceptibility to oxidisation.

Oxides that form on H188 are generally CoO, NiO, spinels and Cr_2O_3. Co–Ni-oxide maybe seen at temperatures around 1050 °C, and Co–Cr-oxide may be observed at temperatures around 1100 °C with longer exposures [76].

“As a class, the cobalt-base alloys are not as resistant to oxidation as the nickel-base alloys. This is mainly due to the formation of non-protective oxides such as CoO. According to Haynes the chromium in H188 partially addresses this issue and the addition of lanthanum, to modify the protective oxide scale, enables the development of a tenacious oxide that retards diffusion.”[76]

When testing the cyclic-crack-growth rates of three superalloys, Lee et al compared the growth rates at different temperatures for periods of 2 mins, 10 mins and 30 mins. Lee et al found that at the highest temperature tested, 927 °C, H188 had the lowest crack growth rate compared with H230 which outperformed Hastelloy X [81].

In a separate study by Lee et al, H188 was found to have an initial grain size of 45 µm [82], which is the smallest of the superalloys studies in this review so far.

2.7.4.5 Welding

The weldability of H188 is considered to be excellent, Lee et al investigated the high temperature behaviour of the alloy and found “From a deformability, flow resistance and microstructural control perspective, the optimum temperature and strain rate conditions for fabricating H188 components are 400-800 °C and 1×10^3–5×10^3 s^{-1},respectively" [83].

H188 is weldable through a variety of methods including: TIG, MIG, electron beam welding and resistance welding methods. Welding of H188 is not recommended using submerged arc welding due to the high heat input and slow cooling of the weld which can cause cracking to occur [77].

Hot cracking as in nickel-based alloys is known to increase in frequency as the number of grains per cross section decreases. The amount of hot cracking however has been shown to be less than those experienced by nickel-base alloys X and 625 [84].

2.7.4.6 Additive manufacturing

H188 has been deposited in the past using LPBF as in the work of Liu et al. [85]. It is not believed that H188 has previously been deposited using a wire-based AM process. However, similar Co-based alloys, such as Stellite 6, have been deposited using WAAM in previous studies, such as in the work of Lin et al. [86].

2.7.5 Waspaloy

2.7.5.1 Overview

Waspaloy is known for its ability to perform in the high temperature environments of aerospace propulsion systems. Haynes Waspaloy is an age hardenable nickel-based mainly Ni-Cr-Co alloy, it is described as having excellent high-temperature strength and good resistance to corrosion most notably to oxidation [87][88].

Waspaloy was developed in the 1940s and was a trademark of Pratt & Whitney Aircraft in 1946 [89]. Waspaloy was in use as early as the 1950s [90], and saw its first production use as gas turbine blades in the Pratt & Whitney J48 in 1952. Waspaloy along with IN718 was considered by Kracke to be the most successful alloys of modern time, due to the advanced properties and performance of the alloy, the increased performance that vacuum melting can provide, and the continuation of the development of alloys from the bases that Waspaloy and IN718 provided [89].

In 1979 Waspaloy was one of the most widely used alloys in the aerospace industry, particularly in gas turbine disk applications [91]. Waspaloy has been applied across several applications from aerospace to the chemical industry [92]. Waspaloy has been seen as a replacement for IN718 in some applications due to its strengthened precipitation and lack of any significant iron in its matrix [93]. According to Haynes, in a significant number of settings Waspaloy is now being replaced by Haynes 282 due to the increased creep strength and the superior fabricability of the 282 alloy [94].

Waspaloy was widely used in gas turbine engines and was particularly valued for its mechanical properties such as: tensile, low-cycle fatigue, and creep performance [91].

2.7.5.2 Chemical composition

The chemical composition of Haynes Waspaloy is shown in Table 2-8.

Table 2-8 Chemical composition of Haynes Waspaloy (wt. %) [87].

Ni	Cr	Co	Mo	Ti	Fe	Al	Mn	Si	C	Zr	B
58	19	13.5	4.3	3	<2	1.5	<0.1	<0.15	0.08	0.05	0.006

2.7.5.3 Mechanical properties

The mechanical properties of Waspaloy are shown in Table 2-9.

Table 2-9 Mechanical properties of Waspaloy [31].

Tensile		Elongation (%)	Hardness (R_c)	Rupture stress for 1000hr exposure (MPa)		
Strength (MPa)	0.2 % Yield Strength (MPa)			650°C	760°C	870°C
1345	900	26	34-45	460	195	50

2.7.5.4 Metallurgy

Waspaloy, a nickel-based Ni-Cr-Co-Mo alloy [87] formed of a fcc matrix with precipitates of the intermetallic Ni_3Al arrayed in a periodic structure [95]. The alloys major precipitation strengthening additives are Al and Ti [96]. Much like other nickel-based alloys its main strengthening carbide precipitate is $M_{23}C_6$.

Lerch et al found that when heat treated at 1010 °C for 2 hours and quenched at 875 °C for 24 hours, Waspaloy's grain size was ASTM size 9, or an average diameter of 16 μm, at which size $M_{23}C_6$ carbides precipitated along the grain boundaries; matrix carbides in this setting were noted as numerus and large. When heat treated at 1100 °C for 2 hours and quenched at 730 °C for 6 hours, a coarser grain structure was noted at ASTM size 3, or 125 μm. With this treatment and grain size no carbides were found on the grain boundary; matrix carbides were as noted in the 1010 °C treatment. For comparative purposes Lerch et al notes "The grain size for the as-received billet was between ASTM sizes 9 and 10 and was the same in all orientations." [97], which is between 11.2-15.9 μm [67]. The behaviour of Waspaloy in these conditions is further backed by earlier study by Alex Pinkowish, described by Sims et al in their summary of a symposium held by the High-Temperature Alloys Committee "The primary strengthening phase, γ', was found to consist of spherical ordered particles which are coherent with the matrix" [97].

Wilshire et al analysed existing creep data on Waspaloy, attempting to minimise the requirement for extended test programs to provide engineering design data. It was found that creep ductility of Waspaloy is around 0.07-0.15 (measured in strain) at high temperature (approx. 600 - 700 °C) and high stress (approx. 500-1000 MPa), and increases towards 0.3 as the test duration and the temperature increase further to >750 °C [98].

2.7.5.5 Welding

According to Haynes "Weldability is somewhat limited by susceptibility to strain age cracking under conditions of heavy restraint." Waspaloy requires a post weld heat treatment (PWHT) to re-develop properties. "During PWHT, the gamma-prime phase (Ni3Al,Ti) precipitates and the alloy undergoes a slight volumetric contraction." This encourages strain-age cracking especially if the alloy is heated to the solution annealing temperature [94].

Liquidation cracking is a common issue with arc welding of Waspaloy, Gregoi et al indicates that solution annealing before welding may reduce the formation of heat-affected-zone (HAZ) cracking [99].

2.7.5.6 Additive manufacturing

Waspaloy has been more widely deposited using various AM methods. Waspaloy has been deposited using LPBF as presented in the review by Jinoop et al. [100].

2.7.6 Haynes 282

2.7.6.1 Overview

Haynes 282 (H282) is the most modern alloy to be discussed in this review. H282 allows for a maximum service temperature of around 800 °C, which equates to an approx. increase of 23 % on the maximum service temperature of IN718 [101]. Compared with Waspaloy, H282 offers an improved machinability, better response to heat treatments and an increased creep strength performance particularly in the 649 – 927 °C range [102][103].

H282 was developed in the 2000s [31], making it a relatively recent addition to the family of nickel-based superalloys and the youngest alloy included in the review. The trend has been for the design of higher efficiency gas turbine engines and with increased efficiency comes higher temperatures, hence the need for an alloy that could operate at increasingly higher temperatures [104].

H282 was designed for use in the hot-section of military and commercial gas turbines, with the alloys improved service temperature it is likely that H282 will expand in its use [60]. H282 should allow for the development of gas turbines and allow for the replacement of IN718 in some applications.

2.7.6.2 Chemical composition

The chemical composition of H282 is shown in Table 2-10.

Table 2-10 Chemical composition of Haynes 282 (wt. %) [103].

Ni	Cr	Co	Mo	Ti	Al	Fe	Mn	Si	C	B
57	20	10	8.5	2.1	1.5	<1.5	<0.3	<0.15	0.06	0.005

2.7.6.3 Mechanical properties

The mechanical properties of H282 are shown in Table 2-11.

Table 2-11 Mechanical properties of Haynes 282 [31].

Tensile				Rupture stress for 1000hr exposure (MPa)		
Strength (MPa)	0.2 % Yield Strength (MPa)	Elongation (%)	Hardness (R_c)	650°C	760°C	870°C
1165	720	32	32	550	240	70

2.7.6.4 Metallurgy

H282 is a γ'-strengthened Ni-based mainly Ni-Cr-Co-Mo superalloy [105][77] with a fcc matrix microstructure [106].

Kirka et al, in a report for the US department for energy, observed the precipitates amongst the phases of H282 and found primary carbides and gamma prime strengthening precipitates. Precipitates at the grain boundaries were observed to be mainly Ti and Mo associated and were mainly MC carbides. Two types of morphology were found for carbides at the grain boundaries, which Kirka et al describes as blocky and film-like [107].

Hanning et al studied the H282 in sheet form which showed a hardness value of 265 ± 3 HV. The microstructure was observed to have an average grain size of 55 ± 5 µm and no continuous grain boundary carbide network was present, with the exception of carbides found on some grain boundary segments under high magnification. Hanning et al also states “Large primary MC-type carbides are visible in the microstructure.” When subjected to a heat-treatment consisting of solutionising at 1010 °C for 2 hours, γ’ precipitation at 788 °C for 8 hours followed by air cooling, H282’s hardness was significantly increased with no significant effect on the grain size [101].

Matysiak et al found that in as cast H282 fine MC precipitates at the grain boundary strengthen the alloy and restrict the effect of other elements that would promote phase instability during use and heat-treatment. These MC carbides are known to form $M_{23}C_6$ carbides at 760–980 °C and also M_6C carbides at 815 – 980 °C [105].

Kim et al investigated the difference in the performance of wrought and cast forms of H282. The study indicated that although there was no difference in the performance of H282 in creep performance, in tensile testing saw significant differences. In the wrought alloy Kim et al explains “the tensile strength (TS) and elongation ranged from 1,010 to 1,035 MPa and 45 – 48 %, respectively. In comparison, the cast alloy had a much lower strength of 460 – 475 MPa and an elongation of 1.5 – 1.8 %” Kim et al surmises this may be due to brittle deformation caused by micro-cracks and irregularities in the microstructure of the cast alloy. The wrought alloy failed via a ductile fracture [102].

The high temperature tensile tests conducted by Kim et al, showed that the tensile strength of the alloy dropped significantly at 800 °C due to the thermal activation of dislocations. The tensile strength of the cast alloy only showed a slight decrease in comparison. H282 is strengthened by both its solid-solution and precipitation hardening which gives the alloy the same performance in creep strength as the wrought and cast alloy, so long as the heat-treatment remains the same [102].

2.7.6.5 Welding

According to Haynes, H282 has a greater weldability than Waspaloy and other alloys of similar strength due to its high resistance to strain-age cracking. The best method to weld H282 is by TIG and MIG welding, submerged arc welding is not recommended in H282 due to the increased weld resistance and high heat input [103].

H282 has been reported to be affected by HAZ cracking by grain boundary liquidation [104]. It has also been confirmed in previous studies that liquid films occur at the grain boundary at high temperatures [108].

Hanning et al, in a weldability study was unable to recreate cracking in the HAZ but did however find cracking in the fusion zone deposits, which was identified as solidification cracking. They also found "Crack-like voids in bottom regions of weld deposit layers" which were identified as aluminium-rich oxide layers which had not been removed between deposition layers. It was also found that an increase in welding current increased the likelihood of solidification cracking in the fusion zone layers [104].

2.7.6.6 Additive manufacturing

H282 has been deposited previously using EBM [109], LPBF [110] and more recently using WAAM [111].

2.8 Summary

In summary of the literature review, the requirement for performance in the high-speed flight environment has been discussed. It is understood that structures in service will be subjected to aggressive heating and aeroacoustics loads, but that the severity of this will vary depending on the component's location on the structure. Materials suited to service for this application were also discussed and found that more traditional structural aerospace materials will not be suitable, instead the use of superalloys is more appropriate. In using WAAM to deposit these components potential issues were identified, which mainly centre on the thermal cycles the superalloy would be subjected to and what effect this may have on the metallurgy and thus performance. Environmental factors which could affect the alloys were also discussed and concluded that oxygen could adversely affect alloy performance.

Suitable WAAM methods for the deposition of superalloys was also discussed and found that PAW would be the most suited. In testing the performance of the deposited alloys for the application, it was established that high temperature testing would be required, but that creep would likely not be necessary to investigate due to the short flight times and nature of the single use missions. As the WAAM process would likely affect the performance of superalloys, it was established that some post-processing would likely be required to preserve performance, such as heat-treatment or cold working. Several alloys of interest were then identified for further study.

2.9 References

[1] M.J. Cotteleer, 3D opportunity: Additive manufacturing paths to performance, innovation, and growth, SIMT Addit. Manuf. Symp. (2014) 23. http://simt.com/uploads/4881/SIMT_AM_Conference_Keynote.pdf.

[2] A. Gisario, M. Kazarian, F. Martina, M. Mehrpouya, Metal additive manufacturing in the commercial aviation industry: A review, J. Manuf. Syst. 53 (2019) 124–149. https://doi.org/10.1016/j.jmsy.2019.08.005.

[3] A. Honma, Y. Fukui, Construction methods of three-dimensional shapes based on the nesting behavior of paper wasps, Int. J. Japan Soc. Precis. Eng. 29 (1995) 361–366.

[4] W.E. Frazier, Metal additive manufacturing: A review, J. Mater. Eng. Perform. 23 (2014) 1917–1928. https://doi.org/10.1007/s11665-014-0958-z.

[5] ISO, ASTM International, ISO/ASTM 52900:2021(en) Additive manufacturing — General principles — Fundamentals and vocabulary, (2021). https://doi.org/10.1520/F3177-21.

[6] S.W. Williams, F. Martina, A.C. Addison, J. Ding, G. Pardal, P. Colegrove, Wire + Arc additive manufacturing, Mater. Sci. Technol. 32 (2016) 641–647. https://doi.org/10.1179/1743284715Y.0000000073.

[7] S. Kou, Welding Metallurgy, 2nd ed, Hoboken, N.J. : Wiley-Interscience,

2003.

[8] X. Xu, S. Ganguly, J. Ding, S. Guo, S. Williams, F. Martina, Microstructural evolution and mechanical properties of maraging steel produced by wire + arc additive manufacture process, Mater. Charact. 143 (2018) 152–162. https://doi.org/10.1016/j.matchar.2017.12.002.

[9] B. Baufeld, O. Van der Biest, R. Gault, Additive manufacturing of Ti-6Al-4V components by shaped metal deposition: Microstructure and mechanical properties, Mater. Des. 31 (2010) S106–S111. https://doi.org/10.1016/j.matdes.2009.11.032.

[10] J. Norrish, Advanced welding processes : technologies and process control, [New editi, 2006. https://doi.org/10.1533/9781845691707.136.

[11] F. Martina, Introduction to Additive Manufacturing, Cranf. Univ. (2019).

[12] P.K. Swaminathan, D.F. Rauit, J.C. Taylor, R.E. Erlandson, J. Kouroupis, C.I. Meng, I.S. Diego, Transition Regime Aerodynamic Heating of Missiles 30th AIAA Thermophysics Conference For permission to copy or republish , contact the American Institute of Aeronautics and Astronautics, (1995). https://doi.org/10.2514/6.1995-2117.

[13] P.S. Gilman, Light High-Temperature Aluminium Alloys for Supersonic and Hypersonic Vehicles, in: E.A. Thornton (Ed.), Therm. Struct. Mater. High-Speed Flight, American Institute of Aeronautics and Astronautics, Washington DC, 1992: pp. 141–160.

[14] E.A. Thornton, Aerospace thermal-structural testing technology, Appl Mech Rev. 50 (1997).

[15] A. Cottrell, An Introduction to Metallurgy, 2nd ed., London : Institute of Materials, 1995.

[16] J.R. Davis, ASM Specialty Handbook: Heat-Resistant Materials, in: ASM Spec. Handb. Heat-Resistant Mater., ASM International, 1997: p. 36.

[17] T.M. Pollock, Alloy design for aircraft engines, Nat. Mater. 15 (2016) 809–

815. https://doi.org/10.1038/nmat4709.

[18] E. Fleeman, Missile Design and System Engineering, American Institute of Aeronautics and Astronautics, Inc., 2012.

[19] O. Hedayati, N. Korei, M. Adeli, M. Etminanbakhsh, Microstructural evolution and interfacial diffusion during heat treatment of Hastelloy/stainless steel bimetals, J. Alloys Compd. 712 (2017) 172–178. https://doi.org/10.1016/j.jallcom.2017.04.080.

[20] F. Martina, J. Mehnen, S.W. Williams, P. Colegrove, F. Wang, Investigation of the benefits of plasma deposition for the additive layer manufacture of Ti-6Al-4V, J. Mater. Process. Technol. 212 (2012) 1377–1386. https://doi.org/10.1016/j.jmatprotec.2012.02.002.

[21] G. Marinelli, F. Martina, S. Ganguly, S. Williams, Development of Wire + Arc additive manufacture for the production of large-scale unalloyed tungsten components, Int. J. Refract. Met. Hard Mater. 82 (2019) 329–335. https://doi.org/10.1016/j.ijrmhm.2019.05.009.

[22] Welding Engineering and Laser Processing Centre Cranfield University, MATERIALS AND PROPERTIES, (2019). https://waammat.com/about/materials-and-properties (accessed November 8, 2019).

[23] Gregori, A., A survey of welding and repairing of nickel superalloys for gas turbines, 2003. http://scholar.google.com/scholar_lookup?title=A+survey+of+welding+and+repairing+of+nickel+superalloys+for+gas+turbines&author=A.+Gregori&publication_year=2003.

[24] Wollongong University, Nickel Alloys - Function of the alloying elements, (1999).

[25] M.J. Donachie, S.J. Donachie, Understanding Superalloy Metallurgy, in: Superalloys - A Tech. Guid., 2nd ed., ASM International, 2002: pp. 25–39. https://doi.org/10.31399/asm.tb.stg2.t61280025.

[26] U.S. Titanium Industry Inc., Titanium Alloys - Ti6Al4V Grade 5, AZoM. (2020). https://www.azom.com/article.aspx?ArticleID=1547 (accessed December 6, 2022).

[27] Special Metals, INCONEL® alloy 718, (2007) 1–28. https://www.specialmetals.com/assets/smc/documents/inconel_alloy_718.pdf (accessed May 8, 2020).

[28] F. Martina, G. Marinelli, S. Ganguly, S.W. Williams, Wire + Arc Additive Manufacturing of Refractory Metals, (2016).

[29] W. Gerberich, W. Yang, 8.01 - Interfacial and Nanoscale Failure, in: Compr. Struct. Integr., Elsevier Ltd, 2007: pp. 1–40. https://doi.org/10.1016/B0-08-043749-4/08148-9.

[30] J.F. Lancaster, Metallurgy of Welding, 6th ed., Elsevier, 1999. https://www.elsevier.com/books/metallurgy-of-welding/lancaster/978-1-85573-428-9.

[31] J.C. Lippold, S.D. Kiser, J.N. DuPont, Welding Metallurgy and Weldability of Nickel-Base Alloys, 1st ed., John Wiley & Sons, Incorporated, 2009.

[32] X. Xu, J. Ding, S. Ganguly, C. Diao, S. Williams, Oxide accumulation effects on wire + arc layer-by-layer additive manufacture process, J. Mater. Process. Tech. 252 (2018) 739–750. https://doi.org/10.1016/j.jmatprotec.2017.10.030.

[33] J. Ding, P. Colegrove, F. Martina, S. Williams, R. Wiktorowicz, M.R. Palt, Development of a laminar flow local shielding device for wire + arc additive manufacture, J. Mater. Process. Technol. 226 (2015) 99–105. https://doi.org/10.1016/j.jmatprotec.2015.07.005.

[34] X. Bai, P. Colegrove, J. Ding, X. Zhou, C. Diao, P. Bridgeman, H. Zhang, S. Williams, International Journal of Heat and Mass Transfer Numerical analysis of heat transfer and fluid flow in multilayer deposition of PAW-based wire and arc additive manufacturing, Int. J. Heat Mass Transf. 124 (2018) 504–516. https://doi.org/10.1016/j.ijheatmasstransfer.2018.03.085.

[35] K.C. Mills, B.J. Keene, R.F. Brooks, A. Shirali, Marangoni effects in welding, Philos. Trans. R. Soc. A Math. Phys. Eng. Sci. 356 (1998) 911–925. https://doi.org/10.1098/rsta.1998.0196.

[36] A.G. Abdulsalam, S. Ganguly, Study on the effect of oxygen content on the impact toughness of weld metal, Cranfield University, 2011. https://mta.cranfield.ac.uk/handle/1826.1/4748.

[37] X. Xu, J. Ding, S. Ganguly, S. Williams, Investigation of process factors affecting mechanical properties of INCONEL 718 superalloy in wire + arc additive manufacture process, J. Mater. Process. Technol. 265 (2019) 201–209. https://doi.org/10.1016/j.jmatprotec.2018.10.023.

[38] J. Beddoes, Prediction of creep properties for two nickel-base superalloys from stress relaxation testing, J. Strain Anal. Eng. Des. 46 (2011) 416–427. https://doi.org/10.1177/0309324711407707.

[39] ASTM International, ASTM E139-11(18): Standard Test Method for Conducting Creep, Creep-Rupture, and Stress-Rupture Tests of Metallic Materials, ASTM B. Stand. 11 (1958) 1–14. https://doi.org/10.1520/E0139-11R18.responsibility.

[40] B. Nagarajan, D. Kumar, Z. Fan, S. Castagne, Effect of deep cold rolling on mechanical properties and microstructure of nickel-based superalloys, Mater. Sci. Eng. A. 728 (2018) 196–207. https://doi.org/10.1016/j.msea.2018.05.005.

[41] J. Xu, H. Gruber, D. Deng, R.L. Peng, J.J. Moverare, Short-term creep behavior of an additive manufactured non-weldable Nickel-base superalloy evaluated by slow strain rate testing, Acta Mater. 179 (2019) 142–157. https://doi.org/10.1016/j.actamat.2019.08.034.

[42] W.L. Chan, H.K.F. Cheng, Hammer peening technology—the past, present, and future, Int. J. Adv. Manuf. Technol. 118 (2022) 683–701. https://doi.org/10.1007/s00170-021-07993-5.

[43] J.T. Tharappel, J. Babu, Welding processes for Inconel 718- A brief review,

IOP Conf. Ser. Mater. Sci. Eng. 330 (2018) 0–6. https://doi.org/10.1088/1757-899X/330/1/012082.

[44] T.L. Jones, Frank Whittle's W2B Turbojet: United Kingdom versus United States Development, Aircr. Engine Hist. Soc. Inc. (2002). https://web.archive.org/web/20160330052504/http://enginehistory.org/GasTurbines/W2B.shtml (accessed May 6, 2020).

[45] Special Metals, Special Metals Corporation: History, (2013). https://web.archive.org/web/20080421064350/http://www.specialmetals.com/history.php (accessed May 6, 2020).

[46] A. Lingenfelter, Welding of Inconel Alloy, Superalloy 718- Metall. Appl. (1989) 673–683.

[47] E. Hosseini, V.A. Popovich, A review of mechanical properties of additively manufactured Inconel 718, Addit. Manuf. 30 (2019) 100877. https://doi.org/10.1016/j.addma.2019.100877.

[48] B. Baufeld, Mechanical properties of INCONEL 718 parts manufactured by shaped metal deposition (SMD), J. Mater. Eng. Perform. 21 (2012) 1416–1421. https://doi.org/10.1007/s11665-011-0009-y.

[49] E. Akca, A. Gürsel, A Review on Superalloys and IN718 Nickel-Based INCONEL Superalloy, Period. Eng. Nat. Sci. 3 (2015). https://doi.org/10.21533/pen.v3i1.43.

[50] Battelle Memorial Institute, Heat-Resistant Alloys, in: Met. Mater. Prop. Dev. Stand., Battelle Memorial Institute, 2017. https://app.knovel.com/hotlink/pdf/id:kt00CX2NX1/metallic-materials-properties/metallic-m-mechanical.

[51] X. Xu, Wire + Arc Additive Manufacture of New and Multiple Materials, Cranfield University, 2018. http://dspace.lib.cranfield.ac.uk/handle/1826/15107.

[52] R. Kayacan, R. Varol, O. Kimilli, The effects of pre- and post-weld heat

treatment variables on the strain-age cracking in welded Rene 41 components, Mater. Res. Bull. 39 (2004) 2171–2186. https://doi.org/10.1016/j.materresbull.2004.08.003.

[53] M.J. Donachie, S.J. Donachie, Superalloys - A Technical Guide, 2nd ed., ASM International, 2002. https://app.knovel.com/hotlink/toc/id:kpSATGE003/superalloys-technical/superalloys-technical.

[54] Rolled Alloys, Data Sheet Rene 41, (2011). http://www.rolledalloys.com/alloys/cobalt-alloys/rene-41/en/ (accessed July 5, 2022).

[55] S.E. Atabay, O. Sanchez-Mata, J.A. Muñiz-Lerma, R. Gauvin, M. Brochu, Microstructure and mechanical properties of rene 41 alloy manufactured by laser powder bed fusion, Mater. Sci. Eng. A. 773 (2020) 1–10. https://doi.org/10.1016/j.msea.2019.138849.

[56] J. Li, H.M. Wang, Microstructure and mechanical properties of rapid directionally solidified Ni-base superalloy Rene’41 by laser melting deposition manufacturing, Mater. Sci. Eng. A. 527 (2010) 4823–4829. https://doi.org/10.1016/j.msea.2010.04.062.

[57] M. Haack, M. Kuczyk, A. Seidel, E. López, F. Brueckner, C. Leyens, Comprehensive study on the formation of grain boundary serrations in additively manufactured Haynes 230 alloy, Mater. Charact. 160 (2020) 110092. https://doi.org/10.1016/j.matchar.2019.110092.

[58] P.S. McNeff, B.K. Paul, Electroplasticity effects in Haynes 230, J. Alloys Compd. 829 (2020) 154438. https://doi.org/10.1016/j.jallcom.2020.154438.

[59] D. Ewest, P. Almroth, B. Sjödin, D. Leidermark, K. Simonsson, Isothermal and thermomechanical fatigue crack propagation in both virgin and thermally aged Haynes 230, Int. J. Fatigue. 120 (2019) 96–106. https://doi.org/10.1016/j.ijfatigue.2018.11.004.

[60] C. Sponaugle, History of Haynes International, Inc., Pittsburgh Eng. (2000)

7–9. http://www.titanmf.com/wp-content/uploads/docs/Hastelloy-History-of-Haynes-Intl-Haynes-Intl.pdf.

[61] Haynes International, Haynes Alloy Portfolio, (n.d.). http://www.haynesintl.com/alloys/alloy-portfolio_ (accessed May 7, 2020).

[62] Y.L. Lu, L.J. Chen, P.K. Liaw, G.Y. Wang, C.R. Brooks, S.A. Thompson, J.W. Blust, P.F. Browning, A.K. Bhattacharya, J.M. Aurrecoechea, D.L. Klarstrom, Effects of temperature and hold time on creep-fatigue crack-growth behavior of HAYNES® 230® alloy, Mater. Sci. Eng. A. 429 (2006) 1–10. https://doi.org/10.1016/j.msea.2005.07.039.

[63] H.M. Tawancy, D.L. Klarstrom, M.F. Rothman, N. Superalloy, H.M. Tawancy, D.L. Klarstrom, M.F. Rothman, Development of a New Nickei-Ba ~ e Superalloy · Development of a New, 36 (1984) 58–62.

[64] J.G. Yoon, H.W. Jeong, Y.S. Yoo, H.U. Hong, Materials Characterization In fl uence of initial microstructure on creep deformation behaviors and fracture characteristics of Haynes 230 superalloy at 900 ° C, Mater. Charact. 101 (2015) 49–57. https://doi.org/10.1016/j.matchar.2015.01.002.

[65] L. Jiang, R. Hu, H. Kou, J. Li, G. Bai, H. Fu, The effect of M 23 C 6 carbides on the formation of grain boundary serrations in a wrought Ni-based superalloy, Mater. Sci. Eng. A. 536 (2012) 37–44. https://doi.org/10.1016/j.msea.2011.11.060.

[66] Haynes International, HAYNES ® 230 ® alloy, (2020). http://haynesintl.com/docs/default-source/pdfs/new-alloy-brochures/high-temperature-alloys/brochures/230-brochure.pdf (accessed March 6, 2020).

[67] ASTM International, ASTM E112-13: Standard test methods for determining average grain size, ASTM Int. (2013) 1–28. https://doi.org/10.1520/E0112-13.1.4.

[68] K.A. Rozman, M.A. Carl, M. Kapoor, N. Doğan, J.A. Hawk, Creep performance of transient liquid phase bonded haynes 230 alloy, Mater. Sci. Eng. A. 768 (2019). https://doi.org/10.1016/j.msea.2019.138477.

[69] S.Y. Lee, P.K. Liaw, Y.L. Lu, D. Fielden, L.M. Pike, D.L. Klarstrom, ELEVATED-TEMPERATURE CREEP-FATIGUE CRACK-GROWTH BEHAVIOR OF NICKEL-BASED HAYNES® R-41, HAYNES® 230® and HASTELLOY® X AllOYS, in: Proc. Int. Symp. Superalloys, The Minerals, Metals & Materials Society, 2008: pp. 509–514. https://www.tms.org/Superalloys/10.7449/2008/Superalloys_2008_509_514.pdf.

[70] D.L. Klarstrom, The development of HAYNES® 230® alloy, in: Mater. Des. Approaches Exp., 2001.

[71] S.C. Ernst, Weldability studies of Haynes[reg sign] 230 alloy, Weld. J. (Miami); (United States). 73:4 (1994) 80–89.

[72] J.A. Schneider, D. Williston, T.L. Murphy, C. Varner, J. Hawkins, B. Walker, Solid state joining of nickel based alloy, Haynes 230, J. Mater. Process. Technol. 225 (2015) 492–499. https://doi.org/10.1016/j.jmatprotec.2015.04.034.

[73] B. Yang, Z. Shang, J. Ding, J. Lopez, W. Jarosinski, T. Sun, N. Richter, Y. Zhang, H. Wang, X. Zhang, Investigation of strengthening mechanisms in an additively manufactured Haynes 230 alloy, Acta Mater. 222 (2022). https://doi.org/10.1016/j.actamat.2021.117404.

[74] T. Bauer, K. Dawson, A.B. Spierings, K. Wegener, Microstructure and mechanical characterisation of SLM processed Haynes® 230®, Proc. - 26th Annu. Int. Solid Free. Fabr. Symp. - An Addit. Manuf. Conf. SFF 2015. (2020) 813–822.

[75] G.R. Halford, J.F. Saltsman, S. Kalluri, High temperature fatigue behavior of Haynes 188, in: Adv. Earth-to-Orbit Propuls. Technol. Conf., NASA, Marshall Space Flight Center, Huntsville, AL, 1988: pp. 497–509. https://doi.org/19900019326.

[76] T.P. Levi, K.J. Stevens, Oxidation behaviour of LM 6000 gas turbine engine substrate cobalt-base alloy 188, Mater. High Temp. 24 (2007) 173–185.

https://doi.org/10.3184/096034007X265198.

[77] Haynes International, HAYNES 188 Alloy, (2008).

[78] Haynes International, HAYNES® 188 alloy: Principle Features, (2015). http://www.haynesintl.com/alloys/alloy-portfolio_/High-temperature-Alloys/HAYNES188alloy.aspx (accessed May 9, 2020).

[79] S.Y. Lee, Y.L. Lu, P.K. Liaw, L.J. Chen, S.A. Thompson, J.W. Blust, P.F. Browning, A.K. Bhattacharya, J.M. Aurrecoechea, D.L. Klarstrom, Hold-time effects on elevated-temperature low-cycle-fatigue and crack-propagation behaviors of HAYNES® 188 superalloy, J. Mater. Sci. 44 (2009) 2945–2956. https://doi.org/10.1007/s10853-009-3391-1.

[80] S. Kalluri, G. Halford, Damage Mechanisms in Bithermal and Thermomechanical Fatigue of Haynes 188, in: Thermomechanical Fatigue Behav. Mater., NASA, San Diego, CA, 1992. https://doi.org/10.1520/stp24253s.

[81] S.Y. Lee, Y.L. Lu, P.K. Liaw, H. Choo, S.A. Thompson, J.W. Blust, P.F. Browning, A.K. Bhattacharya, J.M. Aurrecoechea, D.L. Klarstrom, High-temperature tensile-hold crack-growth behavior of HASTELLOY ® X alloy compared to HAYNES® 188 and HAYNES ® 230® alloys, Mech. Time-Dependent Mater. 12 (2008) 31–44. https://doi.org/10.1007/s11043-008-9049-6.

[82] S.Y. Lee, Y.L. Lu, P.K. Liaw, H. Choo, S.A. Thompson, J.W. Blust, P.F. Browning, A.K. Bhattacharya, J.M. Aurrecoechea, D.L. Klarstrom, Elevated-temperature creep-fatigue crack-growth behavior of HAYNES®188 superalloy, in: Key Eng. Mater., 2007.

[83] W.S. Lee, H.C. Kao, High temperature deformation behaviour of Haynes 188 alloy subjected to high strain rate loading, Mater. Sci. Eng. A. 594 (2014) 292–301. https://doi.org/10.1016/j.msea.2013.11.076.

[84] S.J. Matthews, Weldability Studies on High Performance Alloys in Thin Sheet Form., Weld. J. (Miami, Fla). 54 (1975).

[85] Y. Liu, Z. Huang, C. Zhang, J. Lu, N. Ouyang, Q. Shen, F. Chen, Hierarchical Microstructure and Strengthening Mechanism of Haynes 188 Alloy Manufactured by Laser Powder Bed Fusion, 2022. https://doi.org/10.2139/ssrn.4137485.

[86] Z. Lin, W. Ya, V.V. Subramanian, C. Goulas, B. di Castri, M.J.M. Hermans, B. Pathiraj, Deposition of Stellite 6 alloy on steel substrates using wire and arc additive manufacturing, Int. J. Adv. Manuf. Technol. 111 (2020) 411–426. https://doi.org/10.1007/s00170-020-06116-w.

[87] Haynes International, HAYNES ® Waspaloy alloy, (2017). http://haynesintl.com/docs/default-source/pdfs/new-alloy-brochures/high-temperature-alloys/brochures/waspaloy.pdf?sfvrsn=e77229d4_24 (accessed May 8, 2020).

[88] K.A. Mumtaz, P. Erasenthiran, N. Hopkinson, High density selective laser melting of Waspaloy®, J. Mater. Process. Technol. 195 (2008) 77–87. https://doi.org/10.1016/j.jmatprotec.2007.04.117.

[89] A. Kracke, Superalloys, the most successful alloy system of modern times - Past, present and future, in: 7th Int. Symp. Superalloy 718 Deriv. 2010, 2010: pp. 13–50.

[90] C.T. Sims, A history of superalloy metallurgy for superalloy metallurgists, Superalloys 1984. (1984) 399–419. https://pdfs.semanticscholar.org/fe6e/0258a494591cabaf9c2ee84afecd3708199b.pdf.

[91] D.J. Deye, W.H. Couts, Super Waspaloy Microstructure and Properties., ASTM Spec. Tech. Publ. (1979) 601–615.

[92] K.M. Chang, X. Liu, Effect of content on the mechanincal behavior of the WASPALOY alloy system, Mater. Sci. Eng. A. 308 (2001) 1–8. https://doi.org/10.1016/S0921-5093(00)02042-6.

[93] V. Dhinakaran, J. Ajith, A. Fathima Yasin Fahmidha, T. Jagadeesha, T. Sathish, B. Stalin, Wire Arc Additive Manufacturing (WAAM) process of

nickel based superalloys-A review, Mater. Today Proc. 21 (2020) 920–925. https://doi.org/10.1016/j.matpr.2019.08.159.

[94] Haynes International, HAYNES® Waspaloy alloy: Priciple Features, (2015). http://www.haynesintl.com/alloys/alloy-portfolio_/High-temperature-Alloys/haynes-waspaloy-alloy (accessed May 10, 2020).

[95] D.L. Davidson, R.G. Tryon, M. Oja, R. Matthews, K.S. Ravi Chandran, Fatigue crack initiation in WASPALOY at 20 °C, Metall. Mater. Trans. A Phys. Metall. Mater. Sci. 38 A (2007) 2214–2225. https://doi.org/10.1007/s11661-007-9178-6.

[96] REHRER WP, MUZYKA DR, HEYDT GB, Solution Treatment and Al Plus Ti Effects on the Structure and Tensile Properties of Waspaloy, J Met. 22 (1970) 32–38.

[97] B.A. Lerch, N. Jayaraman, S.D. Antolovich, A study of fatigue damage mechanisms in Waspaloy from 25 to 800°C, Mater. Sci. Eng. 66 (1984) 151–166. https://doi.org/10.1016/0025-5416(84)90177-0.

[98] B. Wilshire, P.J. Scharning, Theoretical and practical approaches to creep of Waspaloy, Mater. Sci. Technol. 25 (2009) 242–248. https://doi.org/10.1179/174328408X361508.

[99] A. Gregoi, D. Bertaso, Welding and deposition of nickel superalloys 718, waspaloy and single crystal alloy CMSX-10, Weld. World. 51 (2007) 34–47. https://doi.org/10.1007/bf03266607.

[100] A.N. Jinoop, C.P. Paul, K.S. Bindra, Laser-assisted directed energy deposition of nickel super alloys: A review, Proc. Inst. Mech. Eng. Part L J. Mater. Des. Appl. 233 (2019) 2376–2400. https://doi.org/10.1177/1464420719852658.

[101] F. Hanning, A.K. Khan, J. Steffenburg-Nordenström, O. Ojo, J. Andersson, Investigation of the effect of short exposure in the temperature range of 750–950°C on the ductility of haynes® 282® by advanced microstructural characterization, Metals (Basel). 9 (2019).

https://doi.org/10.3390/met9121357.

[102] Y.-J. Kim, J.-H. Park, Y.-S. Ahn, Comparison of Creep Properties of Cast and Wrought Haynes 282 Superalloy, Adv. Mater. Sci. Eng. 2018 (2018) 1–7. https://doi.org/10.1155/2018/2048959.

[103] Haynes International, HAYNES ® 282 ® alloy, (2019). http://haynesintl.com/docs/default-source/pdfs/new-alloy-brochures/high-temperature-alloys/brochures/282-brochure.pdf?sfvrsn=20 (accessed March 2, 2020).

[104] F. Hanning, J. Andersson, Weldability of wrought Haynes® 282® repair welded using manual gas tungsten arc welding, Weld. World. 62 (2018) 39–45. https://doi.org/10.1007/s40194-017-0508-z.

[105] H. Matysiak, M. Zagorska, J. Andersson, A. Balkowiec, R. Cygan, M. Rasinski, M. Pisarek, M. Andrzejczuk, K. Kubiak, K.J. Kurzydlowski, Microstructure of haynes® 282® superalloy after vacuum induction melting and investment casting of thin-walled components, Materials (Basel). 6 (2013) 5016–5037. https://doi.org/10.3390/ma6115016.

[106] C.J. Boehlert, S.C. Longanbach, A comparison of the microstructure and creep behavior of cold rolled HAYNES® 230 alloy^{TM} and HAYNES® 282 alloy^{TM}, Mater. Sci. Eng. A. 528 (2011) 4888–4898. https://doi.org/10.1016/j.msea.2011.03.019.

[107] M. Kirka, K. Unocic, K. Kruger, A. Forsythe, Process Development for Haynes® 282® Using Additive Manufacturing, (2018). https://doi.org/10.2172/1435227.

[108] L.O. Osoba, O.A. Ojo, Influence of laser welding heat input on HAZ cracking in newly developed Haynes 282 superalloy, Mater. Sci. Technol. 28 (2012) 431–436. https://doi.org/10.1179/1743284711Y.0000000078.

[109] K.A. Unocic, M.M. Kirka, E. Cakmak, D. Greeley, A.O. Okello, S. Dryepondt, Evaluation of additive electron beam melting of haynes 282 alloy, Mater. Sci. Eng. A. 772 (2020) 138607.

https://doi.org/10.1016/j.msea.2019.138607.

[110] K.A. Christofidou, H.T. Pang, W. Li, Y. Pardhi, C.N. Jones, N.G. Jones, H.J. Stone, Microstructural Control and Optimization of Haynes 282 Manufactured Through Laser Powder Bed Fusion, in: Superalloys 2020. Miner. Met. Mater. Ser., Springer, Cham, 2020: pp. 1014–1023. https://doi.org/10.1007/978-3-030-51834-9_99.

[111] H. Zhang, Y. Wang, R.R. De Vecchis, W. Xiong, Evolution of carbide precipitates in Haynes® 282 superalloy processed by wire arc additive manufacturing, J. Mater. Process. Technol. 305 (2022). https://doi.org/10.1016/j.jmatprotec.2022.117597.

3 SELECTION AND PERFORMANCE OF AM SUPERALLOYS FOR HIGH-SPEED FLIGHT ENVIRONMENTS

This chapter is based on the following publication.

***W.S. James**, S. Ganguly, G. Pardal, Selection and Performance of AM Superalloys for High-Speed Flight Environments, Int. J. Adv. Manuf. Technol. (2022).*

Aside from a general review of literature, this chapter presents the research conducted towards the first research objective. Identifying suitable alloys for both the high-speed flight application, as described by the sponsor, and for deposition using WAAM technology. The chapter first identifies the requirements for the final alloy application and then analyses literature data to shortlist and finally select alloys for ongoing study. A preliminary investigation into RT mechanical properties and overall microstructure is also conducted.

Abstract

In developing the Wire + Arc Additive Manufacturing (WAAM) process for the manufacture of components used in high-speed flight environments, a selection process for suitable alloys was devised. Using material properties from literature sources, creep-resistant alloys were down selected based on the requirement for service in a high temperature, high stress environment and the need for an alloy suitable for manufacture using the WAAM process. Down selected alloys, Inconel 718 (IN718), Rene 41 (RE41), Haynes 188 (H188) and Inconel 625 (IN625), were deposited by a plasma transferred arc WAAM process in an oxygen-controlled environment. Wall structures were built, and samples extracted for mechanical testing. The performance of as deposited material was then compared against the wrought literature data.

Tensile testing at room temperature revealed a performance mismatch, in comparison with wrought literature data, for precipitation strengthened IN718 & RE41, however this performance mismatch was less significant for solution strengthened H188 and IN625. Results revealed that the AM material did not meet the wrought strength, likely due to significant cracking, with performance varying depending on each alloy's strengthening mechanism. Results illustrate the need for further processing to return the mechanical performance to wrought values.

Keywords: Additive manufacturing, Alloy selection, Mechanical properties, Rene 41, Inconel 718, Haynes 188, Inconel 625

3.1 Introduction

In this paper 73 alloys are ranked against the application of a structural component in a high-speed flight environment of short duration (< 1 hour), where the external structural component could reach service temperatures of +1200 K. Representing the environment experienced by a hypersonic flight system, the performance of the components will be optimised for strength at maximum operating temperature. Components for such an application will also be highly stressed to minimise structural mass.

The only group of alloys suitable for this application are creep-resistant superalloys, which are predominantly alloys intended for service at high temperatures which often contain high volumes of Ni and Cr, with a base element other than Fe [1]. The alloys investigated in this study are Ni-based and Co-based superalloys. These materials are alloyed specifically with Cr to offer oxidisation resistance which is obtained through the formation of oxide scale Cr_2O_3 at the component's surface. Traditionally these alloys have included Ni, Fe, and Co based superalloys, which have been specifically developed for high temperature applications and often boast significant retention of mechanical strength at elevated temperatures and low surface deformation. These alloys often feature a primary austenitic, face-centred-cubic (fcc) matrix, and an array of secondary strengthening phases and carbides to enhance creep resistance. Fe-Ni based alloys are strengthened by precipitation of intermetallic compounds within the matrix, most commonly by γ' precipitates, but can also be solid-solution strengthened. Ni based superalloys are mostly strengthened by the precipitation of intermetallic compounds in an austenitic fcc matrix. When Ti and Al are included in the composition, γ’ is often the strengthening precipitate. For alloys including Nb, γ’’ is also a strengthening precipitate. Ni based alloys can also be solid solution strengthened but this is less common. Some Ni alloys, called oxide-dispersion-strengthened alloys, are strengthened by the inclusion of inert particles in the matrix. Co based alloys are usually strengthened by both solid solution strengthening and carbides. [2][3]

An investigation into the effects that the Wire + Arc Additive Manufacturing (WAAM) process has on these alloys was also required, to ensure no adverse effects on the material properties. The WAAM process uses welding power sources and wire as a feedstock to deposit material in a layer-by-layer process [4]. Due to the repetitive layer-by-layer process, WAAM components also undergo a successive heating and cooling cycle which would significantly affect the metallurgical response of an alloy. Xu et al found a difference in the hardness of WAAM walls deposited from maraging steel, where the bottom of the wall was made harder due to precipitation from the aging effect of the process. They found that the amount of precipitates in the bottom of the wall, i.e. earlier layers, was roughly double the amount found in the top of the wall [4]. Li et al found, while investigating the deposition of IN625 using WAAM, that this heating cycle was most significant with each 10 successive layers and that beyond 10 layers no significant change in temperature was observed [5]. WAAM material tested during this study was extracted beyond the 10 initial layers to minimise any variation in structural integrity.

A large volume of literature exists on alloy selection for a huge variety of applications, each selection method is dependent on application and what the intended use is. The selection of materials for high-speed flight applications is a well explored and continuously developing area, however most selection processes consider the application only and not the suitability for a pre-set manufacturing method before the material is found, such various methods are examined by Huda and Edi in their review of materials selection for supersonic applications [6]. This selection process is somewhat different in considering not only the end application but also in selecting alloys suitable for the manufacturing process, in this case WAAM.

3.2 Method

3.2.1 Alloy Selection

An analysis of existing data found in literature was utilised for the purpose of ranking alloys against the application criteria. Several comprehensive sources of data were utilised for this purpose:

- Metallic Materials Properties Development and Standardization (MMPDS-12) [1]
- Superalloys - A Technical Guide by Donachie, M. J. and Donachie S. J. [7]
- Materials Properties Database for Selection of High-Temperature Alloys and Concepts of Alloy Design for SOFC Applications [8]
- High-Temperature High-Strength Nickel-Base Alloys No. 393, Nickel Institute [9]

In addition, respective manufacturer data sheets were utilised, and in some cases where data was otherwise unavailable, properties were estimated via both interpolation and extrapolation depending on the missing value (estimated figures are indicated in the Appendix, section 3.7).

The MMPDS-12 document is a source of aerospace materials data and is widely recognised as a reliable source for aircraft materials selection. Consistent methods are used to generate data which is used to present statistically based materials properties. MMPDS replaces the MILHDBK-5 document which was used previously. [1]

73 alloys were considered, and each alloy was scored against the chosen criteria, where the highest score indicates the most appropriate choice, and the lowest score indicates the least appropriate alloy. Each alloy was ranked in each category out of a possible maximum of 73. The score from each category was then totalled to give a final rank. The scoring formula, which was generated based on the research sponsors requirements for a high-speed flight application, is

comprised of a series of simplified equations intended to easily identify potentially suitable alloys amongst an extensive list. An example of the mechanical data extracted from literature is included in **Figure 3-1**. Note that cost of material is not included in the selection parameters, as the sponsor did not consider this to be a qualifying factor.

The scoring formula is as follows:

Equation 3-1 Scoring formula for alloy ranking system.

$$R_{Total} = R.UTS_{1000} + R.UTS_{1400} + R.YS_{1000} + R.YS_{1400} + R.\eta_{W_{1000}} + R.\eta_{W_{1400}} + R.\eta_{B_{1000}} + R.\alpha_{1000} + R.E_{1000} + R.(\alpha \cdot E)_{1000} + R.s$$

$R_{total} = \sum R.X_T$ Where R indicates ranked position, X is representing the category (UTS for example) and T is the temperature in °F. UTS is the ultimate tensile strength, YS is the yield strength, α is the coefficient of thermal expansion, E is the dynamic modulus of elasticity.

Weight efficiency (η_W) also known as specific strength is given by:

Equation 3-2 Specific strength (Weight efficiency).

$$\eta_W = \frac{UTS}{\rho}$$

Specific modulus referred to here as Buckling efficiency (η_B) is given by:

Equation 3-3 Specific modulus (Buckling efficiency).

$$\eta_B = \frac{E^{0.5}}{\rho}$$

Susceptibility to post weld heat treat (PWHT) cracking (s) is given by:

Equation 3-4 Susceptibility to PWHT cracking. Adapted equation from [10]**.**

$$s = \frac{|k + mx_0 - y_0|}{\sqrt{1 + m^2}} = \frac{|4.5 - Ti_{\%wt} - Al_{\%wt}|}{\sqrt{2}}$$

The equation of the line in **Figure 3-2** is given by $y = mx + k$ and the coordinate of each point is given as (x_0, y_0). The susceptibility to PWHT in Equation 3-4 above, is a calculation based on Ti and Al content of each alloy and is the distance of the points on **Figure 3-2** from the 'increased strain-age cracking' line indicating the max. content while remaining within the weldable zone. A lower value in this category represents alloys which are closer to the line, indicating better suitability. Alloys that were significantly above the 'increased strain-age cracking' line were excluded from selection. As stated by Donachie and Donachie, Ti and Al are the γ' forming elements in nickel superalloys and that when Al+Ti exceeds a critical value PWHT cracking becomes a significant issue for performance [11].

To select alloys for mechanical testing, the top performing alloy from the alloy selection process, RE41, was down selected. IN718 was also selected as the alloy has been the subject of previous research using WAAM and is included for comparative purposes due to the alloy having larger volumes of data existing in the literature. H188 was selected to better understand the performance of cobalt-based alloys manufactured using the WAAM system, and IN625 as a solid solution strengthened Ni-base alloy.

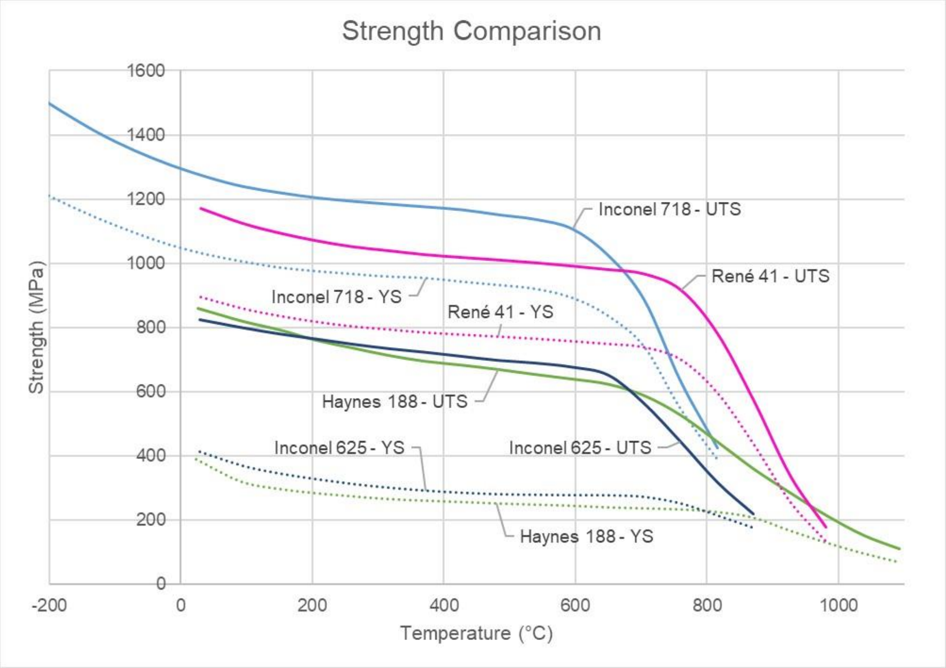

Figure 3-1 Literature data of alloy strength at temperature. [1]

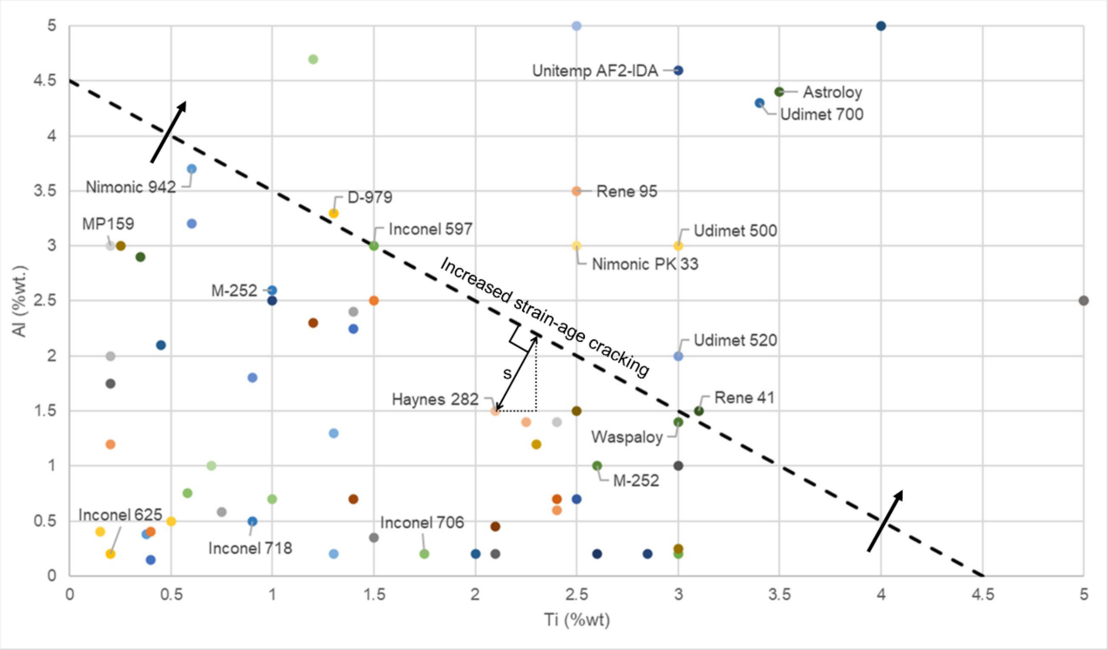

Figure 3-2 Diagram of Ti and Al content illustrating weldability of alloys. Adapted from Donachie et al Superalloys - A Technical Guide [11]**.**

3.2.2 WAAM Deposition

The selected alloys were deposited using a WAAM system consisting of a FANUC six-axis robotic arm, a plasma water-cooled welding torch mounted to the robotic arm, a wire feeder, and a part-rotator - which allowed for WAAM walls to be built on both sides of the substrate plate. Building on both sides of the substrate has the effect of reducing the residual stresses in the material and also increases productivity as material can be deposited on one side while cooling is taking place on the opposite side, reducing the time the WAAM system is idle [12].

The WAAM deposition process took place inside of an inert enclosure, which provided an Argon atmosphere of less than 800 ppm of oxygen and was monitored using an oxygen analyser. The experimental set-up is shown in **Figure 3-3**.

Wall structures were deposited from commercially available wires on both sides of a 10 mm thick Inconel 718 substrate plate. The composition of the welding wires is given in Table 3-1 and welding parameters in Table 3-2. The welding parameters were selected based partly in the work of Xu et al. on IN718 [13] and adjusted in a pilot study to suit the requirements of the WAAM system setup, the parameters vary in accordance with the wire diameter, in order to maintain a similar deposition rate across the alloys, the wire feed speed was adjusted accordingly.

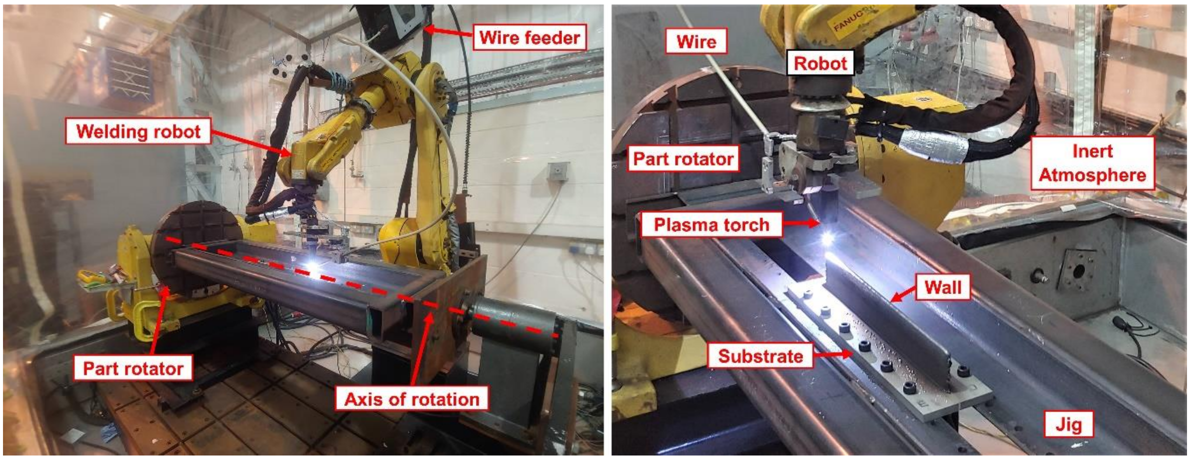

Figure 3-3 Experimental set-up for WAAM deposition.

Table 3-1 Composition of welding wires. (% weight)

Inconel 718

Ni	Cr	Fe	Nb	Mo	Ti	Al	Mn	Si	Cu	C	Others
53.57	18.56	17.8	5.01	2.87	0.97	0.60	0.10	0.08	0.07	0.04	0.51

Rene 41

Ni	Cr	Co	Mo	Ti	Fe	Al	Nb	V	Si	C	Cu	Mn	Others
53.7	18.9	10.2	9.08	3.20	2.72	1.64	0.12	0.12	0.09	0.07	0.04	0.03	0.007

Haynes 188

Co	Ni	Cr	W	Fe	Mn	Si	C	La	P	Others
37.12	22.90	22.20	13.90	2.65	0.81	0.22	0.107	0.06	0.011	0.005

Inconel 625

Ni	Cr	Mo	Nb	Fe	Ti	Al	Si	Cu	Mn	C	Others
64.75	22.16	8.79	3.60	0.24	0.19	0.17	0.04	0.02	0.02	0.01	0.006

Table 3-2 Welding parameters.

	IN718	RE41	H188	IN625
Wire Diameter (mm)	1.2	1	1.14	1.2
Torch to work distance (mm)	8	8	8	8
Current (A)	180	180	180	180
Wire feed speed (m/min)	1.8	2.4	2	1.8
Travel speed (m/min)	0.3	0.36	0.36	0.3
Inter-pass temperature (°C)	170	170	170	170
Deposition rate (kg/hour)	3.34	3.73	3.78	3.44

3.2.3 Mechanical Testing

For each selected alloy to undergo tensile testing, samples were extracted from the WAAM walls and machined into coupons. The room temperature (RT) coupon, conforming to ASTM E8(M) sub-size specification, is shown in Figure 3-4. Three coupons were tested from each alloy in the build height orientation (vertical direction). Samples were tested at RT, using an Instron 8801 Servo hydraulic Universal Testing System, and tested to failure using ASTM E8(M). Tensile tests used a strain rate of 0.005 min^{-1} until the onset of plastic deformation and thereafter a crosshead speed of 1.6 mm/min. Specimens were extracted from similar locations on the WAAM wall to minimise variation caused by the WAAM aging effect.

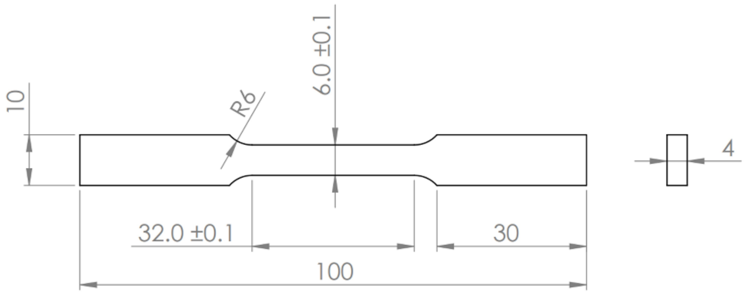

Figure 3-4 RT Tensile testing coupon. (Dimensions in mm).

3.2.4 Microstructure

Specimens of each alloy were extracted from the WAAM walls in build direction – thickness cross-sections. Specimens were then prepared for metallographic analysis by mounting, grinding, and polishing successively. Samples were then etched to reveal the microstructure using the following etchants:

IN718 – Swab etched with Kalling’s 2 for 10 seconds.

RE41 – Swab etched with a solution consisting of 3 g $CuSO_4$, 80 ml HCl, 20 ml absolute alcohol [14], for 30 seconds.

H188 – Electrolytically etched in a solution consisting of 5 g oxalic acid, 95 ml HCl, using 6 V DC with a carbon cathode and a stainless anode probe, for 1-2 sec [15].

IN625 – Swab etched with aqua regia [16] for 10 seconds.

3.3 Results

3.3.1 Alloy Selection

The top five alloys and their score in each category are given in Table 3-3, as well as the scores of each of the selected alloys (RE41, IN718, H188, IN625).

As can been seen in Table 3-3, there is not a significant difference in total score between most of the alloys presented. Alloys MP159 and H188 could not be ranked in the susceptibility to cracking category due to both alloys lacking Al and Ti in their composition. In fact, little to no cracking was visually observed in H188 samples.

Table 3-3 Ranking of alloys.

Designation	Total Score	UTS		YS		η_W		η_B	α	E	Stress (α·E)	Cracking
		1000 F	1400 F	1000 F	1400 F	1000 F	1400 F	1000 F	1000 F	1000 F		
Rene 41	673	67	66	63	66	68	66	41	65	37	64	70
MP159	608	71	70	72	72	71	71	35	25	51	15	55
MP35N	593	72	72	71	71	73	73	54	25	72	8	(2)
M-252	591	56	58	46	51	57	57	36	69	30	68	63
Inconel 617	567	19	42	19	25	21	43	48	111	64	111	64
Inconel 718	560	61	59	66	54	61	59	26	50	26	57	41
Inconel 625	314	36	30	26	29	35	31	24	20	37	18	28
Haynes 188	280	25	37	20	23	22	35	1	37	22	56	(2)

3.3.2 Mechanical Testing

The results of tensile testing are given in Table 3-4 and Figure 3-5, where wrought (Wro) values are presented alongside testing results for as deposited (AD) samples. The data shows a mismatch with the wrought data from literature, with AD samples performing someway behind the wrought values. The best UTS performance was achieved by RE41 where the performance was 72 % of the wrought value, followed by H188, IN625 and IN718, which achieved 69, 64 and 54 % of the wrought values respectively. Comparing the YS performance there is a correlation between the performance of solid solution strengthened alloys and the precipitation strengthened alloys. H188, IN625, RE41 and IN718 achieved 85, 81, 72, and 41 % of the wrought YS respectively.

The difference in performance between the alloys could be explained by the differences in strengthening mechanisms. For example, IN718 undergoes an extensive aging process to achieve maximum strength, whereas RE41 although also precipitation strengthened typically undergoes a less extensive treatment, H188 and IN625 are both primarily solid solution strengthened, which helps to explain why the performance of these alloys more closely resembles the wrought values.

Table 3-4 RT Mechanical results, and comparison with wrought (Wro) literature data [17]**.**

Alloy	Condition	UTS (MPa)	0.2 % YS (MPa)	Elongation (%)
IN718	Wro	1435	1185	21
	AD	774	485	23
RE41	Wro	1420	1060	14
	AD	1017	764	26
H188	Wro	960	485	56
	AD	660	412	56
IN625	Wro	965	490	50
	AD	622	396	57

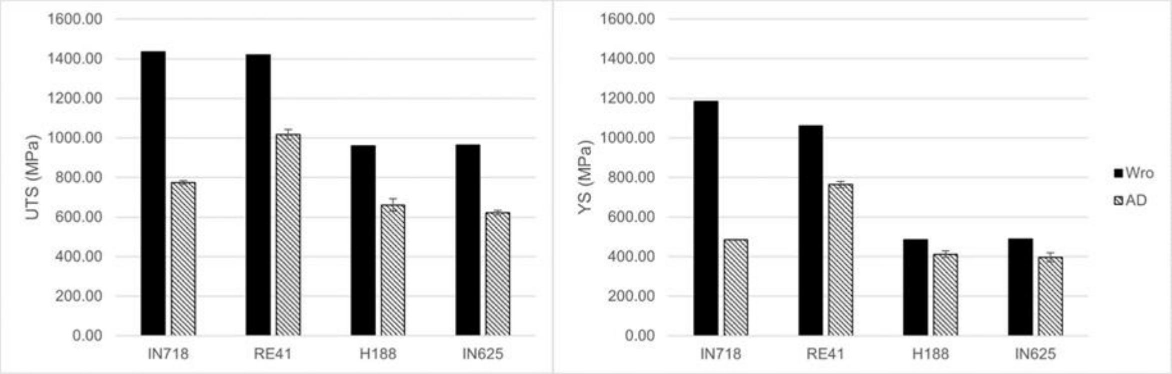

Figure 3-5 Graphical representation of data presented in Table 3-4.

3.3.3 Microstructure

The microstructure of all four alloys exhibits large columnar grains and a typical solidified dendritic structure for nickel superalloys. In Figure 3-6 lighter and darker bands can be observed along the height of the samples, which correlate to the deposited and re-heated material. The curvature of these bands, labelled as ‘Remelting line’ in Figure 3-6, are mostly curved which is thought to be due to the spreading of molten metal towards the edges during deposition. The difference observed in this spreading is thought to be due to the different viscosities of the alloys and/or slight variations in the deposition process. The grains in RE41 and H188 appear larger although less clearly defined than IN718 and IN625. The grains also extend outward with build height, indicating the flow of heat. In Figure 3-6 significant cracking can be observed in IN718, and to a lesser extent in RE41, with cracks extending through the layers. No cracking was observed in H188 or IN625.

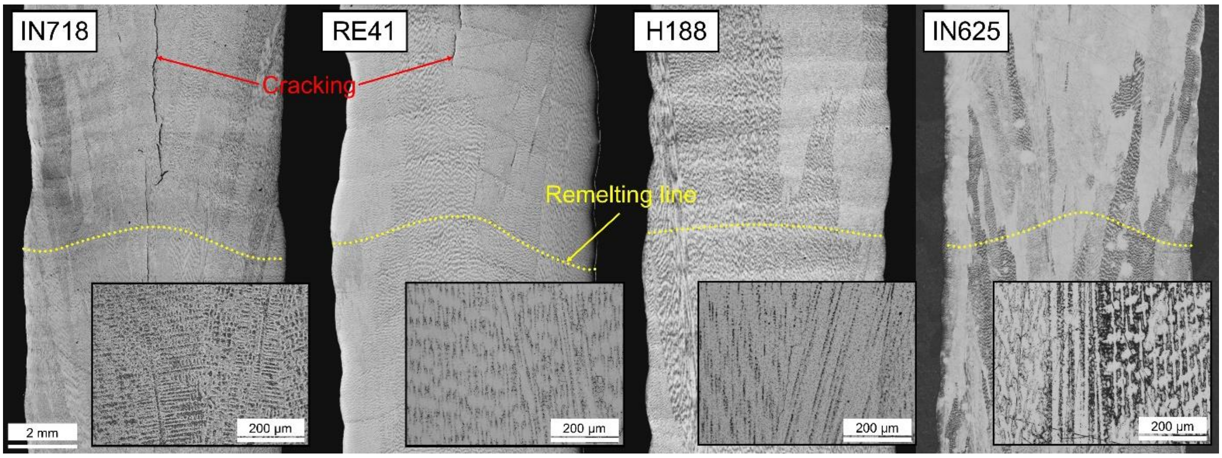

Figure 3-6 Microstructure of as deposited alloys.

3.4 Discussion

The alloy ranking method, although basic, provides an insight into the performance of the alloys in relation to the application. For the high-speed flight environment, performance at elevated temperature such as strength, weight efficiency, and elongation are important factors. The ranking formula (Equation 3-1) naturally weights more importance on the alloy’s strength, by having the UTS and YS input into the equation in five separate terms in total, including weight efficiency (specific strength) where UTS is also a term. Although strength is a large factor in the ranking formula, it does include several other factors which are important for high-speed flight, such as density which will affect the overall weight of any components. Elastic modulus and coefficient of thermal expansion are also used on the basis that they will largely dictate the deformation and corresponding thermal stress that any component will experience under a high levels of service loading at an elevated temperature. Finally, components are ranked on their suitability for welding, which eliminates any alloys that would experience a large degree of strain age cracking as a result of welding. The volume of Ti and Al in the matrix of precipitation-hardened alloys is a factor in how susceptible the alloy will be to strain-age cracking. As the alloys are effectively heated at and beyond their aging temperature during deposition, they precipitate γ' particles during the process affecting their ductility [11]. Interestingly, six of the studied alloys were eliminated due to weldability concerns that otherwise would have appeared within the top 10. This indicates that the majority of superalloys with high strength at temperature are both susceptible to cracking during welding and contain high volumes of Al and/or Ti. To further understand the effect the WAAM process has on the microstructure and fracture methods, this will be the subject of a future article.

The microstructure of the alloys was observed in Figure 3-6. The darker and lighter banding seen in the alloys was also observed by Seow et al in WAAM built IN718, their opinion agreed that the banding is the appearance of newly deposited and re-heated material [18]. Seow et al also observed the epitaxial growth of grains upwards and outwards towards the edges of the samples, which was suggested is due to the slight thermal gradient created by the increased cooling experienced at the edges of the deposition [18]. The viscosity difference in the molten alloy could explain the difference observed in the curvature of the remelting lines in Figure 3-6. In a study of the melt pool dynamics in laser powder bed fusion using IN718, Ahsan et al found that fluid flows on the sides of the melt pool due to the high temperature gradient and that the pool expands in both x and y due to Marangoni convection, buoyancy, and recoil pressure [19]. This explains the curved appearance, although further investigation is required to establish if a difference in viscosity is responsible for the differing shapes seen across the four alloys.

The strengthening mechanisms of each alloy are somewhat different but fall into two distinct categories. IN718 and RE41 are precipitation hardened alloys whereas H188 and IN625 are solid-solution-strengthened alloys. H188 is the only alloy included that is Co-based however it is alloyed significantly with Ni and Cr. H188 is not hardenable except through cold working and its strength is derived through its solid-solution-strengthened fcc matrix [20]. IN625 was also designed as a solid-solution-strengthened alloy, however the alloy has been observed to be subject to precipitation of intermetallic phases and carbides [21]. RE41 is strengthened by the precipitation of phases within its matrix, intermetallic phase γ' is the main strengthening phase and forms with Ni, Al and/or Ti [22]. IN718 is also strengthened primarily by γ' phases but is also strengthened by precipitation of γ'' phases, which forms from Ni and Nb [13]. Some correlation can be observed in the tensile results, between the level of precipitation hardening the alloy is ordinarily subjected to and the shortfall in performance of AD material. With less age hardenable alloys experiencing the least decline in performance due to the WAAM process.

The difference in cracking observed between the alloys is thought to be related to the precipitation hardening of the alloys, with the most hardenable alloy, IN718, experiencing the most cracking, followed by RE41. Whereas the other less age hardenable alloys IN625 and non-hardenable H188 did not experience any cracking. This cracking could also be responsible for the larger shortfall in tensile performance observed in IN718 and RE41.

To increase the strength of the alloys further an inter-pass cold working process could be included in the WAAM process, combined with a post deposition heat-treatment, which will be investigated in a future article. A previous study by Xu et al found that cold rolling IN718 after each deposited layer resulted in non-uniform recrystallization, which worked to increase the strength to meet and exceed the wrought performance [13]. The difference observed between the AD samples and the wrought strength highlights the need for additional processing of the alloys, such as post-process heat-treatments and/or mechanical working to return to wrought performance. Precipitation of secondary phases at the grain boundary are one of the main sources of strength for precipitation strengthened alloys. In a previous study on IN718 by Xu et al, it was suggested that the presence of large columnar grains in the WAAM structure make the precipitation of these phases less likely, due to the reduced grain boundary area [23]. This makes the use of a mechanical process to disrupt the large WAAM grains a necessity to achieve peak strength.

Further research is required to establish processing methods which can return WAAM deposited creep resistant alloys to their wrought performance.

3.5 Conclusions

In conclusion, suitable alloys for the high-speed flight application were identified using a scoring method. The method was calculated using material properties from literature sources, input into a series of simplified equations. The selected alloys then underwent mechanical testing after WAAM deposition, to understand the AD performance of the alloys compared with the wrought data from literature.

The study found:

1. Alloy RE41 is the most suitable alloy for both WAAM deposition and for application in high temperature - high stress environments.
2. Mechanical testing shows a similarity between precipitation strengthened alloys (RE41 & IN718), where these AD alloys significantly underperformed compared to wrought material. Solid solution strengthened alloys (H188 & IN625) also underperformed but the difference was less significant.
3. WAAM deposition of solid solution strengthened alloys, H188 and IN625 achieves YS performance closer to wrought values.
4. WAAM deposition of precipitation strengthened alloys can result in significant cracking, which is not experienced when depositing solid-solution-strengthened alloys.
5. Additional investigation is required into methods of returning WAAM superalloys to their wrought strength.

3.6 References

[1] Battelle Memorial Institute, Heat-Resistant Alloys, in: Met. Mater. Prop. Dev. Stand., Battelle Memorial Institute, 2017. https://app.knovel.com/hotlink/pdf/id:kt00CX2NX1/metallic-materials-properties/metallic-m-mechanical.

[2] M.J. Donachie, S.J. Donachie, Understanding Superalloy Metallurgy, in: Superalloys - A Tech. Guid., 2nd ed., ASM International, 2002: pp. 25–39. https://doi.org/10.31399/asm.tb.stg2.t61280025.

[3] Z. Yang, K.S. Weil, D.M. Paxton, J.W. Stevenson, Selection and Evaluation of Heat-Resistant Alloys for SOFC Interconnect Applications, J. Electrochem. Soc. 150 (2003) A1188. https://doi.org/10.1149/1.1595659.

[4] X. Xu, S. Ganguly, J. Ding, S. Guo, S. Williams, F. Martina, Microstructural evolution and mechanical properties of maraging steel produced by wire + arc additive manufacture process, Mater. Charact. 143 (2018) 152–162. https://doi.org/10.1016/j.matchar.2017.12.002.

[5] S. Li, J.Y. Li, Z.W. Jiang, Y. Cheng, Y.Z. Li, S. Tang, J.Z. Leng, H.X. Chen, Y. Zou, Y.H. Zhao, J.P. Oliveira, Y. Zhang, K.H. Wang, Controlling the columnar-to-equiaxed transition during Directed Energy Deposition of Inconel 625, Addit. Manuf. 57 (2022). https://doi.org/10.1016/j.addma.2022.102958.

[6] Z. Huda, P. Edi, Materials selection in design of structures and engines of supersonic aircrafts: A review, Mater. Des. 46 (2013) 552–560. https://doi.org/10.1016/j.matdes.2012.10.001.

[7] M.J. Donachie, S.J. Donachie, Superalloys - A Technical Guide, 2nd ed., ASM International, 2002. https://app.knovel.com/hotlink/toc/id:kpSATGE003/superalloys-technical/superalloys-technical.

[8] Z.G. Yang, J.W. Stevenson, D.M. Paxton, P. Singh, K.S. Weil, Materials Properties Database for Selection of High-Temperature Alloys and

Concepts of Alloy Design for SOFC Applications, 2002. https://doi.org/doi:10.2172/15010553.

[9] INCO, High-Temperature High-Strength Nickel-Base Alloys No. 393, 2020. https://nickelinstitute.org/media/8d93486143182f5/nickel_incopub393_updated-june-2021.pdf.

[10] R. Larson, R. Hostetler, Trigonometry, 7th ed., Houghton Mifflin, Boston, MA, 2007.

[11] M.J. Donachie, S.J. Donachie, Joining Technology and Practice, in: Superalloys - A Tech. Guid., 2nd ed., ASM International, 2002: pp. 65–78. https://app.knovel.com/hotlink/pdf/id:kt008GQY5K/superalloys-technical/joining-superalloys.

[12] S.W. Williams, F. Martina, A.C. Addison, J. Ding, G. Pardal, P. Colegrove, Wire + Arc additive manufacturing, Mater. Sci. Technol. 32 (2016) 641–647. https://doi.org/10.1179/1743284715Y.0000000073.

[13] X. Xu, S. Ganguly, J. Ding, C.E. Seow, S. Williams, Enhancing mechanical properties of wire + arc additively manufactured INCONEL 718 superalloy through in-process thermomechanical processing, Mater. Des. 160 (2018) 1042–1051. https://doi.org/10.1016/j.matdes.2018.10.038.

[14] J. Li, H.M. Wang, H.B. Tang, Effect of heat treatment on microstructure and mechanical properties of laser melting deposited Ni-base superalloy Rene’41, Mater. Sci. Eng. A. 550 (2012) 97–102. https://doi.org/10.1016/j.msea.2012.04.037.

[15] L.A. Middleton, N.F. Kennon, D.P. Dunne, N. South, Metallographic Preparation, Metallography. 17 (1985) 51–59.

[16] X. Xing, X. Di, B. Wang, The effect of post-weld heat treatment temperature on the microstructure of Inconel 625 deposited metal, J. Alloys Compd. 593 (2014) 110–116. https://doi.org/10.1016/j.jallcom.2013.12.224.

[17] M.J. Donachie, S.J. Donachie, Selection of Superalloys, in: Superalloys -

A Tech. Guid., 2nd ed., ASM International, 2002: pp. 11–24. https://app.knovel.com/hotlink/pdf/id:kt008GQQU1/superalloys-technical/superalloy-forms.

[18] C.E. Seow, H.E. Coules, G. Wu, R.H.U. Khan, X. Xu, S. Williams, Wire + Arc Additively Manufactured Inconel 718: Effect of post-deposition heat treatments on microstructure and tensile properties, Mater. Des. 183 (2019) 108157. https://doi.org/10.1016/j.matdes.2019.108157.

[19] F. Ahsan, J. Razmi, L. Ladani, Global local modeling of melt pool dynamics and bead formation in laser bed powder fusion additive manufacturing using a multi-physics thermo-fluid simulation, Prog. Addit. Manuf. (2022). https://doi.org/10.1007/s40964-022-00302-w.

[20] R.B. Herchenroeder, Haynes Alloy No. 188 Aging Characteristics, in: Int. Symp. Struct. Stab. Superalloys, Seven Springs, PA, 1968: pp. 460–500. https://doi.org/10.7449/1968/superalloys_1968_460_500.

[21] V. Shankar, K. Bhanu Sankara Rao, S.L. Mannan, Microstructure and mechanical properties of Inconel 625 superalloy, J. Nucl. Mater. 288 (2001) 222–232. https://doi.org/10.1016/S0022-3115(00)00723-6.

[22] M. Kaufman, Control of Phases and Mechanical Properties in Nickel-base Alloys of Rene 41 Type, Trans. Metall. Soc. AIME. 227 (1963) 405.

[23] X. Xu, J. Ding, S. Ganguly, S. Williams, Investigation of process factors affecting mechanical properties of INCONEL 718 superalloy in wire + arc additive manufacture process, J. Mater. Process. Technol. 265 (2019) 201–209. https://doi.org/10.1016/j.jmatprotec.2018.10.023.

3.7 Appendix: Sample of Mechanical Properties from Literature

Designation	**Score**	**Form**	**Density**	**UTS (MPa)**			**YS (MPa)**			**Tensile elongation (%)**		
			kg/m^3	21°C	538 °C	760 °C	21°C	538 °C	760 °C	21°C	538 °C	760 °C
Nickel base												
Inconel 617	260	Bar	8360	740	580	440	295	200	180	70	68	84
Inconel 625	304	-	8440[9]	965	910	550	490	415	415	50	50	45
Inconel 718	557	Bar	8220	1435	1275	950	1185	1065	740	21	18	25
M-252	587	Bar	8250	1240	1230	945	840	765	720	16	15	10
Rene 41	703	Bar	8250	1420	1400	1105	1060	1020	940	14	14	11
Cobalt base												
Haynes 188	280	Sheet	8980	960	740	635	485	305	290	56	70	43
MP35N	588	Bar	8410	2025	(1773)	(1548)	1620	(1430)	(1415)	10	-	-
MP159	594	Bar	8330*	1895	1565	(1340)	1825	1495	(1480)	8	8	-

Designation	Mean coefficient of thermal expansion *α* (10^{-6} K)	Dynamic modulus of elasticity *E*		Content (%wt)	
	538 °C	21 °C	538 °C	Al	Ti
Nickel base					
Inconel 617	13.9	210	176	1	0
Inconel 625	15.3[8]	208[9]	179[9]	0.2	0.2
Inconel 718	14.4	200	171	0.5	0.9
M-252	13.0	206	177	1	2.6
Rene 41	13.5	220[9]	191[9]	1.5	3.1
Cobalt base					
Haynes 188	14.8	207	192[9]	0	0
MP35N	(15.3)	231	(192)	0	0
MP159	15.1[9]	206[9]	(167)	0.2	3

Data from Donachie Superalloys – A Technical Guide [17], unless otherwise specified.

* Manufacturers data

(Extrapolated/ interpolated values are shown in parentheses

3.8 Appendix: Full Ranking Table

Designation	Total	UTS		YS		Weight Eff.		Buck. Eff.	TEC	Elast. Mod	Stress	Cracking
		1000	1400	1000	1400	1000	1400	1000	1000	1000		
Rene 41	673	67	66	63	66	68	66	41	65	37	64	70
Unitemp AF2-IDA6	662	69	69	65	67	69	70	40	70	37	70	36
Rene 95	650	70	68	70	70	72	68	53	42	56	29	52
Udimet 700	628	61	62	55	59	65	64	73	58	73	24	34
Astroloy	627	57	67	60	64	62	69	67	58	37	55	31
Udimet 500	621	57	63	49	53	60	63	71	53	70	30	52
MP159	608	71	70	72	72	71	71	35	25	51	15	55
Nimonic 105	597	46	55	47	54	48	61	70	58	61	43	54
MP35N	593	72	72	71	71	73	73	54	25	72	8	2

M-252	591	56	58	46	51	57	57	36	69	30	68	63
Nirnonic PK 33	585	38	51	41	48	39	52	66	68	70	53	59
Nimonic 115	585	45	64	49	57	46	67	72	66	64	54	1
Udimet 720	579	68	71	67	68	70	72	58	17	37	14	37
Inconel 617	567	19	42	19	25	21	43	48	111	64	111	64
Udimet 630	565	66	60	68	62	66	58	27	42	37	36	43
Nimonic 942	563	64	52	61	62	64	53	18	40	17	60	72
Waspaloy	562	52	38	41	49	52	41	59	53	57	45	75
Inconel 718	560	61	59	66	54	61	59	26	50	26	57	41
Inconel 718 Direct Age Bar	559	65	65	69	69	67	65	42	42	37	36	2
Udimet 400	556	53	54	52	56	55	55	48	42	37	36	68
Nimonic 90	539	44	40	41	37	45	42	65	58	68	33	66

Udimet 710	530	49	61	54	58	51	62	68	17	66	7	37
D-979	528	63	42	57	45	63	43	45	36	32	32	70
Incoloy 903	524	51	50	62	61	53	51	6	71	1	71	47
Udimet 520	517	57	43	51	52	58	44	47	34	37	27	67
Pyromet 860	511	60	53	53	60	59	54	20	19	21	44	68
Inconel 718 Super	510	54	57	63	65	56	56	42	42	37	36	2
Inconel X750	505	43	47	41	44	43	48	52	49	57	26	55
Nimonic 80A	498	34	34	32	36	34	36	64	58	64	41	65
Inconel 597	485	47	55	40	47	50	60	63	9	37	4	73
Incoloy 907(c)	477	55	40	59	40	54	40	11	72	14	72	20

Nimonic 263	476	29	38	29	33	31	38	55	64	68	42	49
Inconel 587	463	42	48	34	41	44	50	68	9	66	1	60
Inconel 706	453	48	43	56	46	49	46	57	16	35	12	45
Incoloy 909	444	50	35	58	37	47	37	7	72	8	73	20
V-57	440	38	36	45	34	42	39	33	38	13	65	57
Nimonic PE 11	438	38	46	38	39	40	47	32	30	17	51	60
Alloy 901	422	41	43	48	43	41	44	19	20	19	47	57
Haynes 282	393	37	49	35	42	38	49	4	15	3	58	63
Hastelloy S	381	28	32	22	25	26	33	9	66	55	63	22
AirResist 213	338	33	25	27	28	32	25	17	25	51	15	60
Haynes 230	338	23	32	16	22	21	32	10	53	57	45	27
Nimonic PE 16	333	25	27	29	27	30	30	31	20	14	50	50

Cabot 214	318	22	31	31	35	27	34	22	8	10	25	73
Inconel 625	314	36	30	26	29	35	31	24	20	37	18	28
Stellite 6B	312	27	29	28	30	29	29	30	34	51	23	2
Incoloy 825(b)	282	10	8	12	9	13	9	38	53	27	62	41
Haynes 188	280	25	37	20	23	22	35	1	37	22	56	2
A-286	280	35	19	33	31	37	22	34	2	10	9	48
Nimonic 75	277	21	11	8	8	20	11	46	40	61	22	29
Inconel 601	275	24	9	24	13	28	10	51	20	28	28	40
Hastelloy X	269	17	18	19	19	18	21	12	32	6	61	46
Discaloy	267	32	25	36	31	36	28	14	4	3	35	23
MAR-M918	260	15	16	39	50	14	15	13	25	61	10	2
L-605	257	29	22	14	19	25	16	2	50	30	48	2
Nimonic 81	256	1	1	1	1	1	1	61	52	37	49	51

Incoloy 801	228	19	12	21	23	23	13	49	3	24	6	35
16-25-6	227	31	15	37	26	33	18	28	5	12	20	2
Haynes 150	226	20	21	16	19	24	24	60	5	32	3	2
Incoloy 802	219	12	14	7	12	15	17	62	7	23	11	39
Haynes 556	206	16	23	13	13	17	26	15	14	14	31	24
Hastelloy C-22	199	14	28	16	17	12	27	8	20	37	18	2
Incoloy 807	197	5	13	15	15	6	14	3	30	5	67	24
Hastelloy G-30	193	6	5	5	5	7	6	42	42	37	36	2
Inconel 600	192	8	7	10	9	9	8	37	32	57	13	2
19-9 DL	190	13	10	25	6	16	12	56	1	25	2	24
N-155	187	17	17	22	18	19	19	21	12	19	21	2
Incoloy 904	177	1	1	1	1	1	1	16	38	8	66	43

Incoloy 800	152	7	6	6	7	8	7	29	12	6	34	30
Elgiloy	138	1	1	1	1	1	1	39	25	51	15	2
Inconel 596	126	1	1	1	1	1	1	5	42	2	69	2
Inconel 690	106	1	1	1	1	1	1	50	9	34	5	2

4 MICROSTRUCTURE AND MECHANICAL PROPERTIES OF INCONEL 718 AND INCONEL 625 PRODUCED THROUGH THE WIRE + ARC ADDITIVE MANUFACTURING PROCESS

The chapter is based on the following publication.

***W.S. James**, S. Ganguly, G. Pardal, Microstructure and Mechanical Properties of Inconel 718 and Inconel 625 Produced Through the Wire + Arc Additive Manufacturing Process, in: AVT-356 Phys. Fail. Mil. Platf. Crit. Subsystems, STO NATO, 2021.*

This chapter presents the initial findings of the pilot study conducted into the WAAM deposition of IN718 and IN625. The pilot study also fine-tuned the methods used in proceeding chapters. Results were also compared to previous studies on IN718 conducted at Cranfield University and examines the difference between AD and HT WAAM material.

Abstract

In developing the wire + arc additive manufacturing (WAAM) process for heat and creep resistant alloys, structures were built from nickel-based superalloys Inconel 718 (IN718) and Inconel 625 (IN625). In this paper, wall structures were deposited in both superalloys, using a plasma transferred arc process. The microstructure was analysed optically and under SEM; both alloys revealed typical dendritic structure with long columnar grains, with little variation between the alloys. The findings suggest that the structures included significant segregation of alloying elements, with potential intermetallic phases e.g., Laves phases and δ-phases also found across the alloys, which showed significantly more segregation of Nb and Mo at the grain boundaries and inter-dendritic regions. The alloys also underwent room temperature mechanical testing, in addition to this IN625 specimens were tested after a solutionising and ageing treatment. Hardness measurements indicated that in general the WAAM process has the effect of increasing material hardness by approximately 10 %, when compared to wrought alloy in a solutionised state. In IN625 the heat-treated specimens showed an increase in hardness of around 6 %, when compared with its as-deposited condition. Elongation in IN625 showed much greater values. Overall, IN718 showed a greater strength with less elongation than IN625. A comparison between both alloys and their stated maximum UTS and YS values from literature revealed that WAAM built IN718 and IN625 in its as-deposited condition can achieve just over half the maximum achievable UTS, with no post-process treatment. The heat-treatment process tested in IN625 marginally reduced the gap in UTS performance by 3.5 %.

Keywords: Additive manufacture, characterisation, mechanical properties, Inconel 718, Inconel 625

4.1 Introduction

Wire + Arc Additive Manufacturing (WAAM) has been undergoing development since the 1990’s. WAAM is “the combination of an electric arc as heat source and wire as feedstock” [1]. WAAM is not dissimilar to more traditional manual welding technologies such as TIG/MIG welding [2], with the exception that WAAM uses traditional arc welding technologies with a motion control system, such as a robotic system or retrofitted onto a computer numerical control (CNC) system [1]. The main difference in automated welding systems and the WAAM system is the thermal profile of as-deposited WAAM components. To build shapes and subsequent components WAAM deposits the wire feedstock in a layer-by-layer manner [3]. Unlike other more well established additive manufacturing (AM) methods WAAM is often not used to manufacture a finished product, instead WAAM is used to deposit a near net-shape product [4], which can then be further processed, if required, to achieve a finished product.

As a method to rapid prototype metal structures WAAM is often advantageous over more traditional methods such as machining. As WAAM only deposits the near net shape of the product, compared with machining, WAAM is capable of reducing: the waste material, cost, and lead time. Machining of WAAM components is still required in some cases to achieve the finished product [4].

Superalloys are defined as “a group of nickel-, iron-nickel-, and cobalt-base materials that are used at temperatures of 540 ºC and above” [5]. Superalloys were initially developed for use in superchargers in aircraft piston engines, however much of their later development was in components for gas-turbines. Nickel-based superalloys can be found in gas-turbines for a variety of applications from aerospace to power generation. Newer gas-turbines operate at higher temperatures than has been seen historically, due to increasing demand for more efficient engines, the nickel superalloys in these environments experience operating temperatures of between 650-700+ ºC [6].

The use of WAAM to manufacture components from heat resistant alloys is a relatively new area of study with a relatively low volume of research published in this area. The impact of the WAAM process on the high temperature material properties of heat resistant alloys is largely unknown. Alloys that have been investigated in this study include those suitable for high temperature applications, including largely nickel-based superalloys, this is due to the high temperature performance of these alloys.

Another type of AM process that has been considered as less appropriate for the high-speed flight application include the powder-bed laser AM process. The powder bed process is also a process by which shapes are produced by a layer-by-layer process, however metallic powder particles are used as the feedstock which is then melted to form the part via laser. Benefits that the powder-bed AM process shares with the WAAM process includes the ability to produce complex shapes that would be difficult to produce by traditional machining methods [7], as well as greater efficiency brought by the minimal waste that is produced by most AM processes. There are, however, some limitations of powder-bed over WAAM which makes WAAM more appropriate for this application. WAAM is more suited to the production of larger scale parts as well as being capable of a higher deposition rate of material [1]. The metallic powder used in powder-bed is more expensive to produce than wire feedstock, which being coupled with powder loss (which can be as high as 25 % even for more advanced versions of the technology), makes powder-bed produced parts less economical [8], dependant on application and machining requirements. Larger powder-bed produced components can include pores in the structure which reduces the mechanical performance. In terms of loss of material, WAAM can operate with near to no loss of raw material and can produce pore free structures [8]. After post-processing heat-treatment Wang et al. found that powder-bed produced IN718 was comparable in room temperature tensile strength to the wrought alloy [7]. For IN625, Tanvir et al. found that WAAM built parts needed further research to achieve the same strength level as powder-bed produced parts, and recommended that a solutionising treatment for IN625 might further increase the performance [8].

High temperature metals that have been deposited by WAAM at Cranfield University so far include:

Nickel alloys:

- Inconel 625 [9]
- Inconel 718 [9]

Refractory metals:

- Tungsten; WAAM is capable of depositing high purity tungsten and other refractory metals [10].
- Molybdenum [11]
- Tantalum [11]
- Ti–6Al–4V [12] + other less heat resistant alloys [13].

In this paper, research performed towards deposition and wall building of IN625 and IN718 using a plasma transferred arc WAAM process are discussed. A comparison of the two WAAM built alloys was completed and their suitability for high-speed flight applications was discussed.

4.2 Materials and Methods

4.2.1 Overview of Design Parameters

There is interest in developing AM alloys specifically for use as structural components in high-speed missiles with short flight times (< 1 hour). In service temperatures could reach 1000 K (727 °C) for external structural components, or even >1200 K (927 °C) for components in the propulsion flow path. These components will be highly stressed to minimise structural mass. The desired aim is for the WAAM built alloys to achieve properties similar to currently available wrought materials, such as IN718 (standard) or Haynes 282 (best case), and ideally have low thermal expansion. Creep is not considered to be a major issue due to the short flight time, but there is a lack of data in this regime (high stress, high temperature and short duration). With a focus on very good short-term properties and a particular importance on high temperature performance of these alloys, the room temperature data shown in this paper is a precursor to further high temperature investigations.

4.2.2 Deposition Process

4.2.2.1 Inconel 625

IN625 was deposited via a WAAM system consisting of a Kuka six-axis robot, a plasma power source, a water-cooled plasma welding torch mounted to the robot, an external wire feeder, and a part rotator – allowing for symmetrical layer-by-layer WAAM wall building. Also attached to the robot head was a trailing shield (shown in Figure 4-1) which surrounded the welding torch and extended behind the torch, this provided an argon environment during the WAAM process to prevent excessive oxidisation. The experimental set-up is shown in Figure 4-2.

The process used for IN625 was a symmetrical wall building process, where two wall structures were built simultaneously on opposite sides of the substrate plate and the part rotator is utilised to alternate between the two sides of the substrate plate. The benefits of this process over a single sided operation is intended to reduce residual stresses on the structure as the warping of the substrate is effectively ‘cancelled out’ when welded on both sides [1]. It also has the effect of increasing productivity as inter-pass cooling can partially take place on one side when the process is ongoing on the opposite side, minimising the time the system remains inactive while cooling takes place.

Directly below the trailing shield at a torch-to-work distance of 8 mm, argon shielding was provided to keep the level of oxygen below 800 ppm, with an argon flow of approx. 80 L/min.

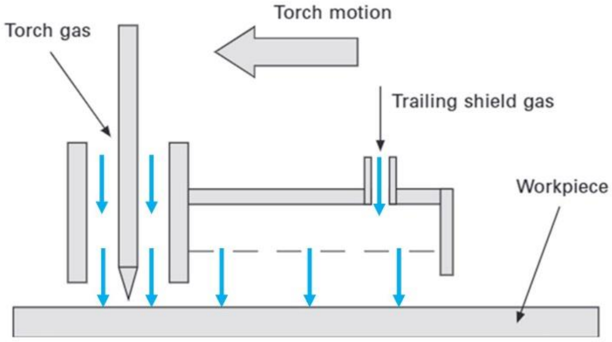

Figure 4-1: Trailing shield device used during deposition of IN625 [14]**, blue arrows indicate gas flow direction.**

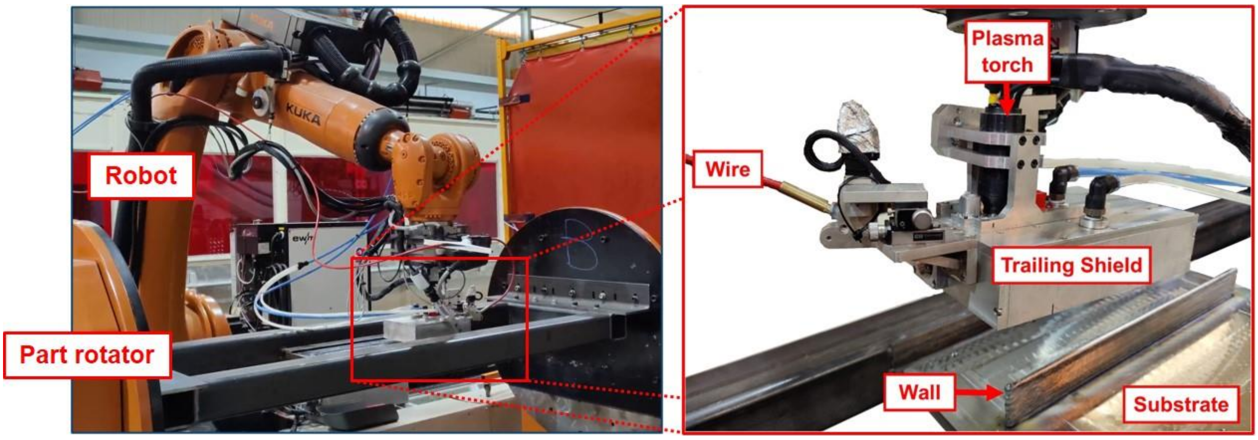

Figure 4-2: Experimental set-up used to deposit IN625. Boxed area in the LH image is shown in further detail in RH image.

4.2.2.2 Inconel 718

For the Inconel 718 (IN718) alloy, a WAAM system consisting of a three-axis linear CNC system, a Tecarc 320 A AC/DC plasma power source, a water-cooled plasma torch mounted to an adjustable jig on the CNC system, an external wire feeder and a glove box filled with Pureshield argon, controlled below 800 ppm controlled as in section 4.2.2.1.

The process used for the deposition was a linear wall building system where the layers were deposited in a single direction on a single side of the substrate, due to the limitations of the system used. The experimental set-up used to deposit IN718 is shown in Figure 4-3.

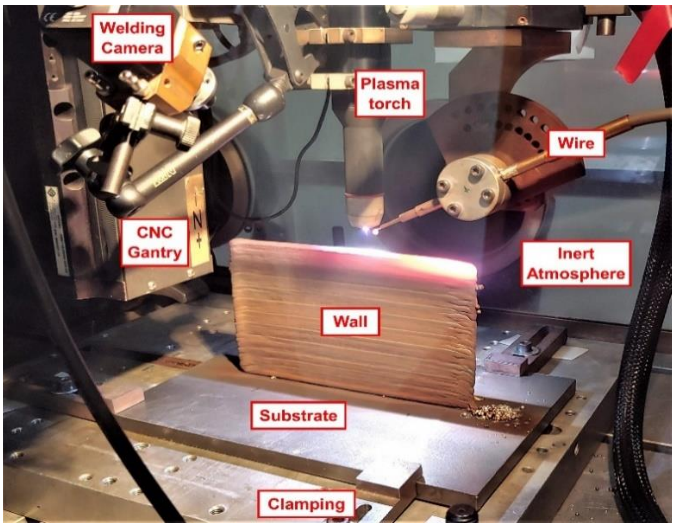

Figure 4-3: Experimental set-up used to deposit IN718.

4.2.3 Materials

The dimension of the nickel wires used and the welding parameters for each alloy are shown in Table 4-1 and the chemical composition of these wires is shown in Table 4-2. For both alloys a 10 mm thick mild steel plate was used as the substrate. Large linear wall structures were deposited in each alloy measuring approx. 500×110×8 mm for IN625 and 315×110×8 mm for IN718, Figure 4-4 shows directional axes and orientation of extracted tensile specimens. The welding parameters were kept constant, with the exception of the initial welding layers, which experience a greater rate of cooling due to proximity to the substrate. A slower travel speed and reduced wire feed speed were used to better the wetting of the initial layers onto the substrate plate.

Table 4-1: Wire and welding parameters. Adapted from [15]**.**

	IN718	IN625
Wire Diameter (mm)	1.2	1.2
Torch to work distance (mm)	8	8
Current (A)	180	180
Wire feed speed (m/min)	1.8	2
Travel speed (mm/sec)	5	6
Inter-pass cooling time (min)	3	3

Table 4-2: Elemental composition of IN718 and IN625 filler wires, %wt. (Elements <0.01% omitted)

	C	Ni	Cr	Mo	Fe	Al	Ti	Nb	Mn	Si	Cu
IN718	0.04	53.57	18.56	2.87	17.8	0.60	0.97	5.01	0.10	0.08	0.07
IN625	0.01	64.75	22.16	8.79	0.24	0.17	0.19	3.60	0.02	0.04	0.02

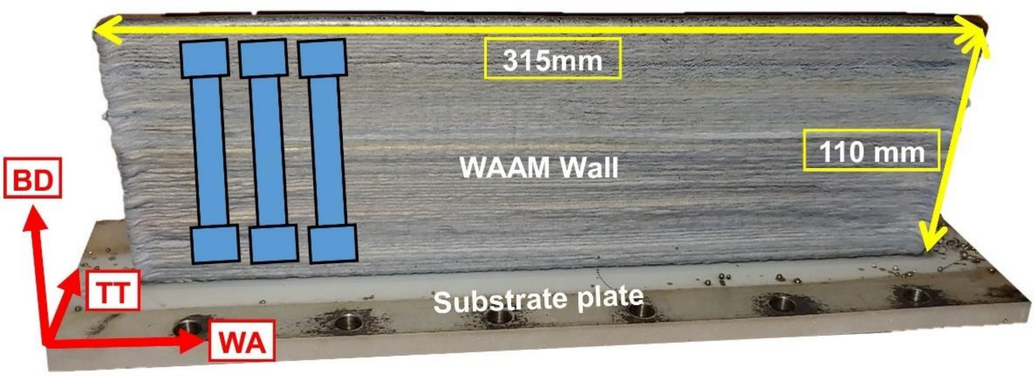

Figure 4-4 WAAM wall labelled with build dimensions and directional axes. Build direction (BD), through thickness (TT), wall axis (WA).

4.2.4 Analytical Methods & Mechanical Testing

In IN718 and IN625 alloys, WAAM walls of a total height of approx. 111 mm were built and these walls were formed of 226, and 130 layers, with layer heights of approx. 0.49 and 0.86 mm for IN718 and IN625, respectively. Layer height was tracked by measuring the total wall height at several intervals. The difference in layer height is likely due to the difference in process parameters used in each case and could also be influenced by the composition of the alloys. Once completed the walls were cut from the substrate plates and samples were extracted by machining, along the wall height. Note that the substrate is not intended to form part of a finished component for this application. Cross-sections were extracted and prepared for metallographic analysis following a procedure consisting of mounting, grinding, polishing, and etching. IN718 samples were etched in Kalling's 2 while IN625 was etched in aqua regia. The microhardness was measured using a Zwick/Roell hardness tester under a load of 500 g and holding time of 15 s, welding filler wire samples of the alloys also underwent a similar process as above to obtain comparative results for the hardening effect of the WAAM process. The microstructure was also analysed, using a Tescan VEGA 3 scanning electron microscope, and optically using a Leica DM 2700M Microscope. To determine composition an Oxford Instruments X-Max 20 mm was used in combination with the SEM for the EDS analyses.

For room temperature mechanical testing an Instron 5500R Electro-mechanical testing machine was used with a load cell of 100 kN and a crosshead speed of 1 mm/min. Elongation was measured using a laser extensometer over a gauge length of 25 mm. At least three samples were tested for each condition (orientation, as deposited and heat-treated variants), and samples conformed to ASTM E8/E8M subsize specimen standard. A schematic drawing of the tensile specimens used is shown in Figure 4-5.

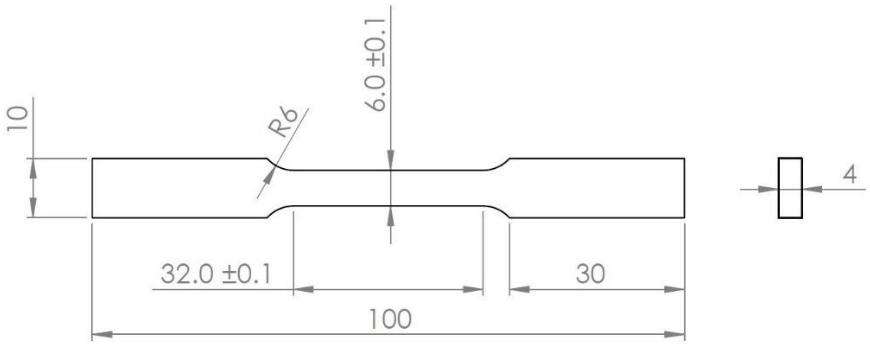

Figure 4-5: Dimensions (in mm) of the tensile specimens used for RT tensile testing, conforming to ASTM E8/E8M subsize standard.

4.2.5 Post-process Treatment of Inconel 625

A heat-treatment was conducted on several IN625 tensile specimens. The heat-treatment made use of a Carbolite Gero CWF 11/13 furnace and consisted of a two-stage heating process, a solutionising and heat-treating process. The first stage included heating the samples in the furnace to 1100 °C holding at this temperature for 15 mins, with the aim to dissolve Laves and secondary phases. After this process the specimens were water quenched to room temperature. The specimens then underwent an ageing process at 750 °C for 8 hours, followed by air cooling to room temperature. The aim of the second stage was to increase the mechanical strength through the precipitation of γ″ Ni_3Nb in the inter-dendritic regions [16]. This treatment was used in a previous study on IN625 by Cortial et al [17].

4.3 Results

4.3.1 Macrostructure

The macrostructure seen in the samples of the as-deposited IN718 WAAM wall, i.e., without any additional heat or solution treatment to the material are shown in Figure 4-6 with an enlarged image at higher magnification shown in Figure 4-7. In the macrostructure large cracks can be seen extending through the layers. IN718 exhibits a typical solidified dendritic structure made up of large columnar grains which appear to extend along the height of the wall in the build direction

(BD seen in Figure 4-6), this structure was expected and has been seen in previous studies namely by Xu et al [15].

IN625 exhibits a similar structure to IN718 as can be seen in Figure 4-8. Nearest the substrate in both alloys, it can be seen that the structure has much finer cellular grains, whereas in later layers extending though the build direction grains get steadily longer exhibiting a more columnar dendritic structure. Overall, more cracking was seen in IN718.

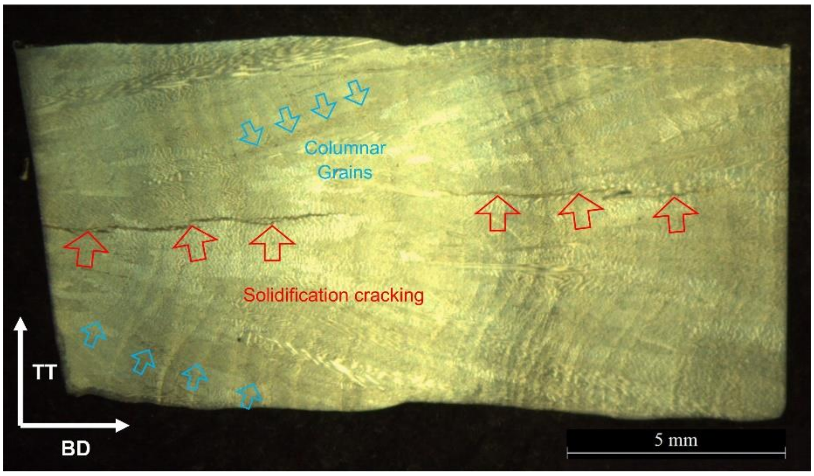

Figure 4-6: Macrograph cross-section of as-deposited IN718. This is a sample near to the top of the wall. From bottom to top of the build direction is shown from left to right. Red arrows indicating solidification cracking, blue arrows show columnar grains.

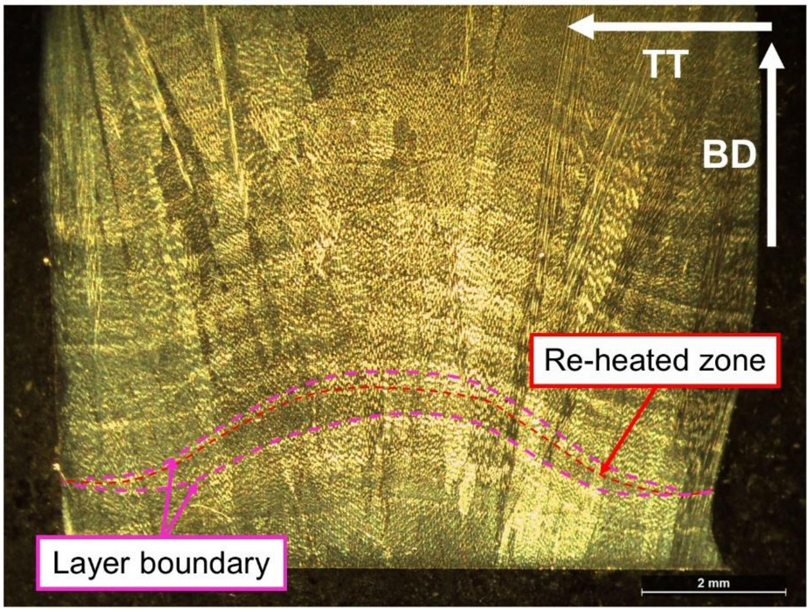

Figure 4-7: Macrograph cross-section of as-deposited IN718, showing layer boundary and re-heated zone Pink dotted line and arrows showing boundary between layers and red dotted line shows re-heated zone.

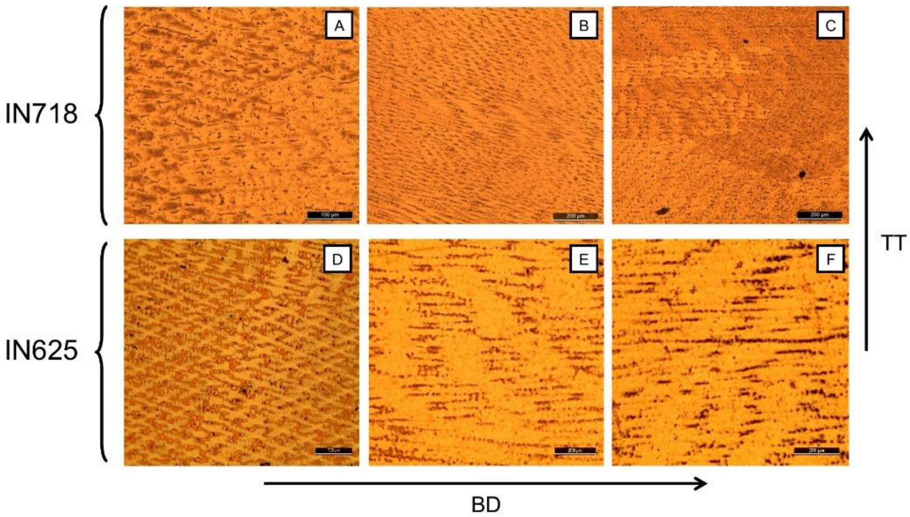

Figure 4-8: Optical micrograph of as-deposited macrostructure of IN718 and IN625 samples. Top three images show IN718, bottom three images show IN625.

4.3.2 Microstructure

The microstructure seen in IN718 at the grain boundary is shown in Figure 4-9. The as-deposited WAAM structure shows significant amounts of segregation of Nb and Mo at the grain boundaries, an EDS analysis of the area revealed the lighter coloured phases to be Ni_2Nb (green arrows), purely based on the similarity in the composition and closeness to the atomic percentages of the A_2B type Ni_2Nb Laves phase seen in literature [15]. This phase can also clearly be seen on the elemental map (Figure 4-10), which shows the segregation of Nb as well as the depletion of heavier metals such as Nb and Mo in the surrounding regions.

The red arrows in Figure 4-9 are indicating Ti rich phases, which appears as smaller darker precipitates. These precipitates have been identified as a possible MC type carbide TiC based on appearance seen in literature and composition of approximately 50 % Ti [18].

An analysis into the composition of the above precipitates seen in IN718 was carried out, the composition is shown in Table 4-3. The composition of area B, highlighted in yellow in Figure 4-9, shows a significant increase over base values of Nb while the amount of Ni has decreased significantly. Comparing the values in terms of atomic percentage, suggests that the composition is very close to that of Ni_2Nb. While area D shows a significant increase in both Ti, Nb and Al without any other indicated elements.

The solidification cracks seen in IN718 were also analysed based on composition and found to contain Ni_2Nb Laves phase at the crack edge, as seen in Figure 4-11 the lighter coloured phases along the crack also form the root of the crack.

The microstructure of IN625 is shown in Figure 4-12, although the images are not of a grain boundary location, the phases seen appear smaller and more evenly distributed. In comparing the as deposited and heat-treated samples there appears to be more precipitation in the heat-treated sample, although the difference is somewhat negligible. The purpose of the post-deposition heat-treatment was to dissolve Laves phase and allow for the formation of more useful γ'' strengthening phase. It does appear that a significant amount of potential Laves phases have been dissolved compared to as-deposited IN718, although some that remains are similar in appearance however smaller in size than was seen in IN718. In IN625 the darker Ti rich zones (shown as area F in Figure 4-12, with composition in Table 4-3) also appear and typically vary in size, which are seen at a greater frequency than those seen in IN718.

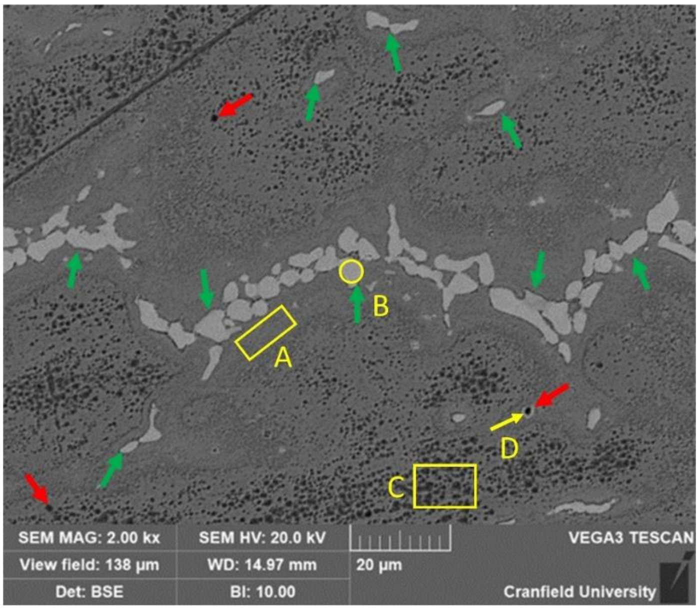

Figure 4-9: As deposited microstructure of IN718, showing grain boundary and segregated zones, in the through thickness (TT) and wall axis (WA) cross-section. This sample is located mid-height in the build direction. Green arrows showing lighter coloured segregated Ni_2Nb, red arrows indicating Ti rich carbides. In yellow are areas where the composition was analysed (Table 4-3).

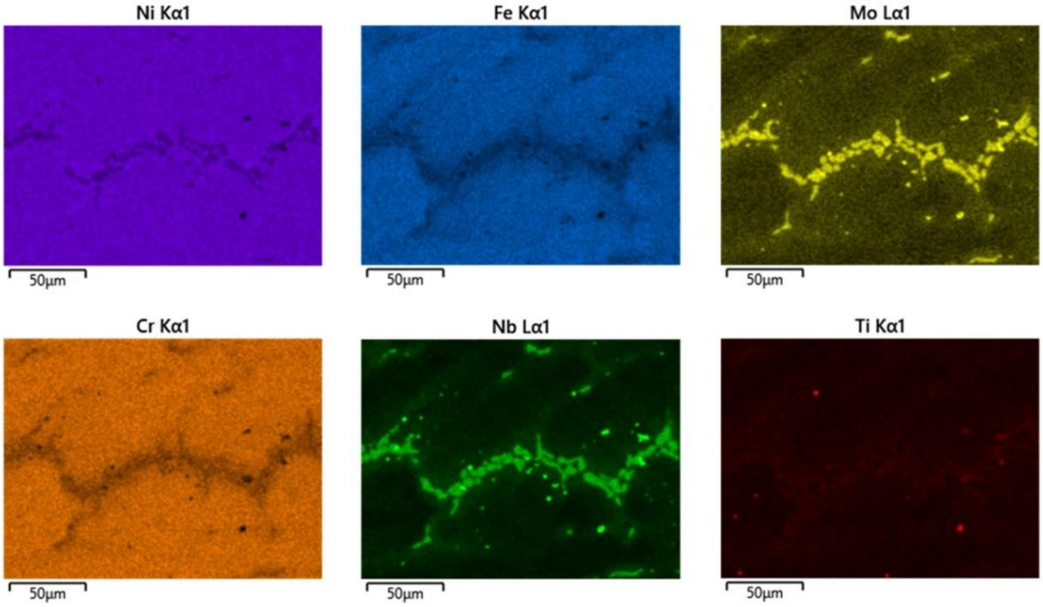

Figure 4-10: EDS Elemental map of IN718 segregated zone.

Table 4-3: EDS composition of alloys, labelled A – D on IN718 SEM image (Figure 4-9), E – F on IN625 SEM image (Figure 4-12). Values proceeded by a (+) represent a significant increase over base values, values with a (–) represent significantly less and a (*) represent anomalous elements.

Spectrum Label	% At.						
	IN718				IN625		
	A	B	C	D	E	F	G
C	(+)12.04	(–)0	(+)10.02	(–)0	(+)18.35	(+)12.82	(+)9.73
F	(*)6.95						
Al	1.11	(–)0	1.25	(+)15.20	(–)0.22	0.31	0.38
Si					(*)0.73	(*)0.18	(*)0.12
Ti	1.50	1.95	0.63	(+)51.85	0.25	(+)1.52	0.17
Cr	16.64	(–)17.67	19.97	(–)0	(–)17.24	20.32	23.64
Fe	13.77	(–)12.96	18.30	(–)0		(–)0.17	(–)0.21
Ni	42.51	(–)46.26	46.92	(–)0	(–)35.18	(–)50.61	60.36
Nb	3.91	(+)21.15	(–)1.39	(+)32.95	(+)16.46	(+)7.81	(–)1.00
Mo	1.58	(–)0	1.53	(–)0	(+)11.58	6.25	4.39

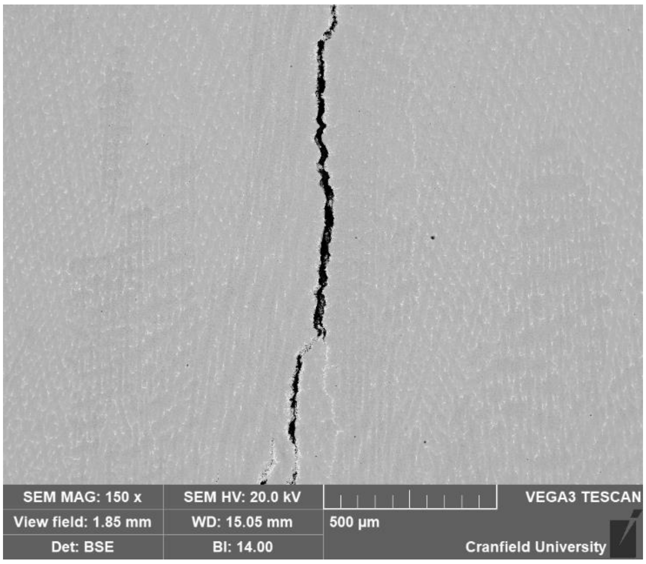

Figure 4-11: Solidification crack seen in IN718, showing lighter coloured Laves phases in crack root. Through thickness (TT) and build direction (BD) cross-section.

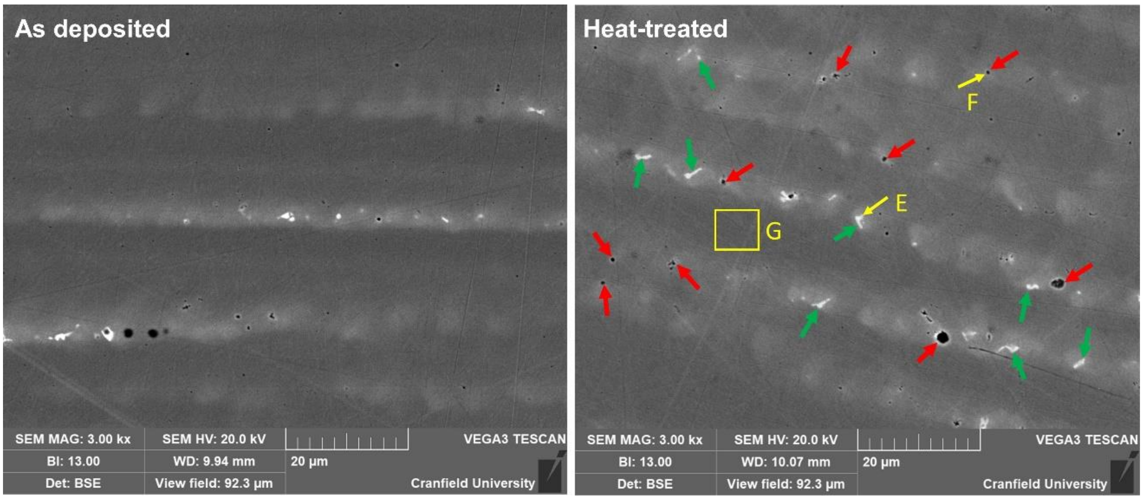

Figure 4-12: Microstructure of IN625 showing segregated zones, in the through thickness (TT) and wall axis (WA) cross-section. Mid-height in the build direction. Green arrows showing lighter coloured segregated Ni_2Nb, red arrows indicating Ti rich zones possible Ti rich carbides. In yellow are areas where the composition was analysed for the heat-treated specimen (Table 4-3).

4.3.3 Hardness Comparison

Hardness between both alloys, in their as-deposited condition was compared. As-deposited IN625 was also compared with its heat-treated variant. The hardness was tested at 1 mm increments along the surface of the samples. Micro hardness results were obtained and are displayed as Vickers Hardness in Table 4-4. A comparison of the data revealed that IN718 is harder than IN625, with average values for both alloys at 293.9 HV and 248.5 HV respectively. The heat-treatment that IN625 underwent showed a marginal increase in the average micro hardness with a value of 262.75 HV, representing a 5.7 % increase over the as-deposited average.

Table 4-4: Vickers hardness values. [a][15]**, [b]**[19]**, [c]** [16]**, [d]** [20]

Alloy	**Condition**		**Hardness (HV)**	**Standard Deviation (HV)**
IN718	**WAAM**	**as-dep**	**293.9**	**14.6**
		Heat treated	**388 [a]**	**unknown**
	Wrought		**354 [b]**	**-**
IN625	**WAAM**	**as-dep**	**248.5 [c]**	**2.69**
		Heat treated	**262.8 [c]**	**1.64**
	Wrought		**238 [d]**	**-**

4.3.4 Room Temperature Tensile Comparison of Inconel 718 & 625

Room temperature tensile test comparison between as-deposited IN718 and IN625 revealed that IN718 had an average UTS of 841.7 MPa compared with an average of 622.2 MPa for IN625. YS for both IN718 and IN625 was calculated to be 528.8 MPa and 396.7 MPa respectively. Elongation on average was substantially higher in IN625 than was seen in IN718, with the IN625 specimens breaking on average at +57 % of their original length and IN718 specimens breaking at an average of +30.5 % of their original length. Overall IN718 showed greater strength with less elongation than IN625. The alloys were then compared against their stated maximum UTS and YS values from literature, which revealed that WAAM built IN718 and IN625 in their as-deposited condition can achieve approximately 62 % of the maximum achievable UTS (64.5 % for IN625, 58.7 % for IN718), with no post-process treatment. With heat-treatment however, IN625 was able to reduce the gap slightly in UTS performance compared to literature to 68 % of maximum performance. Heat-treated IN625 also resulted in a reduction in elongation compared with as-deposited material, bringing it below the value given for the wrought alloy. Tensile testing results compared with wrought alloy are shown in Table 4-5. A stress/strain graph of the best and worst performing sample in each category is shown in Figure 4-13, where the suffix (A) is the best performance and (B) the worst. As IN718 is more age-hardenable than IN625, IN718 did not undergo a heat-treatment. A comparison between the alloys in their partially aged (as-dep) condition is more prudent.

Table 4-5: Mechanical tensile testing results for IN718 and IN625, with wrought data [21]**.**

Alloy	Condition		UTS (MPa)	0.2 % YS (MPa)	Elongation (%)
IN718	**WAAM**	**as-dep**	**841.70**	**528.84**	**30.47%**
	Wrought		**1435**	**1185**	**21%**
IN625	**WAAM**	**as-dep**	**622.21**	**396.67**	**57.26%**
		Heat treated	**659.70**	**328.36**	**41.88%**
	Wrought		**965**	**490**	**50%**

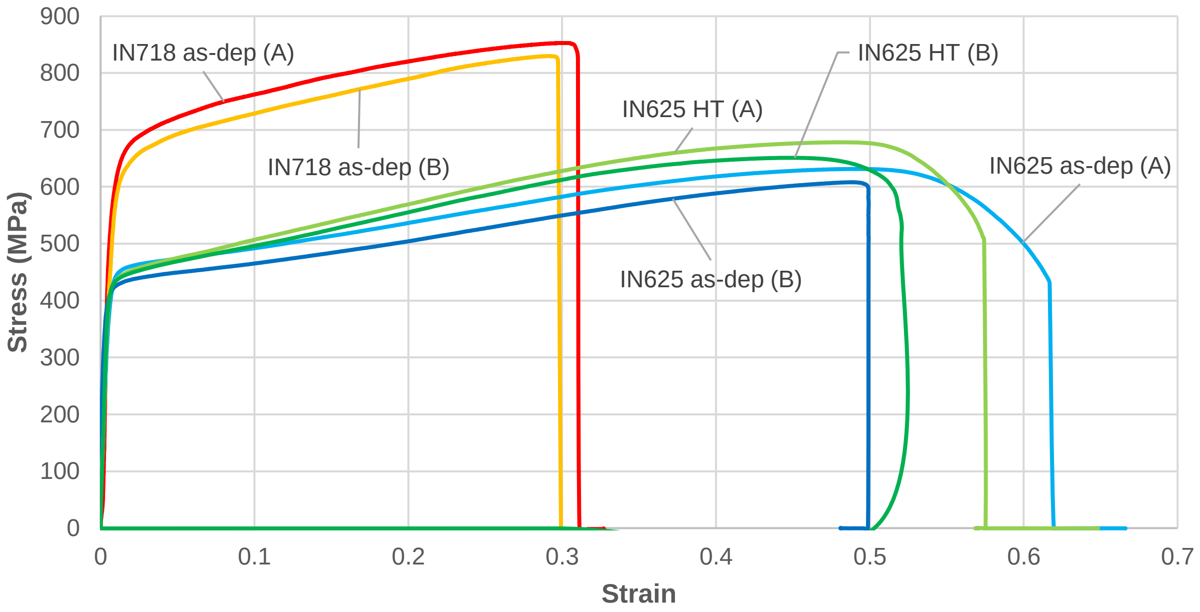

Figure 4-13: RT stress vs. strain for as-deposited IN718, IN625 & heat-treated (HT) IN625. Best (A) and worst (B) performing samples are shown in each category.

4.4 Discussion

4.4.1 Macro and Microstructure

The macrostructure of both alloys is very similar in appearance and exhibit the same characteristics in relation to the earlier and later built layers, as shown in Figure 4-8. In IN718 much more cracking was observed compared to IN625, the different building processes could be the cause as slightly different equipment and parameters were used to deposit the alloys, even though conditions inside the enclosure should induce less oxidisation cracks. It is also possible that as IN625 was built in a more open environment and onto larger equipment/tooling and the rate of cooling for IN625 was faster than IN718, meaning IN718 was effectively aged more as part of its WAAM process than IN625 experienced, controlling inter-pass temperature should minimise this variation. The data for hardness would also suggest that IN718 was harder in its as deposited condition than IN625 which could suggest that IN718 was more brittle and hence more prone to cracking, this would also explain the large difference between the elongation of the alloys during tensile testing, with IN718 relativity restrained compared with IN625.

The columnar grains (seen to grow through the layers and across the height of the walls in both alloys), are similar to what has been seen in previous studies on as-deposited material, where the columnar dendrites are not precisely vertical but extend at an angle of approx. 70 ° to the substrate. This was also seen in a study by Wang et al, in which the reason for this was related to heat flux direction, where dendrite growth follows the maximum temperature gradient, which is opposite to the unidirectional heat flux direction [22]. In subsequent studies inter-pass cooling temperatures will be controlled more closely, the use of an inter-pass cooling time does not provide significant control over cooling, as the cooling of deposition varied as the wall structures were built and heat takes longer to dissipate with distance from the substrate, which is particularly true for initial layers [23].

The potential Ni_2Nb Laves phase seen at the edge of the crack in Figure 4-11 suggest that the heavier metals in the alloy, such as Nb, which has a higher melting point than the other elements, are segregating from the rest of alloy during solidification. The root of the cracks also appears to be filled with the same compound suggesting that the formation of these Laves phase are the cause of the cracking seen in the alloy. The size however of the columnar grains seen, especially in the as-deposited material, of both alloys may suggest that there is in fact less grain boundary area for these precipitates to form and consequently they have less of a reducing effect on the strength.

Laves phase formation in alloys are known to be detrimental to the performance as it depletes the elements that would otherwise form more useful substances, such as precipitation hardening carbides [21], or strengthening phases. The solution treatment that IN625 underwent was performed to homogenise the microstructure and by dissolving Laves phases into the matrix which could then form the γ'' strengthening phase, which is shown under SEM to have reduced the size and frequency of Laves phases. Generally, the results from the SEM and EDS analysis of the microstructure give a good indication of the presence of the Laves phases described, such as Ni_2Nb in IN625 and IN718. For example, looking at Table 4-3 a simple calculation of multiplying the value for Nb by two to get a rough value for Ni, seems to confirm the presence of Ni_2Nb for both spectrum B and E within 2-4 % At.

However, further work to confirm the presence of Laves phases would help to eliminate any doubt that remains. Another point for further investigation is the appearance of Ti rich zones in both alloys, but specifically the appearance of the Ti rich zones in IN625 which appeared in a greater frequency in heat-treated IN625 than those seen in as-dep IN718 despite the matrix containing significantly less Ti than IN718.

The heat-treatment process that IN625 underwent was based on a previous study on the alloy by Cortial et al. In the study, Cortial et al found that the treatment resulted in increased mechanical strength due to the precipitation of γ″ Ni_3Nb phase in the inter-dendritic spaces, which is a strengthening phase in IN625 [17]. Longer aging time tends to provide a more uniform distribution of these precipitates. γ″ Ni_3Nb and aging of IN625 produces more carbides in the alloy. Carbides that have been observed in a study by Shaikh et al included carbides rich in Ti, Nb and Si [24]. The fact that Ti rich carbides have been observed in the literature in the IN625, suggests that the Ti rich zones that exist in the alloys with no other significant increase are Ti carbide. The potential Ti carbides found in IN625 and IN718 were observed to be smaller in size, dark in colour as well as more sparsely distributed, compared to potential Laves phases. Area D of Figure 4-9 suggest with the significant increase in the percentage of Nb, Ti and Al (over the base values), without the presence of the other elements, that perhaps this is indicative of a complexed carbide where carbon has been removed by the etching process, although the presence of carbon in EDS results is often unreliable.

4.4.2 Mechanical Properties

The increase in material hardness of IN625 in the as-deposited condition suggests that the cyclic heating of the WAAM process has at least a partial ageing effect on the alloy. This was also seen when IN625 underwent a post-process aging treatment which resulted in an approximate 5.7 % increase in hardness vs. as-deposited material. In the case IN718, the as-deposited hardness was shown to be significantly less than manufacturer’s data for the wrought alloy. This is probably due to the more extensive ageing process that IN718 typically undergoes to achieve the best mechanical properties, with proper aging treatment it is anticipated that hardness would further increase. In a study on heat treating WAAM built IN718 Xu et al. found that heat treated material showed an increase in hardness of 158 HV compared with as-deposited material. This represents an approx. 69 % increase [15], highlighting the difference between the aging processes of the two alloys and why a comparison between the aged material is less useful than a comparison between the partially aged as-deposited material.

Overall, the improvement in performance by heat-treating IN625 specimens was disappointing, with only a marginal increase in UTS performance compared to the wrought values given by Donachie in the superalloys technical guide [21]; which provided data in suitably comparable format. WAAM built IN625 and IN718 has some improvements to be made before it can achieve the performance of the wrought alloys. Xu et al in a paper based on IN718 found that inter-pass rolling was able to increase the UTS performance of the WAAM built material up to and above what was achievable in wrought alloy, and meet the wrought standard for YS and elongation [15]. Adapting the heat-treatments used for both alloys could also result in additional performance and a sensitivity study on the WAAM alloy response to heat-treatments could be beneficial to selecting the most appropriate treatment.

In evaluating these two WAAM built alloys for a high-speed flight application, IN718 and IN625 show promise, however further work is required to understand their high temperature performance at a temperature range of RT to 1000 °C, and what effect the heat-treatment process will have on the performance at elevated temperatures. An investigation into the inter-pass rolling process described by Xu et al would also be desirable to understand the performance of the rolled WAAM alloys. Finally, IN718 at least at RT would appear to be preferable over IN625 for its higher strength performance, however IN718 does appear to be a harder more brittle alloy and the results of the RT study do correlate to what the data suggested for the wrought alloys. Further study into the high temperature performance of both these WAAM built alloys will help to understand their performance for high-speed flight.

4.5 Conclusions

1. WAAM built material of IN718 at room temperature had a higher UTS and YS performance, however IN625 had a much greater elongation under testing. Perhaps, although a high frequency of Nb rich segregated compounds were found along the grain boundary in IN718, the larger columnar grains provided less grain boundary area for the precipitation of segregated compounds to form. This difference may also be due to IN718 potentially being partially aged to a larger extent during the deposition process than IN625.

2. A heat-treatment consisting of solutionising, and aging had the effect of increasing the performance of IN625 by approx. 6 %, which was less than anticipated, but may have been due to cracking seen in the alloy which potentially reduced its performance.

3. Refractory elements Nb & Mo segregate and contribute to formation of Laves phases, specifically Ni_2Nb, which were indicated in both alloys with precipitation seen at the grain boundaries and interdendritic regions.

4. The heat-treatment process was found to increase hardness of IN625 by an average of 5.7 % compared with as-deposited WAAM material, and when compared with manufacturer’s data on the wrought alloy an increase of 10.4 %.

4.6 References

[1] S.W. Williams, F. Martina, A.C. Addison, J. Ding, G. Pardal, P. Colegrove, Wire + Arc additive manufacturing, Mater. Sci. Technol. 32 (2016) 641–647. https://doi.org/10.1179/1743284715Y.0000000073.

[2] S. Kou, Welding Metallurgy, 2nd ed, Hoboken, N.J. : Wiley-Interscience, 2003.

[3] X. Xu, S. Ganguly, J. Ding, S. Guo, S. Williams, F. Martina, Microstructural evolution and mechanical properties of maraging steel produced by wire + arc additive manufacture process, Mater. Charact. 143 (2018) 152–162. https://doi.org/10.1016/j.matchar.2017.12.002.

[4] B. Baufeld, O. Van der Biest, R. Gault, Additive manufacturing of Ti-6Al-4V components by shaped metal deposition: Microstructure and mechanical properties, Mater. Des. 31 (2010) S106–S111. https://doi.org/10.1016/j.matdes.2009.11.032.

[5] J.R. Davis, ASM Specialty Handbook: Heat-Resistant Materials, in: ASM Spec. Handb. Heat-Resistant Mater., ASM International, 1997: p. 36.

[6] E. Akca, A. Gürsel, A Review on Superalloys and IN718 Nickel-Based INCONEL Superalloy, Period. Eng. Nat. Sci. 3 (2015). https://doi.org/10.21533/pen.v3i1.43.

[7] X. Wang, X. Gong, K. Chou, Review on powder-bed laser additive manufacturing of Inconel 718 parts, Proc. Inst. Mech. Eng. Part B J. Eng. Manuf. 231 (2017) 1890–1903. https://doi.org/10.1177/0954405415619883.

[8] A.N.M. Tanvir, M.R.U. Ahsan, G. Seo, J. duk Kim, C. Ji, B. Bates, Y. Lee, D.B. Kim, Heat treatment effects on Inconel 625 components fabricated by wire + arc additively manufacturing (WAAM)—part 2: mechanical properties, Int. J. Adv. Manuf. Technol. 110 (2020) 1709–1721. https://doi.org/10.1007/s00170-020-05980-w.

[9] X. Xu, Wire + Arc Additive Manufacture of New and Multiple Materials, Cranfield University, 2018. http://dspace.lib.cranfield.ac.uk/handle/1826/15107.

[10] G. Marinelli, F. Martina, S. Ganguly, S. Williams, Development of Wire + Arc additive manufacture for the production of large-scale unalloyed tungsten components, Int. J. Refract. Met. Hard Mater. 82 (2019) 329–335. https://doi.org/10.1016/j.ijrmhm.2019.05.009.

[11] F. Martina, G. Marinelli, S. Ganguly, S.W. Williams, Wire + Arc Additive Manufacturing of Refractory Metals, (2016).

[12] F. Martina, J. Mehnen, S.W. Williams, P. Colegrove, F. Wang, Investigation of the benefits of plasma deposition for the additive layer manufacture of Ti-6Al-4V, J. Mater. Process. Technol. 212 (2012) 1377–1386. https://doi.org/10.1016/j.jmatprotec.2012.02.002.

[13] Welding Engineering and Laser Processing Centre Cranfield University, MATERIALS AND PROPERTIES, (2019). https://waammat.com/about/materials-and-properties (accessed November 8, 2019).

[14] J. Norrish, Advanced welding processes : technologies and process control, [New editi, 2006. https://doi.org/10.1533/9781845691707.136.

[15] X. Xu, S. Ganguly, J. Ding, C.E. Seow, S. Williams, Enhancing mechanical properties of wire + arc additively manufactured INCONEL 718 superalloy through in-process thermomechanical processing, Mater. Des. 160 (2018) 1042–1051. https://doi.org/10.1016/j.matdes.2018.10.038.

[16] N. Kasravi, R. Hidayat, C. Tuncer, M. Themistokleous, A.M. Sambo, Additive manufacture of alloys for high temperature application, Cranfield University, 2021.

[17] F. Cortial, J.M. Corrieu, C. Vernot-Loier, Influence of heat treatments on microstructure, mechanical properties, and corrosion resistance of weld alloy 625, Metall. Mater. Trans. A. 26 (1995) 1273–1286.

https://doi.org/10.1007/BF02670621.

[18] A. Mitchell, Primary Carbides in Alloy 718, in: 7th Int. Symp. Superalloy 718 Deriv. 2010, The Minerals, Metals & Materials Society, 2010: pp. 161–167. https://www.tms.org/superalloys/10.7449/2010/Superalloys_2010_161_167.pdf.

[19] Special Metals, INCONEL® alloy 718, (2007) 1–28. https://www.specialmetals.com/assets/smc/documents/inconel_alloy_718.pdf (accessed May 8, 2020).

[20] Special Metals, INCONEL® alloy 625, (2013) 1–18. https://www.specialmetals.com/assets/smc/documents/alloys/inconel/inconel-alloy-625.pdf (accessed June 4, 2020).

[21] M.J. Donachie, S.J. Donachie, Superalloys - A Technical Guide, 2nd ed., ASM International, 2002. https://app.knovel.com/hotlink/toc/id:kpSATGE003/superalloys-technical/superalloys-technical.

[22] J.F. Wang, Q.J. Sun, H. Wang, J.P. Liu, J.C. Feng, Effect of location on microstructure and mechanical properties of additive layer manufactured Inconel 625 using gas tungsten arc welding, Mater. Sci. Eng. A. 676 (2016) 395–405. https://doi.org/10.1016/j.msea.2016.09.015.

[23] S. Li, J.Y. Li, Z.W. Jiang, Y. Cheng, Y.Z. Li, S. Tang, J.Z. Leng, H.X. Chen, Y. Zou, Y.H. Zhao, J.P. Oliveira, Y. Zhang, K.H. Wang, Controlling the columnar-to-equiaxed transition during Directed Energy Deposition of Inconel 625, Addit. Manuf. 57 (2022). https://doi.org/10.1016/j.addma.2022.102958.

[24] M.A. Shaikh, M. Ahmad, K.A. Shoaib, J.I. Akhter, M. Iqbal, Precipitation hardening in Inconel 625, Mater. Sci. Technol. 16 (2000) 129–132. https://doi.org/10.1179/026708300101507613.

5 HIGH TEMPERATURE FAILURE AND MICROSTRUCTURAL INVESTIGATION OF ADDITIVE MANUFACTURED RENE 41

This chapter is based on the following publication.

***W.S. James**, S. Ganguly, G. Pardal, High Temperature Failure and Microstructural Investigation of Wire – Arc Additive Manufactured Rene 41, Int. J. Adv. Manuf. Technol. (2023).*

This chapter represents the bulk of data collected on RE41 before the final down selection of a single alloy. The data presented here includes high temperature performance data and an examination of microstructural features both before and after fracture.

Abstract

In developing a wire-arc direct energy deposition process for creep resistant alloys used in high-speed flight applications, structures were built from nickel-based superalloy Rene 41. Samples of AM material were analysed for their microstructural and mechanical properties, in both as deposited (AD) and heat-treated (HT) conditions. Tensile specimens were tested at room-temperature, 538, 760, and 1000 °C. Macroscopically, large columnar grains made up of a typical dendritic structure were observed. Microscopically, significant segregation of heavier elements, grain boundary precipitates, and secondary phases were observed, with key differences observed in HT material. There was a clear distinction between failure modes at different testing temperatures and between AD and HT variants. A fractographic investigation found a progressive move from brittle to ductile fracture with increasing testing temperature in both AD and HT conditions, as well as microstructural features which support this observation.

Keywords: Additive manufacturing, Direct energy deposition, Mechanical properties, Fractography, Microstructure, Rene 41

5.1 Introduction

The use of a wire-arc based direct energy deposition (DED) process for the manufacture of creep resistant superalloys is a relatively new area of study and the effect of DED on material performance at high temperatures is little understood. The DED process where an electrical arc is used to melt and deposit a metal wire feedstock, is also known as Wire + Arc Additive Manufacturing (WAAM). WAAM has a proven capability for the deposition of a range of different alloys and metals. Williams et al. describes how the process can be used to build components in titanium, aluminium, and steel alloys [1], and Marinelli et al. had success with depositing refractory components, using a tungsten inert gas (TIG) process to deposit high purity tungsten [2]. As well as the above, Xu et al. deposited creep-resistant alloys such as nickel-based superalloy Inconel 718 [3]. WAAM can take advantage of a variety of different deposition processes such as TIG, MIG, and plasma transferred arcs (PTA). WAAM is currently a developing technology in the early stages of commercialising.

In developing the WAAM process for creep-resistant alloys used in high-speed flight environments, Rene 41 (RE41) was deposited using a PTA WAAM process in an oxygen-controlled environment. RE41 is a Ni-based, Cr, Co superalloy with applications in aerospace components, where high strength is required at operating temperatures between 650 – 980 °C, such as afterburner and gas turbine parts [4]. Wile gives more specific high-profile applications of RE41, such as its use in the skin on the Mercury space capsule and its application in components for the nuclear power industry [5].

There is little published research on specifically wire-based DED of RE41 using PTA. There is, however, more literature published on the deposition of RE41 using laser-based AM. Li et al. used a laser melting deposition (LMD) process to manufacture RE41 specimens for analysis. They found LMD RE41 had a fine rapid directionally solidified granular structure. They also found that the standard heat-treatment for RE41 was not suitable for LMD built RE41, due to the extensive precipitation of γ’ particles, the primary strengthening phase, which resulted in high hardness and ductility and ultimately worked to decrease the strength of the alloy compared with AD material [6]. In another study by Li and Wang, RE41 was again deposited using LMD and underwent mechanical testing. When testing at 800 °C RE41 was described as having excellent performance with a UTS of 855 MPa and a YS of 682 MPa. They also found the fracture surfaces contained secondary cracking and a local stepwise fracture surface [7].

Atabay et al. investigated RE41 deposited by a laser powder bed fusion (LPBF) process. Much like Li et al they found that RE41 fabricated by LPBF had a fine columnar grain structure. Atabay et al. also observed γ' precipitation after heat-treatment using transmission electron microscopy (TEM) but did not observe the precipitates in AD condition. When they were observed after heat-treatment they were considerably smaller than suggested in literature. They also observed the formation of Mo rich carbides at the grain boundaries. Specimens tested at RT achieved a UTS and YS of approx. 1165 and 857 MPa respectfully. The fractographic analysis revealed samples fractured in a ductile manner. In contrast to Li et al., Atabay et al. found the standard heat-treatment was satisfactory to meet their requirement. [8][6]

The intended outcome of this study is to understand the microstructural effects the WAAM process has on RE41 and how to maximise the performance for use in a high-speed flight environment, where external structures could reach service temperatures as high as 1000 K (727 °C) and 1200+ K (927 °C) for components in the propulsion flow path.

5.1.1 Physical Metallurgy

The phases seen throughout superalloys are dependent on their composition and are described by Donachie and Donachie in their book, Superalloys - A Technical Guide. Most superalloys have an austenitic face-centred cubic (fcc) phase known as γ phase and consist of several other secondary phases. Carbides are a secondary phase and take the form of MC, M_6C, $M_{23}C_6$ and M_7C_3, where 'M' represents the metallic element. Other secondary phases consist of intermetallic compounds, which commonly include: γ' fcc phase $Ni_3(Al,Ti)$, γ'' body-centred tetragonal (bct) phase Ni_3Nb, η hexagonal ordered phase Ni_3Ti, and δ phase orthorhombic Ni_3Nb. In most superalloys given the right conditions undesirable phases can form, which can harm the performance if present in larger amounts. These typically include topologically close-packed (tcp) phases: µ Co_2W_6 / $(Fe,Co)_7(Mo,W)_6$, Laves phase A_2B type where 'A' and 'B' represent metallic elements, and σ which can include more complex intermetallic phases. [9]

Schwartz et al. describes the basic metallurgy and strengthening mechanism of RE41 when they investigated the use of the alloy in extrusion dies; the alloy is a precipitation strengthened Ni based superalloy with a fcc austenitic matrix, RE41 also contains a large amount of Cr, Co & Mo. The main strengthening phase is γ' $Ni_3(Al,Ti)$ [10]. More historic research by Kaufman describes the formable phases in RE41 in more detail. Ni_3Al, & Ni_3Ti form fine uniform particles at 760 °C which are coarser at higher temperatures. Ni_3Ti appears fine below 760 °C and acicular above 760 °C. Ni_3Al appears course and curved and is seen in larger amounts at grain boundaries. δ phases are not seen generally due to Cr & Mo being tied up in the carbides. Laves phase can form where C is less than 0.05% and Al less than 1% at 815 °C. [11] Weisenberg and Morris describe how the main strengthening phase, γ', forms as the alloy ages, γ' is mostly prevalently between 760 – 1010 °C and the particles increase in size with temperature until dissolved at around 1050 °C. The phases present in the alloy vary with exposure to temperature [12]. The characterisation of RE41 by Collins and Quigg gives an estimation as to the probability of certain phases being present in the alloy. Of the formable phases, the MC type carbide is the most dominant at lower temperatures until 816 °C, and again at higher temperatures between 1150 – 1200 °C. Tcp µ phase is most stable around 930 °C. M_6C is most dominant between 980 – 1150 °C. The amount of $M_{23}C_6$ increases with temperature until it reaches a maximum at 870 °C and starts to become unstable at 980 °C. The amount of σ phase also increases with temperature, reaching a maximum at 980 °C and becomes unstable thereafter. [13] An interpretation of the phases formable with aging temperature is presented in Figure 5-1. In the more recent study using LPBF, Atabay et al. found that of the formable carbides observed, MC was rich in Mo and Ti, M_6C was rich in Mo and Co, and $M_{23}C_6$ was found to be rich in Cr [8].

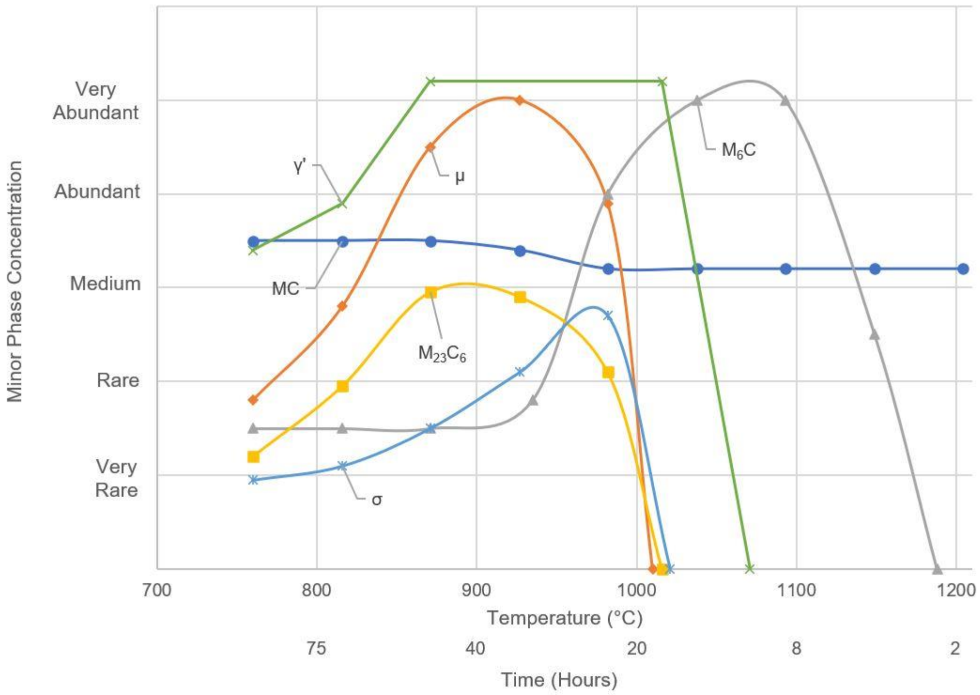

Figure 5-1 Minor phase concentration as a function of aging temperature. Adapted from [13] **and** [12]**.**

5.2 Experimental Method

5.2.1 Manufacturing Process

A symmetrical PTA WAAM process was used to produce samples for analysis from a commercially available 1 mm diameter RE41 wire. The WAAM system consisted of: a water-cooled plasma welding torch and wire feeder mounted to a FANUC six-axis robotic arm, a part-rotator, and a gas enclosure. The enclosure provided an inert argon atmosphere for deposition, where the concentration of oxygen was controlled below 800 ppm with the use of an oxygen analyser. The process used was symmetrical, meaning that material was deposited on both sides of the substrate plate, the main advantages of which are increased productivity and a reduction in residual stress, as described by Williams et al. [1]. Two wall structures measuring 350 x 110 x ~8 mm were deposited onto both sides of an Inconel 718 (IN718) substrate plate, using an arc current of 180 A, a wire-feed speed of 2.4 m/min, a torch travel speed of 0.36 m/min, a torch to work distance of 8 mm and an inter-pass temperature of 170 °C after approx. 3 mins of cooling time. A diagram of the set-up is shown in Figure 5-2.

After deposition samples were extracted and underwent the heat-treatment recommended by Weisenberg and Morris for achieving maximum tensile performance. The heat-treatment consisted of: a solutionising treatment at 1065 °C for 4 hours, after which the material was air cooled to RT, followed by an aging treatment at 760 °C for 16 hours, and completed by air cooling to RT [12].

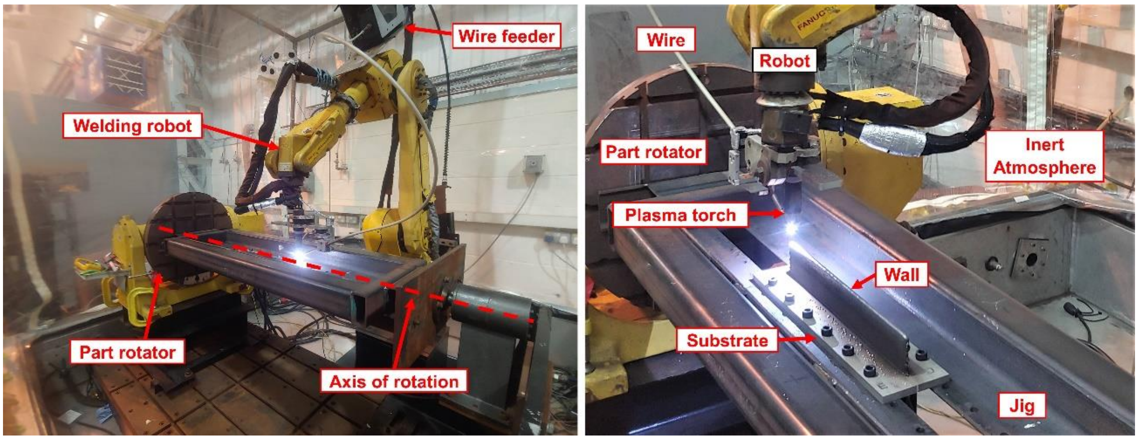

Figure 5-2 Experimental WAAM set-up.

5.2.2 Composition

The wire feedstock underwent a chemical analysis to verify the alloy wire met the requirements for UNS N07041, the results of which are given in Table 5-1. To determine composition, the material was combusted and analysed using inductively coupled plasma - optical emission spectroscopy (ICP-OES).

Table 5-1 Composition of RE41 wire (wt.%)

Ni	Cr	Co	Mo	Fe	Ti	Al	Nb	V	Si	C	Cu	Mn	B	S
53.7	18.9	10.2	9.08	2.72	3.20	1.64	0.12	0.12	0.09	0.07	0.04	0.03	0.004	<0.003

5.2.3 Metallographic Preparation and Analysis

The WAAM walls were cut from the substrate plates and samples were extracted through both the wall height and length. Cross-sections were extracted and prepared for metallographic analysis following a procedure consisting of mounting then grinding and polishing successively, followed by etching. Samples were etched to reveal the microstructure using 3 g $CuSO_4$, 80ml HCl, 20 ml absolute alcohol [6] swabbed for 30 seconds.

The microstructure was analysed, using a Tescan VEGA 3 scanning electron microscope (SEM), and optically using a Leica DM 2700M Microscope. To give an indication of composition a semi-quantitative analysis of phases was conducted using the VEGA 3 SEM equipped with an Oxford Instruments X-Max 20 mm energy-dispersive spectrometry (EDS) detector. To determine the presence of lighter elements within the matrix a Tescan Solaris X SEM was equipped with xenon plasma focused ion beam (FIB) and a TOFWERK time-of-flight secondary ion mass spectrometer (TOFSIMS).

The specimens were extracted in several locations across the WAAM walls, their locations in reference to the wall structure are shown in **Figure 5-5**. From a total of four WAAM walls built in pairs three walls were utilised for testing. After testing, the fracture surface of specimens in each category and condition were observed. The axis by which samples were observed are indicated going forwards with reference to Figure 5-5, where BD is the build direction, WA is the wall axis and TT is the through-thickness.

To determine the dilution of the IN718 substrate into the RE41 matrix, samples containing both the deposited WAAM wall, and a section of the substrate were extracted. The line scan function of the SEM-EDS system was then utilised to determine dilution of specific elements.

5.2.4 Mechanical Testing

Samples were extracted from the WAAM walls and machined into coupons from the locations and in the orientations shown in Figure 5-5. The room temperature (RT) coupon, conforming to ASTM E8(M) sub-size specification, is shown in Figure 5-3, and the elevated temperature (538-1000 °C) coupon is shown in Figure 5-4. A campaign of three coupons per test condition was used, where tests were conducted in both AD and HT condition from each alloy. Samples were tested at RT, 538, 760, and 1000 °C, using an Instron 8801 Servo hydraulic

Universal Testing System and tested to failure using ASTM E8(M) specification for RT testing and ASTM E21 for high temperature testing. Tensile tests used a strain rate of 0.005 min^{-1} until the onset of plastic deformation and thereafter a crosshead speed of 1.6 mm/min. Prior to the start of testing, high temperature specimens were held for 30 mins at the testing temperature. Specimens were extracted from a variety of locations on the WAAM wall to minimise variation in results due to the WAAM aging effect. The fracture surfaces were carefully preserved for analysis.

The alloys in both AD and HT conditions also underwent microhardness testing using a Zwick/Roell hardness tester under a load of 500 g and holding time of 15 s.

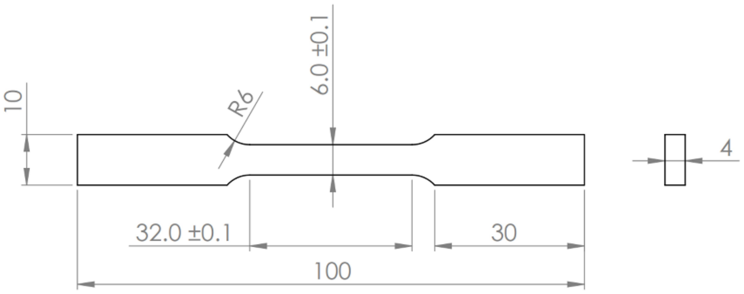

Figure 5-3 RT Tensile testing coupon. (Dimensions in mm).

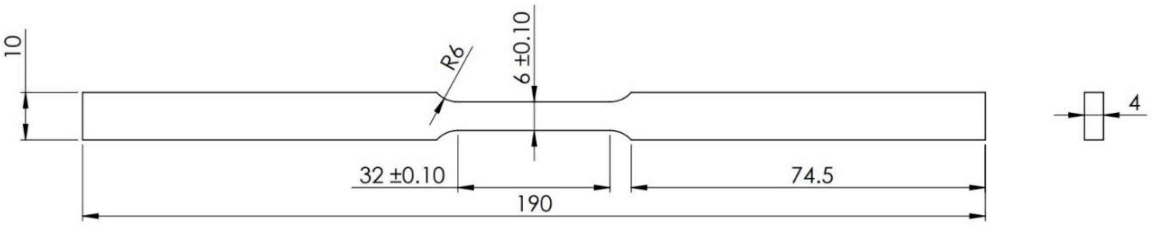

Figure 5-4 Elevated temperature testing coupon. (Dimensions in mm).

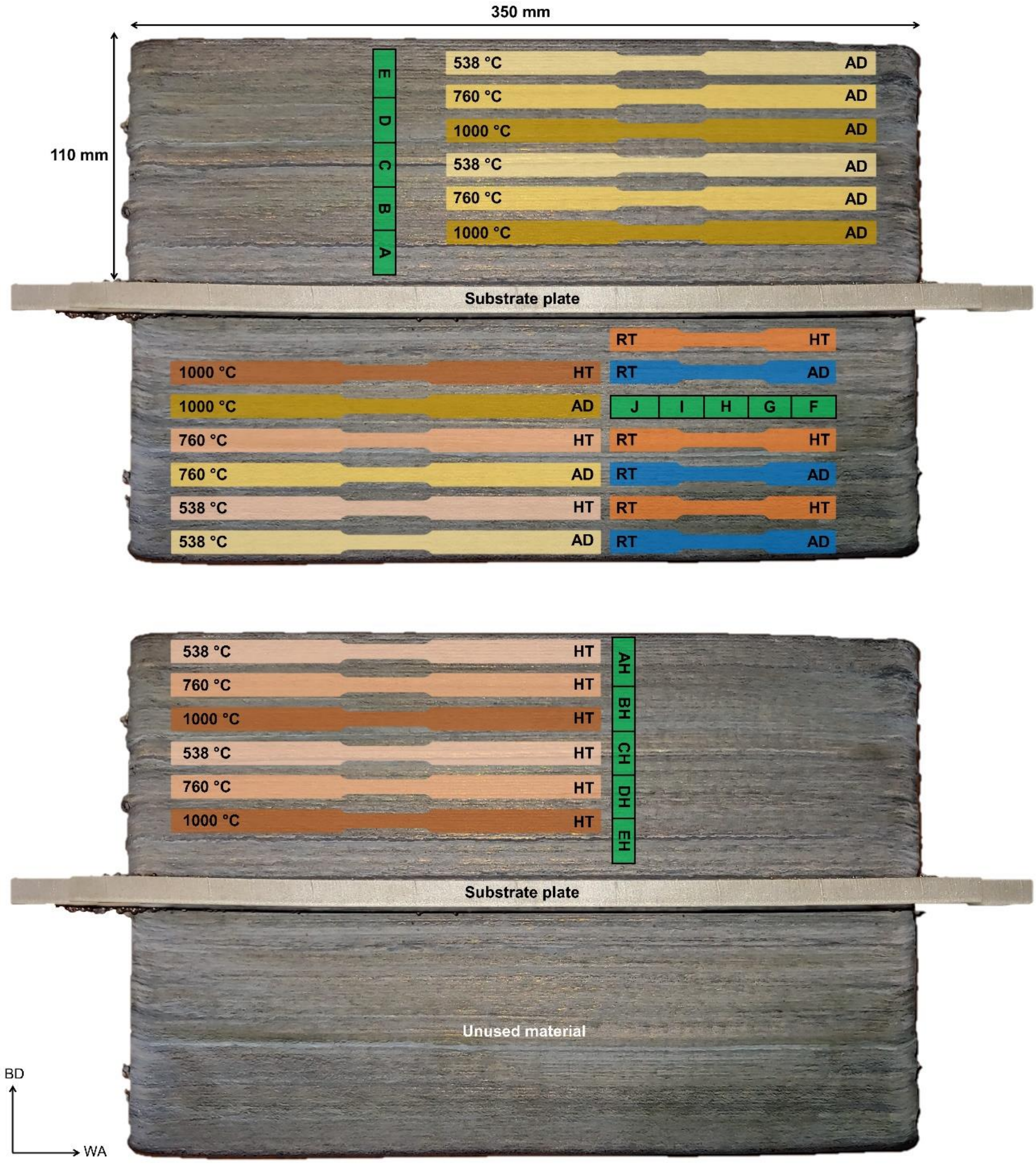

Figure 5-5 Location of extracted samples from WAAM walls. Green areas indicate location of metallographic samples. Temperature given on the left of the coupon indicates testing temperature and on the right the condition AD or HT. Metallographic samples AH-EH are HT whereas single letter A-J are AD.

5.3 Results

5.3.1 Macrostructure

The macrostructure exhibits a typical solidified dendritic structure made up of large columnar grains which appear to extend along the BD from bottom to top. The ripples of the successive welded layers are also observed and appear to have no effect on the grain structure. Several cracks were observed in the structure at the macro level (Figure 5-6 - top/centre). This grain structure was expected and is similar to that of IN718 seen in a previous study by Seow et al [14].

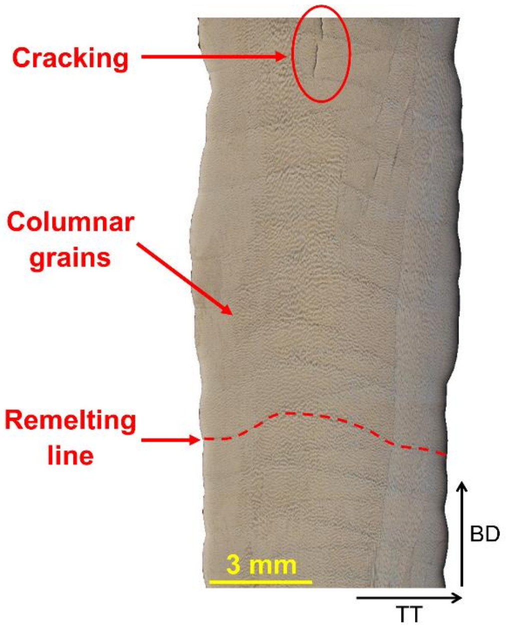

Figure 5-6 Elongated grain structure seen in HT specimen.

5.3.2 Microstructure

The microstructure was analysed both optically and under SEM. Optical images of the microstructure at comparable locations in both the AD and HT conditions are presented in Figure 5-7. It can be clearly seen that the grain structure is similar in appearance, with long dendrites extending through the height of the samples in the BD axis. Grain boundary locations are shown for both samples, with the AD images displaying an intergranular crack. The micrographs show the directionally solidified grain structure, where the HT samples show a thicker dendritic structure and darker grain boundaries. A comparison at greater magnification in Figure 5-7 is given in the top left of the micrographs. Precipitates can be seen at the crack edges in Figure 5-7. Phases and carbides in this section going forward have been identified based on EDS composition and appearance using ASM Atlas of Microstructures [15]. It becomes clearer at greater magnification the thicker and darker grain boundaries after heat-treating.

In HT samples of RE41 (RH of Figure 5-7), the grain boundary area presented is seen to consist of lighter coloured stringer type precipitates, measuring 0.5 µm, surrounded by a darker grain-boundary background. With larger, irregular shaped grey precipitates, measuring mostly 1-4 µm, distributed in the matrix. The lighter coloured precipitates at the grain boundary are thought to be M_6C or $M_{23}C_6$, while the grain boundaries are darkened in HT condition due to precipitation of γ'. The larger white, irregular shaped precipitates, seen mostly at the grain boundaries are thought to be a complex intermetallic phase.

When viewed in the transverse plane (WA-TT) in Figure 5-8 a typical dendritic structure is apparent, with precipitates of 1-2 µm seen mostly in the interdendritic regions. Also seen in Figure 5-8 is a darkened grain boundary consistent with the HT material seen in Figure 5-7, although the precipitates along the grain boundary in AD material appear finer, which suggests the precipitates are carbides.

The AD WAAM structure shows significant amounts of segregation of Mo at Ti throughout the matrix, as seen in the elemental maps (Figure 5-10). It can be seen clearly the segregation of Mo, which corresponds to the lighter coloured phases in the BSE images, in these areas Ni is depleted but Cr is not, indicating possible σ intermetallic phase (CrNiMo), which is supported by spectrum A in Table 5-2.

The darker grey coloured phases correspond to areas rich in Ti. These smaller Ti rich zones were analysed using TOFSIMS to detect the presence of Ti and specifically C, which is less reliably indicated using EDS. In these areas C and Ti were detected where Ni and Cr were shown to be depleted, indicating the presences of Ti rich carbides, most likely TiC. Elemental maps of these areas are shown in Figure 5-11 for AD material and correspond to the smaller grey coloured precipitates seen in the matrix, labelled as B in Figure 5-9 with EDS composition in Table 5-2. HT material was also analysed using the TOFSIMS facility, which identified similar formations of Ti rich zones, corresponding to areas with higher concentrations of C. The HT material appears to have much larger precipitate formations, as well as detecting Al rich precipitates. The carbide formations seen in HT material are thought to be $M_{23}C_6$ where M is a combination of Ti and Al which was also observed by Franklin and Savage [16].

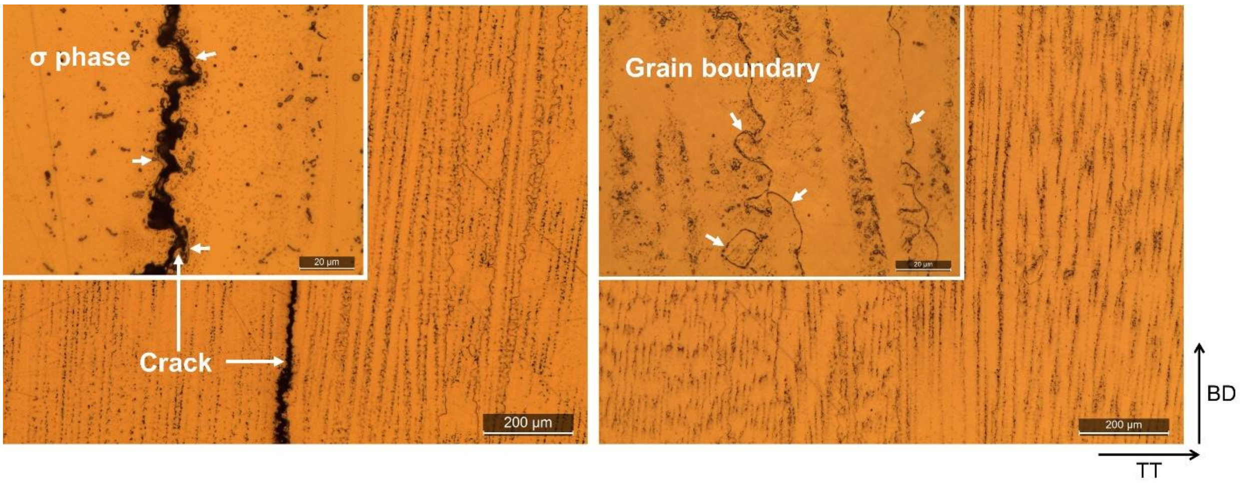

Figure 5-7 AD (left) & HT (right) optical observations.

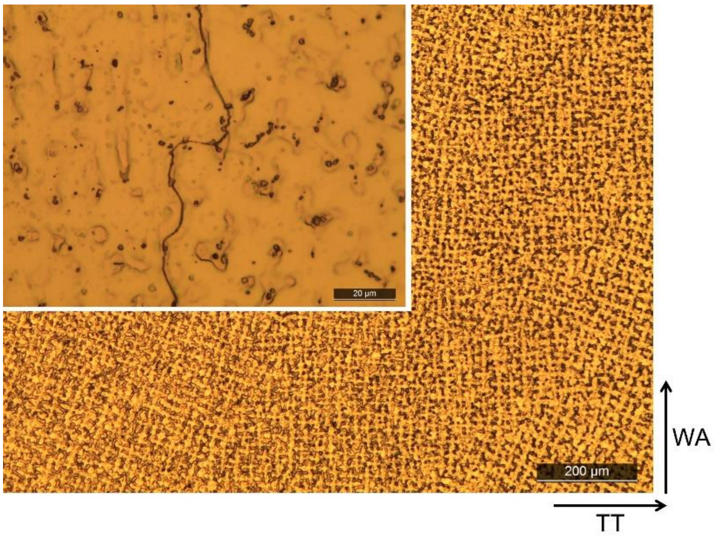

Figure 5-8 AD microstructure viewed in transverse (WA-TT) plane, showing cellular dendritic structure and precipitates in the interdendritic regions.

Table 5-2 EDS analysis of areas marked in Figure 5-9. (%at)

Spectrum Label	Al	Ti	Cr	Fe	Co	Ni	Mo
A		1.55	34.16		10.86	30.26	23.17
B		15.61	22.21			62.18	
C	1.77	4.35	22.86	2.53	9.94	39.79	18.26

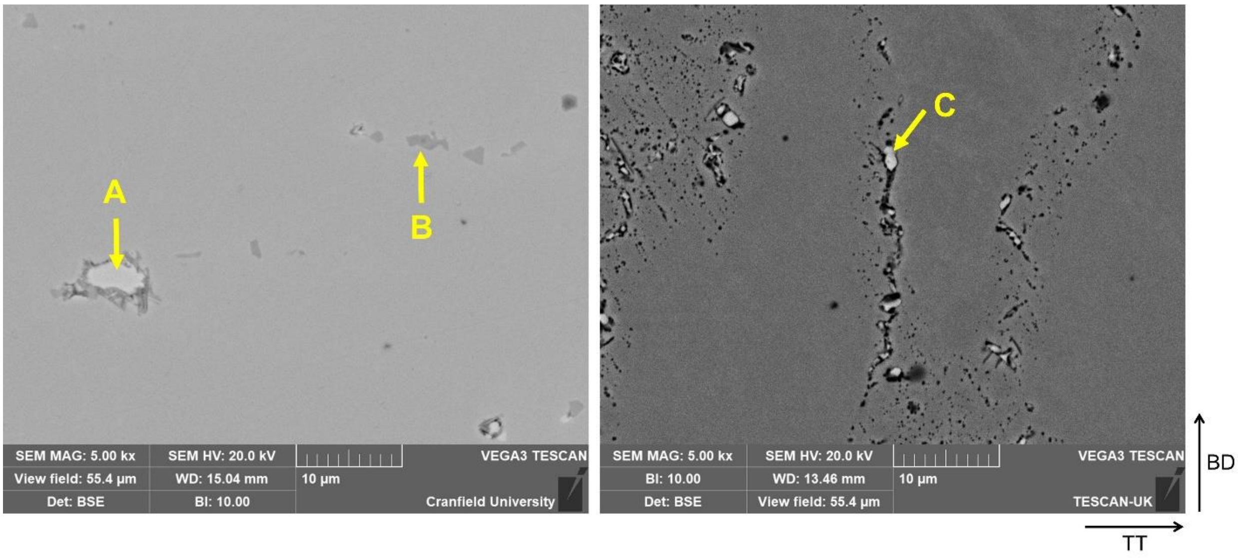

Figure 5-9 BSE images of AD (left) & HT (right) samples.

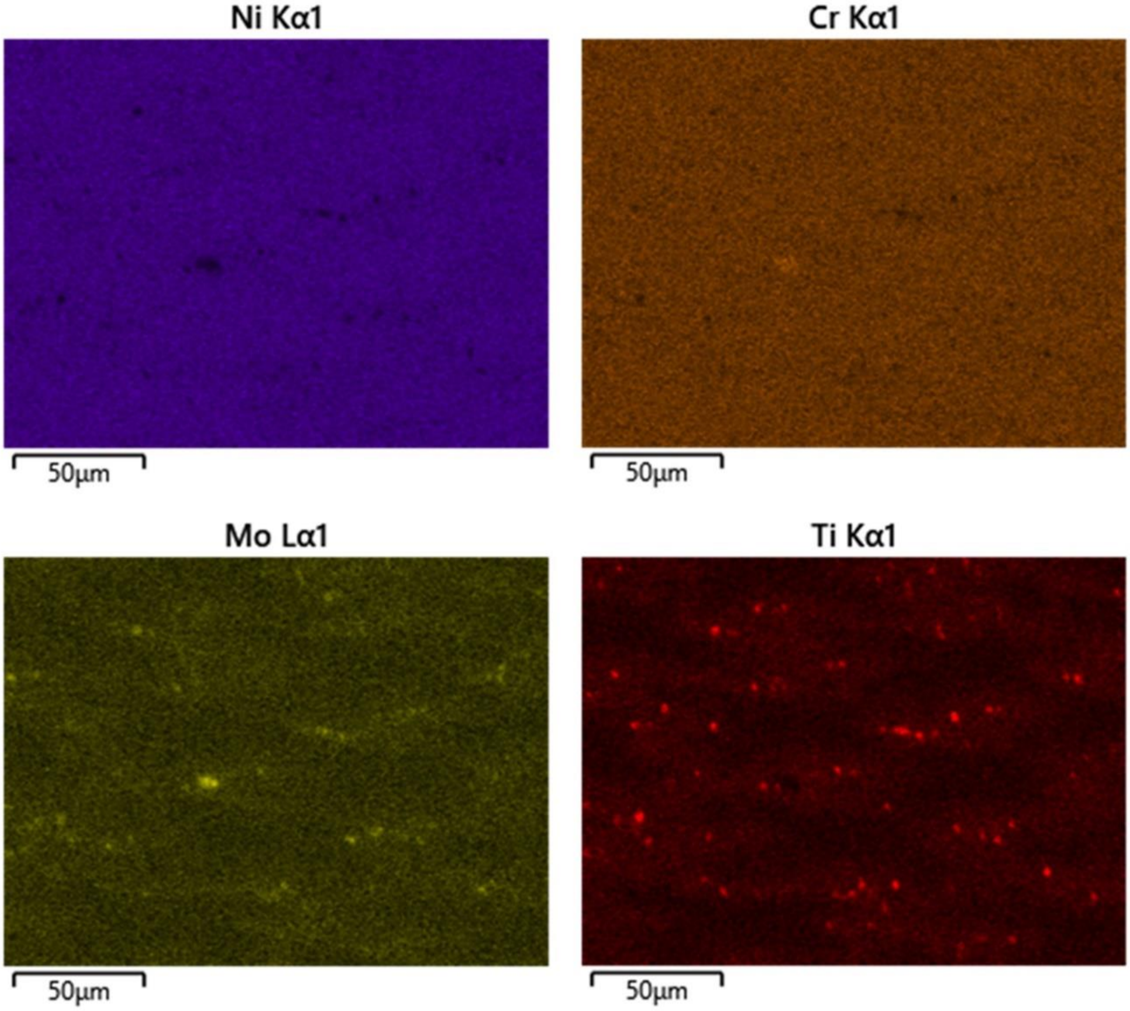

Figure 5-10 EDS elemental map of AD material.

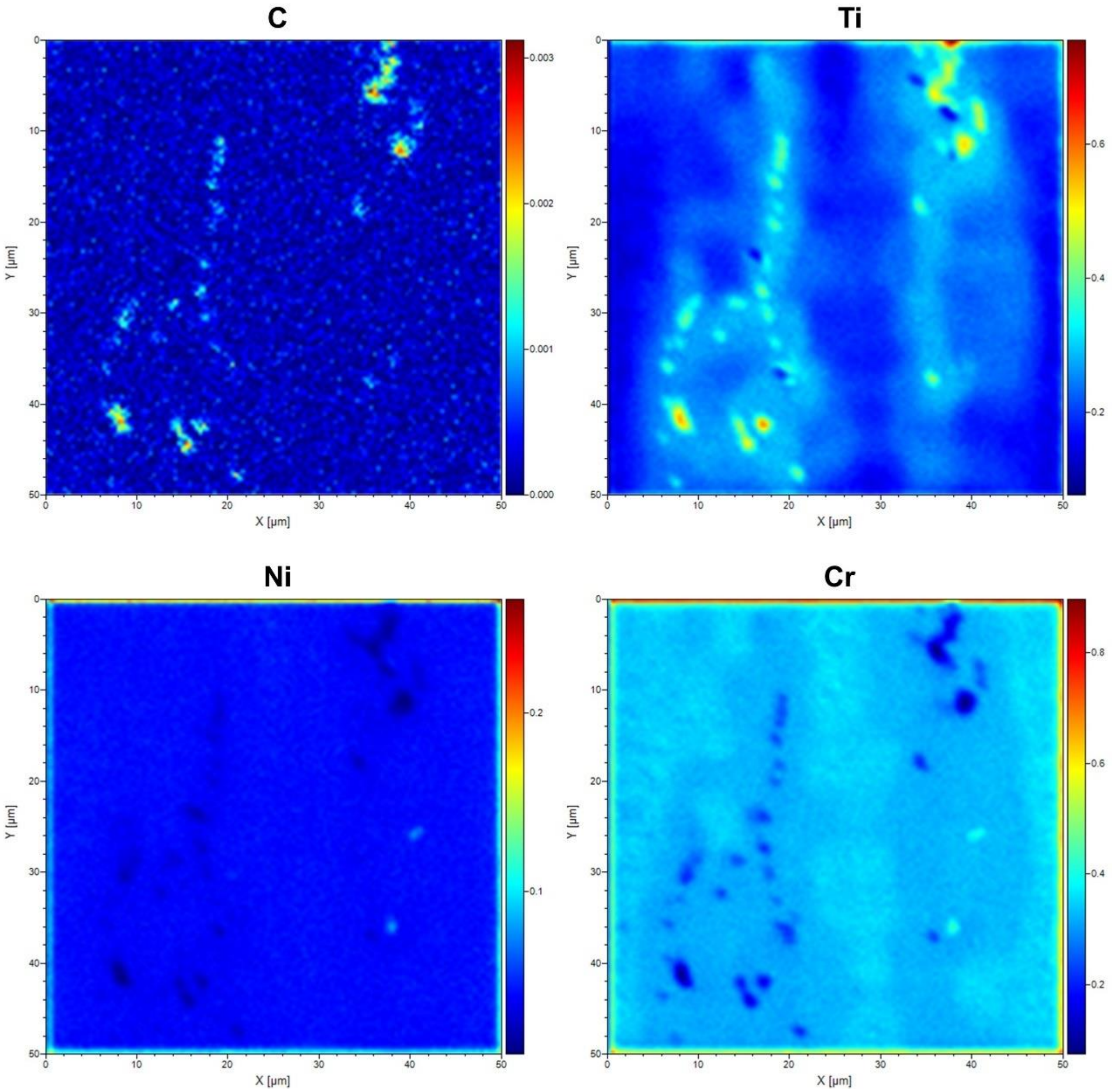

Figure 5-11 TOFSIMS elemental maps of AD material, showing potential carbides in areas rich in Ti and C, with depletion of Ni and Cr.

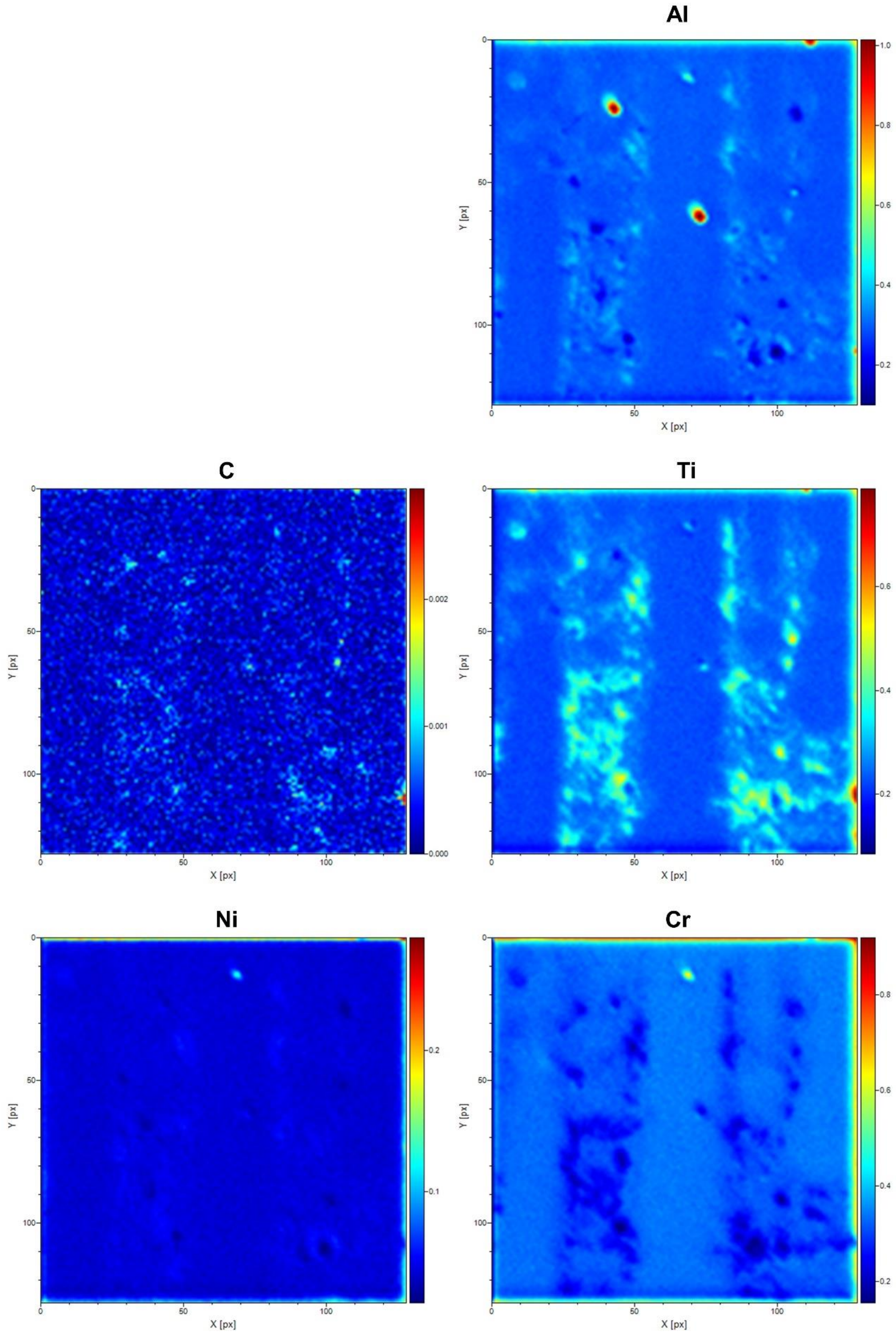

Figure 5-12 TOFSIMS elemental maps of HT material, showing potential carbides in areas rich in Ti with increased levels of Al and C.

5.3.3 Dilution of IN718 Substrate into RE41

As stated in the method section 5.2.1, the deposition process utilised an IN718 substrate plate, this was ultimately due to difficulties in obtaining a supply of RE41 in plate form. It is therefore necessary to examine the dilution of IN718 into the RE41 WAAM wall to determine the how the composition of the WAAM material might be affected by using a different Ni-based alloy as a substrate, and the extent of dilution into the RE41 matrix. For this purpose, abundant elements which are not common between the two alloys were analysed, Fe forms 18.5 %wt of IN718 and 2.72 %wt. of the RE41 wire, whereas Co forms 10.2 %wt in RE41 and is not present in IN718. The line scan results shown in Figure 5-13 show how the level of Fe and Co change with distance from the substrate. It can be seen the level of Fe stabilises after approx. 2.1 mm. Co levels begin to stabilise after 1.2 mm increasing slightly until 2.1 mm beyond which remains relatively stable. To avoid any doubt in the reliability of mechanical results, samples were extracted more than 10 mm from the substate.

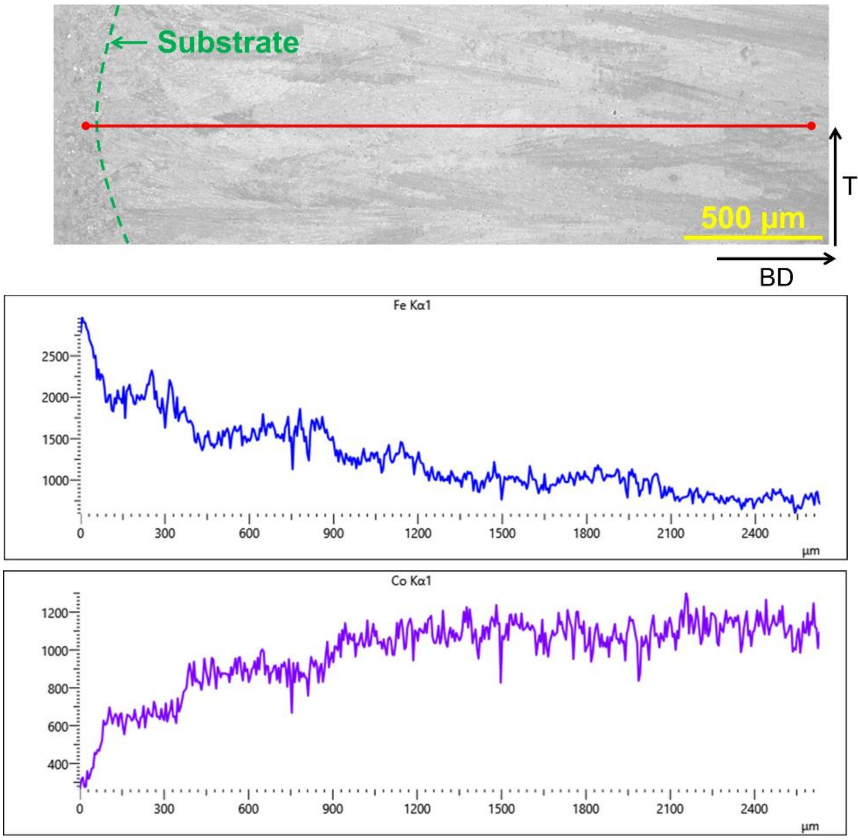

Figure 5-13 Dilution of Fe and Co at substrate interface.

5.3.4 Mechanical Testing

The results of tensile testing are given in Table 5-3, where wrought (Wro) values from the superalloys book by Donachie and Donachie [17] are presented alongside results for AD and HT samples. The data shows that even after heat-treating the WAAM material has not regained its wrought strength.

Graphs comparing the performance across the range of temperatures are shown in Figure 5-14. An increase in performance was observed in the AD material during the 760 °C test and affected an increase in the performance compared with the 538 °C test which was unexpected. AD material achieved an average of 58.8 % of the wrought maximum, and when heat-treated the performance increases to an average of 61.4 %. The scatter in results is likely due to the cracking present in the depositions.

Wrought RT hardness is provided in the manufacturers data sheet as a minimum of 363 HV [18]. When tested the AD and HT material had a hardness of 410 HV and 497 HV respectively. The reason that there is an increase in hardness after heat-treating is due to RE41 being precipitation strengthened.

It should be noted that unlike other alloying systems, the elastic modulus of Ni-based alloys is dependent on composition. As discussed by Parveen and Murthy, the elastic modulus is sensitive to minor changes in chemical composition that occur during heat-treatment with the formation of intermetallic phases [19]. By extension this could also apply to AD samples due to the partial aging effect which was observed by Xu et al. in WAAM built maraging steel [20].

Table 5-3 Tensile results [21] **comparing Wrought data (Wro)** [17] **with AD and HT material from RT-1000 °C.**

Temperature (°C)	UTS (MPa)			0.2 % YS (MPa)			Elastic Modulus E (GPa)		
	Wro	AD	HT	Wro	AD	HT	Wro	AD	HT
RT	1420	855 ±52	945 ±55	1060	733 ±22	812 ±22	220	140 ±11	149 ±13
538	1400	703 ±21	757 ±30	1020	611 ±11	688 ±24	191	120 ±7	120 ±1
760	1105	728 ±67	704 ±36	940	669 ±23	671 ±22	173	103 ±4	107 ±11
1000		183 ±6	179 ±2		135 ±3	106 ±32		70 ±10	74 ±5

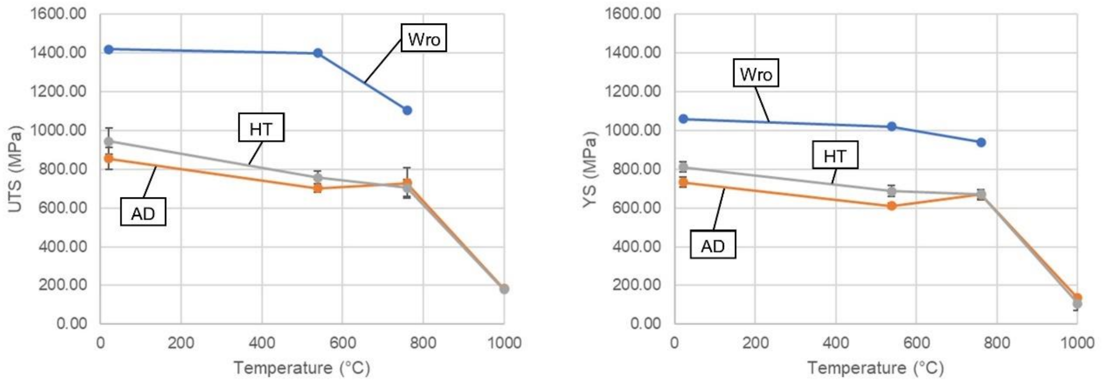

Figure 5-14 Graphical representation of data presented in Table 5-3. UTS (left), YS (right).

5.3.5 Fracture Surfaces

In the macrographs most of the fracture surfaces have a woody appearance, indicating a shearing action across the grain plane which has produced cracking along many parallel longitudinal planes. Further to this, most samples failed on an inclined plane also suggest a shearing action. The woody appearance suggests that most fractures seen here are intergranular, a good example of this is seen in Figure 5-15 image HT 1, that shows the surface of which is fibrous. On several samples the lines sometimes take a chevron shape, these are theorised to be slip steps, although similar in appearance to striations which occur microscopically. Chevron patterns appear on mostly RT, 538 °C and to a lesser extent 760 °C specimens, these patterns are indicative of rapid fracture associated with more brittle fractures, as seen in the ASM fractography atlas [22].

On 1000 °C specimens the fractures appear more ductile in nature with distorted cross-sections. Specimens appear to have deep central void type cracks which extend a good distance into the length of each specimen, suggesting much larger intergranular separation. The fracture surface of the 760 °C specimen appears far rougher and woodier in appearance. Fracture surfaces at this temperature appear to have areas seen as blue in colour, this perhaps indicates the formation of an oxide scale at this temperature, as samples were tested in air.

In Figure 5-16, the microstructure 3 mm directly behind the fracture surface is shown for both conditions at each testing temperature. The grain boundaries appear to grow thicker with increased testing temperature, the difference is most noticeable in the difference at 1000 °C compared to the other temperatures (Images AD 7 & AD 8). The grain boundaries are also noticeably thicker and more pronounced in HT specimens.

When looking at the features present 3 mm behind the fracture surfaces of specimens tested at 760 and 1000 °C (Figure 5-17) differences were observed. The 760 °C specimen presents two distinct phases, of which one is bright in colour and is rich in the alloying elements Cr, Ni and Mo (spectrum A, Table 5-4) and is consistent with the appearance of σ intermetallic phase (CrNiMo). σ phase is formed with exposure between 540-980 °C, is seen to be irregularly shaped in the atlas of microstructures [15] and was also observed by Donachie and Donachie in Ni-Co alloys [9]. The second phase present (indicated by green arrows in Figure 5-17) is rich in Ti (spectrum B, Table 5-4) and suggests the presence of carbide formation, likely TiC. A secondary crack in shown for the 1000 °C tested specimen. There appears to be, based on initial appearance, δ phase precipitates (indicated by red arrows and C in Figure 5-17). However, this is not the case, but on closer inspection using EDS analysis (Table 5-4) they appear to be entrapped oxide, which retain a good distribution of the alloying elements. This differentiates them from precipitates labelled D which is seen as the bright irregular shaped areas central to the crack and forming along the crack edges, which is consistent with possible σ phase (CrNiMo).

When the fracture surfaces were examined microscopically in AD samples tested at RT and 760 °C (Figure 5-18), the fracture surface exhibits a stepped surface with some evidence of beach marks in RT specimens which although commonly associated with fatigue crack propagation, can be evidence of brittle fracture modes. Secondary cracking was observed in 760 °C specimens which showed an oxidised fracture surface.

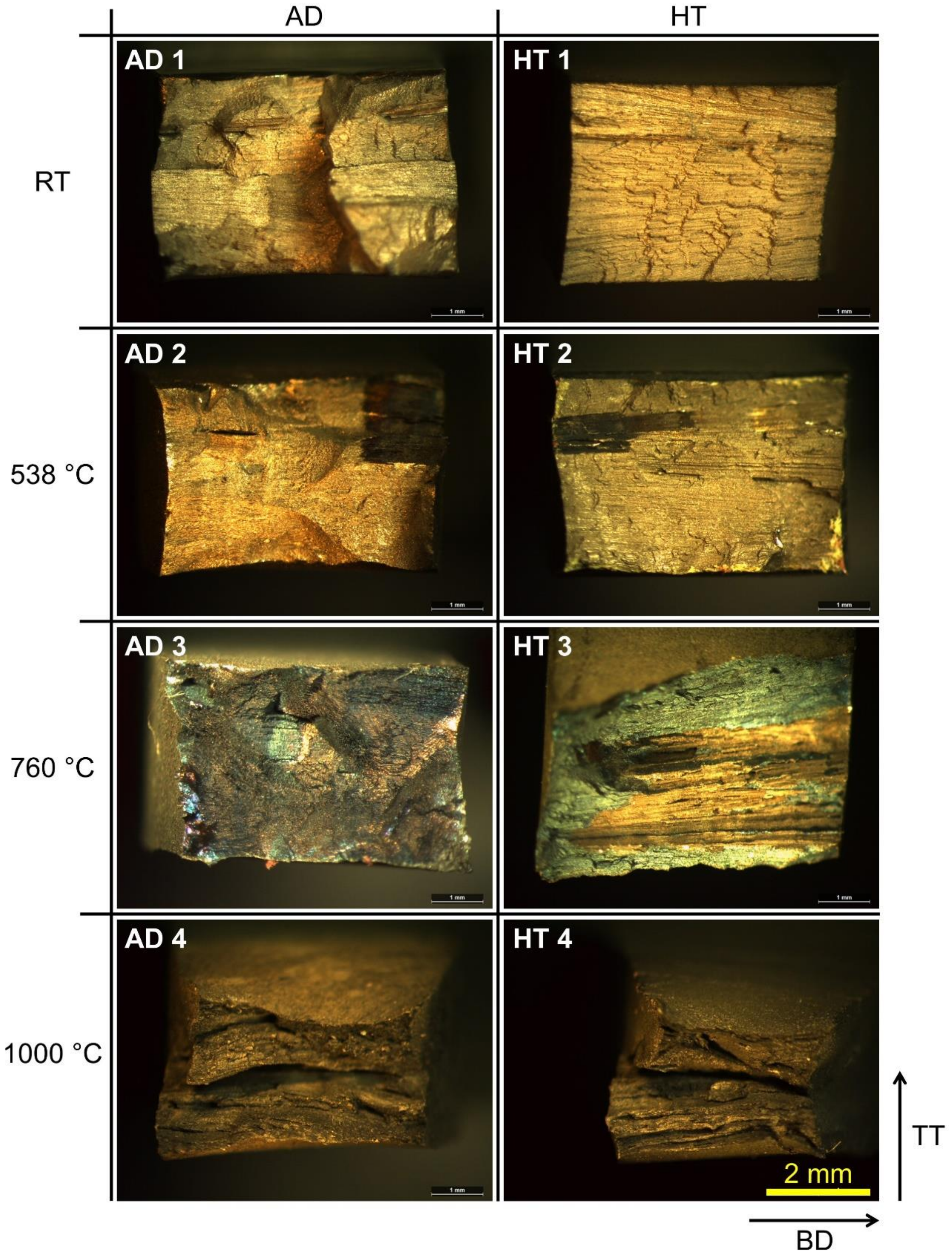

Figure 5-15 AD & HT macro fractographic images of fracture surfaces.

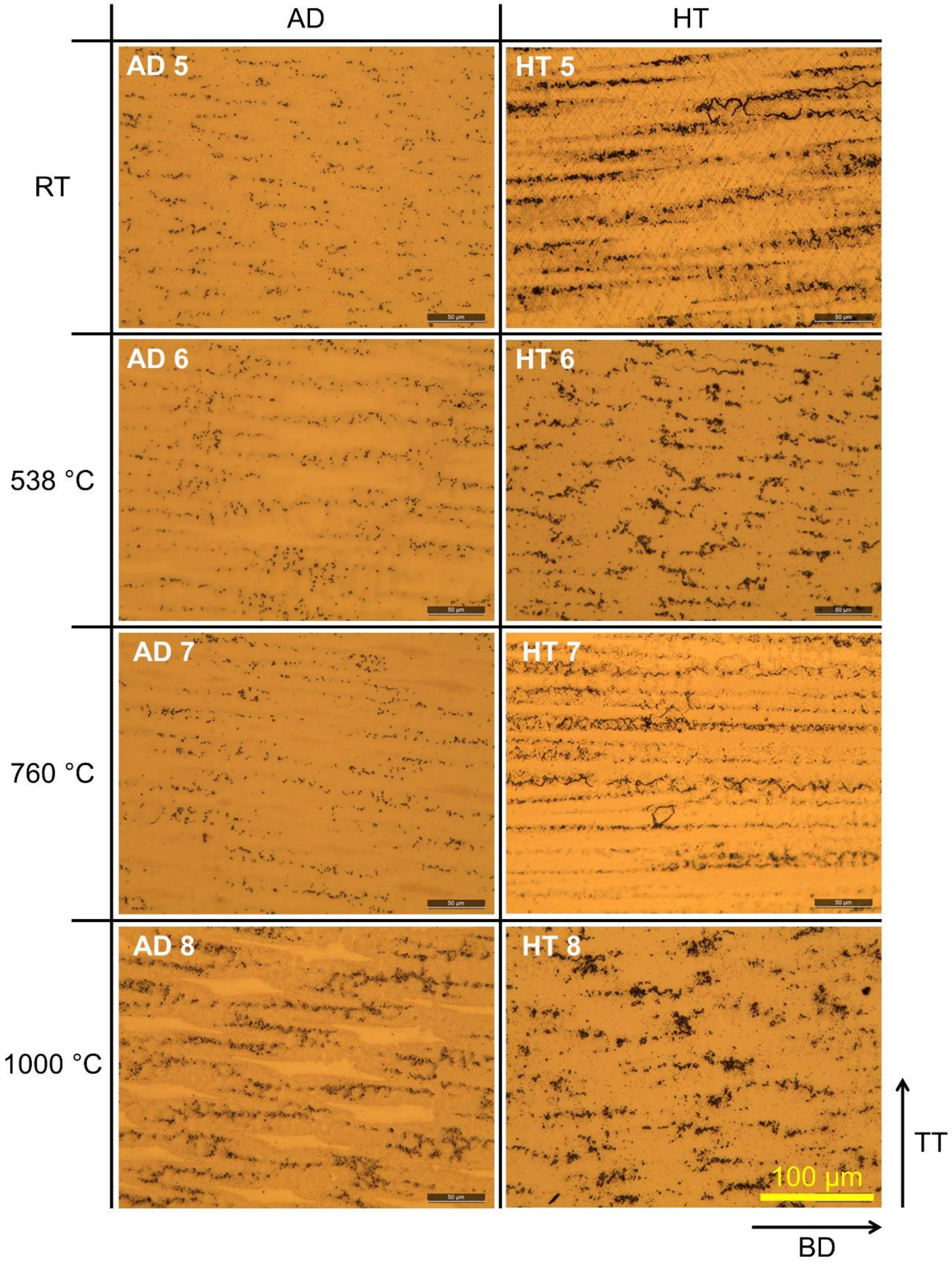

Figure 5-16 Microstructure of AD & HT tensile specimens directly behind fracture surface.

Table 5-4 EDS Analysis of areas marked in Figure 5-17. (%at)

Label	O	Al	Si	Ti	Cr	Fe	Co	Ni	Mo	Possible phase
A		1.17		2.18	33.29	2.39	10.36	29.22	21.25	σ (CrNiMo)
B		3.13		15.16	18.68	2.09	7.95	41.89	10.87	MC (TiC)
C	9.13	2.85	2.57	3.56	19.74	2.66	9.12	45.34	5.04	Oxide
D	13.17	1.23	1.73	4.40	20.76	1.73	8.16	28.58	20.25	σ (CrNiMo)

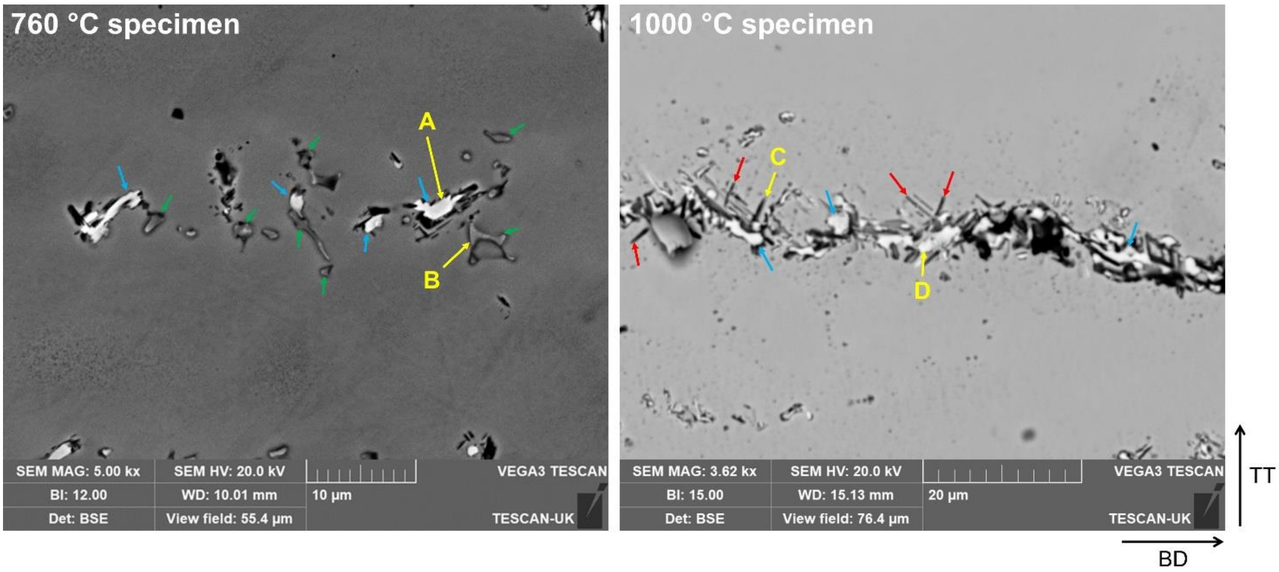

Figure 5-17 BSE images behind fracture surface: 760 °C tested specimen (left), 1000 °C tested specimen (right). Green arrows indicate Ti-rich potential MC carbides, blue arrows indicate σ phase, red arrows indicate oxide formation.

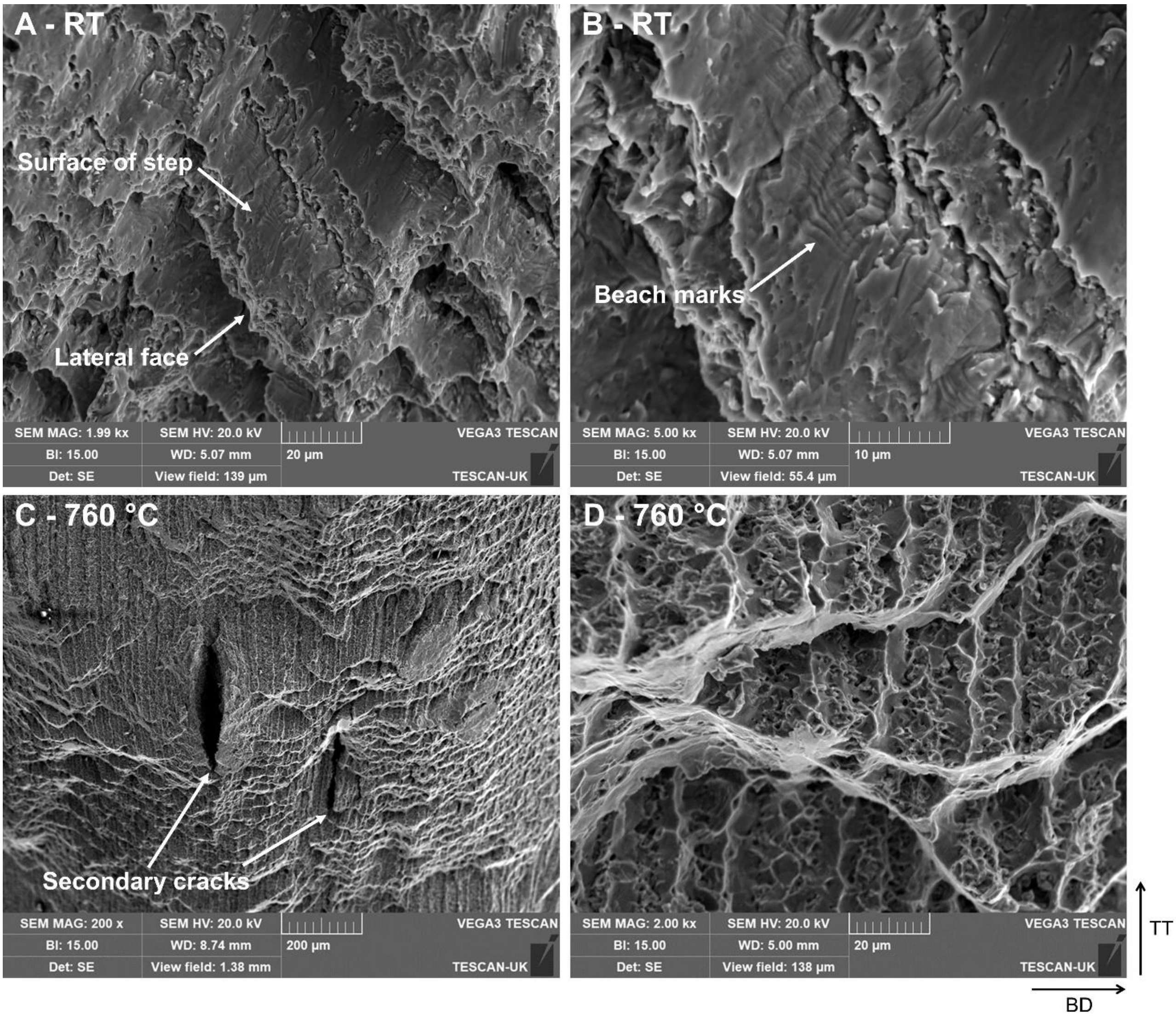

Figure 5-18 Fractography of AD material tested at RT (top) and 760 °C (bottom). Images show stepwise fracture surface. Image B shows beach marks on step surface. Image C shows secondary cracks and D the oxidisation on the fracture surface.

5.4 Discussion

5.4.1 Macro & Microstructure

The macrostructure seen in RE41 is similar in appearance to that of IN718 observed by Seow et al. in AD WAAM material. Large columnar grains extending through the BD axis, which extend outward with the flow of heat in the material in IN718 were also observed [14]. The appearance in RE41 of this effect is also noticeable and it is likely that the same heat flux influenced grain structure seen by Wang et al. [23], is also occurring in WAAM built RE41.

The comparison in Figure 5-7 between AD and HT samples is especially interesting. The microstructure is similar in appearance to that which Li and Wang observed in their study of LMD of RE41 [7]. They observed the same epitaxial growth of the dendritic structure along the heat flux direction that was observed in this study. When the microstructure of HT RE41 is viewed optically, there are clear stringer like precipitates at the intergranular regions surrounded by a darker background which became more pronounced after heat-treating, best seen in Figure 5-7. Further investigation into literature suggested that these precipitates are MC, M_6C or $M_{23}C_6$ carbides while the darker background is indicative of γ' precipitation, as seen in the microstructures atlas [15], which is expected post-aging. Franklin and Savage found that grain boundary carbides in RE41 form as M_6C type in solution annealed material and $M_{23}C_6$ in overaged material [16]. These precipitates, which appear darker grey in colour on the BSE images (Figure 5-9), are thought to be Ti rich carbides. This is supported by the EDS analysis of spectrum B in Table 5-2. The TOFSIMS analysis (Figure 5-11) further indicates the presence of carbides by confirming the presence of C in these precipitates and the depletion of Ni and Cr. The larger white precipitates seen most clearly in image (Figure 5-9), are thought to be σ intermetallic phase (CrNiMo) which is further supported by the EDS analysis in Table 5-2 spectrum A. These phases are also seen in HT samples, indicating that the standard 1065 °C solutionising treatment is not sufficient to dissolve these intermetallic tcp phases.

When the microstructure is viewed in the transverse (WA-TT) plane (Figure 5-8), the dendritic structure is more apparent and is similar to the LMD microstructure observed by Li and Wang [7], however the cellular-dendritic structure observed in the WAAM material shows a more pronounced formation of secondary dendrite arms, and the precipitates forming in the interdendritic area are smaller with sizes of 1-2 µm. Precipitates forming at the grain boundary in AD material appear finer than was observed in HT samples, which is indicative of carbide formation, most likely $M_{23}C_6$ during heat-treatment which was observed by Franklin and Savage, who found that a network of $M_{23}C_6$ carbides forming in intergranular locations can be a cause of cracking in RE41 [16].

5.4.2 Effect of Microstructure on Mechanical Performance

In the tensile results from RT-760 °C a significant difference is observed in the performance of both variants of WAAM material and their stated maximum values from literature. Comparing UTS values, the HT specimens achieve roughly 67, 54 and 64 % of their stated maximum at RT, 538, and 760 °C respectively. This difference was also observed in a previous study on IN718 by Xu et al. in which wrought IN718 was compared with WAAM material. The study showed that WAAM IN718 had a grain structure of far greater thickness and less grain boundary area than the wrought material. The strength of the wrought material is gained through its finer equiaxed grain structure and smaller dendrite arm spacing, allowing for more effective strengthening by precipitation of secondary phases at the grain boundaries. The larger columnar grains seen in the WAAM material made precipitation of these phases less likely. In this study, large columnar grains in RE41 also appear to have affected the strength in a similar way. A very similar mismatch between HT WAAM specimens at the wrought strength was seen in Xu et al.'s study on IN718, which went further to examine the effect of differing heat-treatments and found that unless a mechanical process was used to produce a more favourable starting microstructure, little to no additional enhancement in performance can be made. [24]

An increase was also observed in the UTS and YS performance of the AD specimens when tested at 760 °C, which appear to have undergone aging during testing to 'catch-up' to the HT specimens, which was an intriguing finding. This finding is consistent with the microstructure observed in tested specimens (Figure 5-16), where a clear darkening effect was observed around precipitates as the testing temperature was increased. The result of the increased stress performance is consistent with the results of Franklin and Savage when they examined the stress relaxation effect with temperature in RE41, they found that when tested at 760 °C the alloy precipitates larger γ' particles and also precipitates $M_{23}C_6$ carbides in a continuous network at the grain boundaries, resulting in increased stress but also results in greater levels of grain boundary cracking [16].

At 1000 °C there was a sharp decrease in the performance, which is consistent to what was expected to be seen if the literature data is extrapolated to this temperature. Excessive blackening and oxidisation cracking was observed on the 1000 °C samples post-testing and is consistent with the findings of Greene and Finfrock with IN718, who found that at temperatures of 1000+ °C, volatile Cr_2O_3 forms and results in the loss of the protective Chromia scale [25]. As the samples were tested in air at all temperatures, it is reasonable to assume that RE41 underwent this loss of protection, contributing to the performance reduction. The results from Collins and Quigg indicate that at temperatures around 900 °C, $M_{23}C_6$ carbides dissolve leaving the grain boundaries free of precipitates [13], which would explain why the elastic modulus and mechanical performance was significantly reduced and the reason for the ductile behaviour when tested.

In general, the WAAM process is thought to partially age alloys in varying amounts dependant on the process used and the metallurgy of the alloy being deposited. This was observed in IN718 by Xu et al. who found that the hardness increase due to the WAAM process is also variable, dependent on the amount of successive heating cycles the material has been subjected to [3]. For example, the WAAM walls produced for this study had roughly the same number of deposited layers, for RE41 this was between 147-153 layers per wall, meaning roughly the same number of successive thermal cycles has occurred during the process. However, only the very first layer has experienced all of these cycles, whereas the very last layer i.e., the top of the WAAM wall, has only experienced one heating cycle. This means that the partial aging effect is more pronounced at the bottom of the WAAM wall, whereas the top of the wall is significantly less aged. This effect was investigated by Xu et al. in a study on maraging steel, in which it was found that the bottom part of the WAAM walls were harder than the top parts. Xu et al. found that the number of precipitates in the bottom part of AD walls were roughly double the number of precipitates found in the top part. With an aging treatment however, the precipitates in the top part of the wall increased to be approximately the same as the bottom part [20]. The location of AD samples extracted for hardness testing in this study was in the centre of each wall, where the WAAM aging effect is roughly half the number of deposited layers. The heat-treatment used in this study was not able to homogenise the material, as it is likely a specifically designed heat-treatment for WAAM RE41 will be required to achieve this.

5.4.3 Fractography

With the largely different performance of AD samples at 760 °C and the suggestion that these samples appear to undergo aging during testing to ‘catch-up’ to the pre-HT specimen, it was not surprising to see the macro fractography show a visible difference in the fracture surfaces at this temperature. The surface of the fractures appear blue in colour. This is useful evidence for the theory that the alloy has undergone a change during testing at 760 °C, which is not entirely surprising given that RE41 is routinely aged around this temperature. What is surprising is the change in appearance even on the macro scale which suggests that this is merely the appearance of an oxide formation.

The fracture surfaces of specimens tested at 1000 °C suggest fractures were very much ductile in nature, due to the distorted cross-sections and ‘hour-glass’ shape. The testing data also showed a clear reduction in elastic modulus of samples tested at this temperature. Again this is consistent with the findings of Greene and Finfrock on IN718, in which it was found that at temperatures of 1264 °C, not hugely removed from 1000 °C, the deformation in the alloy became unacceptable for the application [25]. It is also noticeable that with increasing testing temperature the grain boundaries become much thicker. This was seen in RE41 by Schwartz et al. in a study where RE41 underwent heating cycles which affected the thickness of the grain boundaries and also the susceptibility to the metallographic etchant [10], this was also observed in this study especially 1000 °C tested specimens (Figure 5-16: image AD 8 & HT 8). Specimens tested at RT, 538 and to a lesser extent 760 °C showed signs of more brittle fractures, which is supported by the elongation data that shows only a fraction of the elongation expected compared with wrought data. Furthermore, chevron patterns seen in these specimens add to evidence of brittle type fractures, as the fractography handbook suggests they are indicative of more rapid fracture modes [22].

In Figure 5-17, oxide formation at the grain boundaries of RE41 tested at 1000 °C was observed, the oxide takes a similar shape to that of δ phase commonly seen in IN718, with its acicular needle like shape and its formation in close proximity to potential intermetallic phases, however this is not possible in RE41 due to the lack of Nb needed for its precipitation. Upon investigating the composition using EDS, it was found that the composition retains the distribution of the alloying elements, however, shows an increase in the amount of detected O. This is consistent with the finding of Ungureanu et al. . In their study, RE41 underwent a thermal shock process to understand the effects on the microstructure, and at 1000 °C it was found that with increased thermal shock oxide layers were seen to grow and retain a similar distribution of the alloying elements [26]. Ultimately, the formation of oxide in the samples is consistent with the tensile results, as the elongation of the samples represent only a fraction of the expected elongation from wrought material, indicating that the presence of oxide has affected the ductility of the alloy. Entrapped oxides formed during the welding process would not be possible to dissolve into the matrix during solutionising, due to their extremely high melting point. The low viscosity of Ni alloys makes them particularly susceptible to oxide entrapment, which is also consistent with the findings of Xu et al. in their study on maraging steel, in which oxides were also found to have a strengthening effect on the matrix when dispersed on the hundred-nanometre scale [27]. It appears that controlling the oxygen level below 800 ppm during deposition was not sufficient to prevent oxidisation. In future studies the level should therefore be controlled to a lower concentration to prevent oxide entrapment. Further worked would be required to industrialise this process, this could however include the use of a enclosed environment or the use of a properly controlled trailing shield, such as was developed by Ding et al. [28]. Microscopically in Figure 5-18, fracture surfaces generally exhibited a local stepwise method of fracture with signs of brittle fracture at RT, and secondary cracking was observed at increased testing temperature where fracture surfaces were also oxidised.

5.4.4 High-speed Flight Application

In reference to the introduction of this paper, the intended application of this research is in understanding the high temperature performance of RE41, for highly stressed service in temperatures of 1000+ K for durations of < 1 hour.

In terms of tensile performance, RE41 achieves high stress values at most tested temperatures. However, toward the 1000 °C testing temperature the performance of RE41 decreases somewhat exponentially, illustrating that the alloy has a much better performance definitively at temperatures <1000 °C.

Elastic modulus is another important factor for high-speed flight applications, as components need to retain their shape at service temperatures, a lower deformation during loading is therefore preferred. However, alloys need to retain some ductility to avoid the devastating impacts of brittle type fractures during service. RE41 showed only a fraction of the expected elastic modulus from wrought material. The majority of fractures were brittle in nature, however with increasing temperature the fracture mode tends toward more ductile fractures, with the noted exception of the 760 °C test.

A small amount of intergranular cracking was observed in both AD and HT material. It is hoped that a further mechanical process, introduced during WAAM deposition, will help to alleviate the cracking issues through the relief or residual strain induced by the process. This will be the subject of a future study.

5.5 Conclusion

1. AD WAAM RE41 achieves 58.8 % of the maximum wrought performance. Heat-treating results in a performance increase to 61.4 % and in the alloy being 37 % harder than the minimum wrought values.
2. When tested at 760 °C the performance of AD precipitation-strengthened alloys increases to meet the performance of pre-HT specimens, indicating an in-test aging process.

3. Subjecting RE41 to the standard heat-treatment post-deposition causes the hardness to increase above the minimum wrought values. Which is likely due to the formation of potential tcp phases during heat-treatment, as a result of the segregation of heavier elements during deposition. A specially designed heat-treatment is likely to be required, to properly homogenise the material.
4. Performance and elastic modulus reduces at a 1000 °C testing temperature, potentially due to the dissolution of carbides and presence of undesirable oxide phases at the grain boundaries.
5. The formation of carbide networks and potential intermetallic phases at the grain boundaries are responsible for intergranular cracking observed in both AD and HT material.
6. A solutionising temperature of 1065 °C is not sufficient to dissolve undesirable potential tcp phases in WAAM built RE41.
7. There is a small dilution of the IN718 substrate into the R41 deposition. This could vary depending upon the deposition parameters and should be accounted for when building dissimilar AM/substrate structures.
8. WAAM built RE41 requires additional investigation to increase performance to wrought values and to make the WAAM built material suited to high-speed flight applications.

5.6 References

[1] S.W. Williams, F. Martina, A.C. Addison, J. Ding, G. Pardal, P. Colegrove, Wire + Arc additive manufacturing, Mater. Sci. Technol. 32 (2016) 641–647. https://doi.org/10.1179/1743284715Y.0000000073.

[2] G. Marinelli, F. Martina, S. Ganguly, S. Williams, Development of Wire + Arc additive manufacture for the production of large-scale unalloyed tungsten components, Int. J. Refract. Met. Hard Mater. 82 (2019) 329–335. https://doi.org/10.1016/j.ijrmhm.2019.05.009.

[3] X. Xu, S. Ganguly, J. Ding, C.E. Seow, S. Williams, Enhancing mechanical properties of wire + arc additively manufactured INCONEL 718 superalloy through in-process thermomechanical processing, Mater. Des. 160 (2018)

1042–1051. https://doi.org/10.1016/j.matdes.2018.10.038.

[4] Battelle Memorial Institute, Heat-Resistant Alloys, in: Met. Mater. Prop. Dev. Stand., Battelle Memorial Institute, 2017. https://app.knovel.com/hotlink/pdf/id:kt00CX2NX1/metallic-materials-properties/metallic-m-mechanical.

[5] G.J. Wile, Superalloys for Aerospace Application, Jom. 15 (1963) 645–647. https://doi.org/10.1007/bf03397242.

[6] J. Li, H.M. Wang, H.B. Tang, Effect of heat treatment on microstructure and mechanical properties of laser melting deposited Ni-base superalloy Rene’41, Mater. Sci. Eng. A. 550 (2012) 97–102. https://doi.org/10.1016/j.msea.2012.04.037.

[7] J. Li, H.M. Wang, Microstructure and mechanical properties of rapid directionally solidified Ni-base superalloy Rene’41 by laser melting deposition manufacturing, Mater. Sci. Eng. A. 527 (2010) 4823–4829. https://doi.org/10.1016/j.msea.2010.04.062.

[8] S.E. Atabay, O. Sanchez-Mata, J.A. Muñiz-Lerma, R. Gauvin, M. Brochu, Microstructure and mechanical properties of rene 41 alloy manufactured by laser powder bed fusion, Mater. Sci. Eng. A. 773 (2020) 1–10. https://doi.org/10.1016/j.msea.2019.138849.

[9] M.J. Donachie, S.J. Donachie, Understanding Superalloy Metallurgy, in: Superalloys - A Tech. Guid., 2nd ed., ASM International, 2002: pp. 25–39. https://doi.org/10.31399/asm.tb.stg2.t61280025.

[10] M. Schwartz, R. Ciocoiu, D. Gheorghe, G. Jula, I. Ciucă, Preliminary research for using Rene 41 in confectioning extrusion dies, Mater. Characterisation VII. 1 (2015) 95–106. https://doi.org/10.2495/mc150091.

[11] M. Kaufman, Control of Phases and Mechanical Properties in Nickel-base Alloys of Rene 41 Type, Trans. Metall. Soc. AIME. 227 (1963) 405.

[12] L.A. Weisenberg, R.J. Morris, How to Fabricate Rene 41, Met. Prog. 78

(1960) 70–74.

[13] H.E. Collins, R.J. Quigg, Carbide and Intermetallic Instability in Advanced Nickel-base Superalloys, Am. Soc. Met. Trans. Q. 61 (1968) 139–148.

[14] C.E. Seow, H.E. Coules, G. Wu, R.H.U. Khan, X. Xu, S. Williams, Wire + Arc Additively Manufactured Inconel 718: Effect of post-deposition heat treatments on microstructure and tensile properties, Mater. Des. 183 (2019) 108157. https://doi.org/10.1016/j.matdes.2019.108157.

[15] ASM Committee of Metallography of Heat-Resisting Alloys, Microstructures of Wrought Heat-Resisting Alloys, in: ASM Met. Handb. Vol. 7 Atlas Microstruct. Ind. Alloy., 8th ed., ASM International, 1972: pp. 165–192.

[16] J.E. Franklin, W.F. Savage, Stress Relaxation and Strain-Age Cracking in Rene 41 Weldments, Weld. J. 53 (1974) 380–387. http://aws.perusion.com/wj/supplement/WJ_1974_09_s380.pdf.

[17] M.J. Donachie, S.J. Donachie, Selection of Superalloys, in: Superalloys - A Tech. Guid., 2nd ed., ASM International, 2002: pp. 11–24. https://app.knovel.com/hotlink/pdf/id:kt008GQQU1/superalloys-technical/superalloy-forms.

[18] Rolled Alloys, Data Sheet Rene 41, (2011). http://www.rolledalloys.com/alloys/cobalt-alloys/rene-41/en/ (accessed July 5, 2022).

[19] N. Parveen, G.V.S. Murthy, Determination of elastic modulus in nickel alloy from ultrasonic measurements, Bull. Mater. Sci. 34 (2011) 323–326. https://doi.org/10.1007/s12034-011-0070-z.

[20] X. Xu, S. Ganguly, J. Ding, S. Guo, S. Williams, F. Martina, Microstructural evolution and mechanical properties of maraging steel produced by wire + arc additive manufacture process, Mater. Charact. 143 (2018) 152–162. https://doi.org/10.1016/j.matchar.2017.12.002.

[21] W.S. James, S. Ganguly, G. Pardal, Rene 41 Tensile Data, Cranf. Online

Res. Data. (2022) Dataset. https://doi.org/10.17862/cranfield.rd.20142737.

[22] ASM Handbook Committee, Visual Examination and Light Microscopy, in: G.F. Vander Voort (Ed.), Fractography, 8th ed., ASM International, 1987: pp. 91–165. https://doi.org/10.31399/asm.hb.v12.a0001834.

[23] J.F. Wang, Q.J. Sun, H. Wang, J.P. Liu, J.C. Feng, Effect of location on microstructure and mechanical properties of additive layer manufactured Inconel 625 using gas tungsten arc welding, Mater. Sci. Eng. A. 676 (2016) 395–405. https://doi.org/10.1016/j.msea.2016.09.015.

[24] X. Xu, J. Ding, S. Ganguly, S. Williams, Investigation of process factors affecting mechanical properties of INCONEL 718 superalloy in wire + arc additive manufacture process, J. Mater. Process. Technol. 265 (2019) 201–209. https://doi.org/10.1016/j.jmatprotec.2018.10.023.

[25] G.A. Greene, C.C. Finfrock, Oxidation of inconel 718 in air at high temperatures, Oxid. Met. 55 (2001) 505–521. https://doi.org/10.1023/a:1010359815550.

[26] E. Ungureanu, D.C. Anghel, D. Negrea, A.G. Plaiau, V. Rizea, M.M. Dicu, C.M. Ducu, M. Abrudeanu, Influence of thermal shocks at high temperatures on microstructure and hardness of RENE 41 alloy, in: IOP Conf. Ser. Mater. Sci. Eng., 2019. https://doi.org/10.1088/1757-899X/564/1/012046.

[27] X. Xu, J. Ding, S. Ganguly, C. Diao, S. Williams, Oxide accumulation effects on wire + arc layer-by-layer additive manufacture process, J. Mater. Process. Technol. 252 (2018) 739–750. https://doi.org/10.1016/j.jmatprotec.2017.10.030.

[28] J. Ding, P. Colegrove, F. Martina, S. Williams, R. Wiktorowicz, M.R. Palt, Development of a laminar flow local shielding device for wire + arc additive manufacture, J. Mater. Process. Technol. 226 (2015) 99–105. https://doi.org/10.1016/j.jmatprotec.2015.07.005.

6 HIGH TEMPERATURE FAILURE AND MICROSTRUCTURAL INVESTIGATION OF ADDITIVE MANUFACTURED HAYNES 188

As in the previous chapter, this chapter on H188 represents the bulk of data collected before the final down selection of a single alloy. The data presented here includes high temperature performance data and an examination of microstructural features both before and after fracture.

Abstract

In developing a wire-arc directed energy deposition (DED) process for Haynes 188, a cobalt-based creep resistant superalloy. Material was analysed for mechanical properties and microstructural features, following fabrication. Specimens were analysed in both as deposited and solutionised conditions, following an industry standard solutionising procedure. Tensile testing was conducted at four testing temperatures between room-temperature – 1000 °C. Large columnar grains were observed in the microstructure, as well as segregation of both chromium and tungsten which formed as intermetallic phases. These intermetallic phases were identified as likely causing changes in the alloy ductility and were observed to dissolute when tested at 1000 °C. Solutionised specimens achieved a greater UTS and YS performance, although saw a reduction in ductility as a result. The overall UTS performance of wire-arc DED fabricated Haynes 188 fell short of the wrought performance, however YS more closely resembled wrought values. Precipitation of intermetallic phases affecting ductility are thought to be responsible for the difference in performance.

Keywords: Additive Manufacturing, Direct energy deposition, Fractography, Microstructure, Haynes 188

6.1 Introduction

Haynes 188 (H188) is a cobalt-based, nickel, chromium superalloy, commonly used in high service temperature applications. H188 has excellent material properties, including strength, ductility and corrosion resistance at temperatures exceeding 1000 °C. Sponaugle stated that H188 was developed for and has seen application in hot components of gas turbines, such as afterburner components and allowed designers to increase engine temperatures for additional performance [1]. Halford et al. summarised NASA's findings and the administrations previous use of the alloy in main engine components of NASA's space shuttles [2]. The development of Co-based alloys was impacted as a result of the 'cobalt crisis' in the 1970s which affected supplies of Co coming from the African continent, which Klarstrom said resulted in a move away from Co-based alloys in preference to Ni-based alloys [3]. However Co-base superalloys offer high-temperature strength, corrosion and wear resistance, which can still outperform more modern Ni-based alloys at high temperature.

There is very little published research on additive manufacturing (AM) for H188, and even less so for its fabrication using a directed energy deposition (DED) process such as wire + arc additive manufacturing (WAAM), a wire-arc DED process. Moradi et al. deposited a similar Co-based alloy, Stellite 6, which was deposited using a laser metal deposition (LMD) process, LMD uses blown power as a feedstock and a laser as the heat source. Moradi et al. found a significant cracking issue with LMD Stellite 6 confirming the previous reports [4]. In a similar process Gaytan et al. deposited a Co-based alloy conforming to ASTM F75, using electron beam melting (EBM), which uses a gravity-fed powder and rake system to create layers of the feedstock, which is then melted by a scanning electron beam in a layer-by-layer process to form parts [5].

The WAAM process has several benefits and drawbacks compared to powder-based AM. The wire feedstock used in WAAM is often much cheaper to purchase than metallic powder and feedstock wastage in WAAM is much reduced compared to powder-bed processes. Koike et al. found that material loss can be as much as 25 % in blown-powder type setups [6]. WAAM is also suited to the manufacture of components with a much larger range in size. With its high deposition rates WAAM can be used to build large components which would not be possible using powder-bed type process. Wang et al. (2017) manufactured and tested specimens of Inconel 718 built using a powder bed process and achieved material properties much closer to that of the wrought alloy than Xu et al achieved using WAAM [7][8]. Xu et al found larger long columnar grains typical of wire-arc DED and surmised that the larger grain structure was adversely affecting the performance. The difference observed between the two studies is likely due to the finer grain structure produced by powder-bed AM being more suited to the precipitation strengthened mechanism of Inconel 718. This larger grain structure issue with WAAM built parts should not have much significance with H188 deposited parts due to its differing strengthen mechanism.

James et al. deposited H188 using wire-arc DED as part of a previous study to investigate the as deposited room-temperature properties. James et al. found typical large columnar grains similar to those observed in Ni-based alloys. They also found that H188 performed better in relation to its wrought strength compared to precipitation strengthened alloys Inconel 718 and Rene 41. [9]

6.1.1 Physical Metallurgy

The high strength, high temperature alloys book published by The International Nickel Company describes the effect different alloying elements have on material properties. Ni-based superalloys containing Al and Ti are generally indicates that the alloy is strengthened through precipitation hardening. The Cr content of these alloys provides oxidisation and sulfidation resistance as well as contributing to the strength. Heavier elements such as Nb, Mo, W and Ta provide solid solution strengthening within the matrix. Bo and Zi can be included to increase high temperature creep and to improve ductility. The addition of Co has the effect of improving workability and increasing high temperature performance. [10]

As H188 is by all practical methods not hardenable, except through cold working. The alloy matrix lacks Al and Ti, and its strength is mainly derived from its solid-solution-strengthened fcc matrix. Herchenroeder investigated the aging characteristics of H188. The alloy has a primary carbide (M_6C) associated with a Lanthanum rich compound. When aged at 760 °C for 200 hrs a secondary carbide ($M_{23}C_6$) is known to form at the grain boundaries with A_2B type Laves phase (Co_2W) and causes increased hardness and reduced ductility. Longer term exposure to temperatures between 760 - 870 °C can precipitate enough Laves to embrittle the alloy. [11] Klarstrom noted that γ' and γ'' phases are possible to see in Co-based alloys containing Mo and Ta, but as these are not present in H188 they are not observed [3]. Co-based alloys are generally seen to be not as resistant to oxidisation as Ni-based alloys, which is true for the most part, however this problem was resolved in H188 with the addition of 0.03 - 0.15 wt.% La. According to Herchenroeder et al. the presence of La in the matrix is largely responsible for the oxidisation resistance of H188, the La content favours the formation of the protective Cr-oxide scale, Cr_2O_3, which prevents the depletion of Cr through CrO_3 evaporation. [12]

Herchenroeder et al. describes the physical metallurgy of H188 and the formable phases at both a range of temperatures and aging times ranging from 10 – 10,000 hrs of exposure. The primary carbide M_6C forms at high temperatures and is stable up until approx. 1315 °C. Prolonged exposure to temperatures above 1150 °C causes substantial solutionising of M_6C. Secondary M_6C forms between 870 – 1175 °C during the first 100 hours of exposure. The secondary carbide $M_{23}C_6$ $(Cr,Co,Ni)_{23}C_6$ precipitates between 650 – 925 °C, and is mainly formed at grain boundaries, twins, and other crystallographic faults. After extensive exposure, beyond the scope of this research, M_6C is replaced mainly by $M_{23}C_6$ and A_2B type Laves, after it is dissolved into the matrix. Aging at 540 °C for 6000 hours precipitates minor amounts of $M_{23}C_6$ along grain boundaries but this does not adversely affect performance. [12]

Laves phase in H188 is rich in Co and W and is isomorphous with Fe_2W. Herchenroeder et al. found that a small amount of Laves phase can form after aging between 928 – 980 °C for 3000 hours. However, it was found that aging beyond this time within the temperature range dissolves Laves. The presence of Laves phase is associated with reduced ductility and dissolution restores ductility. Aging between 760 – 870 °C promotes precipitation of Laves and carbide reactions which can cause a reduction in tensile elongation. It is also noted that no hexagonal close-packed (hcp) phases are observed in the alloy even after >6000 hours exposure to 425 – 705 °C. Aging H188 below 540 °C has little effect on precipitation of phases or on the performance. [12]

6.2 Method

6.2.1 Manufacturing Process

A symmetrical PTA WAAM process was used to produce samples for analysis from a commercially available 1.14 mm diameter H188 wire. The WAAM system consisted of: a water-cooled plasma welding torch and wire feeder mounted to a FANUC six-axis robotic arm, a part-rotator, and a gas enclosure. The enclosure provided an inert argon atmosphere for deposition, where the concentration of oxygen was controlled below 800 ppm with the use of an oxygen analyser. The process used was symmetrical, meaning that material was deposited on both sides of the substate plate, the main advantages of which Williams et al. says includes increased productivity and a reduction in residual stress [13]. Two wall structures measuring 350 x 110 x ~8 mm were deposited onto both sides of an Inconel 718 substrate plate, using an arc current of 180 A, a wire-feed speed of 2.0 m/min, a torch travel speed of 0.36 m/min, a torch to work distance of 8 mm and an inter-pass temperature of 170 °C after approx. 3 mins of cooling time. A diagram of the set-up is shown in Figure 6-1.

After deposition samples were extracted and underwent the recommended heat-treatment for achieving maximum tensile performance. The heat-treatment consisted of solutionising at 1100 °C for 2 hours, after which the material was quenched in water.

Once heat-treated several specimens underwent tensile testing at RT, 538, 760, and 1000 °C. Specimens were tested to the ASTM standard E8(M) for RT testing and E21 for high temperatures. Testing used a strain rate of 0.005 min^{-1} until the onset of plastic deformation and thereafter a crosshead speed of 1.6 mm/min was used until failure. The fracture surfaces were carefully preserved for analysis.

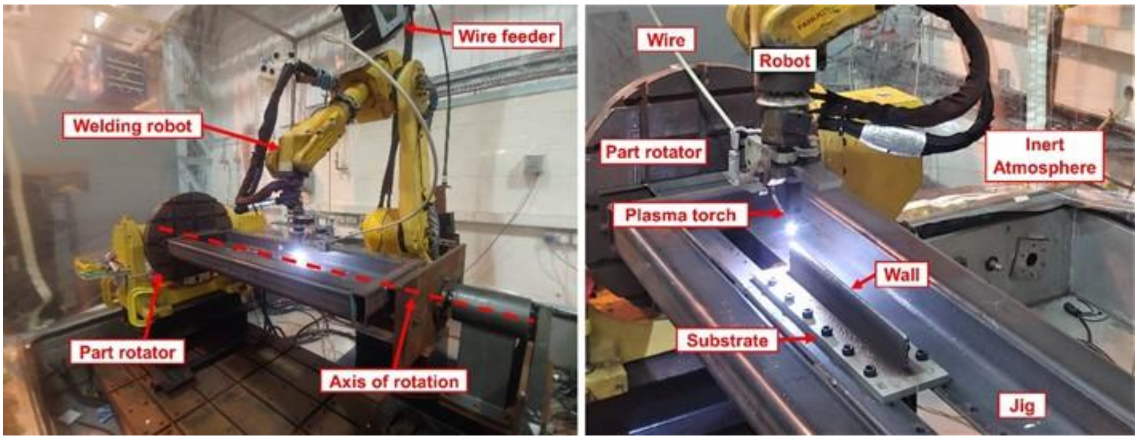

Figure 6-1 Experimental WAAM set-up.

6.2.2 Composition

The wire feedstock was provided by the manufacturer, Haynes International, with a product certificate confirming the material conforms to the requirements for ASM 5801. The composition of the feedstock is given Table 6-1.

Table 6-1 Composition of H188 wire (wt.%)

Co	Ni	Cr	W	Fe	Mn	Si	C	La	P	B	S
Bal.	22.90	22.20	13.90	2.65	0.81	0.22	0.107	0.060	0.011	0.003	<0.002

6.2.3 Metallographic Preparation and Analysis

The WAAM walls were cut from the substrate plates and samples were extracted through both the wall height and length. Cross-sections were extracted and prepared for metallographic analysis following a procedure consisting of mounting then grinding and polishing successively, followed by etching. Samples were etched to reveal the microstructure using 5 g oxalic acid, 95 ml HCl. Electrolytic 6 V DC using a carbon cathode and a stainless anode probe, for 1-2 sec, as suggested by Middleton et al. [14].

The microstructure was also analysed, using a Tescan VEGA 3 scanning electron microscope (SEM), and optically using a Leica DM 2700M Microscope. To determine composition the VEGA 3 SEM was equipped with an Oxford Instruments X-Max 20 mm energy-dispersive spectrometry (EDS) detector. To determine the presence of lighter elements within the matrix a Tescan Solaris X SEM was equipped with xenon plasma focused ion beam (FIB) and a TOFWERK time-of-flight secondary ion mass spectrometer (TOFSIMS).

The specimens were extracted in various locations across the WAAM walls. From a total of four WAAM walls built in pairs three walls were utilised for testing. After testing, the fracture surface of specimens in each category and condition were observed. The axis by which samples were observed are indicated going forwards with reference to the build direction (BD), the through-thickness (TT) and the wall axis (WA).

6.2.4 Mechanical Testing

Samples were extracted from the WAAM walls and machined into coupons in the WA orientation as previous studies have shown this to be the least effective orientation for performance. The locations and orientations of extracted coupons are visualised in Figure 6-4. The room temperature (RT) coupon, conforming to ASTM E8(M) sub-size specification, is shown in Figure 6-2, and the elevated temperature (538-1000 °C) coupon is shown in Figure 6-3. Note that the elevated temperature coupon has been elongated to allow for a clam shell furnace to be attached during testing. Three coupons were tested for each testing condition both in AD and HT condition. Samples were tested at RT, 538, 760, and 1000 °C, using an Instron 8801 Servo hydraulic Universal Testing System and tested to failure using the ASTM E8(M) specification for RT testing and ASTM E21 for high temperature testing. Tensile tests used a strain rate of 0.005 min^{-1} until the onset of plastic deformation and thereafter a crosshead speed of 1.6 mm/min. Prior to the start of testing, high temperature specimens were held for 30 mins at the testing temperature. Specimens were extracted from a variety of locations on the WAAM wall to minimise variation in results due to the WAAM aging effect. The fracture surfaces were carefully preserved for analysis.

The alloys in both AD and HT conditions also underwent microhardness testing using a Zwick/Roell hardness tester under a load of 500 g and holding time of 15 s.

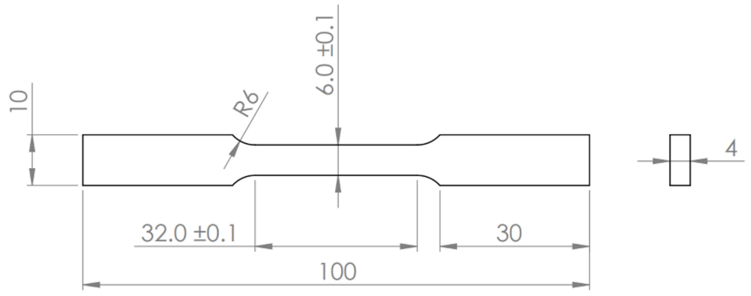

Figure 6-2 RT Tensile testing coupon. (Dimensions in mm).

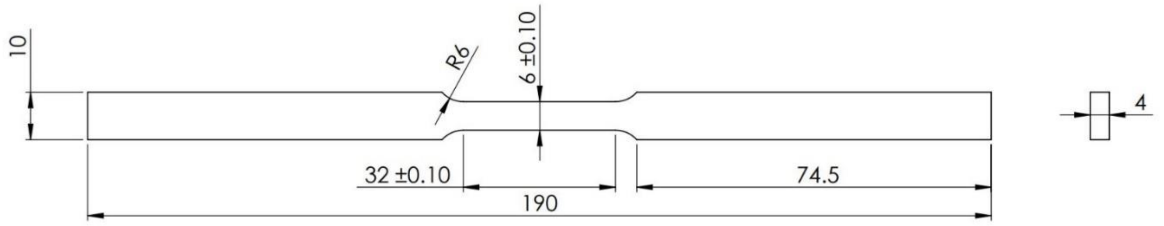

Figure 6-3 Elevated temperature testing coupon. (Dimensions in mm).

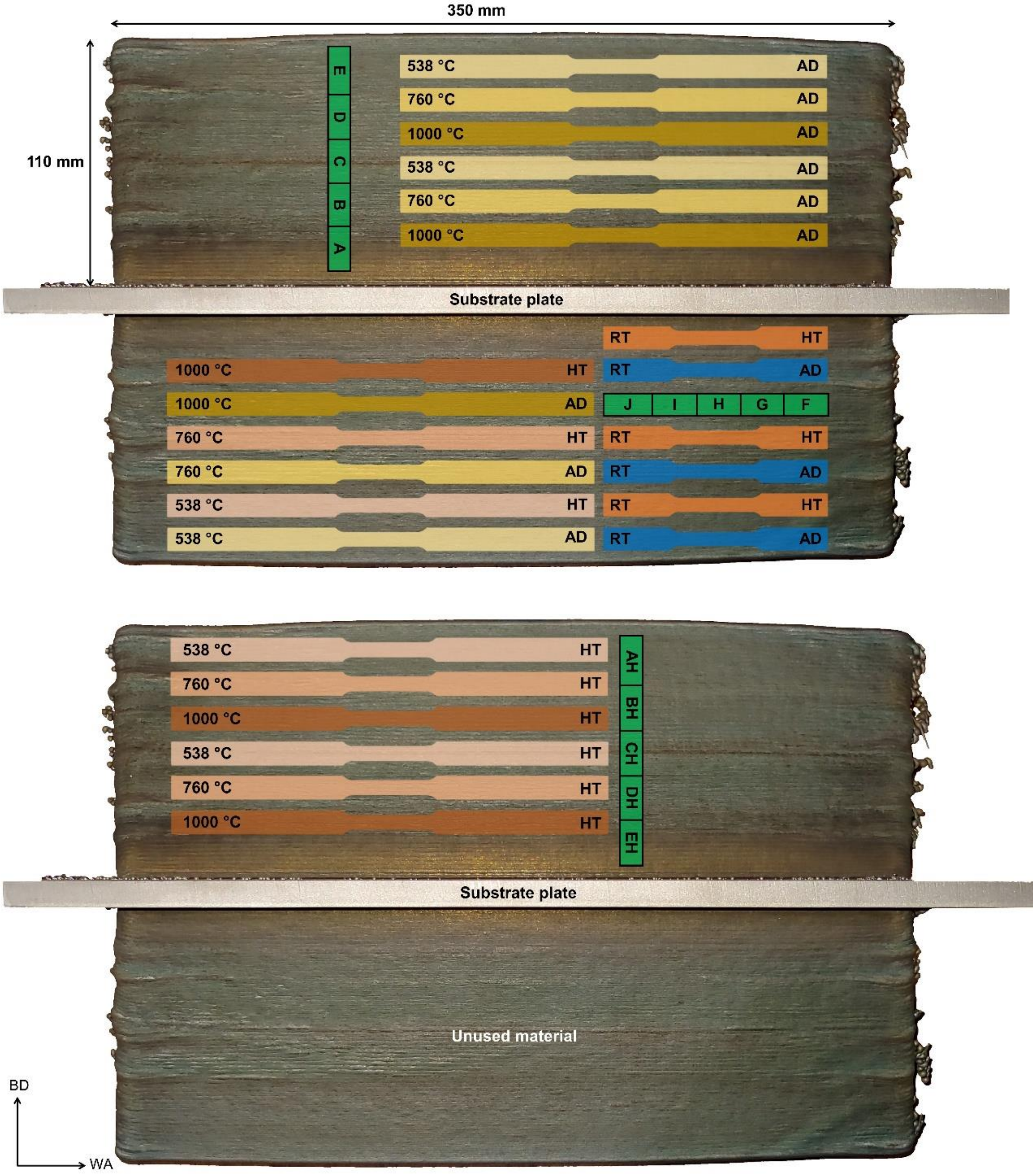

Figure 6-4 Location of extracted samples from WAAM walls. Green areas indicate location of metallographic samples. Temperature given on the left of the coupon indicates testing temperature and on the right the condition AD or HT. Metallographic samples AH-EH are HT whereas single letter A-J are AD.

6.3 Results & Discussion

6.3.1 Macrostructure

The macrostructure of WAAM deposited H188 is not dissimilar to the structure of Inconel 718 observed by James et al. and Xu et al., deposited using a similar process [9][8]. The structure, shown in Figure 6-5, consists of large columnar grains which grow along the height of the wall in the built direction (BD). The remelting lines, which are also observed in the macrostructure, appear to have no effect on the formation of the grains.

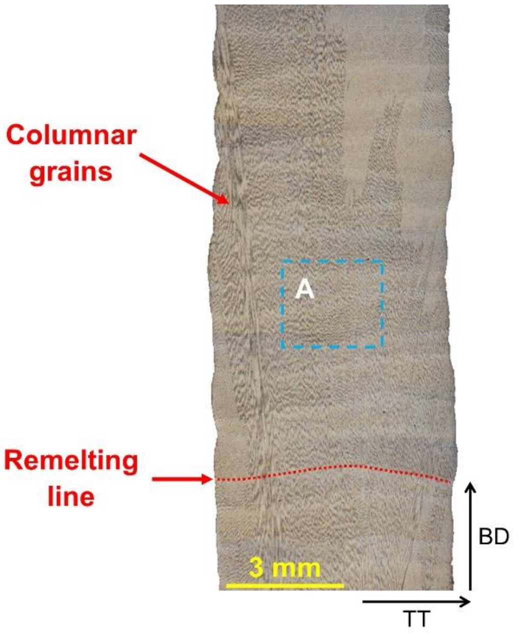

Figure 6-5 Macrostructure observed in AD specimen. Area A presented in Figure 6-6 and Figure 6-7.

6.3.2 Microstructure

A comparison between AD and HT material is presented in Figure 6-6. Potential phases and carbides in this section going forward have been suggested based on EDS composition and a visual comparison using an atlas of Microstructures [15]. Heat-treating the alloy had a clear darkening and thickening effect surrounding precipitates at the grain boundaries and within the matrix compared to AD material. The smaller grain boundary precipitates are thought to be carbides, whereas elsewhere in the matrix brighter coloured precipitates are thought to be Laves (Co_2W) intermetallic phase, which would be supported by spectrum A and B in Table 5-2. It is also noted that potential M_6C carbides seen outside of the grain boundaries are surrounded by smaller darker phases which could be indicative of primary M_6C decomposing in secondary $M_{23}C_6$. Figure 6-8 shows the microstructure in the transverse plane, i.e., looking through the built direction, where precipitates can be seen to form in the interdendritic regions. In some cases (seen in Figure 6-8) areas where $M_{23}C_6$ is observed forming a ring, presumably around what was previously M_6C carbides which has decomposed, leaving only the secondary carbide remaining. Further investigation is required to confirm this.

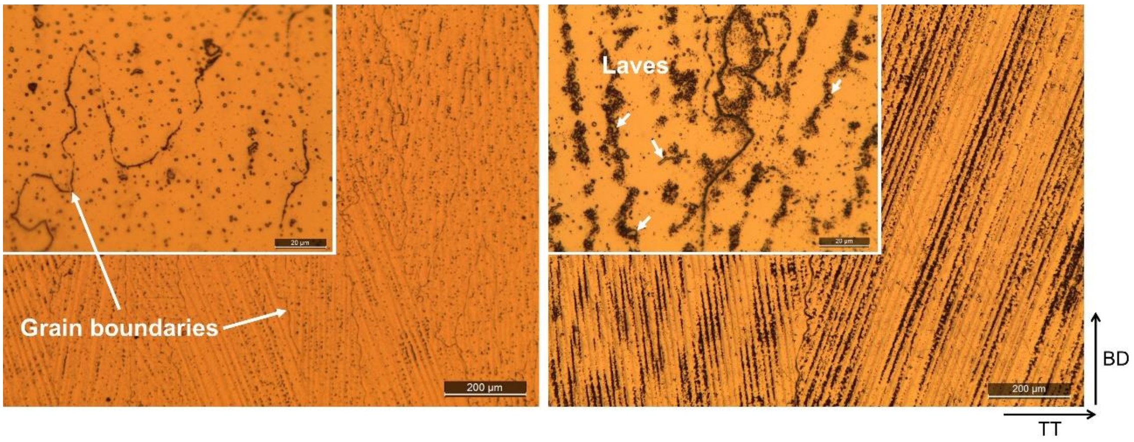

Figure 6-6 Optical observations, AD (left) & HT (right).

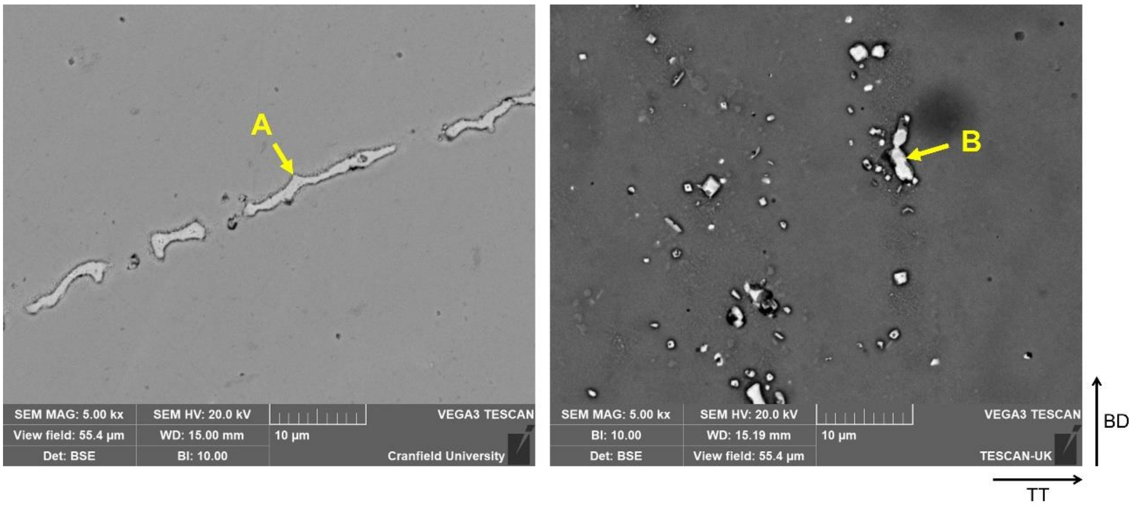

Figure 6-7 BSE Images of AD (left) & HT (right) samples.

Table 6-2 EDS composition of areas marked in Figure 6-7. (%at)

Spectrum Label	C	Cr	Mn	Fe	Co	Ni	W
A	53.65	18.33		0.76	12.62	6.29	7.53
B		38.91	0.91	1.95	28.16	16.57	12.56

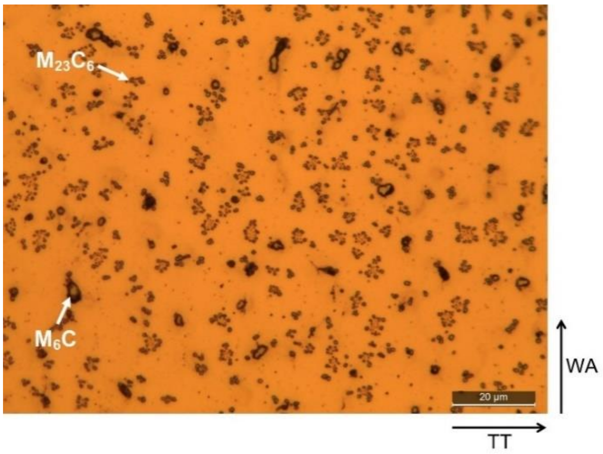

Figure 6-8 AD microstructure viewed in transverse (WA-TT) plane. Showing decomposition of M_6C to $M_{23}C_6$.

6.3.3 Mechanical Testing

The results of tensile testing are given in Table 6-3, where wrought (Wro) values from the Superalloys book by Donachie and Donachie [16], are presented alongside results for AD and HT samples. The data shows that even after heat-treating the WAAM material has not regained its wrought strength.

Graphs comparing the performance across the tested range of temperatures is shown in Figure 6-9. AD material achieved an average of 63.7 % of the wrought maximum, and when heat-treated the performance increases to an average of 72.8 %.

Wrought RT hardness is provided in the manufacturers data sheet as a minimum of 248 HV [17]. When tested the AD and HT material had a hardness of 276 HV and 288 HV respectively. The reason for the small increase in hardness after both depositing via WAAM and again after solutionising is thought to be insignificant, although could be due to the formation of carbides such as M_6C, which Herchenroeder et al. report increase in abundance with exposure to temperature, with intermetallic phases such as Laves reported to be more abundant with significant exposure [12].

Table 6-3 Tensile results comparing Wrought data (Wro) with AD and HT material from RT-1000 °C.

Temperature (°C)	UTS (MPa)			0.2 % YS (MPa)			Elastic Modulus E (GPa)		
	Wro	AD	HT	Wro	AD	HT	Wro	AD	HT
RT	960	694 ±36	811 ±24	485	428 ±3	382 ±6	207	171 ±5	153 ±14
538	740	414 ±17	488 ±24	305	267 ±10	236 ±2	192	131 ±2	120 ±12
760	635	398 ±12	431 ±13	290	246 ±5	206 ±5	175	113 ±5	101 ±11
1000		167 ±8	147 ±2		122 ±3	97 ±2		75 ±5	89 ±6

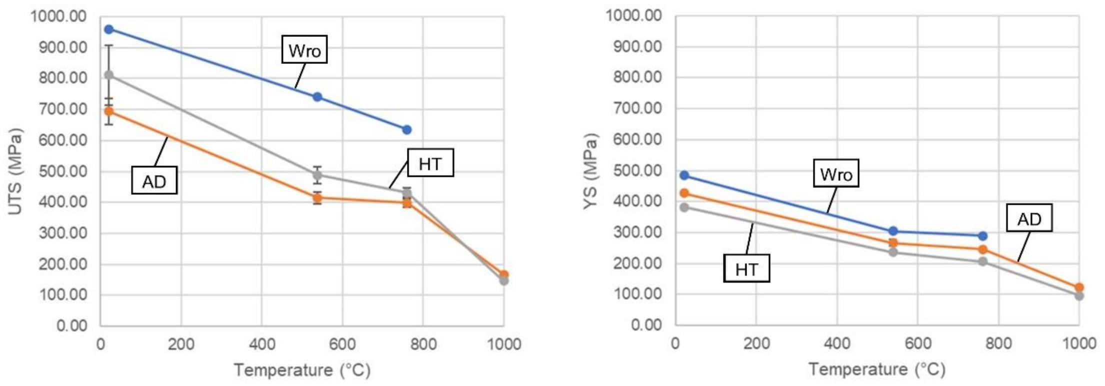

Figure 6-9 Graphical representation of data presented in Table 6-3. UTS (left) & 0.2 % YS (right).

6.3.4 Fracture surfaces

The fracture surfaces give an insight into not only the failure mechanism, but also the effect exposure to the testing temperature has had on the microstructure of the alloy.

The macrographs presented in Figure 6-10 show a progressive move with increasing testing temperature to more ductile behaviour, seen in the deformation of the cross-section, which is confirmed by the decrease in elastic modulus (Table 6-3). The woody, fibrous appearance of the fracture surface particularly in the RT samples and to a lesser extent in 538 °C samples, suggests that the fractures are intergranular. The fracture surface of the 760 °C is much cleaner and comparatively free of texture compared to the other specimens, at this temperature the fracture surface also appears blue in colour, which could suggest the alloy is susceptible to oxidisation at this temperature. At 1000 °C the fracture surface suggests a ductile shearing type failure across the grain planes, with cracks appearing across several longitudinal planes. The difference in fracture method is very clear for samples tested at 1000 °C and suggests a decrease in resistance to slip between grains.

Looking at Figure 6-11 it can be seen how the precipitation of secondary phases changes, at RT grain boundaries are visible as well as precipitation in the matrix. When the alloy is tested at 538 °C there is much greater visibility of the dendritic structure with the larger dark coloured phases forming interdendritically. At 760 °C these phases visibly start to decompose and following this at the 1000 °C testing temperature these secondary phases are all but dissolved into the matrix. The fact that the secondary phases have dissolved when exposed to 1000 °C goes a long way to explain the large reduction in elastic modulus. Although the alloy is not primarily precipitation strengthened, H188 is affected by reduced elongation when Laves phases and carbides are found [12], as discussed in the introduction. The dissolution of these phases is obvious in the micrographs of the specimens tested at 1000 °C (Figure 6-11: AD 11 & AD 12) and confirms the literature findings that the dissolution of these phases restores H188's ductility and gives an explanation for the visible difference in fracture method seen in Figure 6-10.

An EDS analysis of the phases observed in the 760 °C tested specimens which can be seen in the SE images in Figure 6-12, the EDS composition of the phases labelled are given in Table 6-4. A large segregation of Cr and W was identified for spectrum C, as well as the depletion of Ni and Co for this phase. Potentially this phase is a complex intermetallic, and could be Laves phase (Co_2W), although the composition doesn't precisely match the formula. The shape of this phase being an irregular shape, elongated, observed after high temperature exposure, does however, match the description of Laves described in the 'Superalloys – A technical guide' book; Laves is common in alloys with a high amount of W [18].

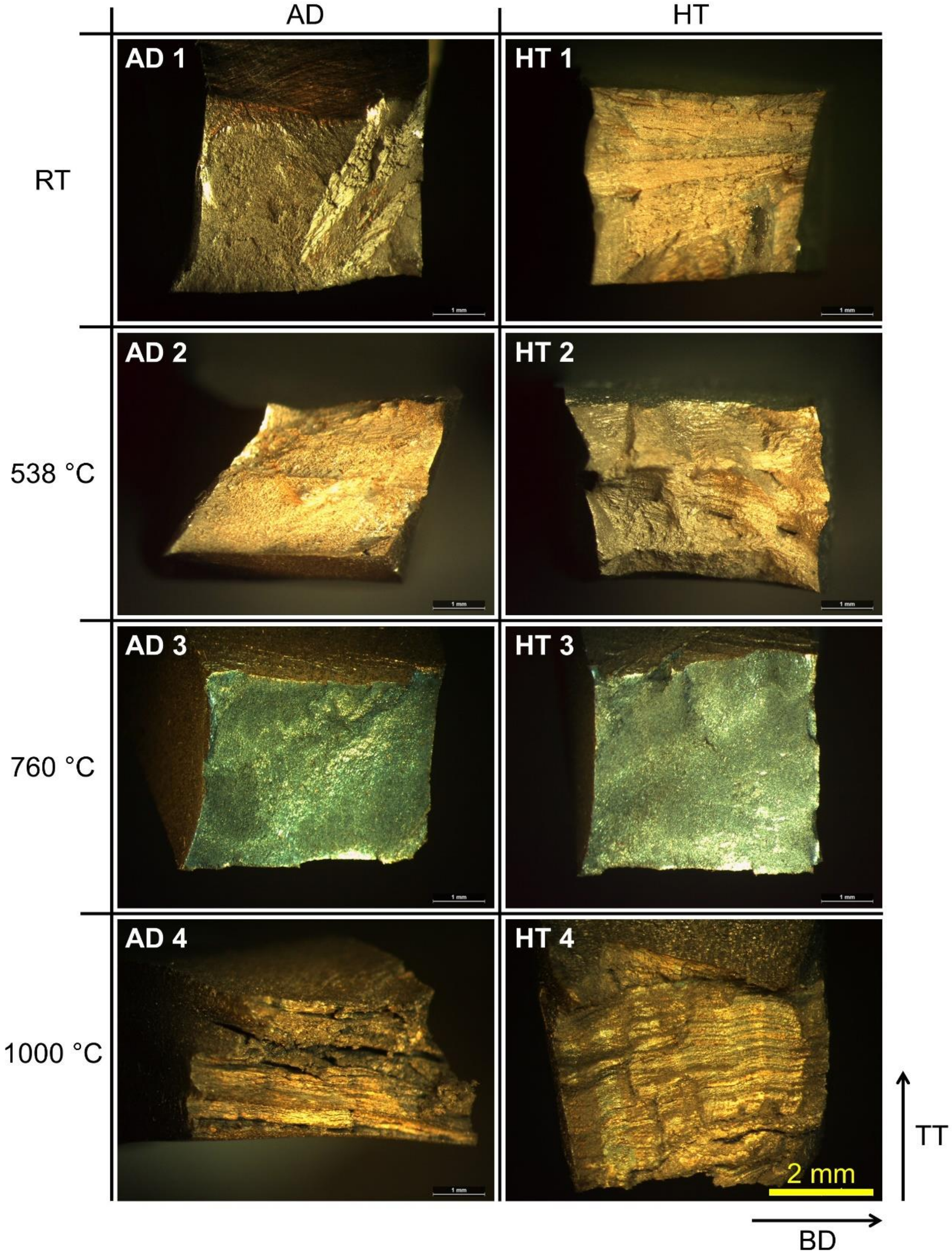

Figure 6-10 AD & HT macro fractographic images of fracture surfaces.

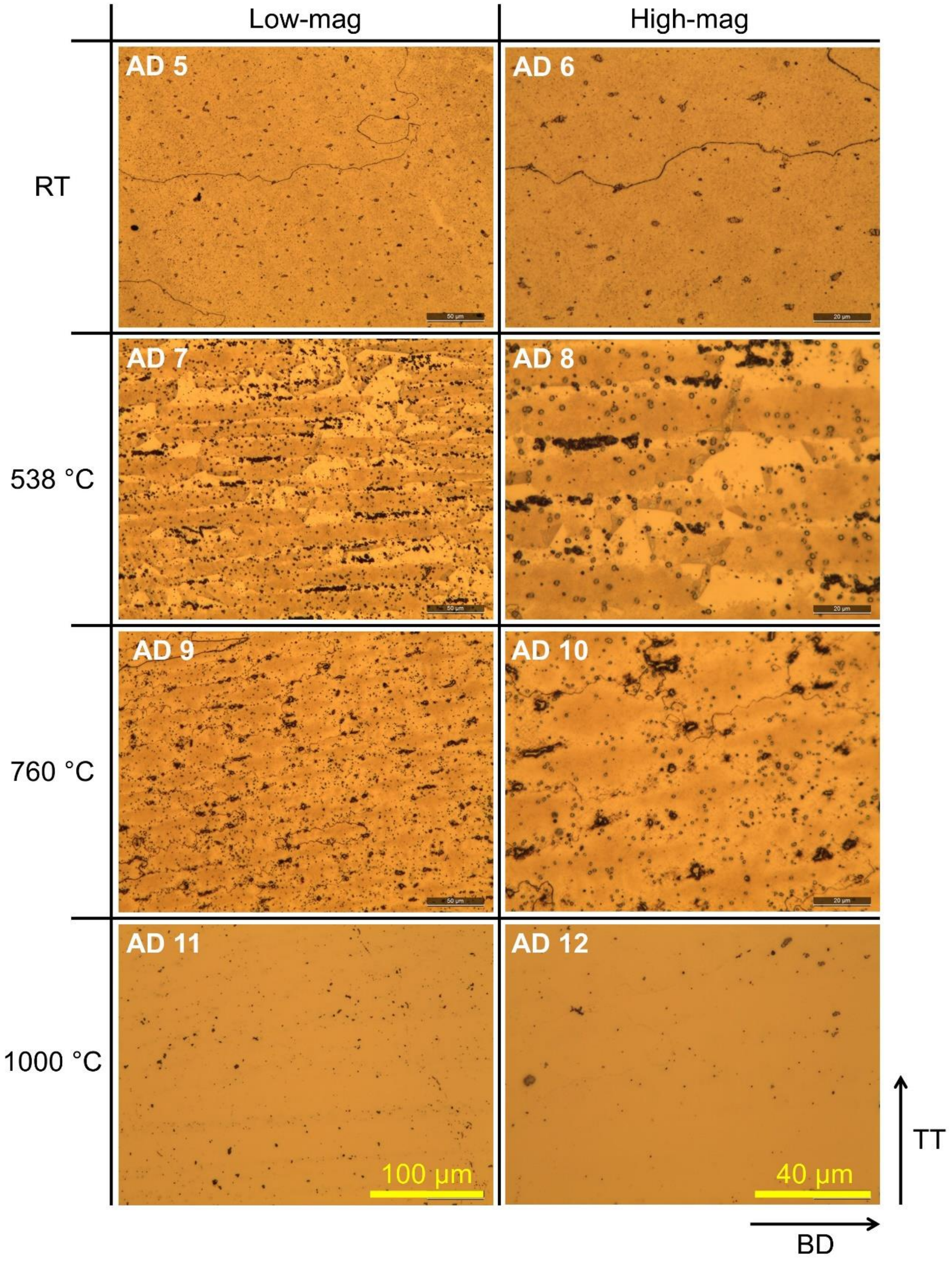

Figure 6-11 Microstructure of AD specimens directly behind fracture surface. Lower magnification (left), higher magnification (right).

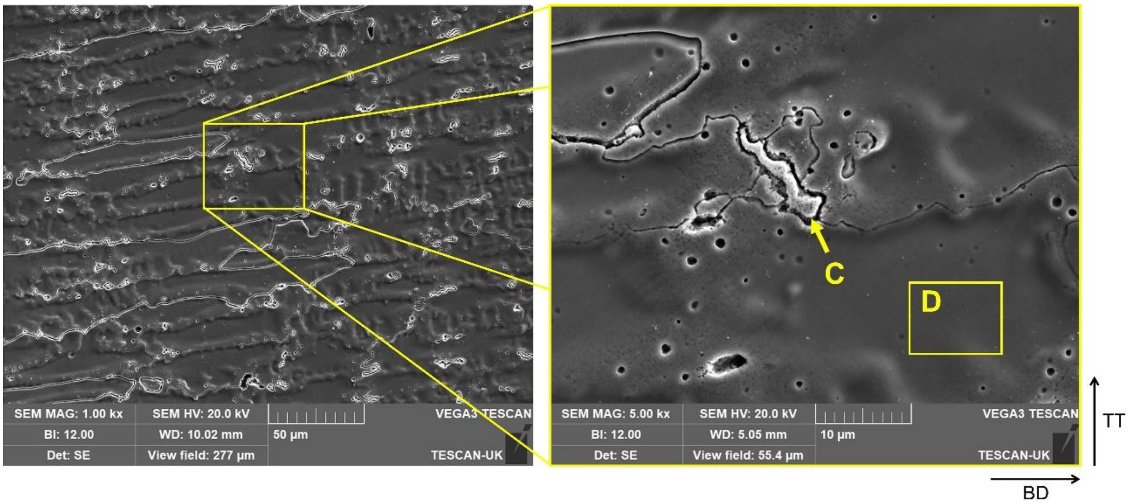

Figure 6-12 SEM images of phases found in 760 °C tested specimen.

Table 6-4 EDS composition of areas marked in Figure 6-12. (%at)

Spectrum Label	C	Cr	Mn	Fe	Co	Ni	W
C		52.29	0.89	1.18	20.23	9.61	15.80
D		26.37	0.83	2.77	40.36	24.96	4.72

6.4 Conclusion

1. Wire arc DED is capable of processing H188.
2. UTS of wire arc DED fabricated H188 does not meet the performance of the wrought alloy, YS more closely resembles the performance of the wrought alloy, precipitation of phases affecting ductility are thought to be responsible for the shortfall in performance, however further research is required to confirm.
3. Although H188 is reported as not age hardenable, results found an increase of precipitation of phases post heat-treatment.
4. Wire arc DED processed H188 experiences segregation of W and Cr, in complex intermetallic phases, and precipitation increases after a standard solutionising process.

5. Precipitation is shown to be mostly solutionised in tensile specimens tested at 1000 °C, and dissolution of the phases is thought to be responsible for an increase in ductility when tested at this temperature.

6.5 References

[1] C. Sponaugle, History of Haynes International, Inc., Pittsburgh Eng. (2000) 7–9. http://www.titanmf.com/wp-content/uploads/docs/Hastelloy-History-of-Haynes-Intl-Haynes-Intl.pdf.

[2] G.R. Halford, J.F. Saltsman, S. Kalluri, High temperature fatigue behavior of Haynes 188, in: Adv. Earth-to-Orbit Propuls. Technol. Conf., NASA, Marshall Space Flight Center, Huntsville, AL, 1988: pp. 497–509. https://doi.org/19900019326.

[3] D.L. Klarstrom, Wrought cobalt- base superalloys, J. Mater. Eng. Perform. 2 (1993) 523–530. https://doi.org/10.1007/BF02661736.

[4] M. Moradi, A. Ashoori, A. Hasani, Additive manufacturing of stellite 6 superalloy by direct laser metal deposition – Part 1: Effects of laser power and focal plane position, Opt. Laser Technol. 131 (2020) 106328. https://doi.org/10.1016/j.optlastec.2020.106328.

[5] S.M. Gaytan, L.E. Murr, D.A. Ramirez, B.I. Machado, E. Martinez, D.H. Hernandez, J.L. Martinez, F. Medina, R.B. Wicker, A TEM Study of Cobalt-Base Alloy Prototypes Fabricated by EBM, Mater. Sci. Appl. 02 (2011) 355–363. https://doi.org/10.4236/msa.2011.25046.

[6] R. Koike, S. Takemura, Y. Kakinuma, M. Kondo, Enhancement of powder supply efficiency in directed energy deposition based on gas-solid multiphase-flow simulation, Procedia CIRP. 78 (2018) 133–137. https://doi.org/10.1016/j.procir.2018.09.061.

[7] X. Wang, X. Gong, K. Chou, Review on powder-bed laser additive manufacturing of Inconel 718 parts, Proc. Inst. Mech. Eng. Part B J. Eng. Manuf. 231 (2017) 1890–1903. https://doi.org/10.1177/0954405415619883.

[8] X. Xu, J. Ding, S. Ganguly, S. Williams, Investigation of process factors affecting mechanical properties of INCONEL 718 superalloy in wire + arc additive manufacture process, J. Mater. Process. Technol. 265 (2019) 201–209. https://doi.org/10.1016/j.jmatprotec.2018.10.023.

[9] W.S. James, S. Ganguly, G. Pardal, Selection and performance of AM superalloys for high-speed flight environments, Int. J. Adv. Manuf. Technol. 122 (2022) 2319–2327. https://doi.org/10.1007/s00170-022-10005-9.

[10] The International Nickel Company Inc., High Temperature High Strength Nickel Base Alloys, 3rd ed., 1977.

[11] R.B. Herchenroeder, Haynes Alloy No. 188 Aging Characteristics, in: Int. Symp. Struct. Stab. Superalloys, Seven Springs, PA, 1968: pp. 460–500. https://doi.org/10.7449/1968/superalloys_1968_460_500.

[12] R.B. Herchenroeder, S.J. Matthews, J.W. Tackett, S.T. Wlodek, Haynes Alloy No. 188, Cobalt. 54 (1972) 3–13.

[13] S.W. Williams, F. Martina, A.C. Addison, J. Ding, G. Pardal, P. Colegrove, Wire + Arc additive manufacturing, Mater. Sci. Technol. 32 (2016) 641–647. https://doi.org/10.1179/1743284715Y.0000000073.

[14] L.A. Middleton, N.F. Kennon, D.P. Dunne, N. South, Metallographic Preparation, Metallography. 17 (1985) 51–59.

[15] ASM Committee of Metallography of Heat-Resisting Alloys, Microstructures of Wrought Heat-Resisting Alloys, in: ASM Met. Handb. Vol. 7 Atlas Microstruct. Ind. Alloy., 8th ed., ASM International, 1972: pp. 165–192.

[16] M.J. Donachie, S.J. Donachie, Selection of Superalloys, in: Superalloys - A Tech. Guid., 2nd ed., ASM International, 2002: pp. 11–24. https://app.knovel.com/hotlink/pdf/id:kt008GQQU1/superalloys-technical/superalloy-forms.

[17] Haynes International, HAYNES® 188 alloy: Principle Features, (2015). http://www.haynesintl.com/alloys/alloy-portfolio_/High-temperature-

Alloys/HAYNES188alloy.aspx (accessed May 9, 2020).

[18] M.J. Donachie, S.J. Donachie, Understanding Superalloy Metallurgy, in: Superalloys - A Tech. Guid., 2nd ed., ASM International, 2002: pp. 25–39. https://doi.org/10.31399/asm.tb.stg2.t61280025.

7 PERFORMANCE COMPARISON OF AM CREEP-RESISTANT SUPERALLOYS

This chapter is based on the following publication.

W.S. James*, S. Ganguly, G. Pardal, A Performance Comparison of Additive Manufactured Creep-Resistant Superalloys, Science and Technology of Welding and Joining. (2023)*

This chapter provides a comparison of the high temperature performance of three alloys tested at temperature: RE41, H188 and IN718. An analysis of the data was utilised to select a single alloy for ongoing study.

Abstract

In trialling a wire-based direct energy deposition (DED) process, commonly known as Wire + Arc Additive Manufacturing (WAAM). Creep-resistant superalloys selected for a high-speed flight application, Haynes 188, Inconel 718, and Rene 41, were deposited and tested for their high temperature tensile properties and the results compared with wrought data from literature. The alloys were tested from ambient temperature up to 1000 °C in their as deposited condition and also after undergoing a post-deposition heat-treatment, in order to down select the best performing alloy.

The performance of the alloys was found to have fallen short of the maximum achievable in wrought condition. Precipitation-strengthened alloys, Inconel 718 and Rene 41 were found to have underperformed the most significantly, whereas solid-solution-strengthened Haynes 188 suffered the least due to the WAAM process. The microstructural features and fracture surfaces of the alloys are also discussed. The WAAM process is thought to be responsible for the precipitation of undesirable phases that are detrimental to performance.

Keywords: Additive Manufacturing, Direct energy deposition, Mechanical results, Superalloys, Fractography, Microstructure.

7.1 Introduction

Wire + Arc Additive Manufacturing (WAAM) has been undergoing development since the 1990's. WAAM is "the combination of an electric arc as heat source and wire as feedstock" [1]. WAAM is not dissimilar to more traditional manual welding technologies such as TIG/MIG welding [2], with the exception that WAAM uses traditional arc welding technologies with a motion control system, such as a robotic system to build components from wire feedstock deposited in a layer-by-layer manner [3]. Unlike other more well established additive manufacturing (AM) methods WAAM is often not used to manufacture a finished product, instead WAAM is used to deposit a near net-shape product [4], which can then be further processed, if required, to achieve a finished product.

As a method to rapid prototype metal structures WAAM is often advantageous over more traditional methods such as machining. As WAAM only deposits the net shape of the product, compared with machining WAAM is capable of: reducing the waste material, hence also reduces the cost, and reducing the lead time. [4].

Superalloys are defined as "a group of nickel-, iron-nickel-, and cobalt-base materials that are used at temperatures of 540^{o}C and above" [5]. Superalloys were initially developed for use in superchargers in aircraft piston engines, however much of their later development has been in gas-turbine components. Nickel-based superalloys can be found in gas-turbines of a variety of applications from aerospace to power generation. It is not uncommon for nickel superalloys to experience operating temperatures of between 150-1500^{o}C.

The use of WAAM to manufacture heat resistant alloys is a relatively new area of study with little literature published in this area. The effect the WAAM process has on the high temperature material properties of heat resistant alloys is largely unknown. Alloys that have been investigated in this study include those suitable for high temperature applications, including largely nickel-based superalloys, this is due to the high temperature performance of these alloys.

High temperature metals that have been deposited using WAAM in the past include Ti–6Al–4V [6]. Tungsten – WAAM is capable of depositing high purity tungsten and other refractory metals [7]. Deposited using WAAM at Cranfield University so far include nickel alloys: Inconel 625 & 718. Refractory metals: tungsten, molybdenum, tantalum. Titanium: grade 2, grade 5, grade 5 with O_2 doping, grade 23, 5553, Timetal 407. Amongst other less heat resistant alloys [8].

In this paper, research is performed towards deposition and wall building of Inconel 718 (IN718), Rene 41 (RE41) and Haynes alloy 188 (H188), using a plasma transferred arc WAAM process. A comparison of the three WAAM built alloys was completed at ambient and at elevated temperatures in as deposited and heat-treated condition, and their suitability for high-speed flight applications was discussed.

The intended outcome of this project is to understand the effect the WAAM process has on these alloys and how to maximise their performance for use in a high-speed flight environment, where external structures could reach service temperatures as high as 1000 K (727 °C) and 1200+ K (927 °C) for components in the propulsion flow path. As a single use system with short flight times of < 1 hour, components will be highly stressed to minimise structural mass. The ideal outcome of this research will be to achieve in WAAM built material similar properties as wrought IN718 or better. Being focused on very good short-term high temperature properties, the alloys investigated in this project were subjected to high temperature testing from room temperature (RT) – 1000 °C.

7.1.1 Physical Metallurgy of H188, IN718 & RE41

The phases seen throughout superalloys are dependent on their composition. Most superalloys have an austenitic face-centred cubic (fcc) phase known as γ phase and consist of several other secondary phases. Carbides are a secondary phase and take the form of MC, M_6C, $M_{23}C_6$ and M_7C_3, where ‘M’ represents the metallic element. Other secondary phases consist of intermetallic compounds, which commonly include: γ’ fcc phase $Ni_3(Al,Ti)$, γ’’ body-centred tetragonal (bct) phase Ni_3Nb, η hexagonal ordered phase Ni_3Ti, and δ phase orthorhombic Ni_3Nb. In most superalloys given the right conditions undesirable phases can form, which can harm the performance if present in larger amounts. These typically include topologically close-packed (tcp) phases: μ Co_2W_6 / $(Fe,Co)_7(Mo,W)_6$, Laves phase A_2B type where 'A' and 'B' represent metallic elements, and σ which can include more complex intermetallic phases. [9]

The metallurgy of the three superalloys is different and each alloy has a unique strengthening mechanism. RE41 and IN718 are somewhat similar in composition both being Ni based, H188 is the odd one out in this study as it is predominantly Co based, however is alloyed significantly with Ni and Cr.

Haynes 188

Co based H188 is strengthened in a significantly different way than the other two Ni-based alloys. It is not hardenable except through cold working, and its strength is derived from its solid-solution-strengthened fcc matrix. It has a primary carbide M_6C associated with a La rich compound, when aged at 760 °C for 200 hrs a secondary carbide $M_{23}C_6$ is known to form at the grain boundaries with A_2B type Laves phase Co_2W and causes increased hardness and reduced ductility. Longer term exposure to temperatures between 760-870 °C can precipitate enough Laves to embrittle the alloy [10]. γ' and γ'' phases are possible to see in Co-based alloys containing Mo and Ta [11] but as these are not present in H188 they are not observed.

Inconel 718

IN718 is an age hardened Ni-based superalloy, with an austenitic fcc matrix. The primary strengthening phases are γ' $Ni_3(Al,Ti)$ L12 structure and γ'' Ni_3Nb bcc D022 structure. Undesirable phases that can form in the alloy include Laves and δ phases. Laves phases take the form of A_2B type $(Ni,Cr,Fe)_2(Nb,Mo,Ti)$ and can form due to variation in composition, processing and high-temperature exposure, formation of Laves is known to deplete Nb required for γ'' formation [12][13]. Carbides formable in IN718 is primarily MC type (Nb,Ti)C, M_6C can also form at the grain boundaries with longer exposure to temperature [14].

Rene 41

RE41 is an age hardened Ni-based superalloy with a fcc austenitic matrix, RE41 also contains a large amount of Co & Mo differing it from IN718. The main strengthening phase is γ’ $Ni_3(Al,Ti)$ [15]. Ni_3Al, & Ni_3Ti form fine uniform particles at 760 °C and are coarser at higher temperatures. Ni_3Ti appears fine bellow 760 °C and acicular above 760 °C. Ni_3Al appears coarse and curved and is seen in larger amounts at grain boundaries. δ phases are not seen generally due to Cr & Mo being tied up in the carbides. Laves phase can form where C is less than 0.05% and Al less than 1% at 815 °C [16]. The main carbides are M_6C $(Mo,Co)_6C$ and/or $M_{23}C_6$ ($Cr_{23}C_6$), which form at higher temperatures due to higher Mo and W content [17][18][19].

Table 7-1 shows the elemental composition by percentage weight of the alloy wires used in this research.

Table 7-1 Composition of alloy wires used for the WAAM process.

Alloy	**Composition (%wt)**														
	C	**Ni**	**Cr**	**Co**	**Mo**	**Fe**	**Al**	**Ti**	**W**	**Nb**	**Mn**	**Si**	**B**	**S**	**Other**
H188	0.107	22.90	22.20	37.12		2.65			13.90		0.81	0.22	0.003	0.002	0.011 P 0.060 La
IN718	0.04	53.57	18.56		2.87	17.8	0.60	0.97		5.01	0.10	0.08	0.002	0.0001	0.07 Cu 0.008 P 0.002 B 0.0001 S 0.5 other
RE41	0.07	53.7	18.9	10.2	9.08	2.72	1.64	3.20		0.12	0.03	0.09	0.004	<0.003	0.04 Cu 0.12 V

7.2 Method

7.2.1 Deposition of Rene 41 & Haynes 188

The following alloys, RE41 and H188, were deposited via a WAAM system consisting of a FANUC six-axis robot, a plasma power source, a water-cooled plasma welding torch mounted to the robot, an external wire feeder, and a part rotator – allowing for symmetrical WAAM wall building. The complete robot set-up and work piece was housed inside a tented enclosure, which was filled with Ar during the WAAM process at an oxygen level controlled below 800 ppm, which was monitored using an oxygen analyser. The experimental set-up is shown in Figure 7-1 & Figure 7-2.

The commercially available wires used and the welding parameters for each alloy are shown in Table 7-2. The chemical composition of these wires is shown in Table 7-1. For RE41 and H188 alloys, a 10 mm thick IN718 plate measuring 400 x 100 mm was used as the substrate. Large linear wall structures were deposited in each alloy measuring approx. 340 x 110 x 8 mm. The welding parameters were kept constant, with the exception of the initial welding layers, where a slower travel speed and reduced wire feed speed were used to better establish the structure onto the substrate plate. The use of different diameter welding wire for the three alloys was due to the availability of wires from suppliers, as such the wire feed speeds were adjusted to achieve a consistent deposition rate between wires.

The process used for RE41 and H188 was a symmetrical wall building process, where two wall structures were built simultaneously on opposite sides of the substrate plate. The part rotator is utilised to alternate between the two sides of the substrate plate. The benefits of this process over a single sided operation is to reduce residual stresses on the structure as the warping of the substrate is effectively cancelled out when an identical structure is welded on both sides [1]. It also has the effect of increasing productivity, as inter-pass cooling can partially take place on one side when the process is ongoing on the opposite side, minimising the time the system remains inactive while cooling takes place.

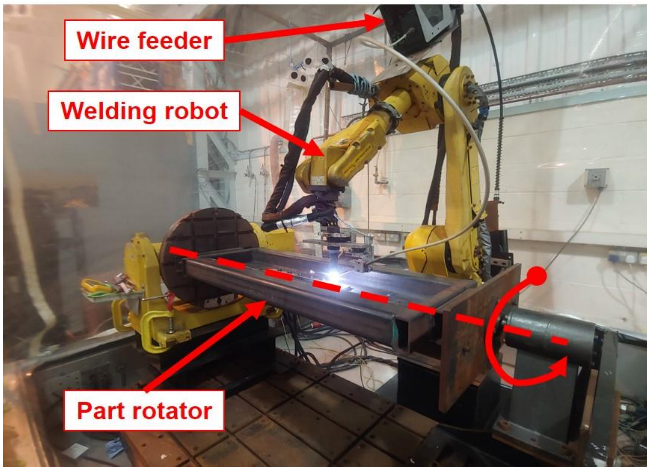

Figure 7-1 Overview of experimental set-up used to deposit RE41 & H188

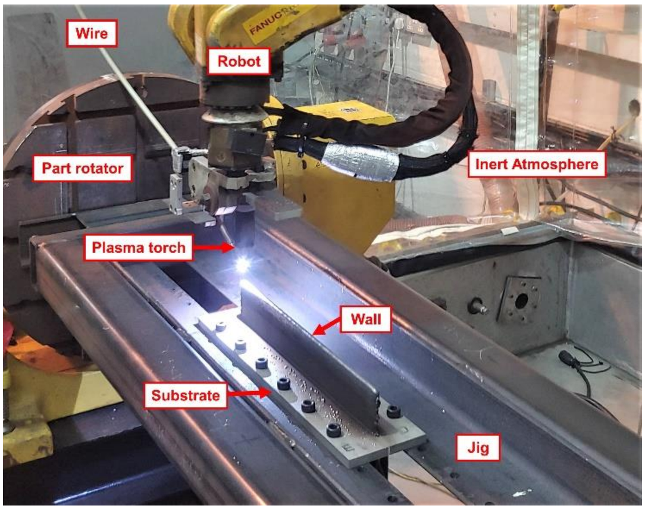

Figure 7-2 Experimental set-up used to deposit RE41 & H188

7.2.2 Deposition of Inconel 718

For the IN718, a different WAAM system was used due to availability, the system consisted of: a three-axis linear CNC system, a Migatronic 320A AC/DC plasma power source, a water-cooled plasma torch mounted to an adjustable jig on the CNC system, an external wire feeder and a glove box filled with Ar at an oxygen level controlled below 800 ppm, as in section 7.2.1.

The process used for the deposition was a linear wall building system where the layers were deposited in a single direction on a single side of the substrate, due to the limitations of the system used.

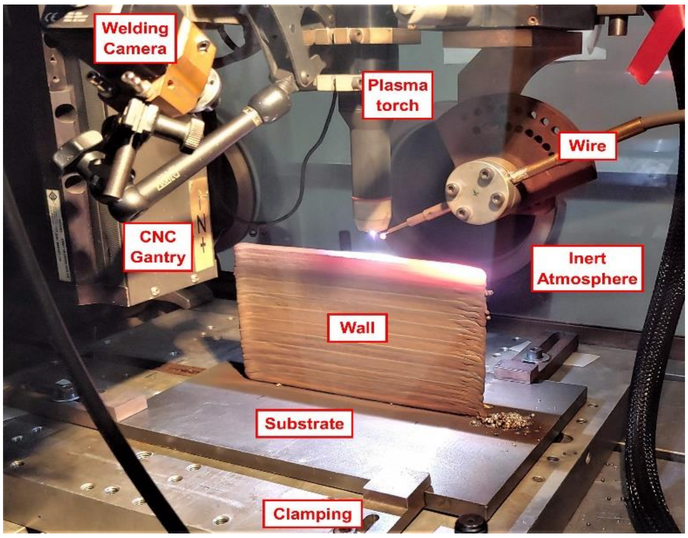

Figure 7-3 Experimental set-up used to deposit IN718

Table 7-2 Wire and welding parameters

	IN718	RE41	H188
Wire Diameter (mm)	1.2	1	1.14
Torch to work distance (mm)	8	8	8
Current (A)	180	180	180
Wire feed speed (m/min)	1.8	2.4	2
Travel speed (mm/sec)	5	6	6
Inter-pass cooling time (min)	3	3	3

7.3 Post-Deposition Heat-Treatments

Samples from each of the alloys underwent a post-deposition heat-treatment appropriate to their strengthening mechanism, IN718 and RE41 underwent both a solutionising and aging process designed to precipitate the main strengthening phase γ’ for both RE41 and IN718, and also γ’’ for IN718, whereas H188 underwent just a solutionising treatment. Details of each process is shown in Table 7-3.

Table 7-3 Heat-treatment processes for IN718, RE41 & H188

	Solutionising	Cooling	Aging	Cooling
IN718	1hr @ 970°C	water	8hrs @ 718 °C; furnace cool, 8hrs @ 620 °C	air
RE41	4hrs @1065°C	air	16hrs @ 760°C	air
H188	2hrs @1100°C*	water	-	-

7.3.1 Metallographic Preparation & Analysis

In the H188, RE41 and IN718 alloys, WAAM walls of 128, 147, and 226 layers respectively were built. Once completed the walls were cut from the substrate plates and samples were extracted through both the wall height and length. Cross-sections were extracted and prepared for metallographic analysis following a procedure consisting of mounting, grinding, polishing, and etching successively. Samples were etched using the following methods to reveal the microstructure:

H188

5 g oxalic acid, 95 ml HCl. Electrolytic 6 V DC using a carbon cathode and stainless anode probe, for 1-2 sec [20].

RE41

3 g $CuSO_4$, 80 ml HCl, 20 ml absolute alcohol. Samples were then immersed in ammonium peroxydisulfate H_2O solution weight ratio of 1:20 for 2-3 mins to remove corrosion products [21].

IN718

Kalling's No.2 Reagent (2 % $CuCl_2$ in acidified alcoholic base) swab etch for 10 sec.

The microstructure was also analysed, using a Tescan VEGA 3 scanning electron microscope (SEM), and optically using a Leica DM 2700M Microscope. To determine composition the VEGA 3 SEM was equipped with an Oxford Instruments X-Max 20 mm energy-dispersive spectrometry (EDS) detector.

7.3.2 Mechanical Testing Methods

The microhardness was measured using a Zwick/Roell hardness tester under a load of 500 g and holding time of 15 s, unused welding filler wire of the alloys also underwent a similar process as above to obtain comparative results for the hardening effect of the WAAM process.

In addition to hardness, all alloys also underwent extensive tensile testing at a range of temperatures. Temperatures were selected to be compared against existing data from Donachie's superalloys technical guide [22], an extra test at 1000 °C was also carried out to extend the understanding of the alloy performance for the high-speed flight application. Three samples from each alloy were tested in each category in both the as deposited and heat-treated condition. Tensile specimens were tested at RT, 538, 760, and 1000 °C.

RT and elevated temperature tensile tests (538-1000 °C) were carried out using an Instron 8801 Servo-hydraulic Universal Testing System and tested to the ASTM E8M specification for RT testing and E21 for the elevated temperature tests, using a strain rate of 0.005 mm/min to proof then 1.6 mm/min thereafter. The coupon shown in Figure 7-4 was used for RT testing and Figure 7-5 shows the coupon used for elevated temperature testing. The specimens were extracted in similar locations across the WAAM walls, their locations in reference to the wall structure is shown in Figure 7-6. From a total of four WAAM walls built in pairs, three walls were utilised for testing. After testing, the fracture surfaces of specimens in each category and condition were observed.

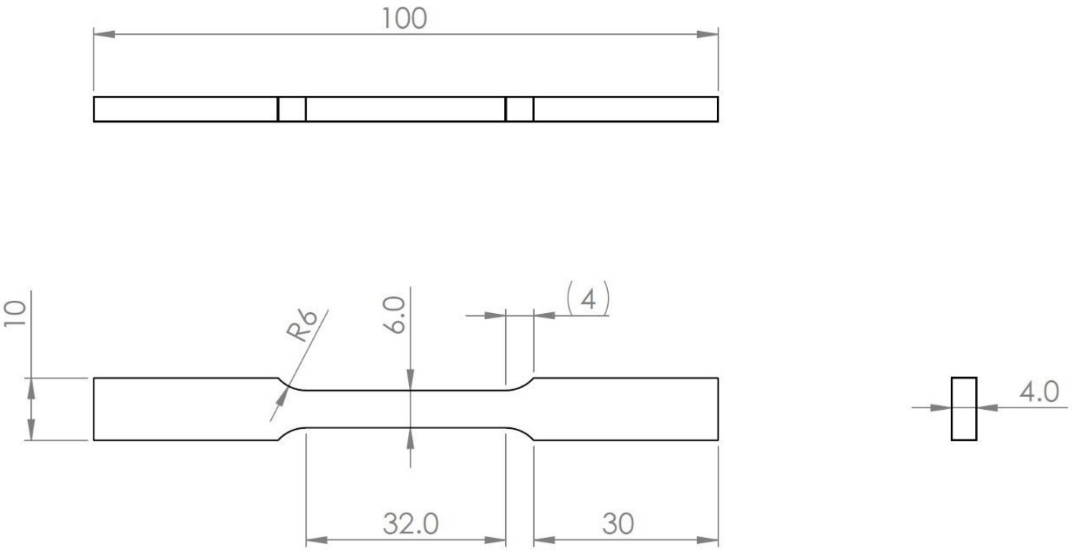

Figure 7-4 RT Tensile testing coupon conforming to ASTM E8M sub-sized specimen. X ±0.5 mm, X.X ±0.1 mm. (Not to scale).

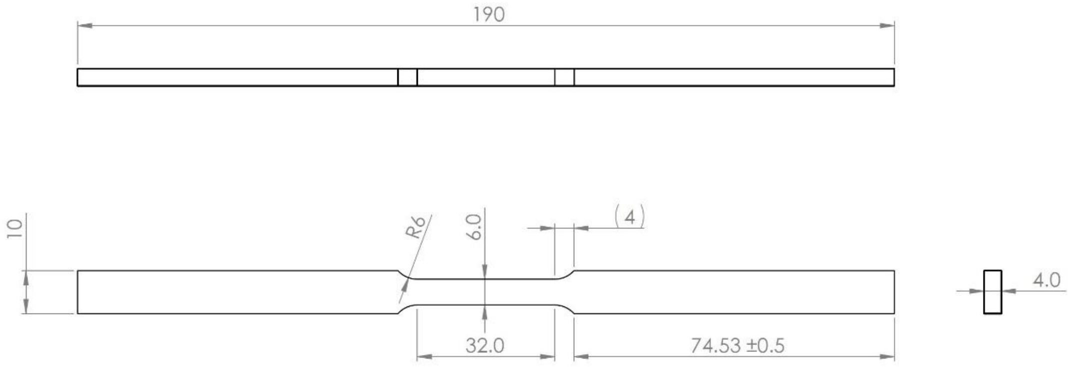

Figure 7-5 Elevated temperature tensile coupon used at 538-1000 °C, conforming to requirements of ASTM E21. X ±0.5 mm, X.X ±0.1 mm. (Not to scale).

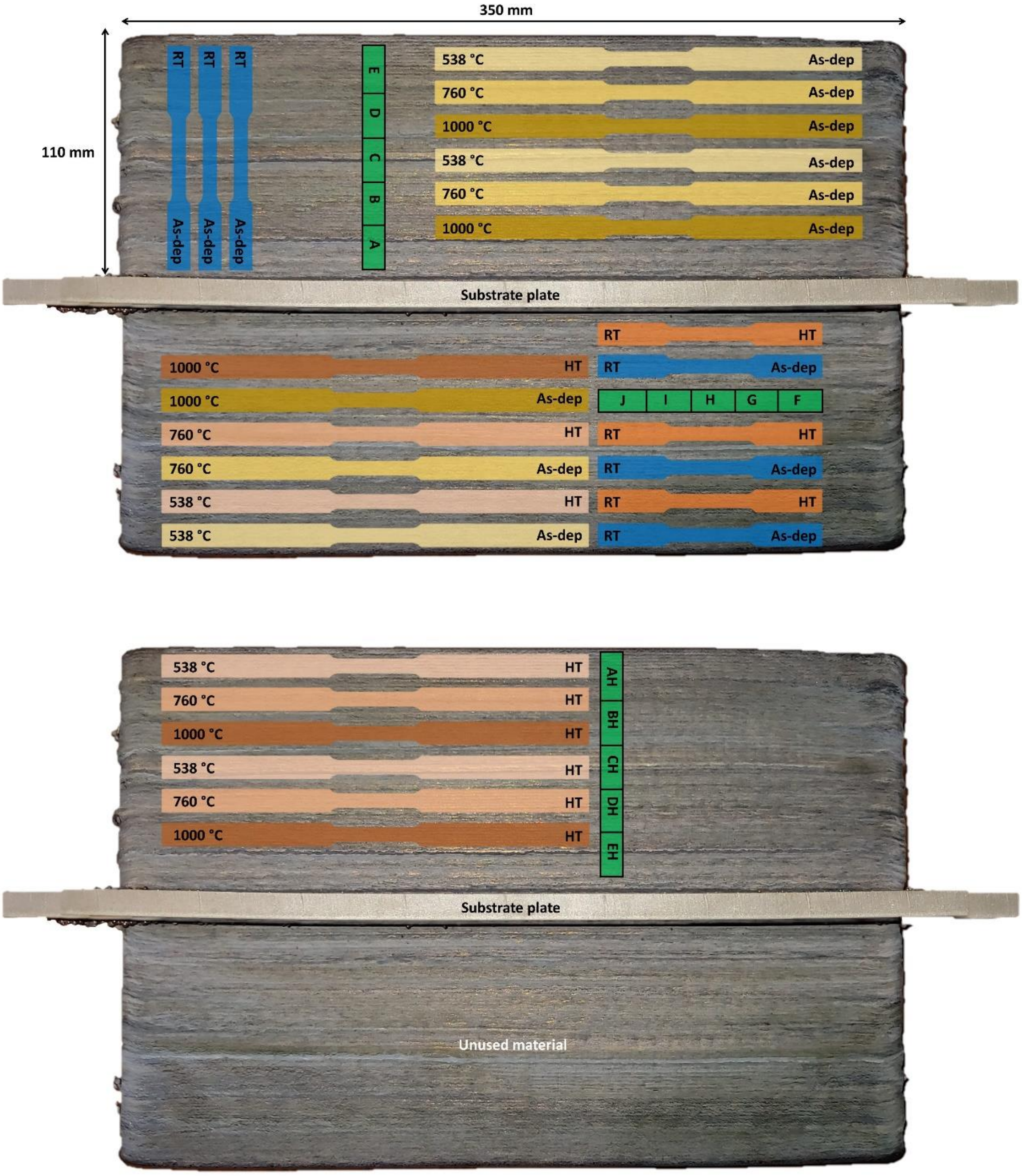

Figure 7-6 Location of extracted samples from WAAM walls in each material (Not to scale). Green areas indicate location of metallographic samples. Temperature given on the left of the coupon indicates testing temperature and on the right the condition as-deposited (as-dep) or heat-treated (HT). Metallographic samples AH-EH are HT whereas single letter A-J are as-dep.

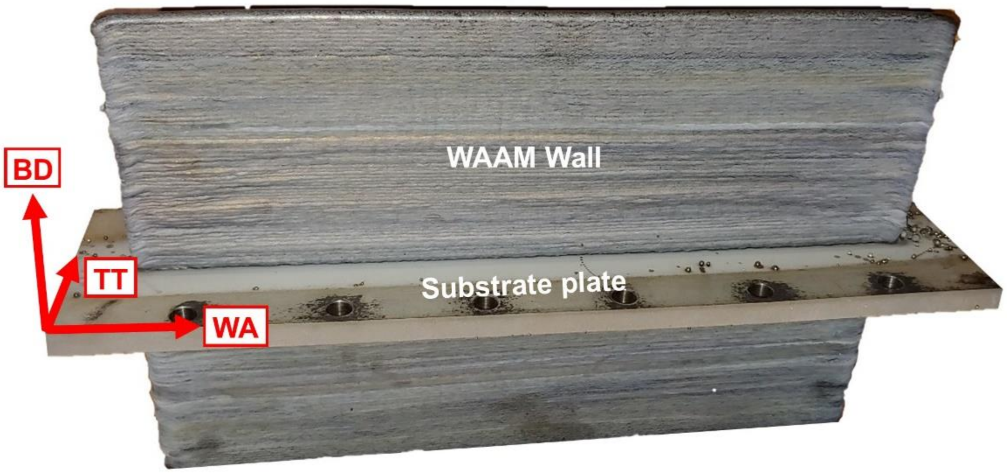

Figure 7-7 Axis relevant to process and labelled throughout micrographs.

7.4 Results

7.4.1 Macrostructure

All three alloys exhibit a typical solidified dendritic structure made up of large columnar grains which appear to extend along the height of the wall in the direction from bottom to top, this structure was expected and can been seen in previous studies on IN718, IN625, RE41 and H188 by James et al. [23] The structure of IN718 can also be found in the work of Xu et al. [13].

7.4.2 Microstructure

The microstructure was analysed both optically and under SEM. The grain morphology was compared between the three alloys to understand the structure. Optical images of the microstructure at comparable locations in both the as deposited and heat-treated conditions are presented in Figure 7-8. It can be clearly seen that the structures are similar in appearance with long dendrites extending through the height of the samples in the BD axis. Grain boundary locations are shown for all samples. In Figure 7-8, the micrographs show the directionally solidified grain structure. The heat-treated samples show a much thicker dendritic structure and grain boundaries.

A comparison between as deposited and heat-treated material is presented at greater magnification in Figure 7-9. Phases and carbides in this section going forward have been identified based on EDS composition and appearance using ASM Atlas of Microstructures [24]. In comparing the alloys, it is even clearer at greater magnification the thicker and darker grain boundaries after heat-treating. In Figure 7-9 image A1 as-deposited IN718, chainlike islands of precipitates are seen at the dendrites, and when the alloy has undergone heat-treatment (image A2) these precipitates are seen to be surrounded by needle like precipitates in a Widmanstätten-Thomson pattern, which are thought to be Ni_2Nb Laves surrounded by Ni_3Nb δ phase. Spectrum A2 in Table 7-4 seems to support the presence of Laves phase.

In heat-treated samples of RE41 (Figure 7-9, image B2), the grain boundary area presented is seen to consist of brightly coloured stringer type precipitates surrounded by a darker grain-boundary background, with larger white and grey precipitates distributed in the matrix. The lighter coloured precipitates at the grain boundary are thought to be M_6C or $M_{23}C_6$, while the grain boundaries are darkened in heat-treated condition due to precipitation of γ’. The larger white precipitates in the matrix are thought to be a complex intermetallic phase, likely Ni_2Mo Laves phase, which is supported by spectrum B2 in Table 7-4.

Heat-treatment in H188 (Figure 7-9, image C2), had a clear darkening and thickening effect surrounding precipitates at the grain boundaries and within the matrix compared to as-deposited material (image C1). The smaller grain boundary precipitates are thought to be $M_{23}C_6$, whereas elsewhere in the matrix brighter coloured precipitates are thought to be Laves Co_2W intermetallic phase and M_6C carbides, which would be supported by spectrum C1 and C2 in Table 7-4. It is also noted that potential M_6C carbides seen outside of the grain boundaries are surrounded by smaller darker phases which could be indicative of primary M_6C decomposing in secondary $M_{23}C_6$. In some cases (seen in Figure 7-11) areas where $M_{23}C_6$ is observed forming a ring, presumably around what was previously M_6C carbides which has decomposed, leaving only the secondary carbide remaining.

The microstructure seen under SEM in IN718 at the grain boundary is shown in Figure 7-12. The as-deposited WAAM structure shows significant amounts of segregation of Nb and Mo at the boundary, as seen in Figure 7-13, where the elemental map shows strong segregation of Mo & Nb, where Cr & Fe has been displaced, also seen in the map are very small areas of Ti rich zones indicating potential Ti rich carbides. Similar features were seen across the other alloys.

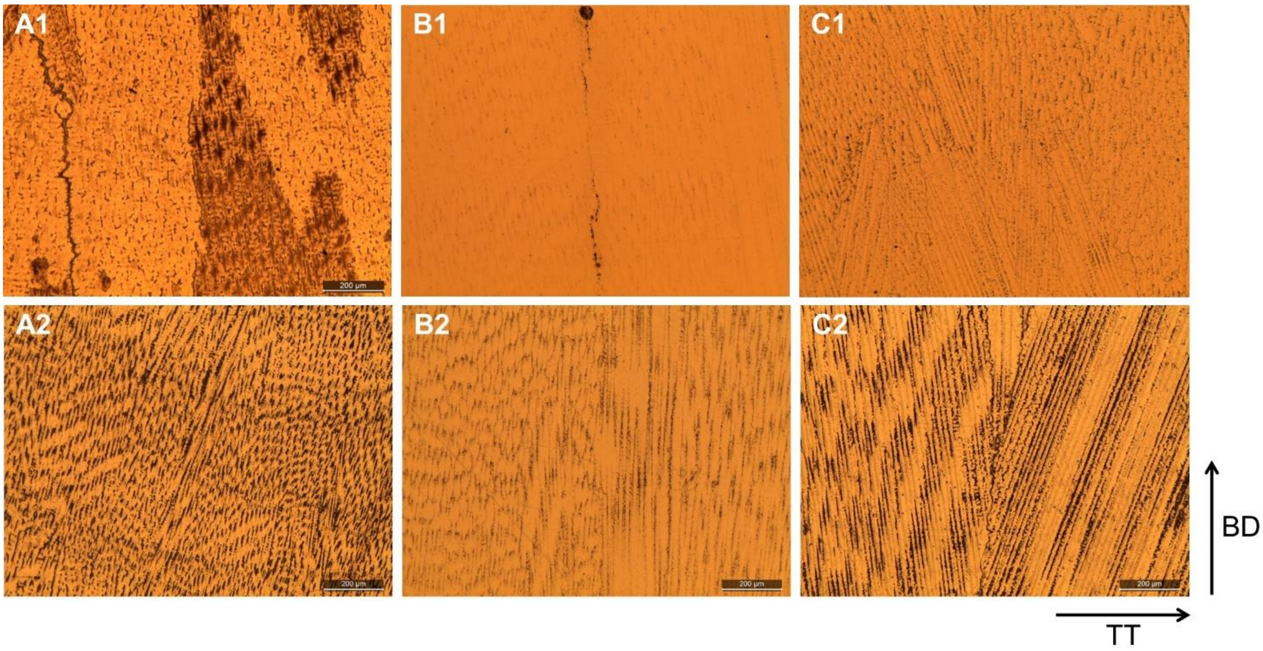

Figure 7-8 Microstructure of IN718 (A), RE41 (B), H188 (C), as deposited (1), heat-treated (2). Seen in the TT & BD axes.

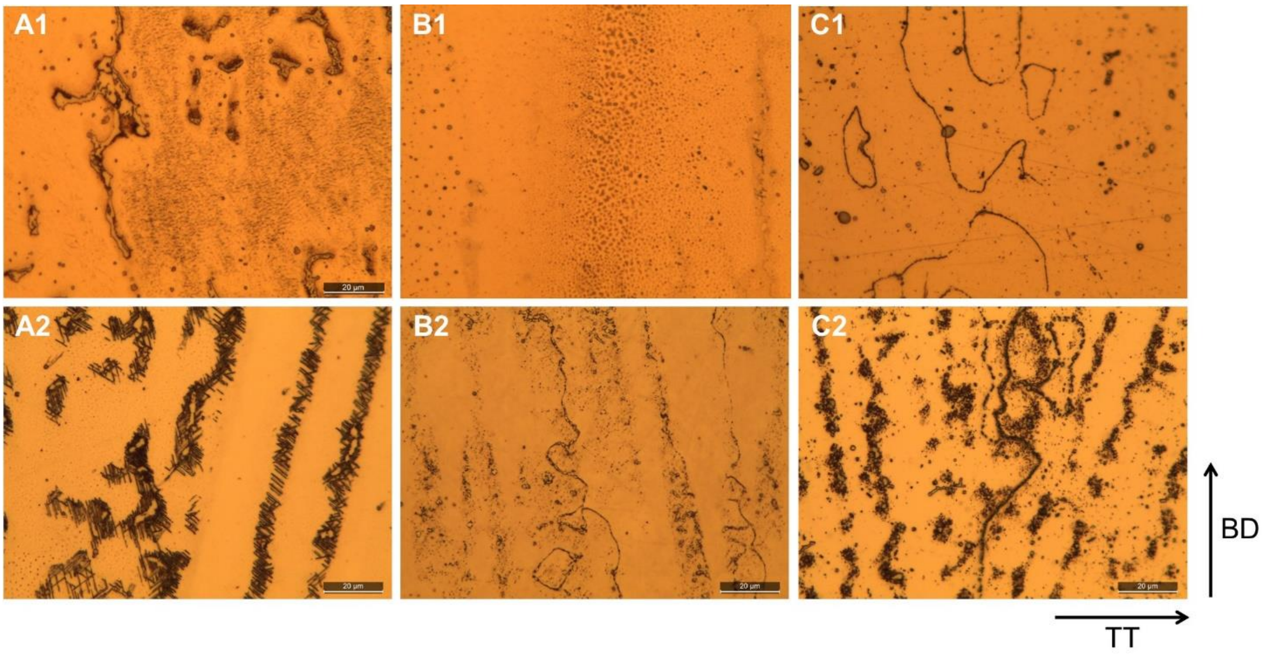

Figure 7-9 Microstructure of IN718 (A), RE41 (B), H188 (C), as deposited (1), heat-treated (2). Seen in the TT & BD axes.

Table 7-4 EDS analysis of areas marked in Figure 7-10. (%at)

Spectrum Label	C	Al	Ti	Cr	Mn	Fe	Co	Ni	Nb	Mo	W
A1			1.95	17.67		12.96		46.26	21.15		
A2	13.88		1.31	13.17		11.17		36.61	18.00	3.98	
B1			1.55	34.16			10.86	30.26		23.17	
B2		1.77	4.35	22.86		2.53	9.94	39.79		18.26	
C1	53.65			18.33		0.76	12.62	6.29		0.81	7.53
C2				38.91	0.91	1.95	28.16	16.57		0.74	12.56

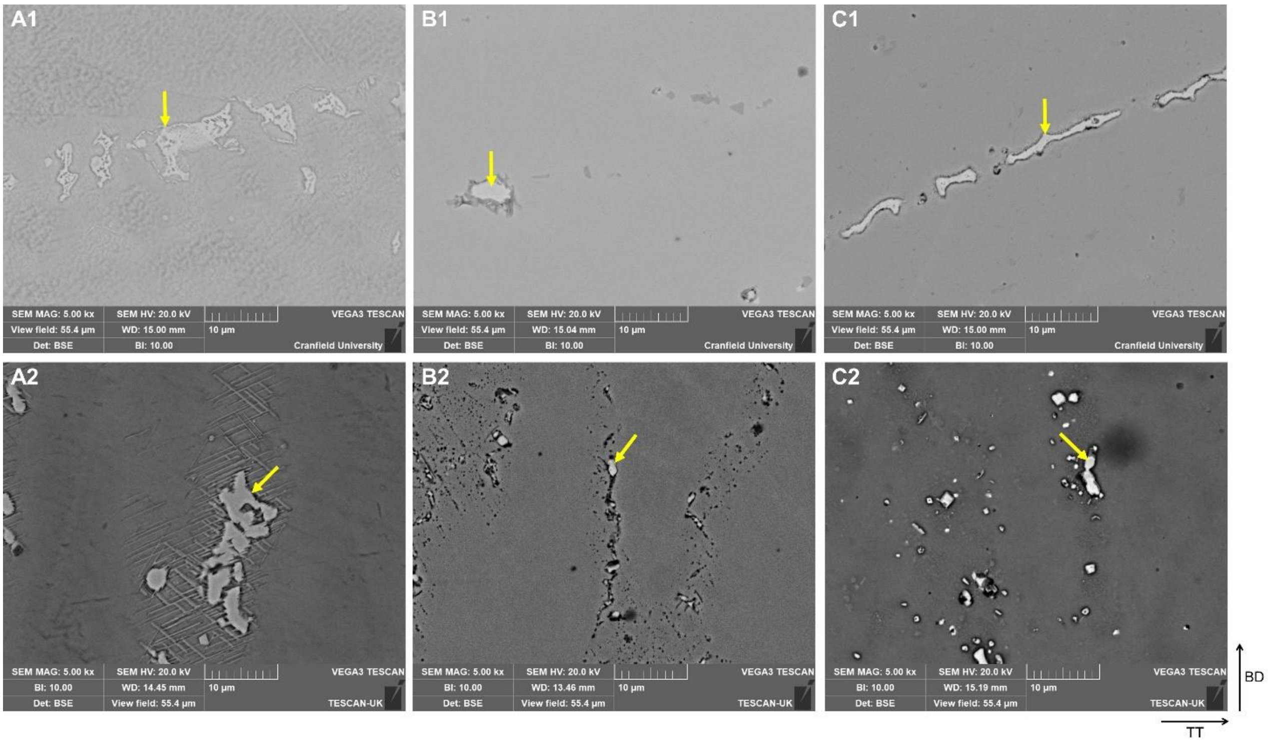

Figure 7-10 BSE images of microstructure of IN718 (A), RE41 (B), H188 (C), as deposited (1), heat-treated (2). Seen in the TT & BD axes.

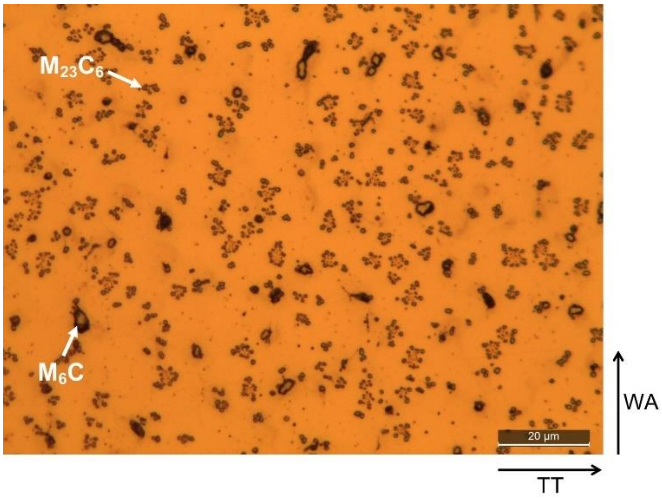

Figure 7-11 Decomposition of M_6C to $M_{23}C_6$ in H188. Seen in the TT & WA axes.

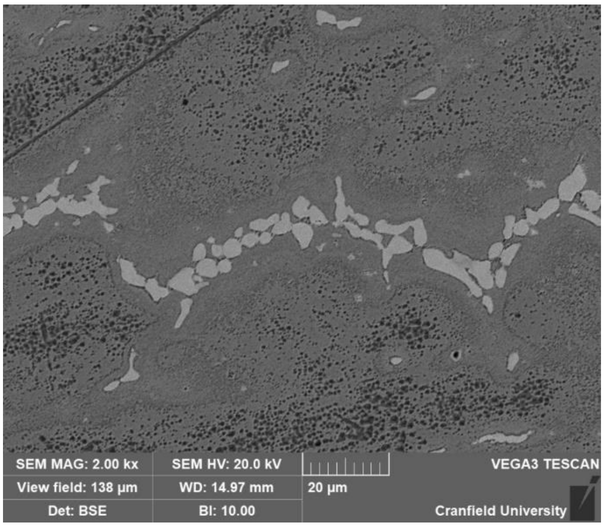

Figure 7-12 BSE image: Microstructure in IN718 showing grain boundary segregated zones.

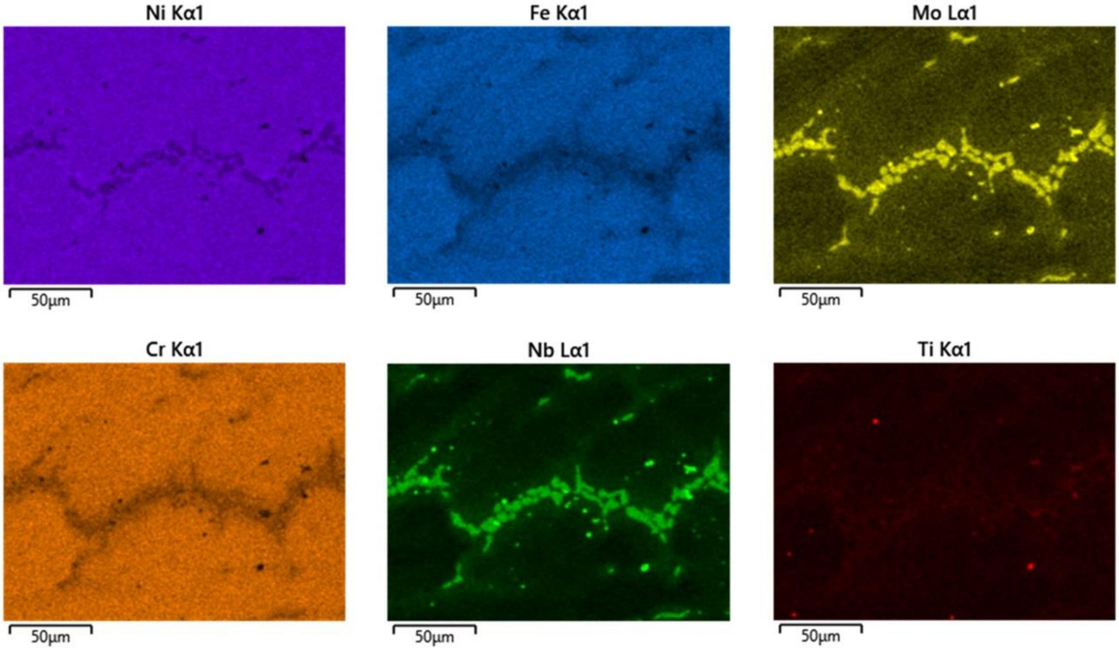

Figure 7-13 EDS Elemental map of IN718 BSE image in Figure 7-12.

7.4.3 Mechanical performance

The performance of all alloys in their as deposited and heat-treated condition is shown in Table 7-5 where the experimental data is shown with wrought data from literature for comparison; note that data for 1000 °C is often not available in the literature.

Graphs comparing the performance of the alloys for the complete range of temperatures is shown in Figure 7-14. The best overall performance, as anticipated from the literature, is RE41 followed by IN718 and H188. In RE41 and IN718 an increase in performance was observed in the as-deposited material during the 760 °C test and affected an increase in the performance compared with the 538 °C test which was unexpected. The worse performing alloy compared with maximum stated values from literature is as-dep IN718 which achieved on average 47.8 % of the maximum values, followed by RE41 58.8 % and the closest performance H188 achieving 63.7 % of the stated maximum. When heat-treated the performance increases to an average of 62.5, 61.4 and 72.8 % for IN718, RE41 and H188 respectively. Results between RE41 and IN718 are largely similar until 760 °C, where the difference in YS performance is more apparent, with RE41 performing better at this temperature. Although the standard deviation is significant in most testing cases, the results still present significant findings, and it is likely that factors such as cracking have affected some of the specimens causing a greater range in tensile performance. Full stress-strain curves can be found in the appendix.

Table 7-5 Mechanical performance of alloys in as-dep and heat-treated (HT) condition, compared with wrought data according to Donachie (STG) [22].

			IN718			RE41			H188		
			STG	As-dep	HT	STG	As-dep	HT	STG	As-dep	HT
Elongation (%)	1000 C	1832 F		46	43		20	16		32	36
	760 C	1400 F	25	3	5	11	4	1	43	31	36
	538 C	1000 F	18	7	5	14	11	3	70	37	32
	RT	RT	21	6	1	14	7	5	56	39	32
YS (MPa)	1000 C	1832 F		62	64		135	106		122	97
	760 C	1400 F	740	546	547	940	669	671	290	246	206
	538 C	1000 F	1065	378	687	1020	611	688	305	267	236
	RT	RT	1185	505	852	1060	733	812	485	428	382
UTS (MPa)	1000 C	1832 F		107	102		183	179		167	147
	760 C	1400 F	950	592	639	1105	728	704	635	398	431
	538 C	1000 F	1275	478	761	1400	703	757	740	414	488
	RT	RT	1435	626	870	1420	854	944	960	694	811

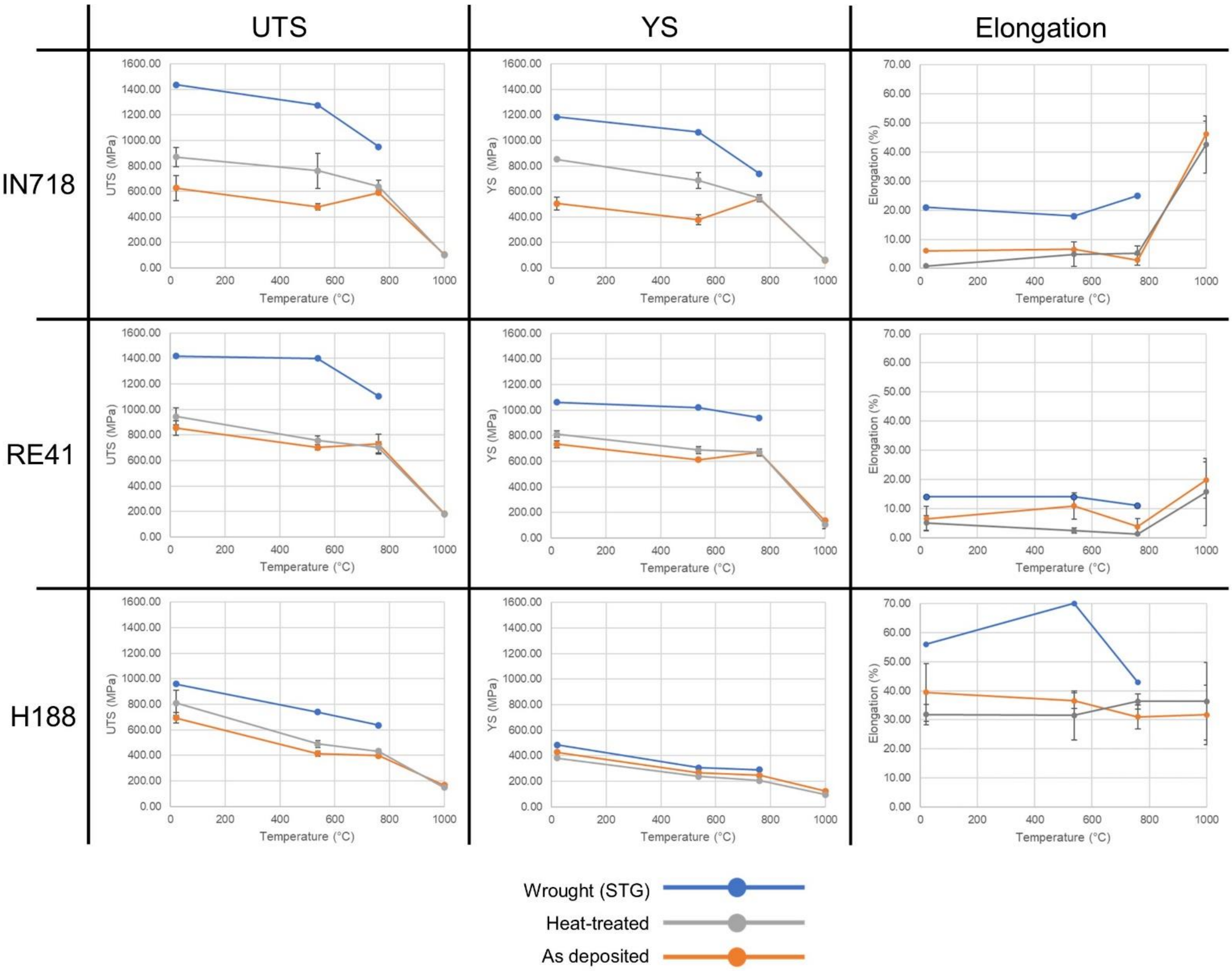

Figure 7-14 Comparison of mechanical testing data and wrought data.

7.4.4 Microhardness

The hardness data presented in Figure 7-15 shows a correlation between the WAAM material and the wrought data. With the exception of IN718, the WAAM process is shown to increase the hardness of deposited alloys over wrought values, as deposited H188 and RE41 increases in hardness by 11.4 and 13.0 % respectively. IN718's as-deposited hardness is shown to be less than the wrought value and this is thought to be due to the extensive ageing process that this alloy typically undergoes to achieve peak performance. When heat-treated the hardness values are significantly higher than both the as deposited value and the wrought data, compared to the wrought value heat-treated IN718 is 31.9 %

harder. A similar situation exists for RE41, when heat-treated the material is 36.8 % harder than the wrought material. The hardening effect is also seen in H188 but to a lesser extent than the other alloys, this is thought to be due to H188 not being an age hardenable alloy and as such only underwent a solutionising treatment; heat-treated H188 is only 15.9 % harder than the wrought value. The hardness values for all alloys in each condition are compared with the wrought value in Table 7-6.

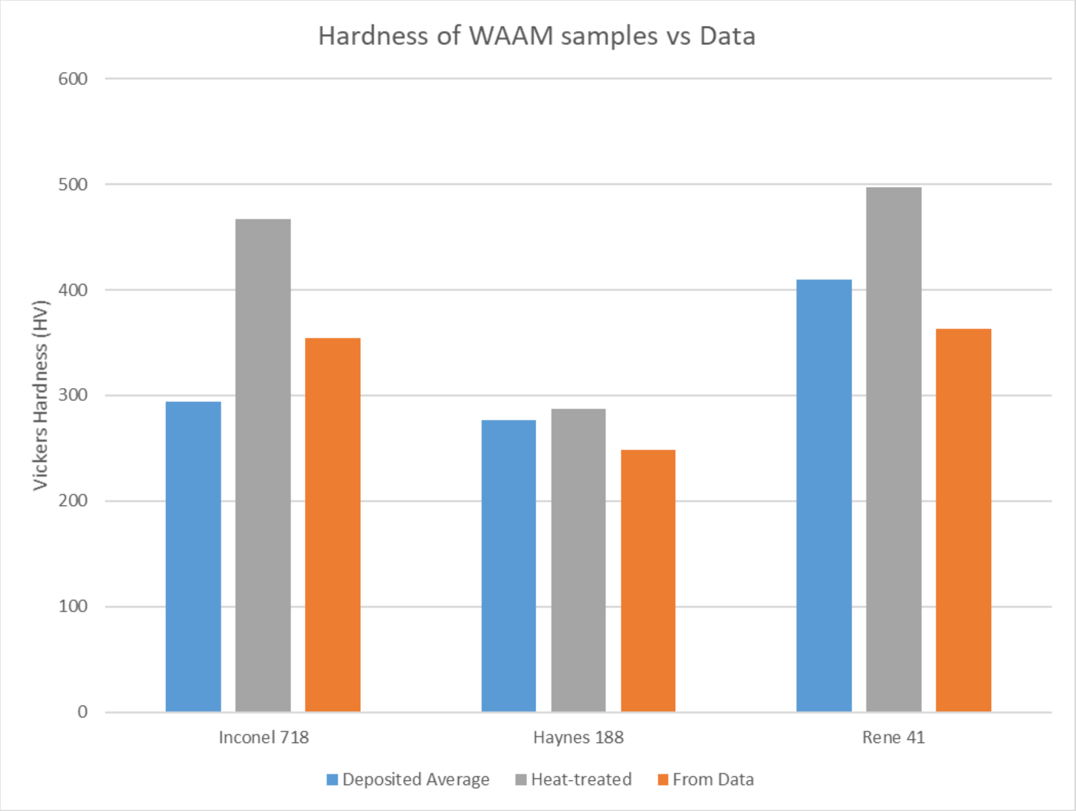

Figure 7-15 Hardness comparison of as-dep and heat-treated WAAM material compared with literature data. [12][25][17].

Table 7-6 Hardness values of alloys in as deposited, heat-treated, and wrought conditions.

		Hardness (HV)
IN718	As-dep	294
	Heat-treated	467
	Wrought [12]	354
H188	As-dep	276
	Heat-treated	288
	Wrought [25]	248
RE41	As-dep	410
	Heat-treated	497
	Wrought [17]	363

7.4.5 Fracture surfaces

In the macrographs most of the fracture surfaces have a woody appearance, indicating a shearing action across the grain plane which has produced cracking along many parallel longitudinal planes. Further to this, most samples failed on an inclined plane further suggesting a shearing action. The woody appearance suggests that most fractures seen here are intergranular. A good example of this is seen in Figure 7-17 image A1, in which a whole section of grains appears to have been dislodged during fracture, the surface of which is fibrous in appearance. On several samples the lines sometimes take a chevron shape (seen clearly in Figure 7-17 images B1 & C1), these are theorised to be slip steps although similar in appearance to striations which occur microscopically. Chevron patterns appear on largely RT, 538 °C and to a lesser extent 760 °C specimens, these patterns are indicative of rapid fracture associated with more brittle fractures [26].

On 1000 °C specimens the fractures appear more ductile in nature with distorted cross-sections. Specimens in IN718 and RE41 appear to have deep central void type cracks which extend a good distance into the length of each specimen, suggesting much larger intergranular separation. Samples in H188 show obvious slip steps at this temperature and large cracking was seen throughout the samples at this temperature. One sample, seen in Figure 7-16 image A4, can be seen to have cracked almost along the entire length of the specimen, a feature that reaches the surface on this sample would suggest a welding imperfection, perhaps introduced by an inclusion. At 760 °C IN718 and RE41 fracture surfaces appear far rougher and woodier in appearance than H188. All fracture surfaces at this temperature appear to have areas seen as blue in colour, this perhaps indicates the formation of an oxide scale at this temperature as samples were tested in air.

In Figure 7-19 the grain boundaries appear to grow thicker with increased testing temperature, the difference is most noticeable in the difference between IN718 and RE41 at 1000 °C compared to the other temperatures (Images A4 & B4 in Figure 7-19), the difference is less pronounced in H188. A comparison between heat-treated RE41 and as deposited samples tested at temperature is shown in Figure 7-20, where the microstructure directly behind the fracture surface is shown. It can be clearly seen that the grain boundaries are even more pronounced in the heat-treated variant, increasing with testing temperature.

When looking at the grain boundaries of RE41 1000 °C tested specimens under SEM, there appears to be, based on initial appearance, δ phase precipitates (indicated by B in Figure 7-21). However, this is not the case but on closer inspection using EDS analysis (Table 7-7) they appear to be entrapped oxide which retain a good distribution of the alloying elements. This differentiates them from area A in Figure 7-21, which is seen as bright and irregular shaped, located central to the grain boundary and forming along the crack edges. This area is also identified as a Mo rich zone, indicating the presence of Laves phase.

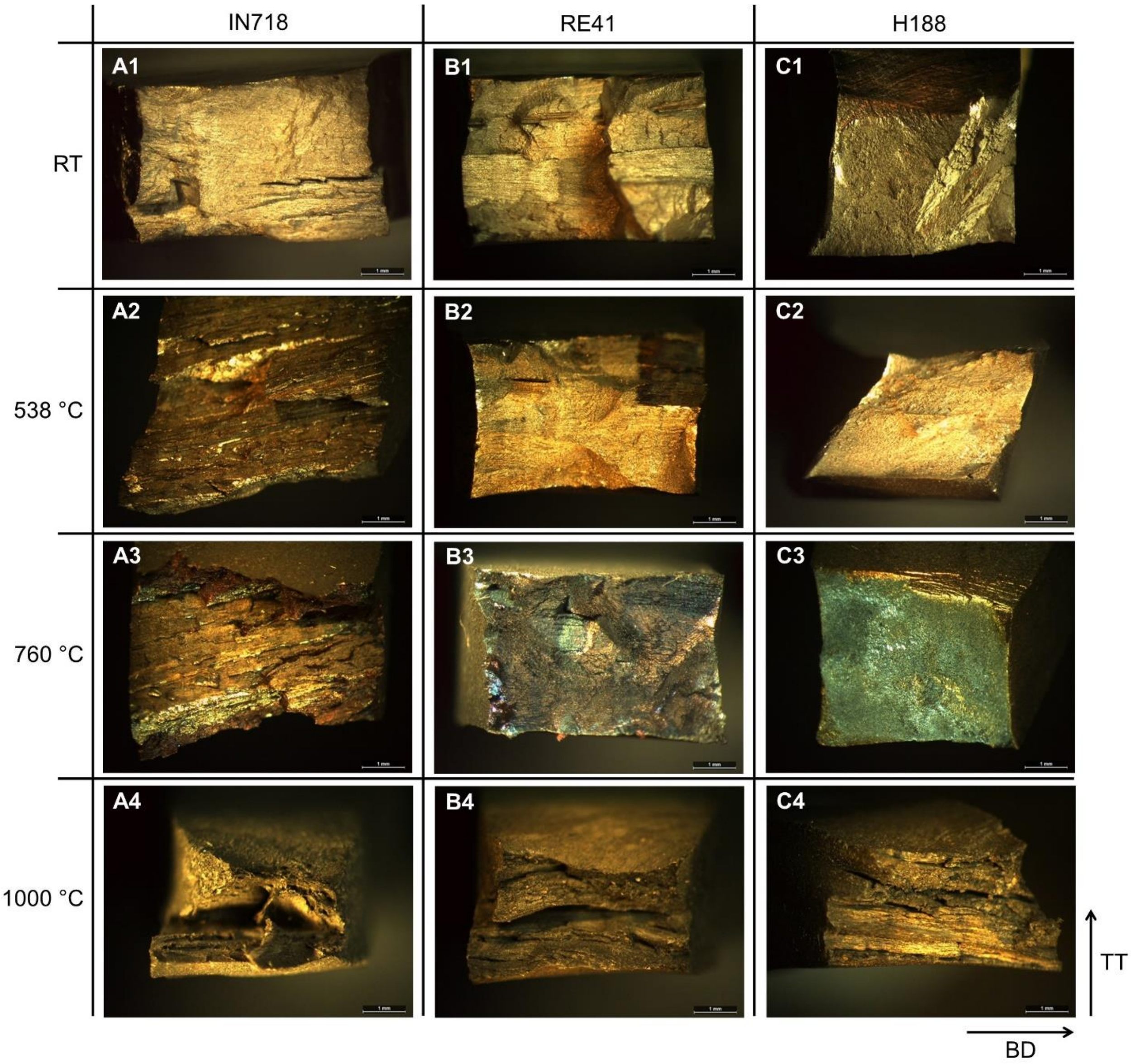

Figure 7-16 As-deposited macro fractographic images of fracture surfaces. (A) IN718, (B) RE41, (C) H188, (1) RT, (2) 538 °C, (3) 760 °C, (4) 1000 °C.

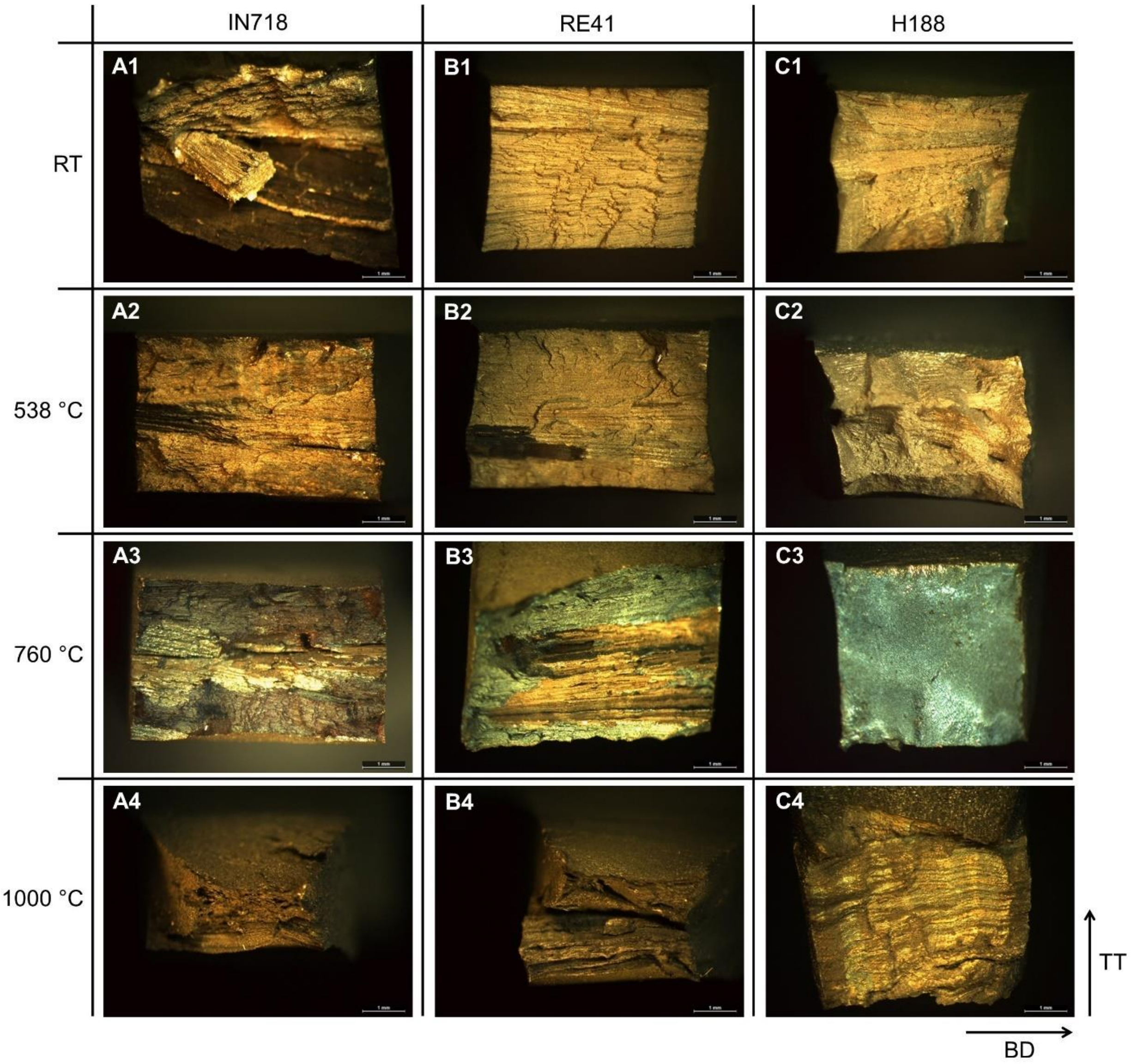

Figure 7-17 Heat-treated macro fractographic images of fracture surfaces. (A) IN718, (B) RE41, (C) H188, (1) RT, (2) 538 °C, (3) 760 °C, (4) 1000 °C.

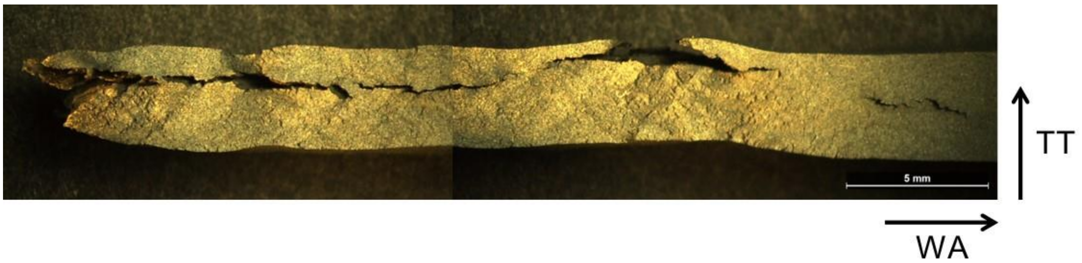

Figure 7-18 Sample A4 from Figure 7-16 seen in WA &TT axes.

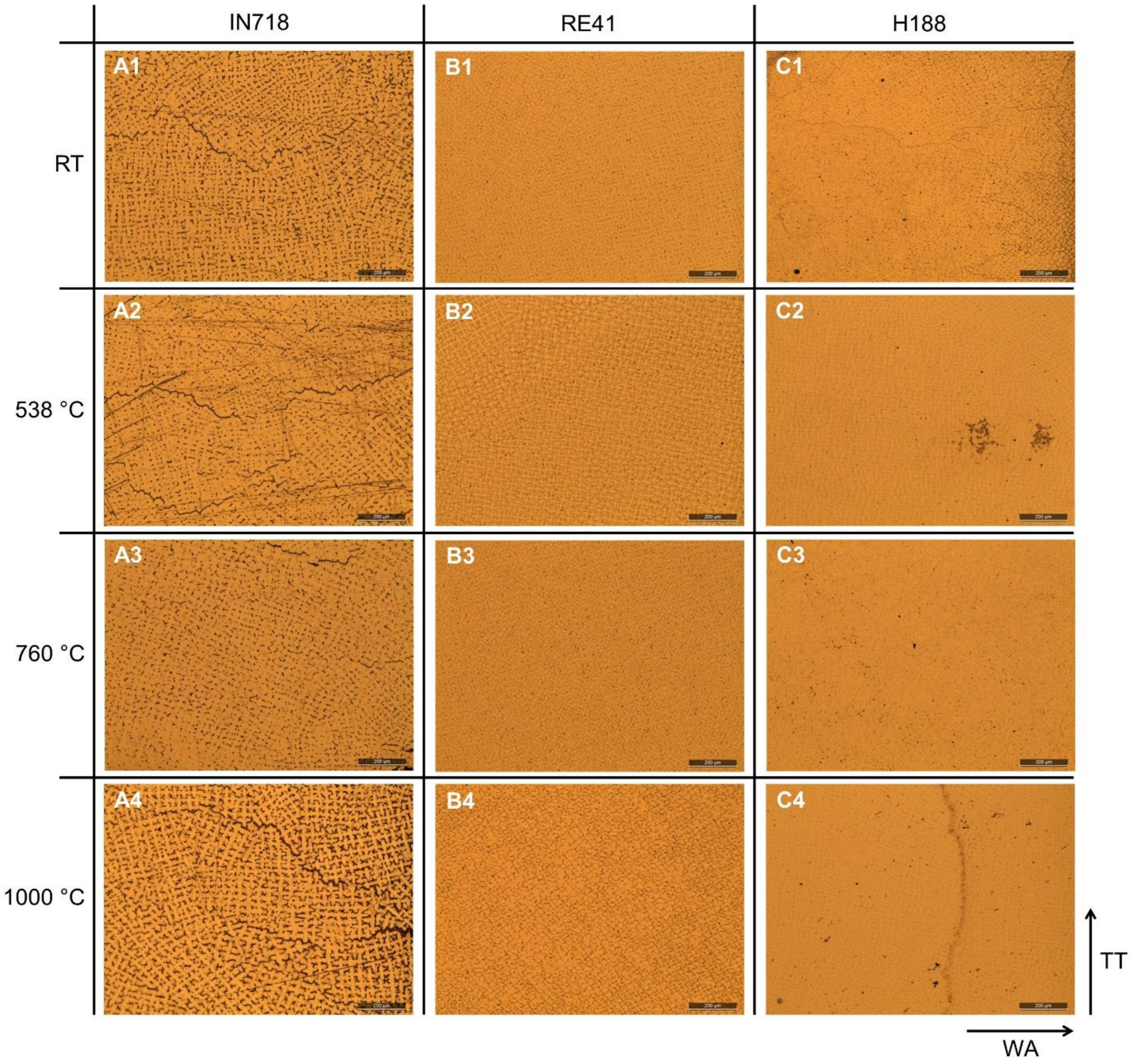

Figure 7-19 As-deposited microstructure of tested alloys at range of temperatures. Viewed in WA & TT axes. (A) IN718, (B) RE41, (C) H188, (1) RT, (2) 538 °C, (3) 760 °C, (4) 1000 °C.

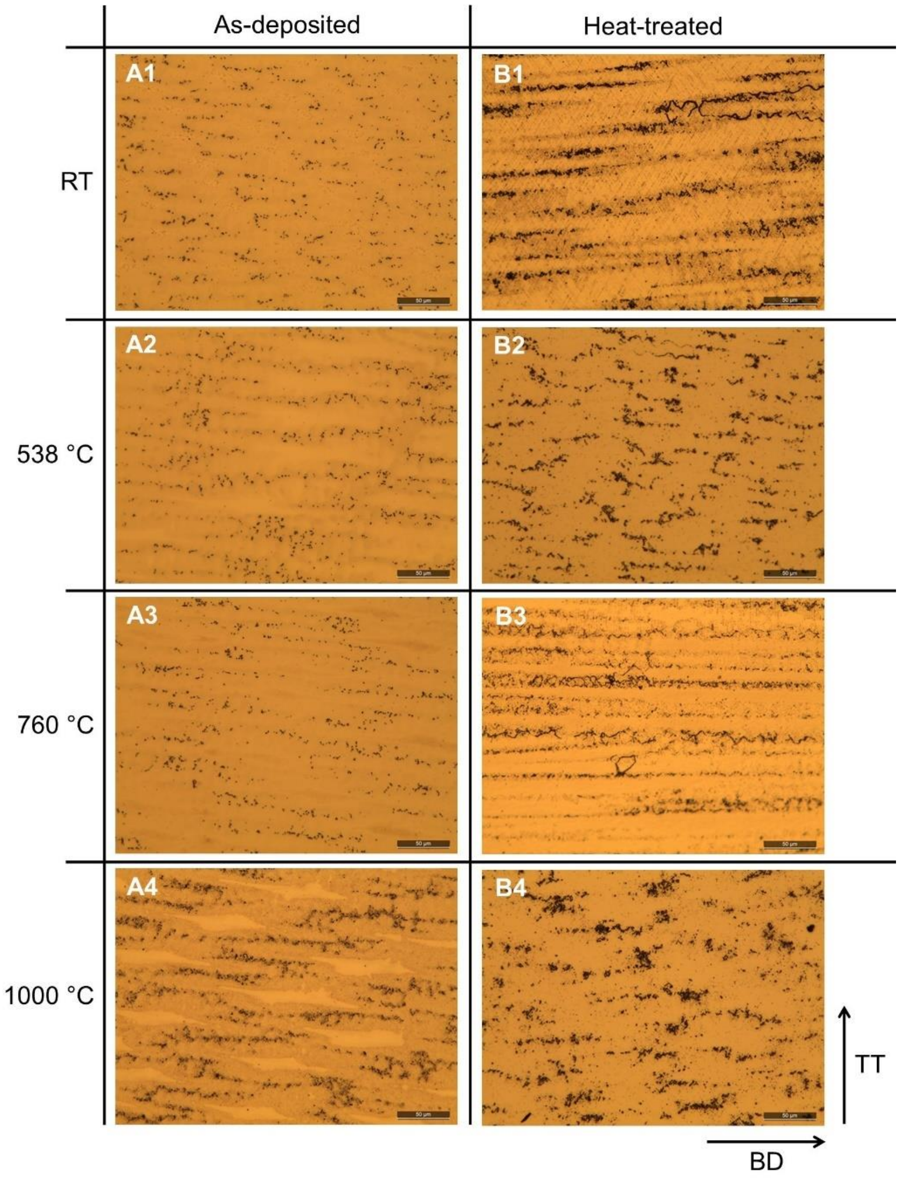

Figure 7-20 RE41 microstructure of tested specimens. Viewed in BD & TT axes. (A) As-deposited (B) Heat-treated, (1) RT, (2) 538 °C, (3) 760 °C, (4) 1000 °C.

Table 7-7 EDS Analysis of areas marked in Figure 7-21. (%at)

Spectrum Label	O	Al	Si	Ti	Cr	Fe	Co	Ni	Mo
A	13.17	1.23	1.73	4.40	20.76	1.73	8.16	28.58	20.25
B	9.13	2.85	2.57	3.56	19.74	2.66	9.12	45.34	5.04

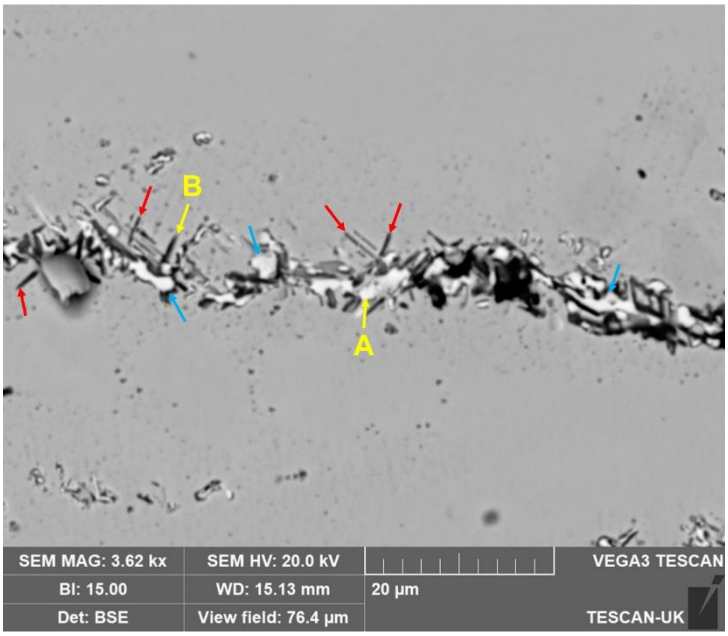

Figure 7-21 BSE image: Grain boundary/ crack location observed in RE41 1000 °C testing specimen. Red arrows indicate oxide formation, blue arrows indicate Laves phase.

7.5 Discussion

7.5.1 Microstructure

The comparison in Figure 7-9 between as deposited and heat-treated samples is especially interesting in both IN718 and RE41. In as-deposited IN718 (image A1) chainlike precipitates are seen at the dendrites. These precipitates are seen in IN718 in the ASM Atlas of Microstructures where they are seen to be light in colour and thought to be Laves phase of the $M_2(Nb,Ti)$ type, based on the compositional analysis in Table 7-4. However, it is thought that these precipitates are more likely to be Ni_2Nb in this case as the %at of Ti seen is not significantly different from the base alloy. After aging (Figure 7-9, image A2) these precipitates are seen to be surrounded by needle like precipitates in a Widmanstätten-Thomson pattern, which is consistent with the ASM atlas, in which needle like Ni_3Nb is seen in the heat-treated γ matrix in combination with Laves phase [24]. These needle like phases are also consistent with δ phase formation in aged IN718, which has been seen to take the form of Widmanstätten-Thomson pattern in Mahadevan et al study, in which it was seen that these phases formed at the grain-boundaries and can form from metastable γ″ particles when the alloy is overaged [27]. It is thought that the formation of δ and Laves phase at the grain boundaries in the samples here, are responsible for the large amount of intergranular cracking that was observed in the alloy.

When the microstructure of heat-treated RE41 is viewed optically, there are clear stringer like precipitates at the intergranular regions surrounded by a darker background which became more pronounced after heat-treating (Figure 7-9, image B1 & B2). Further investigation into literature suggested that these precipitates are M_6C or $M_{23}C_6$ carbides, while the darker background is indicative of γ' precipitation [24], which is not unexpected post-aging. The larger white precipitates seen more clearly in Figure 7-10 image B2, are thought to be a complex intermetallic phase, which is further supported by the EDS analysis B2 in Table 7-4.

H188 saw a similar effect post heat-treatment as was seen in IN718, with a darkening and thickening at the grain boundaries and surrounding precipitates in the matrix. H188, like the other alloys, saw precipitates form at the grain boundaries and larger brighter coloured precipitates elsewhere in the matrix. The larger precipitates are best seen in Figure 7-10 image C2 which is thought to be a Co_2W intermetallic Laves phase, which is supported by the EDS analysis. Intergranular $M_{23}C_6$ is common in solutionised H188 and is seen in ASM atlas of microstructures [24]. Grain boundary $M_{23}C_6$ was also found by Herchenroeder in a report on the aging characteristics of H188, in which $M_{23}C_6$ was found to precipitate more readily after aging at 760 °C. Secondary particles where seen to surround primary M_6C carbides in the same report and it was suggested that the surrounding particles are secondary $M_{23}C_6$ which have decomposed from the primary carbide [10]. What was seen in as-deposited material, in Figure 7-11 in the WA-TT plane, was rings of what appears to be the $M_{23}C_6$ carbides surrounding a seemingly empty region, suggesting that there was once an M_6C carbide in these areas, but it has completely decomposed into the secondary carbide leaving just the remaining ring of secondary carbides. M_6C is also observed in the same micrograph with the same secondary phase in proximity.

7.5.2 Mechanical performance

Throughout the temperature range from RT - 760 °C a significant difference is observed in the performance of both variants of WAAM material and their stated maximum values from literature. Comparing UTS values, the heat-treated WAAM alloys achieve roughly 59, 48 and 64 % of their stated maximum at RT, 538, and 760 °C respectively. This difference was observed in a previous study on IN718 by Xu et al in which wrought IN718 was compared with WAAM material. The study showed that WAAM IN718 had a grain structure of far greater thickness and less grain boundary area than the wrought material. The strength of the wrought material was gained through its finer equiaxed grain structure and smaller dendrite arm spacing, allowing for more effective strengthening by precipitation of the secondary phases at the grain boundaries. The larger columnar grains seen in the WAAM material made precipitation of these phases less likely [28]. In this study large columnar grains were observed in IN718, but also in RE41 and H188 and although this difference was less of an issue for H188, due to it not being strengthened by secondary phases, it also appears to have affected RE41 in a similar way. The observed difference in the performance of H188 and the other alloys further backs up this reasoning as WAAM H188 is the closest performing alloy to the wrought data. Xu et al.'s study on IN718 went further to examine the effect of differing heat treatments and found that unless a mechanical process was used to produce a more favourable starting microstructure, little to no additional enhancement in performance can be made [28].

A difference was observed in both the UTS and YS performance of as-dep RE41 and IN718 in the 760 °C test results, where the as-dep samples effectively 'catch-up' to their heat-treated variant. The difference in the performance is most likely due to the alloys undergoing an aging process during testing, as 760 °C is the approximate temperature at which these alloys are routinely aged. As there was not a similar increase in the already heat-treated samples it can only be suggested that this increase is due to the as-dep WAAM material undergoing aging at the testing temperature. The same increase was not observed in heat-treated IN718 and RE41, and in fact as-dep RE41 when tested at 760 °C actually outperformed the heat-treated variant on average by ~24 MPa. It is suggested that this difference is due to the heat-treated variant over-aging at this temperature. Strength of alloys generally decreases with increasing temperature and time of exposure to temperature. However, age hardenable alloys can temporarily increase in performance, to a limited extent, with increase temperature and exposure, as a result of additional aging [29]. This effect although temporary could be beneficial for this application with short flight times. To further support this theory, when looking at the same testing temperature for H188, a non-age-hardenable alloy, no increase is observed over lower testing temperature and the profile largely follows that of the literature data.

At 1000 °C across all the alloys a sharp decrease in the performance was observed, which is consistent with what is expected to be seen if the literature data is extrapolated to this temperature. Excessive blackening and oxidisation cracking was observed on the 1000 °C samples post-testing and is consistent with the findings of Greene et al on IN718, in which they found that at temperatures of 1000+ °C, volatile Cr_2O_3 forms and results in a loss of protective Chromia scale [30]. As the samples were tested in air at all temperatures it is reasonable to assume that IN718 and by extension RE41 underwent this loss of protection contributing to the performance reduction.

The hardness increase of IN718 when as deposited material is heat-treated is shown to be significantly higher than the wrought value. It is thought that this is due to the WAAM process partially aging the alloy which then undergoes a standard heat-treatment for IN718, further aging the material. In general, the WAAM process is thought to partially age the alloys in varying amounts dependant on the process used and the metallurgy of the alloy being deposited. The hardness increase due to the WAAM process is also variable dependant on the amount of successive heating cycles the material has been subjected to. For example, the WAAM walls produced for this study had roughly the same number of deposited layers, for RE41 this was between 147-153 layers per wall, this means approximately the same number of successive thermal cycles have occurred during the process. However, only the very first layer has experienced all of these cycles, whereas the very last layer i.e., the top of the WAAM wall, has only experienced one heating cycle. This means that the partial aging effect is more pronounced at the bottom of the WAAM wall, whereas the top of the wall is significantly less aged. This effect was investigated by Xu et al in a study on maraging steel in which it was found that the bottom part of the WAAM walls were harder than the top parts. Xu et al also found that the number of precipitates in the bottom part of as-deposited walls was roughly double the number of precipitates found in the top part. With an aging treatment, however, the precipitates in the top part of the wall increased to be approximately the same as the bottom part [3]. The location of as-deposited samples extracted for hardness testing in this study was in the centre of each wall, where the WAAM aging effect is roughly half the number of deposited layers.

The key process variables of the WAAM process should be investigated for the benefit of the strengthening mechanisms of each alloy, for example adjusting the arc current or wire-feed speed would have the effect of changing the heat input into the material, which would affect the way precipitation hardened alloys age during deposition.

7.5.3 Fractography

With the largely different performance of as-dep samples at 760 °C and the suggestion that these samples appear to undergo aging during testing to ‘catch-up’ to their pre-heat-treated duplicate, it was unsurprising to see the macro fractography show a visible difference in the fracture surfaces at this temperature. The surface of the fractures appear blue in colour which could be indicative of an oxide formation at this temperature. This is useful evidence for the theory that the alloys have undergone a change during testing at 760 °C, which is not entirely surprising given that IN718 and RE41 are routinely aged around this temperature. What is surprising is the change in appearance even on the macro scale which suggests that this is just the appearance of an oxide formation.

The fracture surfaces of IN718 and RE41 at 1000 °C suggest fractures were very much ductile in nature, due to the distorted cross-sections and ‘hour-glass’ shape. The testing data also showed a marked increase in elongation at this temperature for both alloys. Again this is consistent with the findings of Greene et al in IN718, in which it was found that at temperatures of 1264 °C, not hugely removed from the 1000 °C testing temperature, the deformation in the alloy became unacceptable for the application [30]. The elongation in H188 throughout the temperature range remained comparatively stable. It is also noticeable that with increasing testing temperature the grain boundaries become much thicker. This was seen in RE41 by Schwartz et al in a study in which RE41 underwent heating cycles which affected the thickness of the grain boundaries and also the susceptibility to the metallographic etchant [15], this was also observed in this study especially in samples tested at 1000 °C. Specimens tested at RT, 538 and to a lesser extent 760 °C showed signs of more brittle fractures, which is supported by the elongation data, which shows that IN718 and RE41 only displayed a fraction of the elongation expected from the wrought data. Furthermore, chevron patterns seen predominantly in RT specimens and to a lesser extent in 538 & 760 °C specimens further add to evidence of brittle type fractures, due to these patterns being indicative of more rapid fracture modes [26].

As well as in as-deposited samples, δ phase was observed post-testing in IN718 tensile coupons. As well as having the effect of depleting Nb needed for γ'' formation, the presence of δ phase could be responsible for reduced elongation that was observed during mechanical testing. Seow et al found that δ phase in a 0.3-1.4% volume fraction has no effect on the YS and UTS performance but decreased the ductility of the material by up to 10 % [31]. At relatively lower temperatures, δ phase nucleates at austenite grain boundaries as well as coherent and incoherent twin boundaries, while at higher temperatures δ precipitates intergranularly [27], which could explain the reason for the reduced ductility seen during testing.

In Figure 7-21 oxide formation at the grain boundaries of RE41 tested at 1000 °C was observed, the oxide takes a similar shape to that of δ phase in IN718 with its acicular needle like shape and its formation in close proximity to potential Laves phase, however this is not possible in RE41 due to the lack of Nb needed for its precipitation. Upon investigating the composition using EDS, it was found that the composition retains the distribution of the alloying elements, however, shows an increase in the amount of detected O. This is consistent with the finding of Ungureanu et al. In the study, RE41 underwent a thermal shock process to understand the effects on the microstructure, at 1000 °C it was found that with increased thermal shock oxide layers were seen to grow and retain a similar distribution of the alloying elements [19]. Ultimately the formation of oxide in the samples is consistent with the tensile results, as the elongation of the samples represent only a fraction of the expected elongation from wrought material, indicating that the presence of oxide has affected the ductility of RE41. Entrapped oxides formed during the welding process would not be possible to dissolve into the matrix during solutionising, due to their extremely high melting point. The low viscosity of Ni alloys makes them particularly susceptible to oxide entrapment, which is also consistent with the findings of Xu et al in a study on maraging steel, in which oxides were also found to have a strengthening effect on the matrix when dispersed on the hundred-nanometre scale [32].

7.5.4 High-speed Flight Application

In reference to the introduction of this paper, the intended application of this research is in understanding the high temperature performance of these alloys, to down select one alloy for highly stressed service in temperatures of 1200+ K for durations of <1 hour.

In terms of mechanical tensile performance, RE41 achieves the highest stress values at every temperature tested. However, toward the 1000 °C testing temperature when the strength of RE41 and IN718 decreases somewhat exponentially, the results would seem to indicate H188's potential performance at 1000+ °C would be higher than that of RE41 and IN718 if another testing temperature was included at 1100 °C, based on an extrapolation of the results. If the application was to exceed 1100 °C it is likely H188 would be a better choice for continuing development, however RE41 has a much better performance definitively at temperatures <1000 °C.

Elongation is another important factor for high-speed flight applications, as components need to retain their shape at service temperatures, so a lower elongation is preferred. However, alloys need to retain some ductility to avoid the devastating impacts of brittle type fractures during service. H188 would not be an ideal choice as elongation in this alloy, although relatively stable, are the highest amongst the three alloys. RE41 would be a better choice as it avoids some of the more extreme brittle type fractures seen in IN718 at lower temperatures while retaining some ductility, at increasing temperatures the elongation changes are not as dramatic as IN718. Further optimisation of the WAAM process may provide improvements in performance.

The cracking and complexity of fractures seen across the three alloys was most concerning for IN718, in which large intergranular cracking was observed in as deposited material. When tested the most cracking was seen in IN718 specimens with some of the most complexed fractures. Cracking was less so in RE41, although the alloy still experiences cracking in as deposited material. It is hoped that a further mechanical process introduced during WAAM deposition will help to alleviate the cracking issues. The least cracking was seen in H188, with no identifiable cracks in as deposited and heat-treated conditions, fracture surfaces were also less complex which appear more ductile at elevated temperatures.

Although cost is not considered to be a deciding factor for this application, there was not a great deal of correlation between performance and cost of these alloys. RE41 was the costliest to purchase at £319 / kg, followed by H188 at £103 / kg, the least costly was IN718 at £73.55 / kg (costs based on quotes from commercial suppliers). Although the performance at 760 °C of RE41 is approx. 19% higher than IN718 the cost is over four times higher. H188, which is mid-range in terms of cost, may have the potential to be the best performer at temperatures exceeding 1000 °C

7.6 Conclusion

1. As deposited WAAM alloys IN718, RE41 and H188 underperforms compared to their maximum stated performance and using a heat-

treatment specific to the alloys results in a marginal performance increase.

2. The WAAM process increases hardness in alloys RE41 and H188, by 11.4 and 13%, and is seen to partly age all alloys.
3. Performance of as deposited alloys IN718 and RE41 at 760 °C increases to largely meet the performance of pre-heat-treated specimens, indicating an in-test aging process.
4. Performance largely drops off at a 1000 °C testing temperature (except for H188 which remains relatively stable). Which is potentially due to precipitation of undesirable oxide phases at the grain boundaries.
5. Precipitation of A_2B Laves phases were found at the grain boundaries in all alloys and at crack edges in IN718 and RE41, indicating an embrittling effect leading to intergranular cracking.
6. RE41 is the best performing alloy for the high-speed flight application based on the evidence presented, however further work is required to confirm.

7.7 References

[1] S.W. Williams, F. Martina, A.C. Addison, J. Ding, G. Pardal, P. Colegrove, Wire + Arc additive manufacturing, Mater. Sci. Technol. 32 (2016) 641–647. https://doi.org/10.1179/1743284715Y.0000000073.

[2] S. Kou, Welding Metallurgy, 2nd ed, Hoboken, N.J. : Wiley-Interscience, 2003.

[3] X. Xu, S. Ganguly, J. Ding, S. Guo, S. Williams, F. Martina, Microstructural evolution and mechanical properties of maraging steel produced by wire + arc additive manufacture process, Mater. Charact. 143 (2018) 152–162. https://doi.org/10.1016/j.matchar.2017.12.002.

[4] B. Baufeld, O. Van der Biest, R. Gault, Additive manufacturing of Ti-6Al-4V components by shaped metal deposition: Microstructure and mechanical properties, Mater. Des. 31 (2010) S106–S111. https://doi.org/10.1016/j.matdes.2009.11.032.

[5] J.R. Davis, ASM Specialty Handbook: Heat-Resistant Materials, in: ASM Spec. Handb. Heat-Resistant Mater., ASM International, 1997: p. 36.

[6] F. Martina, J. Mehnen, S.W. Williams, P. Colegrove, F. Wang, Investigation of the benefits of plasma deposition for the additive layer manufacture of Ti-6Al-4V, J. Mater. Process. Technol. 212 (2012) 1377–1386. https://doi.org/10.1016/j.jmatprotec.2012.02.002.

[7] G. Marinelli, F. Martina, S. Ganguly, S. Williams, Development of Wire + Arc additive manufacture for the production of large-scale unalloyed tungsten components, Int. J. Refract. Met. Hard Mater. 82 (2019) 329–335. https://doi.org/10.1016/j.ijrmhm.2019.05.009.

[8] Welding Engineering and Laser Processing Centre Cranfield University, MATERIALS AND PROPERTIES, (2019). https://waammat.com/about/materials-and-properties (accessed November 8, 2019).

[9] M.J. Donachie, S.J. Donachie, Understanding Superalloy Metallurgy, in: Superalloys - A Tech. Guid., 2nd ed., ASM International, 2002: pp. 25–39. https://doi.org/10.31399/asm.tb.stg2.t61280025.

[10] R.B. Herchenroeder, Haynes Alloy No. 188 Aging Characteristics, in: Int. Symp. Struct. Stab. Superalloys, Seven Springs, PA, 1968: pp. 460–500. https://doi.org/10.7449/1968/superalloys_1968_460_500.

[11] D.L. Klarstrom, Wrought cobalt- base superalloys, J. Mater. Eng. Perform. 2 (1993) 523–530. https://doi.org/10.1007/BF02661736.

[12] Special Metals, INCONEL® alloy 718, (2007) 1–28. https://www.specialmetals.com/assets/smc/documents/inconel_alloy_718.pdf (accessed May 8, 2020).

[13] X. Xu, S. Ganguly, J. Ding, C.E. Seow, S. Williams, Enhancing mechanical properties of wire + arc additively manufactured INCONEL 718 superalloy through in-process thermomechanical processing, Mater. Des. 160 (2018) 1042–1051. https://doi.org/10.1016/j.matdes.2018.10.038.

[14] A. Mitchell, Primary Carbides in Alloy 718, in: 7th Int. Symp. Superalloy 718 Deriv. 2010, The Minerals, Metals & Materials Society, 2010: pp. 161–167. https://www.tms.org/superalloys/10.7449/2010/Superalloys_2010_161_167.pdf.

[15] M. Schwartz, R. Ciocoiu, D. Gheorghe, G. Jula, I. Ciucă, Preliminary research for using Rene 41 in confectioning extrusion dies, Mater. Characterisation VII. 1 (2015) 95–106. https://doi.org/10.2495/mc150091.

[16] M. Kaufman, Control of Phases and Mechanical Properties in Nickel-base Alloys of Rene 41 Type, Trans. Metall. Soc. AIME. 227 (1963) 405.

[17] Rolled Alloys, Data Sheet Rene 41, (2011). http://www.rolledalloys.com/alloys/cobalt-alloys/rene-41/en/ (accessed July 5, 2022).

[18] S.E. Atabay, O. Sanchez-Mata, J.A. Muñiz-Lerma, R. Gauvin, M. Brochu, Microstructure and mechanical properties of rene 41 alloy manufactured by laser powder bed fusion, Mater. Sci. Eng. A. 773 (2020) 1–10. https://doi.org/10.1016/j.msea.2019.138849.

[19] E. Ungureanu, D.C. Anghel, D. Negrea, A.G. Plaiau, V. Rizea, M.M. Dicu, C.M. Ducu, M. Abrudeanu, Influence of thermal shocks at high temperatures on microstructure and hardness of RENE 41 alloy, in: IOP Conf. Ser. Mater. Sci. Eng., 2019. https://doi.org/10.1088/1757-899X/564/1/012046.

[20] L.A. Middleton, N.F. Kennon, D.P. Dunne, N. South, Metallographic Preparation, Metallography. 17 (1985) 51–59.

[21] J. Li, H.M. Wang, H.B. Tang, Effect of heat treatment on microstructure and mechanical properties of laser melting deposited Ni-base superalloy Rene’41, Mater. Sci. Eng. A. 550 (2012) 97–102. https://doi.org/10.1016/j.msea.2012.04.037.

[22] M.J. Donachie, S.J. Donachie, Superalloys - A Technical Guide, 2nd ed., ASM International, 2002.

https://app.knovel.com/hotlink/toc/id:kpSATGE003/superalloys-technical/superalloys-technical.

[23] W.S. James, S. Ganguly, G. Pardal, Selection and performance of AM superalloys for high-speed flight environments, Int. J. Adv. Manuf. Technol. 122 (2022) 2319–2327. https://doi.org/10.1007/s00170-022-10005-9.

[24] ASM Committee of Metallography of Heat-Resisting Alloys, Microstructures of Wrought Heat-Resisting Alloys, in: ASM Met. Handb. Vol. 7 Atlas Microstruct. Ind. Alloy., 8th ed., ASM International, 1972: pp. 165–192.

[25] Haynes International, HAYNES® 188 alloy: Principle Features, (2015). http://www.haynesintl.com/alloys/alloy-portfolio_/High-temperature-Alloys/HAYNES188alloy.aspx (accessed May 9, 2020).

[26] ASM Handbook Committee, Visual Examination and Light Microscopy, in: G.F. Vander Voort (Ed.), Fractography, 8th ed., ASM International, 1987: pp. 91–165. https://doi.org/10.31399/asm.hb.v12.a0001834.

[27] S. Mahadevan, S. Nalawade, J.B. Singh, A. Verma, B. Paul, K. Ramaswamy, Evolution of δ phase microstructure in alloy 718, 7th Int. Symp. Superalloy 718 Deriv. 2010. 2 (2010) 737–750. https://doi.org/10.1002/9781118495223.ch57.

[28] X. Xu, J. Ding, S. Ganguly, S. Williams, Investigation of process factors affecting mechanical properties of INCONEL 718 superalloy in wire + arc additive manufacture process, J. Mater. Process. Technol. 265 (2019) 201–209. https://doi.org/10.1016/j.jmatprotec.2018.10.023.

[29] Battelle Memorial Institute, Heat-Resistant Alloys, in: Met. Mater. Prop. Dev. Stand., Battelle Memorial Institute, 2017. https://app.knovel.com/hotlink/pdf/id:kt00CX2NX1/metallic-materials-properties/metallic-m-mechanical.

[30] G.A. Greene, C.C. Finfrock, Oxidation of inconel 718 in air at high temperatures, Oxid. Met. 55 (2001) 505–521. https://doi.org/10.1023/a:1010359815550.

[31] C.E. Seow, H.E. Coules, G. Wu, R.H.U. Khan, X. Xu, S. Williams, Wire + Arc Additively Manufactured Inconel 718: Effect of post-deposition heat treatments on microstructure and tensile properties, Mater. Des. 183 (2019) 108157. https://doi.org/10.1016/j.matdes.2019.108157.

[32] X. Xu, J. Ding, S. Ganguly, C. Diao, S. Williams, Oxide accumulation effects on wire + arc layer-by-layer additive manufacture process, J. Mater. Process. Technol. 252 (2018) 739–750. https://doi.org/10.1016/j.jmatprotec.2017.10.030.

7.8 Appendix: Stress – strain curves

The following graphs present the stress-strain curves for all samples tested in this study, grouped by testing temperature.

7.8.1 Inconel 718

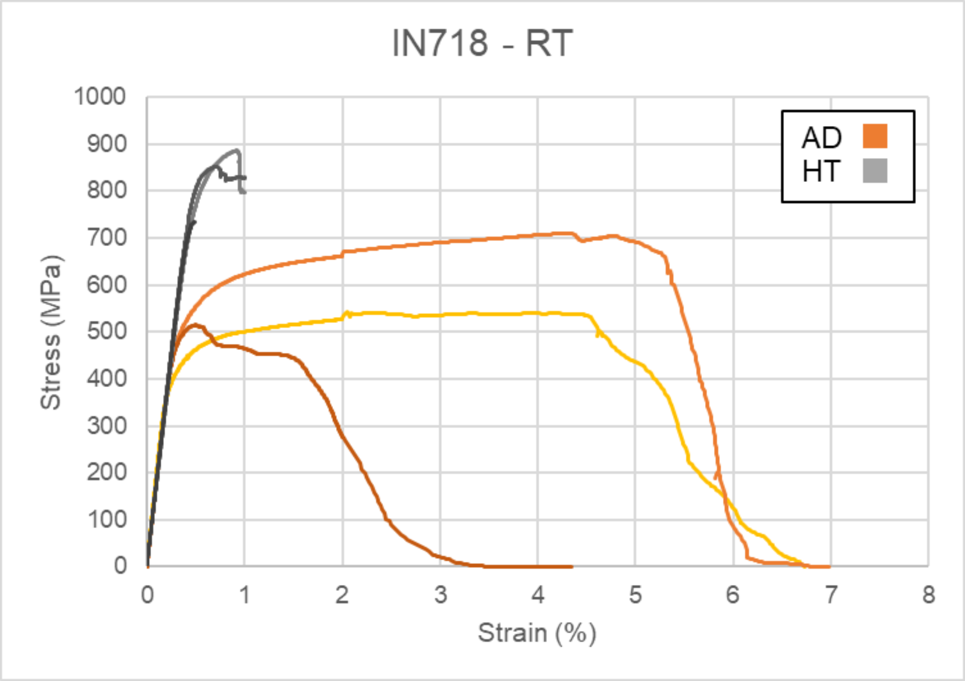

Figure 7-22 Stress-strain IN718 at RT.

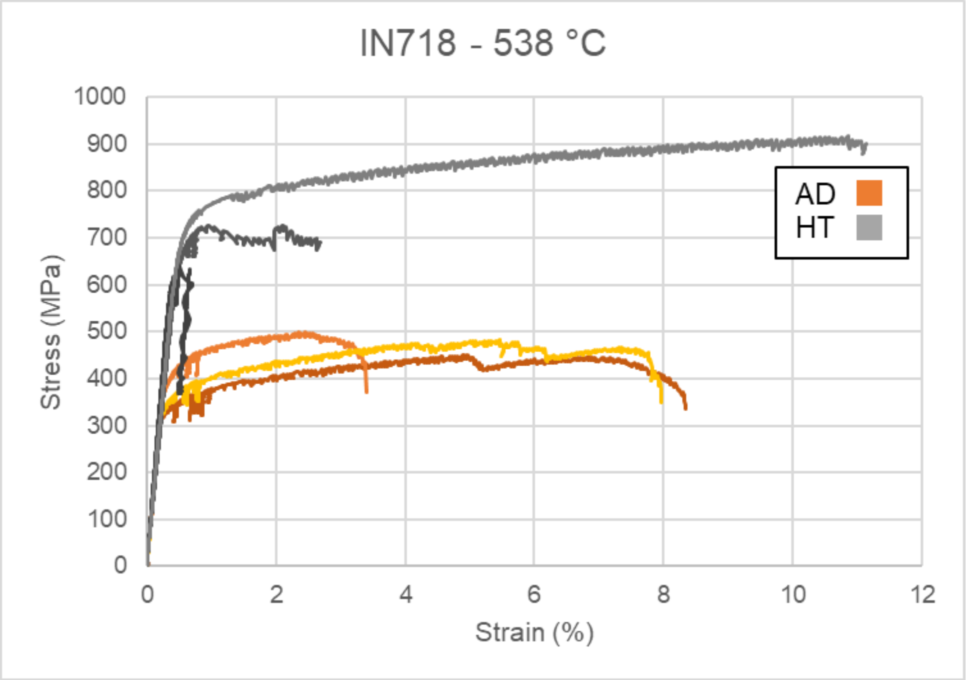

Figure 7-23 Stress-strain IN718 at 538 °C.

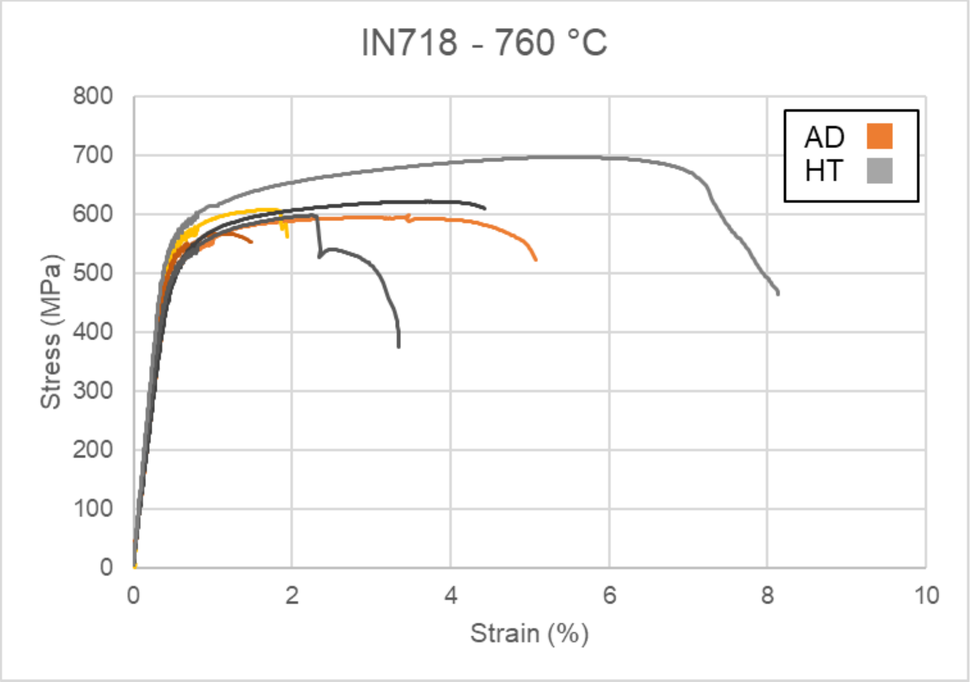

Figure 7-24 Stress-strain IN718 at 760 °C.

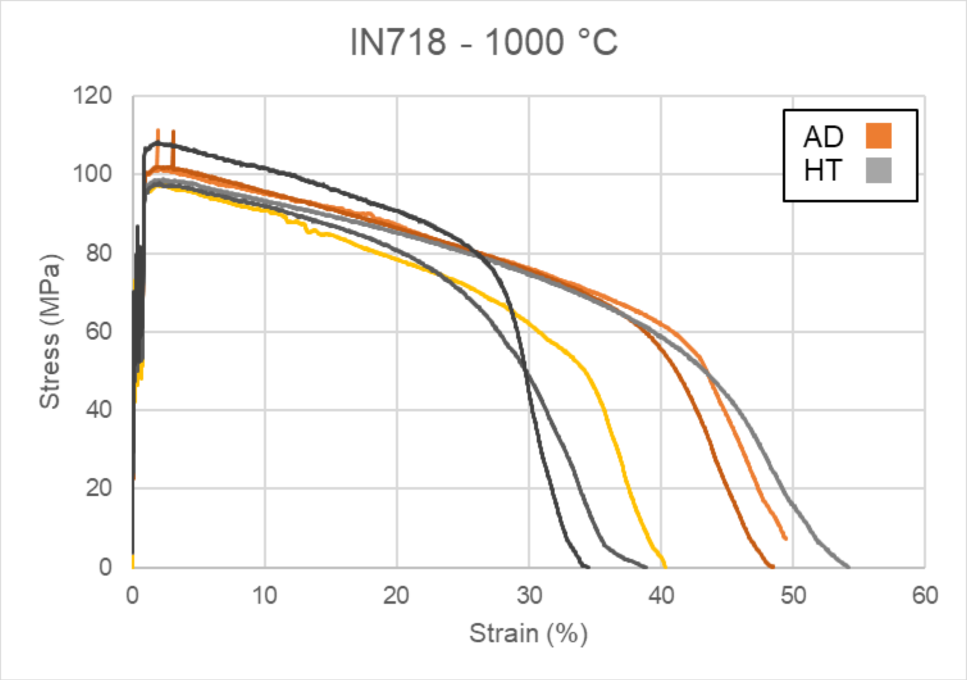

Figure 7-25 Stress-strain IN718 at 1000 °C.

7.8.2 Rene 41

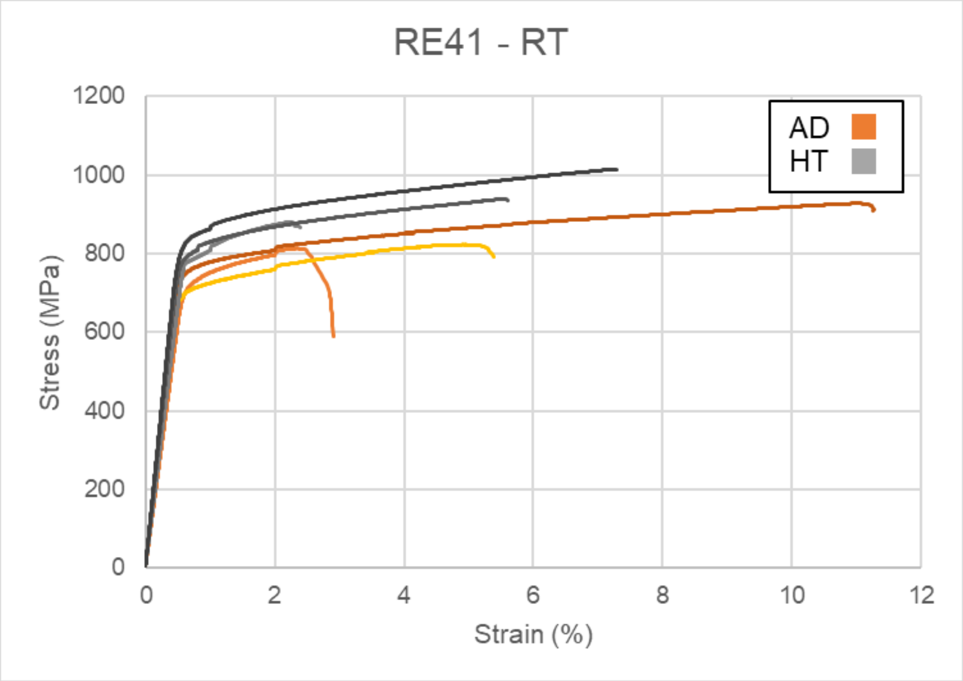

Figure 7-26 Stress-strain RE41 at RT.

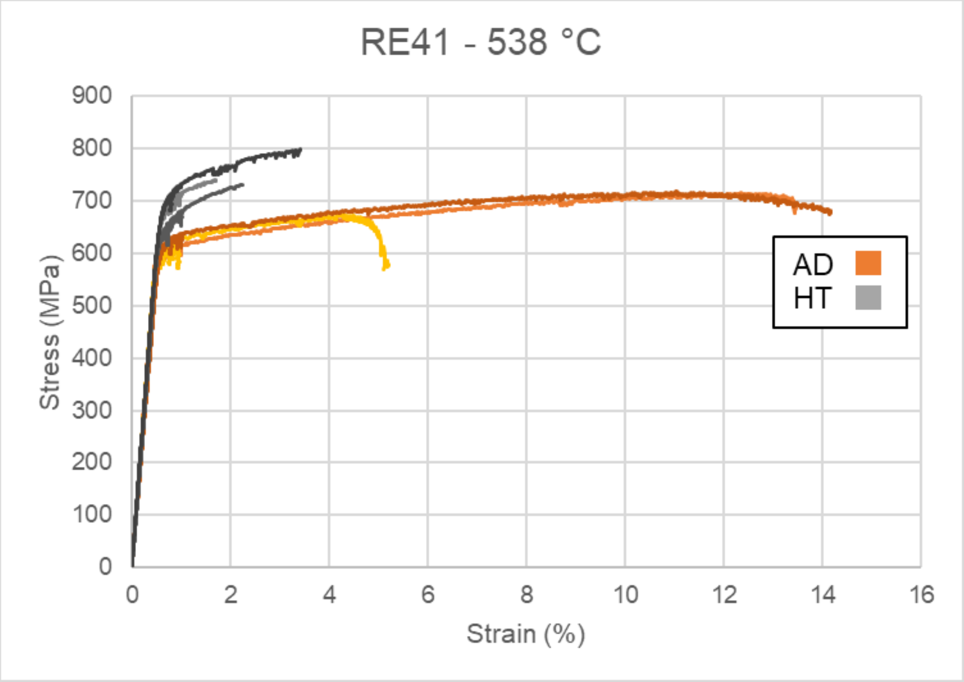

Figure 7-27 Stress-strain RE41 at 538 °C.

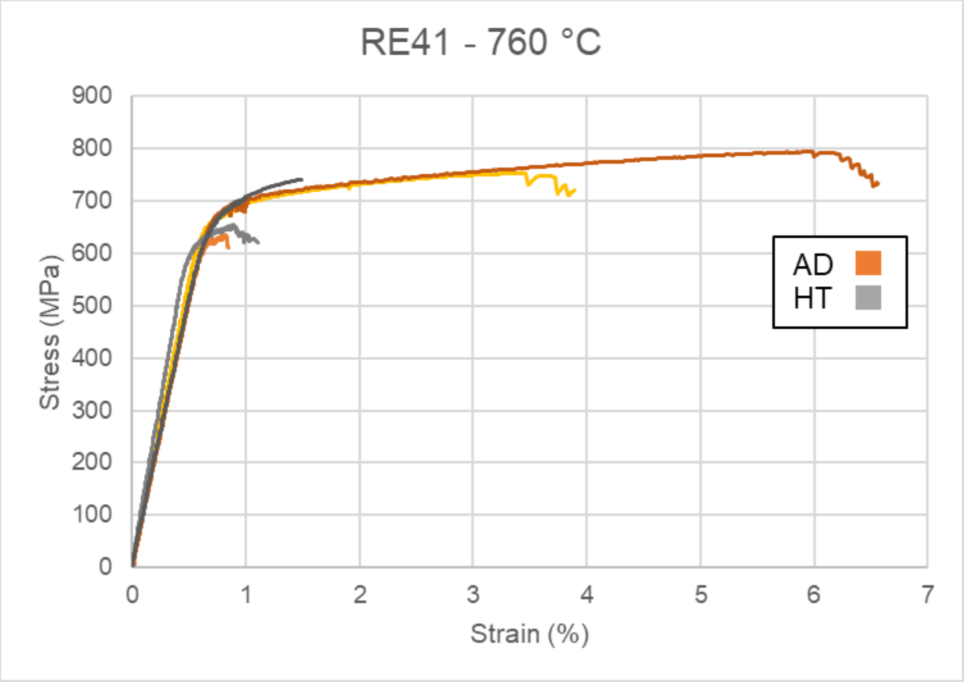

Figure 7-28 Stress-strain RE41 at 760 °C.

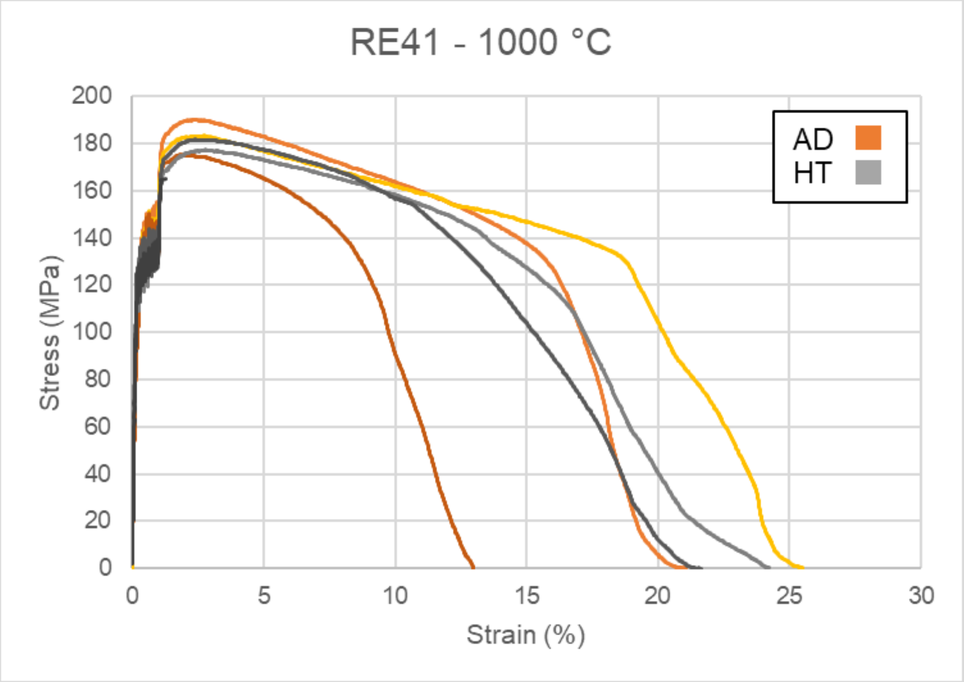

Figure 7-29 Stress-strain RE41 at 1000 °C.

7.8.3 Haynes 188

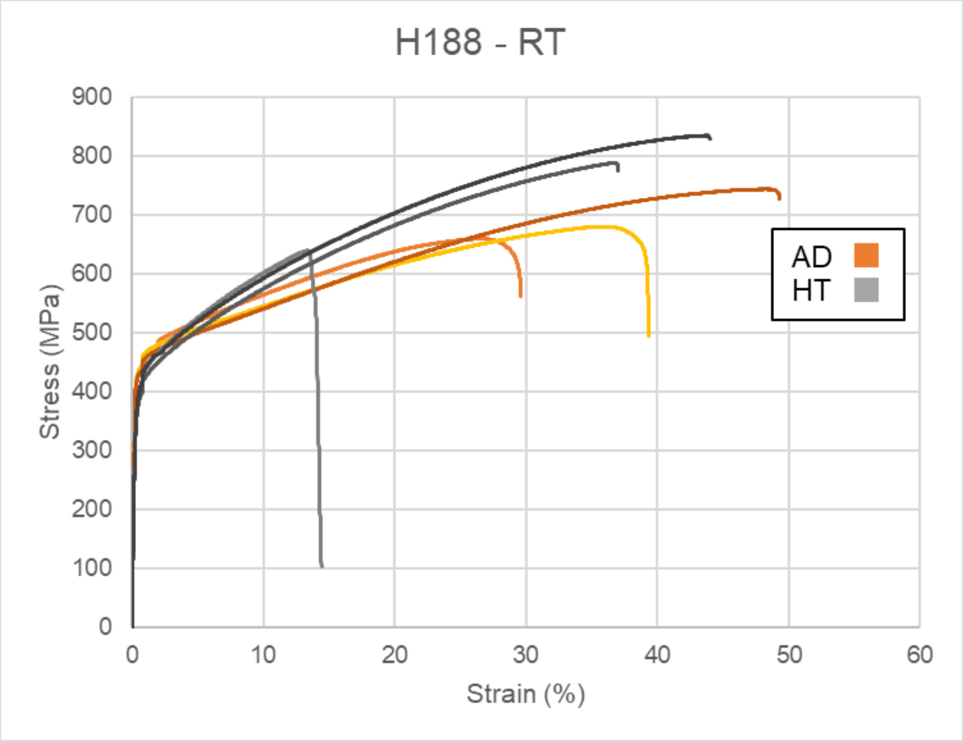

Figure 7-30 Stress-strain H188 at RT.

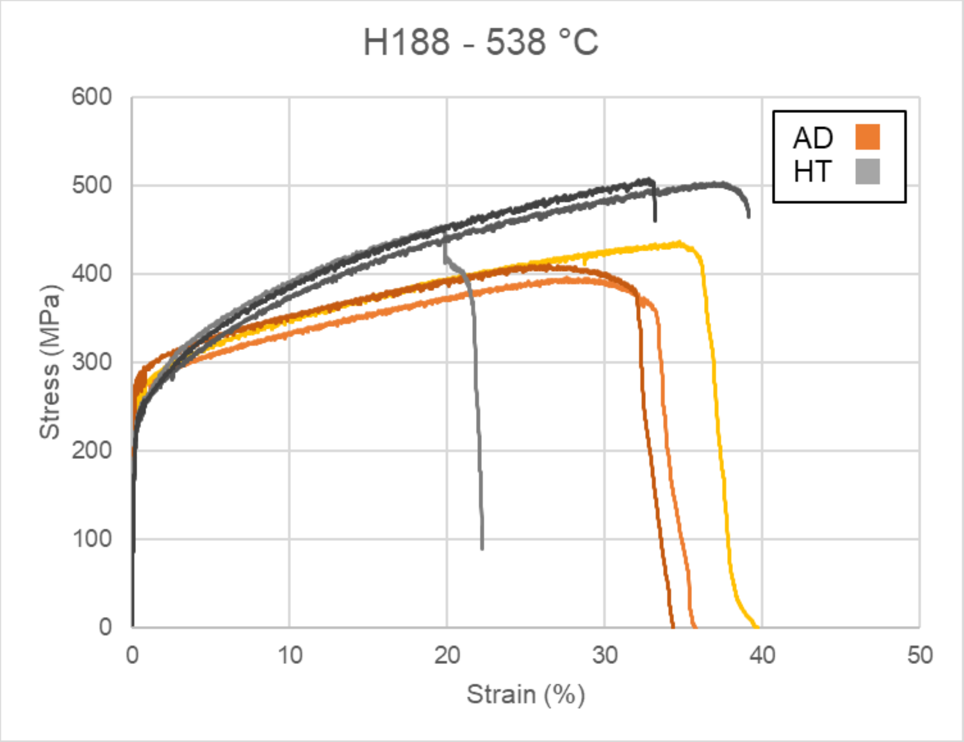

Figure 7-31 Stress-strain H188 at 538 °C.

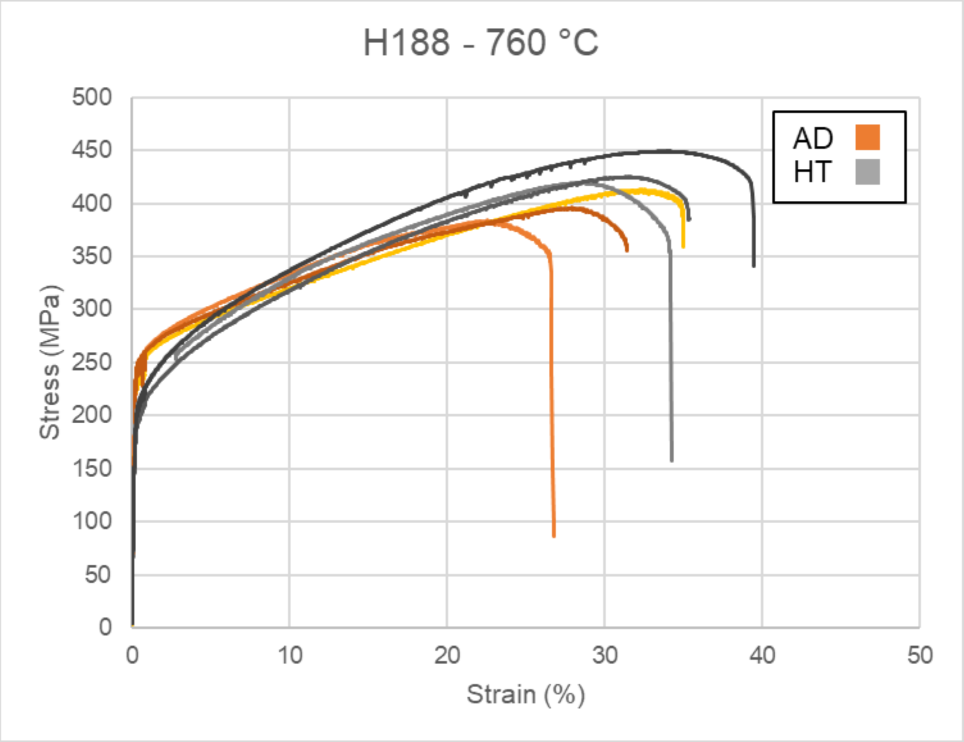

Figure 7-32 Stress-strain H188 at 760 °C.

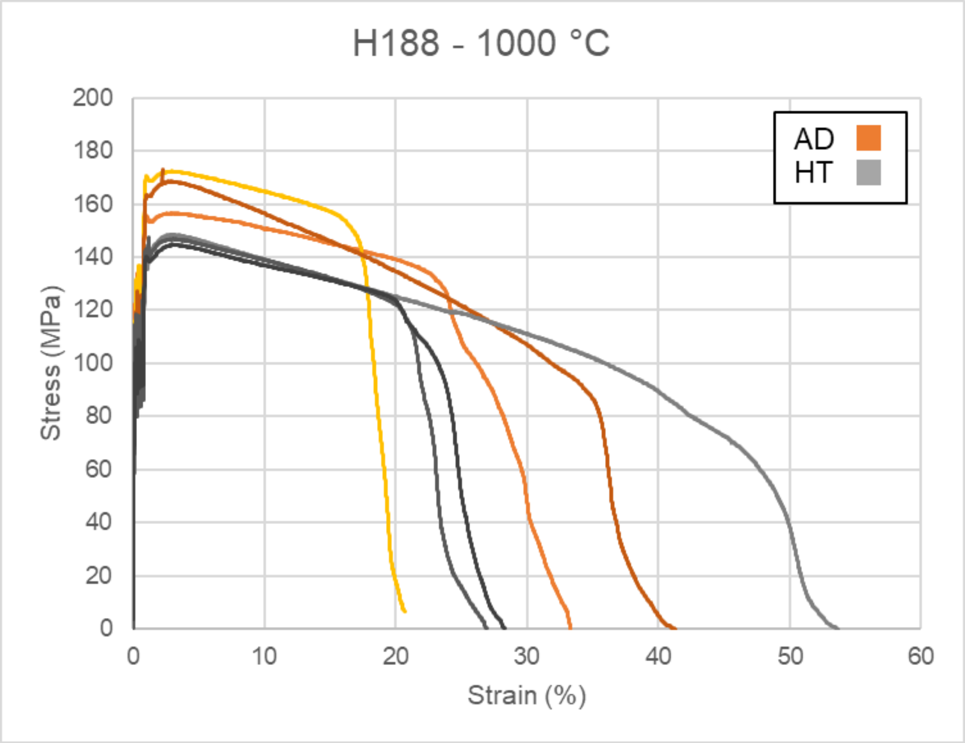

Figure 7-33 Stress-stain H188 at 1000 °C.

8 IN-PROCESS MECHANICAL WORKING OF ADDITIVE MANUFACTURED RENE 41

This chapter is based on the following publication.

***W.S. James**, S. Ganguly, G. Pardal, In-process Mechanical Working of Additive Manufactured Rene 41, in: Int. Addit. Manuf. Conf. I-AM 2022, ASME, 2022.*

After down selecting RE41 as the final alloy for ongoing study, this chapter presents the findings of investigations into the use of inter-pass peening during the WAAM process, in an effort to return the alloy to the wrought performance.

Abstract

In developing the wire + arc additive manufacturing (WAAM) process for creep resistant alloys for defence applications, structures were built from nickel-based superalloy Rene 41 (RE41). The performance of the additive manufactured alloy was analysed for applications including components used in high-speed flight environments, where external structures could reach service temperatures of up to 1000 K. As a single use system with relatively short flight times of < 1 hour, components will be highly stressed to minimise structural mass. In this paper, three wall structures were deposited using a plasma transferred arc process, in a layer-by-layer manner where each layer was mechanically worked by machine hammer peening after each deposited layer. With a constant impact frequency, three different travel speeds for the peening tool were used for each wall structure. To understand the most effective cold working parameters, samples were tested and analysed for their mechanical properties and microstructural characteristics after aging treatment. Samples were tested at room temperature and compared with results of both non-worked heat-treated AM material and wrought data obtained from literature review.

Heat-treated only material showed a typical dendritic structure with large columnar grains, and peened material showed a significantly different grain structure. No noticeable difference was observed in the formed phases between the two conditions. Mechanical testing showed promising results with a significant improvement over the non-worked strength. Intermediate and slow peening speeds were very effective, achieving UTS and YS results close to that of the wrought alloy, with a similar increase in the elastic modulus compared to non-worked material. However, faster peening speeds were less effective at returning the material to wrought strength.

Keywords: Additive manufacturing, Direct energy deposition, Hammer peening, Mechanical properties, Microstructure, Rene 41

8.1 Introduction

Wire + arc additive manufacturing (WAAM) is a directed energy deposition (DED) metal AM process whereby a wire feedstock is deposited using an electrical arc as a heat source [1]. In previous studies using WAAM to deposit nickel-based superalloys, as deposited (AD) material has been unable to match the performance of the fully heat-treated (HT) wrought alloy strength, and heat-treating WAAM material does not result in a sufficient increase to match wrought strength [2]. When deposited via WAAM and tested for mechanical performance, nickel-based superalloy Rene 41 (RE41) achieved just 59 % of the wrought UTS in AD condition and 61 % when the same material was HT post-deposition [3].

Highlighting the need for additional processing to meet the wrought performance, a previous study by Xu et al found that inter-pass cold rolling of WAAM Inconel 718 was able to increase the UTS of the material to where the rolled WAAM material outperformed the wrought material in both the vertical and horizontal orientations when tested [2]. In developing the WAAM process for maximising the performance of components built using RE41, a series of trials using inter-pass peening was investigated and tested to establish the most suitable peening parameters.

Large columnar grains are typically observed in WAAM built nickel-superalloy microstructure with associated segregation, which can have undesirable effects on the material properties, such as reduced strength. In most cases this is due to the nickel-superalloy being precipitation strengthened or age hardened, meaning that the strength is derived mainly from the precipitation of secondary phases, such as γ', within the matrix and at the grain boundaries which inhibit dislocation motion. An elongated dendritic structure with associated segregation makes the solutionising process difficult compared to a wrought structure where smaller grains with high angle grain boundaries facilitate the diffusion process, as such most of the wrought structures are dynamically recrystallised during rolling or other high temperature deformation processes. The large dendritic grains which make up the microstructure in WAAM material make the formation of these secondary precipitates less likely to occur, as the process of diffusion is hindered due to lack of grains with large angle boundary area and segregation owing to solidification from a molten state. Xu et al also examined the effect of heat-treating WAAM built Inconel 718 and found that unless the material underwent a process to produce a more favourable microstructure the mechanical strength is unlikely to meet the wrought performance through an age hardening heat-treatment alone [4]. It should be noted that there are cases where large grains are benefitable to the performance of nickel superalloys, such as in gas turbine blades, where a single crystal is specially formed in the correct orientation to primarily improve fatigue performance [5].

RE41 shares some similarities with the strengthening mechanism of Inconel 718, however the composition varies. RE41 is a nickel-based precipitation strengthened alloy which is alloyed significantly with Cr, Co and Mo. RE41 has a face-centred-cubic austenitic matrix, and is mainly strengthened through the formation of γ' particles $Ni_3(Al,Ti)$ [6].

The benefits of WAAM over other metal AM processes such as powder bed processes, is the ability to build larger components with little adjustment or expensive equipment set-ups. WAAM is also capable of higher deposition rates when compared with power bed, which increases productivity for larger components. The metal wire feedstock used in WAAM is often less expensive than metallic powder and is easier to change for a different alloy without the need for extensive cleaning. Material loss in WAAM is also much reduced compared to powder bed which can be as much as 25 % [7]. Powder-bed does however have some advantages over WAAM, which includes the ability to create more intricate and complex lattice structures and net shape parts, whereas WAAM is a near net shape process. Parts produced using powder bed also more closely match the wrought strength of alloys [8], compared with WAAM where the need for post-processing and/or in-process working is more extensive.

The ability to manufacture larger components makes WAAM ideal for defence applications and the production of high-speed flight components. The application of such components will be in the external structure of a single use system subjected to service temperature of 1000 K for a short flight time of < 1 hour. As such components for use in this system will be highly stressed to minimise structural mass, these components will be optimised for maximum strength at maximum temperature. It is therefore the aim of this research to maximise the performance of WAAM built RE41 for this purpose.

8.2 Materials & Methods

8.2.1 WAAM Process

A commercially available 1 mm diameter RE41 wire was used as the feedstock in a WAAM system (Figure 8-1) consisting of: a Kuka six-axis robotic arm, a plasma water-cooled welding torch mounted to the robotic arm, a local shielding device surrounding the plasma torch, and a wire feeder. To facilitate the inter-pass mechanical working, an Atlas Copco RRH06P riveting hammer was also mounted to the robotic arm and configured to allow for semi-automatic operation. The riveting hammer was manually operated via a gas line valve during the automatic WAAM deposition program.

The composition of the RE41 wire was tested as part of a previous study using inductively coupled plasma - optical emission spectroscopy (ICP-OES), the composition is given in Table 8-1 [3].

A short wall approach was adopted in-order to build enough material to extract specimens for metallographic and tensile analysis. Four walls measuring approx. 360 × 20 × 8 mm were built on an Inconel 718 substrate plate, using an arc current of 180 A, a wire feed speed of 2.4 m/min, a torch travel speed of 0.36 m/min, a torch to work distance of 8 mm, and an inter-pass temperature of 170 °C after an approx. cooling time of 3 mins. Shielding via a local shielding device, as shown in Figure 8-1, was provided at 30 L/min of Argon. To establish the best peening parameters one wall was built AD, without any inter-pass peening to provide a baseline. Three further walls were built using a constant impact frequency of 2160 impacts per min with a load of 30 kg, where the tool travel speed was varied for each wall. Three different travel speeds of 18, 36, and 112.5 mm/s were trialled during manufacture of the walls. The use of these peening parameters provided an input energy of approx. 4.85, 2.43, 0.776 J/mm^2 for the 18, 36, and 112.5 mm/s travel speed respectively. Input energies were calculated as in Equation 8-1.

After the walls were manufactured, specimens for tensile, microhardness and metallographic analysis were extracted. All specimens underwent an aging heat-treatment to maximise tensile performance based on historic research by Weisenberg and Morris. The treatment consisted of: solutionising at 1065 °C for four hours followed by air quenching to room-temperature (RT) followed by a further 16 hours aging at 760 °C after which the material was again air quenched [9].

Equation 8-1 Actual energy input by the peening process.

$$Actual\ Energy\ Input \quad (J/mm^2) = \frac{\frac{1}{2}m\left(\frac{d\cdot f}{0.5}\right)^2}{\left[1-\left(1-\frac{TS}{\emptyset\cdot f}\right)\right]\cdot \pi r^2}$$

m	mass impacting the work piece in kg
d	vertical distance, and range of motion of the peening tool head in metres.
f	frequency the tool is impacting the work piece
TS	travel speed of the tool in the horizontal plane in mm/s
$\emptyset$	diameter of the head that impacts the work piece in mm
r	the radius of the head that impacts the work piece in mm.

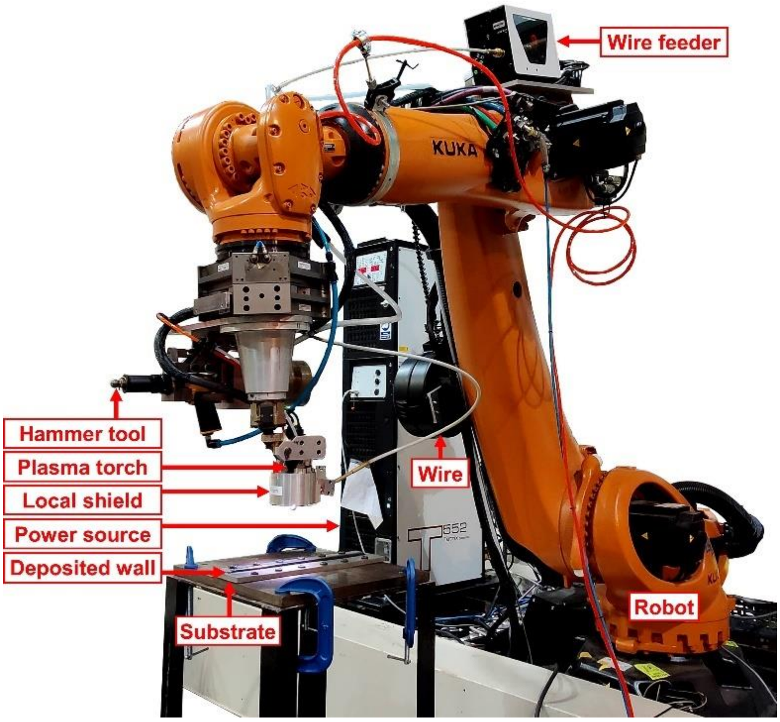

Figure 8-1: WAAM experimental setup.

Table 8-1: Composition of RE41 wire.

Ni	Cr	Co	Mo	Fe	Ti	Al	Nb	V	Si	C	Cu	Mn	B	S
53.7	18.9	10.2	9.08	2.72	3.20	1.64	0.12	0.12	0.09	0.07	0.04	0.03	0.004	<0.003

8.2.2 Mechanical Testing

Three tensile specimens in each condition were tested at RT to failure using an Instron 8801 Servo Hydraulic Universal Testing System. A strain rate of 0.005 mm/min was adopted until plastic deformation whereafter a rate of 1.6 mm/min was used. Testing was conducted according to the ASTM specification E8/E8M, a standard test method for tension testing of metallic materials. The specimen dimensions conformed to the sub-size category, a drawing of which is given in Figure 8-2.

Microhardness was measured using a Zwick/Roell hardness tester under a load of 0.5 kg and a holding time of 15 sec. Measurements were taken at 1 mm increments through the cross-section of the wall height and thickness.

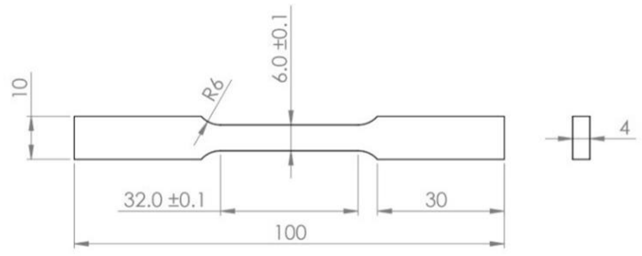

Figure 8-2: Tensile testing specimen. (Dimensions in mm).

8.2.3 Metallographic Preparation and Analysis

Cross-sections in the build direction (BD) and through-thickness (TT) plane were extracted and prepared for metallographic analysis to reveal the microstructure. Following a procedure of successive grinding and polishing, samples were swab etched for 30 sec using a solution containing 3 g $CuSO_4$, 80 ml HCl, and 20 ml Ethanol.

Samples were viewed optically using a Leica DM 2700M Microscope. The microstructure was also examined using a Tescan VEGA 3 scanning electron microscope (SEM). Composition was determined by energy-dispersive spectrometry (EDS), as such the SEM was fitted with an Oxford Instruments X-Max 20 mm EDS detector.

To grain structure of the worked and non-worked material was analysed for comparison using an Oxford Instruments Symmetry electron backscatter diffraction (EBSD) detector, fitted to a Tescan S8000G SEM.

8.3 Results & Discussion

8.3.1 Mechanical

When tested at RT, tensile specimens extracted from material mechanically worked using 4.85, 2.43, and 0.776 J/mm^2, achieved an average UTS of 1284.5, 1299.4, and 1048.3 MPa and a YS of 1048.7, 1054.0, and 906.1 MPa respectively. The full set of results is presented in Table 8-2, where the working energies are abbreviated as W High, W Med, and W Low for 4.85, 2.43, and 0.776 J/mm^2, respectively. Figure 8-3 presents the stress-strain variations of material in the AD [3] and HT condition together with the worked HT material. It can be seen that with the application of higher impact energy per unit area, the elastic modulus of the material increases with the tensile strength and almost meets the performance of the wrought variant. In comparing the UTS and YS results the best performance was achieved through peening at 2.43 J/mm^2. However, when the variation in results is accounted for, it can be assumed that between the 4.85 and 2.43 J/mm^2 impacting energies, the maximum performance increase possible had been achieved by working at just 2.43 J/mm^2, due to the negligible difference in performance. Subsequently in future studies on inter-pass peening of RE41, there would be little advantage to peening beyond 2.43 J/mm^2. Overpeening is possible and the effects can include excessive surface defects and microcracking which is detrimental to fatigue strength [10].

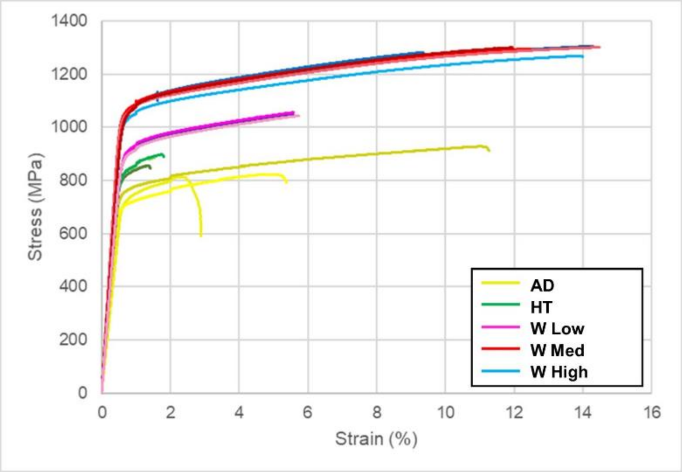

Figure 8-3: Stress-Strain of RT Mechanical Performance.

In comparing the hardness of RE41 in each condition presented in Table 8-2, the hardness is seen to increase with impacts per area and is significantly higher than the wrought minimum. The hardness of the material affects the machinability, and difficulties were encountered during the manufacture of the tensile coupons. It is noted by Weisenberg and Morris that the rate at which RE41 work hardens makes it particularly difficult to machine, and they recommend the use of carbide tools and sulphurated oils [9]. Silicon carbide cutting disks were utilised for cutting the deposited walls from the substrate plates which worked relatively well.

Table 8-2: Mechanical performance at RT.

Condition	UTS (MPa)	YS (MPa)	E (GPa)	HV
Wrought [11]	1420	1060	220	363 (min)
HT	880.8	829.4	161	406
HT + W Low	1048	906.1	157	437
HT + W Med	1299	1054	194	443
HT + W High	1285	1049	186	459

The elastic modulus (E) is also shown to vary in the results, although there is not a great deal of correlation between the working energy. Peening at room temperature hydrostatically deforms the alloy and generates dislocations and other associated metal defects which strain hardens the alloy. Subsequent transitory thermal cycles, during deposition of successive layers, would annihilate some of these dislocations but some hardening effects will remain, which would work to make the deposit stiffer when compared to the non-worked variant. It should also be noted this difference could be due to E being calculated from tensile data which can be error prone. Further investigation is required to fully discuss this observation.

8.3.2 Microstructural Observations

Of the examined specimens there are observable differences in the macrostructure of the HT and worked material, seen in Figure 8-4. The main differences are in the granular structure, where the dendritic structure of the worked material has been disrupted by the peening process, leading to the disruption of the long columnar grain structure which is so typically observed in alloys deposited via wire-arc DED processes. This effect is best observed when comparing HT material in Figure 8-5 and the worked material Figure 8-6.

No cracking was observed in worked material; however, several large solidification cracks were observed in the HT material (Figure 8-4), note that of these cracks only the largest is visible in Figure 8-4. Solidification cracks were identified based on orientation along the BD axis owing to lateral stresses and segregation at the crack edge.

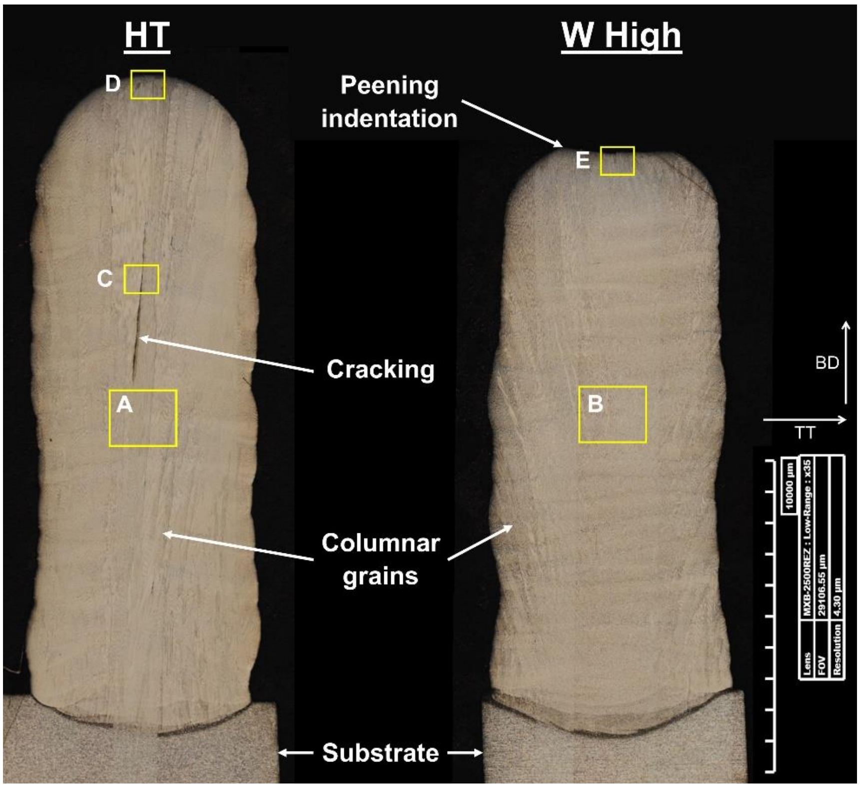

Figure 8-4: Macrostructure of HT and Worked (W High) material. Areas A-E correspond to following micrographs.

The crack edge segregation can be seen in Figure 8-7. It is thought that the stress input into the material due to peening has allowed for relaxation of the strain created during the deposition process, which has subsequently resulted in the elimination of cracking. Cracking has been known to occur in DED built superalloys, notably in WAAM built Inconel 718 [12]. Atabay et al found that RE41 did not experience cracking when used in laser powder bed fusion (LPBF), and attributed this to the fine microstructure produced when using LPBF [13]. It is possible that the disruption of the typically larger grain structure seen in WAAM components has resulted in both an increased strength and a reduction in susceptibility to cracking.

When the microstructure is examined at greater magnification using a SEM the difference between HT only (Figure 8-8) and worked material (Figure 8-9) is negligible, with the same phases observed in both specimens, indicating that the in-process working has no impact on the formed phases. An EDS mapping (Figure 8-10) and composition table (Table 8-3) is provided for the phases observed in the worked material. Lighter coloured areas are indicative of Mo rich phases, likely a complex intermetallic known as σ phase (CrNiMo) which is known to occur in nickel superalloys [14], these phases were analysed using EDS and the results are presented in Table 8-3. The darker grey coloured phases however are indicative of Ti rich precipitates, suggesting the presence of Ti rich carbides.

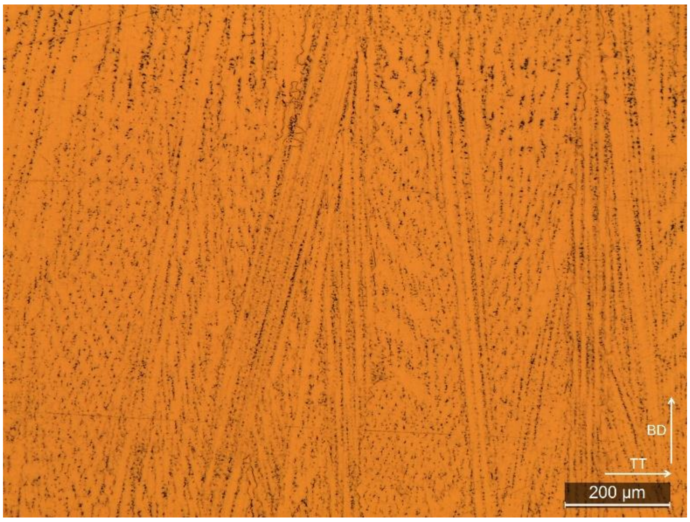

Figure 8-5: Micrograph of HT material displaying long columnar grain structure. Area A in Figure 8-4.

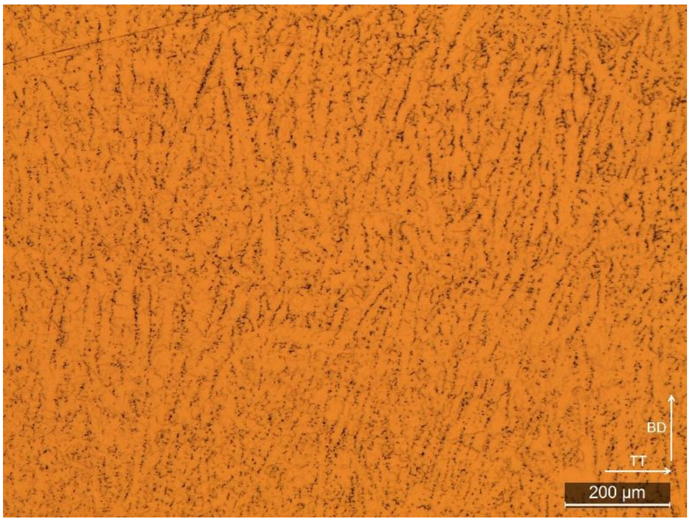

Figure 8-6: Micrograph of worked (W high) showing disrupted dendritic structure. Area B in Figure 8-4.

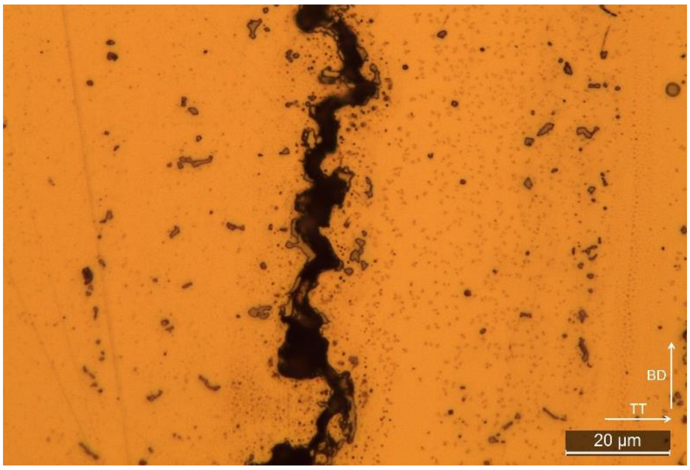

Figure 8-7: Solidification crack observed in HT sample seen in Figure 8-4. Area C in Figure 8-4.

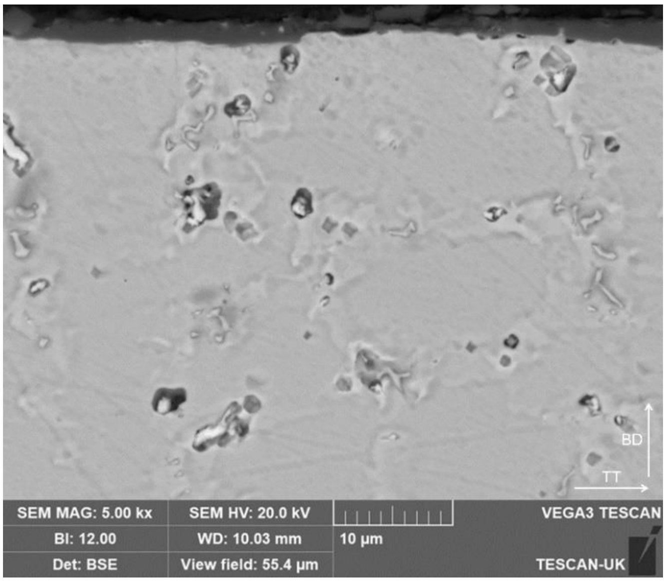

Figure 8-8: SEM BSE image of HT material. Area D in Figure 8-4.

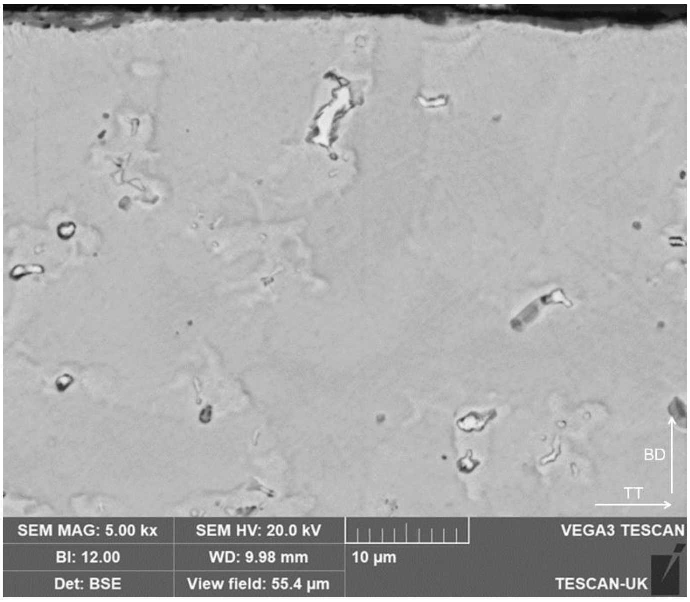

Figure 8-9: SEM BSE image of worked (W high) material. Area E in Figure 8-4.

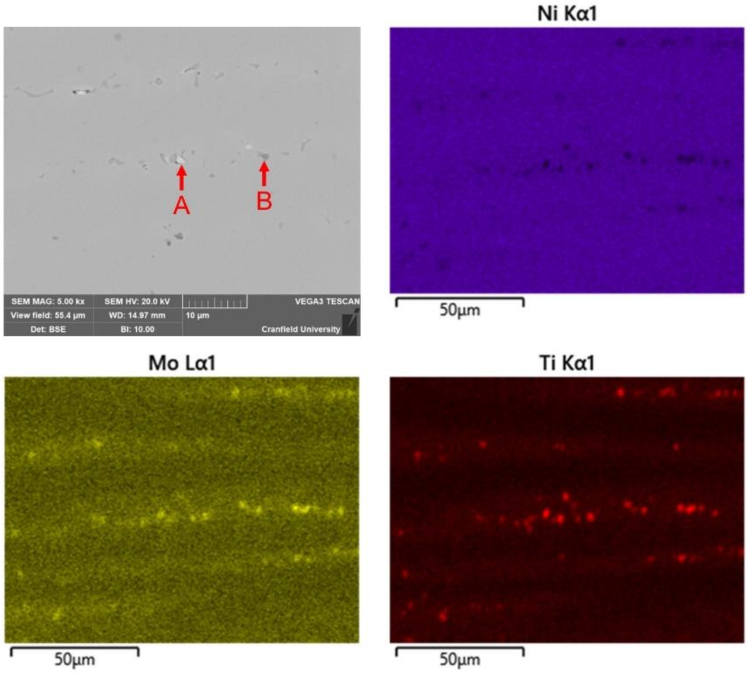

Figure 8-10: EDS elemental mapping of worked (W high) material, central location

Table 8-3: EDS composition of areas marked in Figure 8-10 (% at.).

Element	**Spectrum A**	**Spectrum B**
Al	1.25	1.58
Ti	3.24	28.44
V	0.17	0.38
Cr	31.29	15.68
Fe	2.18	1.78
Co	9.67	6.15
Ni	27.65	31.87
Mo	24.42	14.00

8.4 Grain refinement

The granular structure of RE41 in AD condition is large and columnar in its formation, which is typical of nickel alloys deposited using the WAAM process. However, after working even at the lowest input energy some refinement can be observed in the grain structure, and at the medium and highest input working energy significant refinement is made to the structure; note however that the refinement is largely in the core of the WAAM walls (see near to the top edges of the EBSD maps in Figure 8-11). The grain refinement being localised to the core of the walls is consistent with the findings of Hönnige et al. in MHP WAAM Ti-6Al-4V [15]. To achieve refinement of grains outside of the core in WAAM material McAndrew et al. studied the use of profiled rollers for interpass rolling of Ti-6Al-4V, and they found that using different profile rollers can induce grain refinement is specific areas [16], although the performance of interpass rolled RE41 is yet to be investigated.

Refinement amongst the medium and high working energies varies, with surprisingly more refinement made with the medium working energy, and in areas of refinement a greater level of plastic strain was observed in W High condition compared to W Med (Figure 8-12), which could explain the marginally higher tensile performance of RE41 worked with the medium input energy.

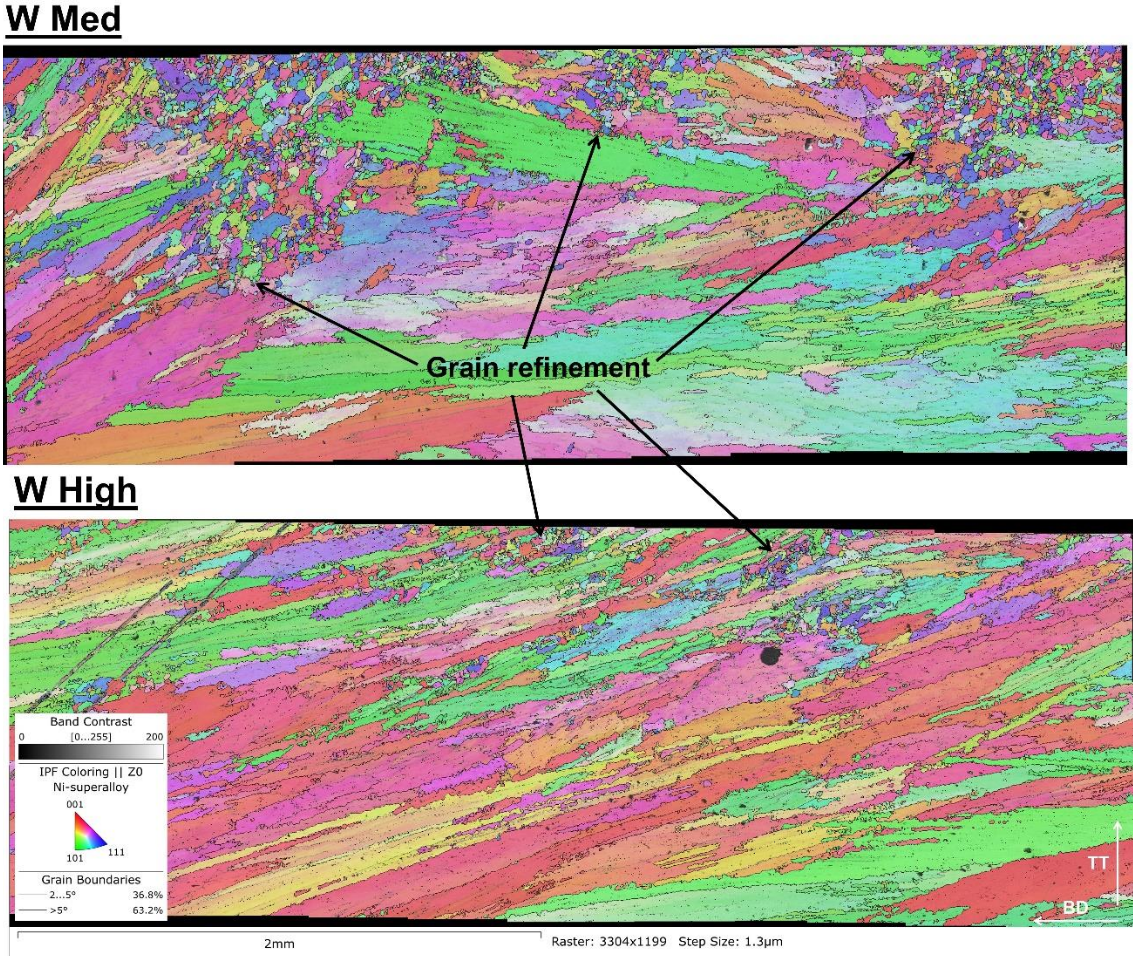
W Med

W High

Figure 8-11 EBSD orientation maps showing grain structure after each process.

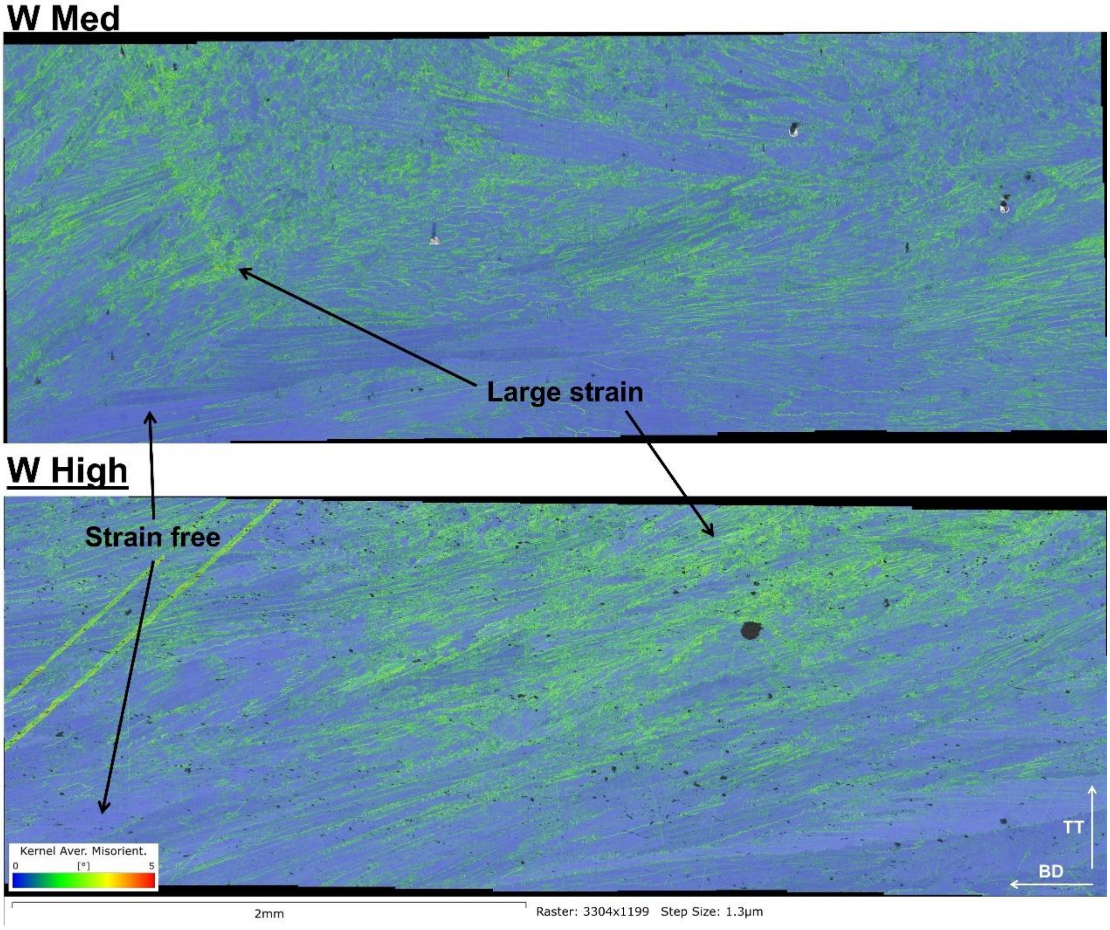

Figure 8-12 Plastic strain maps, showing higher strain in W High condition.

8.5 Conclusions

1. In-process working during WAAM deposition can increase the performance of RE41 to 92 % of the wrought strength, compared to 62 % for the HT only material.
2. Use of a peening energy density of more than 2.43 J/mm^2 does not result in any additional benefit. Although addition study is required to fully understand the relationship between peening energy and grain refinement.
3. RE41 work hardens quickly, and microhardness increases with work done.
4. In-process working of RE41 disrupts and refines the long columnar grain structure typically observed in wire-arc DED built material.

5. In-process working of RE41 results in a decreased susceptibility to cracking.

8.6 References

[1] S.W. Williams, F. Martina, A.C. Addison, J. Ding, G. Pardal, P. Colegrove, Wire + Arc additive manufacturing, Mater. Sci. Technol. 32 (2016) 641–647. https://doi.org/10.1179/1743284715Y.0000000073.

[2] X. Xu, S. Ganguly, J. Ding, C.E. Seow, S. Williams, Enhancing mechanical properties of wire + arc additively manufactured INCONEL 718 superalloy through in-process thermomechanical processing, Mater. Des. 160 (2018) 1042–1051. https://doi.org/10.1016/j.matdes.2018.10.038.

[3] W.S. James, S. Ganguly, G. Pardal, High temperature failure and microstructural investigation of additive manufactured Rene 41, Int. J. Adv. Manuf. Technol. 13 (2023) 4541. https://doi.org/10.1007/s00170-023-10885-5.

[4] X. Xu, J. Ding, S. Ganguly, S. Williams, Investigation of process factors affecting mechanical properties of INCONEL 718 superalloy in wire + arc additive manufacture process, J. Mater. Process. Technol. 265 (2019) 201–209. https://doi.org/10.1016/j.jmatprotec.2018.10.023.

[5] N.K. Arakere, G. Swanson, Effect of crystal orientation on fatigue failure of single crystal nickel base turbine blade superalloys, J. Eng. Gas Turbines Power. 124 (2002) 161–176. https://doi.org/10.1115/1.1413767.

[6] M. Schwartz, R. Ciocoiu, D. Gheorghe, G. Jula, I. Ciucă, Preliminary research for using Rene 41 in confectioning extrusion dies, Mater. Characterisation VII. 1 (2015) 95–106. https://doi.org/10.2495/mc150091.

[7] A.N.M. Tanvir, M.R.U. Ahsan, G. Seo, J. duk Kim, C. Ji, B. Bates, Y. Lee, D.B. Kim, Heat treatment effects on Inconel 625 components fabricated by wire + arc additively manufacturing (WAAM)—part 2: mechanical properties, Int. J. Adv. Manuf. Technol. 110 (2020) 1709–1721. https://doi.org/10.1007/s00170-020-05980-w.

[8] X. Wang, X. Gong, K. Chou, Review on powder-bed laser additive manufacturing of Inconel 718 parts, Proc. Inst. Mech. Eng. Part B J. Eng. Manuf. 231 (2017) 1890–1903. https://doi.org/10.1177/0954405415619883.

[9] L.A. Weisenberg, R.J. Morris, How to Fabricate Rene 41, Met. Prog. 78 (1960) 70–74.

[10] R.A. Antunes, M.C.L. de Oliveira, Effect of surface treatments on the fatigue life of magnesium and its alloys for biomedical applications, in: Surf. Modif. Magnes. Its Alloy. Biomed. Appl., Elsevier, 2015: pp. 283–310. https://doi.org/10.1016/B978-1-78242-077-4.00009-7.

[11] M.J. Donachie, S.J. Donachie, Selection of Superalloys, in: Superalloys - A Tech. Guid., 2nd ed., ASM International, 2002: pp. 11–24. https://app.knovel.com/hotlink/pdf/id:kt008GQQU1/superalloys-technical/superalloy-forms.

[12] W.S. James, S. Ganguly, G. Pardal, Microstructure and Mechanical Properties of Inconel 718 and Inconel 625 Produced Through the Wire + Arc Additive Manufacturing Process, in: AVT-356 Phys. Fail. Mil. Platf. Crit. Subsystems, STO NATO, 2021. https://www.sto.nato.int/publications/STO Meeting Proceedings/STO-MP-AVT-356/MP-AVT-356-21.pdf.

[13] S.E. Atabay, O. Sanchez-Mata, J.A. Muñiz-Lerma, R. Gauvin, M. Brochu, Microstructure and mechanical properties of rene 41 alloy manufactured by laser powder bed fusion, Mater. Sci. Eng. A. 773 (2020) 1–10. https://doi.org/10.1016/j.msea.2019.138849.

[14] H.E. Collins, Relative Stability of Carbide and Intermetallic Phases in Nickel-Base Superalloys, in: Int. Symp. Struct. Stab. Superalloys, TMS, 1968: pp. 171–198. https://doi.org/10.7449/1968/superalloys_1968_171_198.

[15] J.R. Hönnige, P. Colegrove, S. Williams, Improvement of microstructure and mechanical properties in Wire + Arc Additively Manufactured Ti-6Al-4V

with Machine Hammer Peening, Procedia Eng. 216 (2017) 8–17. https://doi.org/10.1016/j.proeng.2018.02.083.

[16] A.R. McAndrew, M. Alvarez Rosales, P.A. Colegrove, J.R. Hönnige, A. Ho, R. Fayolle, K. Eyitayo, I. Stan, P. Sukrongpang, A. Crochemore, Z. Pinter, Interpass rolling of Ti-6Al-4V wire + arc additively manufactured features for microstructural refinement, Addit. Manuf. 21 (2018) 340–349. https://doi.org/10.1016/j.addma.2018.03.006.

9 SUMMARY

9.1 Overall Discussion

The following discussion summarises the outcomes of this project into the real-world impacts they will have. It also makes recommendations to the sponsor based on the findings and the possible impacts they will have for the sponsors desired end application of WAAM components.

9.1.1 Alloy Selection

The selection of alloys suitable for both WAAM and the high-speed flight application was discussed in Chapter 3. The chapter focuses on the design of a selection process for nickel-based, nickel-iron, and cobalt-based superalloys, as well as mechanical testing to validate the chosen method. The selection method created was able to identify suitable alloys for both applications, eliminating alloys unsuitable for welding and alloys that perform poorly at high temperatures. Based on the large bank of literature data compiled for this process, it will be possible to adjust the criteria of the selection process for other applications in the future. For example, if the maximum operating temperature should need to be changed.

The findings in Chapter 3 demonstrate that as deposited precipitation-strengthened alloys perform poorly compared with their equivalent wrought performance. This leads to the recommendation that further investigation is required to establish a method of returning these alloys to their wrought strength. The study also found that as deposited solution-strengthened alloys suffer less so from this issue. This is thought to be due to the precipitation-strengthened alloys suffering from the WAAM aging effect, which is not appropriate to their respective strengthening mechanisms, resulting in formation of tcp type and other phases which negatively impact the performance. Solid-solution-strengthened alloys suffer less from this effect as they are not primarily strengthened by formation of secondary phases.

The conclusion of the chapter recommended RE41 for selection, however further work would be needed to return this alloy to its wrought performance. A further recommendation can be made to the sponsor from the findings of this chapter: If further post-processing is not desired or deemed too extensive to be cost-effective, use of a solution-strengthened alloy might prove more appropriate for selection.

9.1.2 High Temperature Performance

The high temperature tensile testing of WAAM superalloys, resulted in mixed performance, where results varied significantly between alloys. The high temperature performance of RE41 and H188 was discussed at length in Chapters 5 & 6 respectively. Overall, tested WAAM alloys followed their wrought performance albeit at a percentage lower than the wrought, indicating the need for post-processing. However, the difference between as deposited and heat-treated WAAM material was mainly measurable at lower temperatures. When tested at 760 °C and above the difference was negligible and, in some cases, heat-treating proved detrimental to the performance. This led to the conclusion that the precipitation-strengthened alloys, particularly RE41, would not require heat-treatments when subjected to service at or around its aging temperature as this would result in over-aging that would negatively impact its performance. It would seem to be more beneficial to alloy the alloy to age in-service and benefit from the temporary increase in strength that this affords, although further investigation into this temporary increase is required to understand exactly how long this can be benefited from during service,

H188, as was observed in RT tensile testing, performed much closer to its wrought performance, and it is thought that should testing be extended beyond 1000 °C H188 might outperform RE41. Although, given its lack of performance even compared with the reduced performance of RE41, H188 is still significantly weaker at the tested temperatures between RT – 1000 °C.

9.1.3 Microstructural Features

It is logical to assume that the cracking seen in the precipitation-strengthened alloys studied in this project, namely IN718 and RE41, contributed to their comparatively poor performance when compared with wrought material. This same lack of cracking seen in the solid-solution-strengthened alloys suggests that precipitation of phases within the alloy are responsible. Antonsson and Fredriksson observed solidification cracking in IN718 due to formation of NbC and Laves phases along grain boundaries, as a result of the segregation of elements [1]. It is then reasonable to assume that due to the segregation of alloying elements and their formation as detrimental phases, the alloying elements required for the formation of strengthening phases, such as γ’ and γ’’, were depleted, negating the possibility for their precipitation.

Various phases were observed across all of the alloys, mostly phases containing heavier alloying elements. Specifically focusing on the relationship between cracks and phases, these heavy element rich phases were observed at crack edges. This would support the observations of Antonsson and Fredriksson; crack edge phases observed in IN718 were rich in Nb, whereas in RE41 they were rich in Mo.

The more general microstructure of the deposited alloys included large columnar grains, which extended upwards in the build direction and outward as with the flow of heat. This structure was seen in previous studies of Ni-based alloys, particularly in the work of Xu et al [2], and was therefore expected to be observed in this project. The granular structure on this level was insignificantly different between the alloys, and change was only observed with the addition of inter-pass mechanical working into the WAAM process.

9.1.4 Effect of Mechanical Working

Including mechanical working as part of the WAAM process has demonstrated to be beneficial for alloy performance. Xu et al used inter-pass rolling to change the grain structure of WAAM IN718, which resulted in increased performance [3], and in Chapter 8 of this thesis, inter-pass machine hammer peening was found to greatly increase the performance of WAAM RE41. The effect that mechanical working appears to have on alloys is in the grain structure, with significant differences observed in the dendritic structure of RE41 after peening, compared with non-worked WAAM material. There was no observable difference beyond the granular structure, and formed phases appeared unchanged.

The performance increases due to disruption of the long dendritic structures seen in non-worked RE41, resulted in clear benefits for the tensile performance. With the performance on average jumping 48 % vs. non-worked specimens. And with YS and UTS near enough matching the wrought alloy.

The ideal microstructure, based on the increased performance of peened material, would seem to be a refined granular structure, perhaps because of strengthening phases forming at an increased number of grain boundaries, further investigation is however required to confirm this. A standard post-process heat treatment marginally increases the performance, and it is thought that a specially designed heat treatment should have a greater effect.

9.1.5 WAAM & the High-speed Flight Application

Overall, WAAM has been proven to be capable of depositing creep-resistant superalloys that are suited to service in high-speed flight environments. However, use of WAAM to deposit these alloys causes several issues which negatively affects the performance of the alloys. Specifically for precipitation-strengthened alloys which suffer from segregation of alloying elements and solidification cracking, which impacts their performance. With such issues occurring it is unlikely that WAAM alone produced parts would meet the stringent requirements for aerospace components and as such it is difficult to recommend the use of WAAM alone for the application.

With the use of in-process mechanical working the performance of precipitation-strengthened alloys can be restored. In-process working also demonstrates the ability to negate cracking issues. Further development of in-process working is required, but it is a promising area that is anticipated to make the use of WAAM more accessible for aerospace applications.

The following recommendations can be made as a result of the findings of this project (Section 9.1.6).

9.1.6 Recommendations

1. Maximising performance. In-process working should be used with WAAM when depositing precipitation-strengthened alloys, to restore tensile properties. Use of inter-pass peening disrupts the formation of long dendritic structures which are damaging to performance.
2. Alloy selection. If in-process working is not desired, use of a solidification-strengthened alloy is recommended for aerospace applications. This is due to the negative effects WAAM has on the formation of strengthening phases in precipitation-strengthened alloys.
3. Heat-treatments. Use of a standard post-deposition heat-treatment for precipitation hardened alloys is detrimental to performance if subject to service beyond 760 °C, which is thought is due to the alloy over-aging when in service at or around its aging temperature. It is therefore recommended to allow parts to age in service, which is particularly effective for short-duration missions.
4. Diffusion from the substrate. The use of an IN718 substrate with RE41 causes dilution of the substrate into deposited parts. It is therefore recommended, as initial guidance, to extract parts beyond 2.1 mm from the substrate to avoid any uncertainty in performance or, if cost is not a factor, use a substrate of the same alloy.

9.2 Contribution to Knowledge

The research gaps identified in section 1.2 have been filled by the completion of the studies detailed in this thesis. Suitable alloys were selected for high temperature performance and WAAM deposition. The selected alloys were then deposited and analysed for their mechanical performance and microstructural features, to understand the effect the WAAM process had on them compared to the wrought material. For the final down selected alloy, RE41, a processing strategy was developed to return the alloy to its wrought performance.

The work conducted as part of this PhD project resulted in the following scientific contributions:

1. RE41 is the most suitable alloy, of those tested, for performance at high temperature and for deposition using WAAM if additional processing is acceptable.
2. A plasma WAAM process can deposit both RE41 and H188.
3. As deposited superalloys underperform compared to their wrought strength, and standard industry heat-treatments do not result in significant improvements.
4. WAAM deposition causes cracking in RE41 and IN718, but H188 is not susceptible to cracking due to WAAM.
5. Segregation of heavier elements occurs in both RE41 and H188, resulting in intermetallic phase formation.
6. Use of inter-pass peening during WAAM deposition returns RE41 to wrought performance and reduces the susceptibility to cracking.

9.3 Conclusions

The following conclusions have been derived from this research project:

1. A plasma WAAM process can be used to deposit RE41 and H188.
2. As deposited WAAM material suffers from a reduced tensile performance, due to long columnar grains and cracking - due to segregation of heavier alloying elements. This is particularly true for precipitation-strengthened superalloys.
3. Use of solid-solution-strengthened superalloy is more appropriate for use in WAAM if additional processing is not desired.
4. Use of standard heat-treatments for both RE41 and H188 does not result in a significant performance increase.
5. Use of an inter-pass peening process results in an increased performance, as a result of crack mitigation and grain refinement.

9.4 Future Work

To increase the understanding of the effect WAAM has on the high temperature properties of creep-resistant superalloys and to further the development of suitable WAAM processes, the research could be extended as follows:

1. Identification of a process to reduce segregation of heavier elements during WAAM deposition and formation of undesirable intermetallic phases, such as solute additions to the alloy composition, to minimise precipitation of detrimental phases.
2. Testing of in-process peened RE41, with no post-process heat-treatment to access the effect of peening alone on microstructure and mechanical performance.
3. In-process peening and testing of H188, to compare with RE41 and to understand its effect on a solid-solution strengthened alloy.
4. Creep testing of deposited material to understand the effect of WAAM on creep properties, to increase the understanding of AM superalloys for the high-speed application.
5. Development of an optimised heat-treatment specifically designed for maximum strength in WAAM deposited RE41 and H188. Development could involve trailing increased solutionising temperatures to further dissolve tcp phases. Materials modelling could be beneficial in predicting parameters to best homogenise each WAAM alloy.
6. Potential for the application of predictive modelling of the WAAM process, to predict residual stress, distortion, and mechanical properties. This modelling could also benefit down selection of material applied to complex components.
7. Mechanical and microstructural investigation of WAAM material produced through replication of part building type geometries to replicate thermal profiles of built parts more accurately.
8. Investigation into the effect of machine-to-machine variability, to better inform how processes can be controlled for consistency. Review engineering equivalency against standards such as ISO/ASTM 52930.
9. Exploration of sonic or magnetic stirring of the weld pool as an alternative to inter-pass mechanical working. An investigation into this process would identify its feasibility for use with the WAAM process and the scale of impact on grain formation and/or crack mitigation

10. Non-destructive, acoustic resonance examination of precipitation content of depositions, to aid a quantitative understand of secondary phases distribution.
11. Development of a new alloy specifically suited to WAAM and high-speed flight applications. The possibility also exists for in situ alloying within the WAAM process by using multiple wire feedstocks.
12. Optimisation of material properties for high-speed flight by tweaking WAAM process parameters. Exploration of the impact of the WAAM process parameters on material properties. Use of simulation may be beneficial for this investigation.

9.5 References

[1] T. Antonsson, H. Fredriksson, The effect of cooling rate on the solidification of INCONEL 718, Metall. Mater. Trans. B. 36 (2005) 85–96. https://doi.org/10.1007/s11663-005-0009-0.

[2] X. Xu, Wire + Arc Additive Manufacture of New and Multiple Materials, Cranfield University, 2018. http://dspace.lib.cranfield.ac.uk/handle/1826/15107.

[3] X. Xu, S. Ganguly, J. Ding, C.E. Seow, S. Williams, Enhancing mechanical properties of wire + arc additively manufactured INCONEL 718 superalloy through in-process thermomechanical processing, Mater. Des. 160 (2018) 1042–1051. https://doi.org/10.1016/j.matdes.2018.10.038.